

Calorimetric investigation on plasma and ion beam sources used for thin film deposition

Dissertation

zur Erlangung des Doktorgrades
der Mathematisch-Naturwissenschaftlichen Fakultät
der Christian-Albrechts-Universität zu Kiel

vorgelegt von

Sven Gauter

Kiel, 2018

Erster Gutachter: Prof. Dr. Holger Kersten

Zweiter Gutachter: Prof. Dr. Hynek Biederman

Datum der Disputation und Druckreife : 26. September 2018

About this work

This thesis is part of my PhD studies in the Plasma Technology working group at the Faculty of Mathematics and Science of the Christian-Albrechts-University Kiel. Much of the work has been performed in collaborations with national and international partners. The central goal of my research is to study and understand the energy flux to a substrate which is in contact with a process plasma or an ion beam. The distinct focus of these investigation is on magnetron sputtering environments.

The thesis is organized in two main parts: An introductory part which is intended to provide the reader with the relevant theoretical background applicable to the investigations presented in the experimental results. And the second part, where a selection of the results obtained as a part of my PhD studies are presented in the form of peer-reviewed publications which are organized according to the measurement method and type of investigated system.

Additional to the relevant theory, the introductory part includes a chapter about the optimization of the passive thermal probe design and a detailed analysis of the calibration procedure. This part and the detailed description of the passive thermal probe are included, to point out some of the pitfalls that are encountered when working with thermal probes and give the reader insights into the details of this seemingly simple diagnostic method.

Abstract

The use of plasmas as an industrial processing tool is nowadays commonplace in a variety of industries. One of the most versatile plasma based appliances is the ion beam. Originating from atomic and nuclear research as well as from the space propulsion field, nowadays they are used in diverse fields such as medicine, biology or material sciences. A specialized application is the use for thin-film deposition, a domain that is typically dominated by magnetron sputtering processes. Magnetron sputtering is among the oldest and most widespread plasma based coating techniques and is established in the industry as one of the most important techniques for the production of thin functional coatings. For example, the production of products like the integrated circuit, CDs/DVDs or hard disc drives rely on the sputter deposition of thin films of various materials. Besides in these technologically critical products, Magnetron Sputtering is also widely used in more trivial applications like e.g. anti-reflection or decorative coatings.

Especially for surface modification and coating processes many investigations of the last decades have shown that the interaction between the plasma and the substrate is of critical importance. This interaction is characterized by the so called plasma-surface-interactions and is mainly determined by the particle and energy balance between plasma and surface. A substrate or a growing film which is in contact with a plasma, is exposed to an energy flux originating from various different processes. For example, energy can be transferred to the substrate from the impact of fast heavy particles like ions or neutrals or in a much less localized form by radiation or the bombardment by electrons. The distinction between the different processes is of specific importance since they influence the film growth and therefore the properties of the deposited film in different ways. To gain a better understanding and improve existing plasma based surface processes it is of fundamental importance to characterize the particle and energy flux, and through this, understand the underlying mechanisms.

The focus of this thesis is the measurement of the energy flux and the characterization of associated processes. Accordingly, measurements of the energy flux and related parameters were performed in an ion beam and a variety of different magnetron sputtering experiments. In the case of magnetron sputtering, the energy flux is fundamental due to its impact on the growing film, for gas aggregation sources (GAS) it can be used to gain information about the aggregation process of the nanoparticles and for the case of ion beams, relevant parameters regarding beam geometry and composition can be obtained. The measurements were primarily performed with two types of calorimetric probes: the active thermal probe (ATP) and the passive thermal probe (PTP). Although both probes produce the same measurement result, each has its particular advantages which make it more or less suitable depending on the specific environment. In all cases the energy flux measurements were performed in parallel with other techniques which were chosen to create the greatest synergy and allow to obtain a more complete picture.

As part of the advanced electric propulsion diagnostic (AEPD) platform the ATP was in-

tegrated into a measurement array comprised of a variety of beam diagnostics and methods for characterizing of the mechanical state of the thruster. The AEPD platform is designed to provide a standardized tool for thruster characterization which allows for effective classification and comparison between different systems. The results obtained in different environments and with different ion thrusters proofed the functionality of this platform and demonstrated the synergy that can be obtained from the comparison between the different diagnostics.

To investigate the effect of an external magnetic field in a confocal magnetron sputtering experiment, measurements with the ATP and a Langmuir probe (LP) have been performed. The results showed that the plasma conditions and the energy flux to the substrate change dramatically as a function of the additional magnetic field. By proper adjustment of the external field, the 'balance' of the magnetrons could be varied to increase the ion-to-neutral ratio by up to 30 times. The deposited sample films showed a clear correlation between the stress in the film and the ion flux density.

To study the composition of the energy flux in magnetron sputtering systems in a more general way, extensive measurements with PTP, quartz crystal microbalance (QCM) and Langmuir probe have been performed for various gas-target-combinations. The composition as well as the absolute magnitude of the energy flux was found to change strongly, even for the comparably simple case of dc magnetron sputtering with inert process gases. Depending on different process parameters, the energy flux was found to be dominated by either reflected neutrals, sputtered atoms or radiation from the hot target.

A less conventional application of magnetron sputtering can be found in gas aggregation sources (GAS). Here, the sputtered atoms are the starting point for an agglomeration process which produces particle clusters on the nano-scale. These nano-particles, by themselves or as part of functional films, can have astonishing properties and sparked their own field of science. To better understand the agglomeration process in the plasma, it is essential to know the conditions present in the aggregation source. To achieve this, the energy flux and deposition rate along with basic plasma parameters were measured inside a typical GAS. The results showed a comparable composition of the energy flux to the conventional lower pressure regime and indicated an important contribution to come from reflected neutrals, especially in cases where tungsten is part of the target material.

An innovative addition to the magnetron sputtering field is the combination of high-power impulse magnetron sputtering (HiPIMS) and plasma based ion implantation (PBII). This combination allows for cleaning, coating and doping in a single process and promises great possibilities for application. Since both processes are pulsed, it is especially the synchronization between HiPIMS and PBII which adds an additional interesting parameter to the system. To investigate this parameter and its effect on the energy flux to the substrate, a special setup of a PTP and a substrate made of a grid has been used to obtain an indirect measure of the energy flux to the PBII substrate. This setup was found to provide time-resolved information of the ion-density in the substrate region and indicated that ions travel as a relatively well-defined bunch or wave from cathode to substrate. In a subsequent set of measurements the grid-setup was replaced by a modified version of the PTP, which allowed for direct application of high-voltage pulses on the probe substrate. This way absolute values for the energy flux were obtained and the comparison with the substrate current provided insights into the secondary electron yield of the PBII substrate. The observed ion wave was identified in these measurements as well and by use of a time of flight method its transport

was identified to be strongly collision dominated.

As part of this thesis a thorough understanding of the calorimetric diagnostic and processes which create the measured energy flux in plasmas have been developed. These insights allowed to further refine many aspects of the PTP, both regarding its evaluation methods, the calibration process as well as its physical design.

Kurzfassung

Heutzutage ist der Einsatz von Plasmen als industrielles Werkzeug weit verbreitet und in einer Reihe von Industrien etabliert. Eine der vielseitigsten plasmabasierten Anwendungen ist der Ionenstrahl. Beginnend vom Ursprung in der Atom- und Nuklearwissenschaft als auch in der Raumantriebsforschung, findet er heutzutage in verschiedensten Gebieten wie der Medizin, der Biologie oder den Materialwissenschaften seine Anwendung. Eine spezialisierte Anwendung ist in der Nutzung zur Dünnschichtabscheidung zu finden, ein Feld in welchem das Magnetron Sputtering eine vorrangige Stellung einnimmt. Magnetron Sputtering zählt zu den ältesten plasmabasierten Beschichtungstechniken und hat sich in der Industrie zur Herstellung dünner funktioneller Schichten als eine der wichtigsten Techniken etabliert. So basiert beispielsweise die Herstellung von integrierten Schaltungen und auch von Festplatten auf der sputterbasierten Abscheidung von verschiedensten funktionellen Schichten.

Insbesondere im Bereich der Oberflächenmodifikation und Beschichtung zeigten eine Vielzahl von Untersuchungen, dass die Wechselwirkung zwischen Plasmen und dem zu behandelnden Substrat von besonderer Wichtigkeit ist. Diese Wechselwirkung wird unter dem Begriff der Plasma-Wand-Wechselwirkung (PWW) zusammengefasst und ist besonders durch den Teilchen- und Energieaustausch zwischen dem Plasma und der mit dem Plasma in Kontakt befindlichen Oberfläche bestimmt. Ein Substrat oder eine wachsende Schicht welches in Kontakt mit einem Plasma ist, ist einem Energiestrom ausgesetzt welcher durch unterschiedlichste Prozesse verursacht wird. So wird Energie beispielsweise durch das Auftreffen von schnellen schweren Teilchen wie Ionen oder Neutralen oder weniger lokalisierten Prozessen wie der Absorption von Strahlung oder dem Bombardement durch Elektronen übertragen. Die Unterscheidung zwischen den verschiedenen Prozessen ist von besonderer Bedeutung, da sie sich unterschiedlich auf das Schichtwachstum und somit auf die Eigenschaften der abgesetzten Schicht auswirken. Um ein besseres Verständnis über bestehende plasmabasierte Prozesse zur Behandlung oder Beschichtung von Oberflächen zu entwickeln und so diese Prozesse zu optimieren, ist es von grundlegender Wichtigkeit den Teilchen- und Energiefluss zu bestimmen und hierdurch die zugrundeliegenden Mechanismen zu verstehen.

Der Schwerpunkt dieser Arbeit liegt auf der Messung des Energiestroms auf ein Substrat welches in Kontakt mit einem Ionenstrahl oder dem Plasma von verschiedenen Magnetron Sputtering Systemen ist. Im Falle vom Magnetron Sputtering ist die Motivation hierfür wesentlich durch den Einfluss des Energiestroms auf das Schichtwachstum gegeben, während im Falle von Gasaggregationsquellen (GAS) die Bedingungen im Plasma für den Aggregationsprozess von besonderem Interesse sind. Für Ionenquellen wiederum kann die Messung des Energiestroms Aufschluss über die Strahlgeometrie und -zusammensetzung geben. Die Messungen wurden hauptsächlich mit zwei unterschiedlichen Formen von kalorimetrischen Sonden durchgeführt: der aktiven Thermosonde (ATP) und der passiven Thermosonde (PTP). Obwohl beide Sonden dieselbe Messgröße bestimmen, besitzt jede Form seine speziellen Vorzüge, wodurch die Wahl der richtigen Sonde abhängig von dem jeweiligen Experiment

gewisse Vorteile birgt. Bei allen Untersuchungen wurden zusätzlich zu den Energiestrommessungen weitere Diagnostiken verwendet, wodurch aus der Kombination der jeweiligen Ergebnisse ein besseres Gesamtbild erhalten werden kann und zudem Erkenntnisse gewonnen werden können, welche aus der separaten Messung nicht hervorgehen.

Als Teil der ‚advanced electric propulsion diagnostic‘ (AEPD) Plattform wurde die ATP in ein Array von verschiedensten Strahldiagnostiken und Methoden zur Charakterisierung des Triebwerkszustandes integriert. Die AEPD Plattform wurde als standardisierte Diagnostik zur Charakterisierung von Ionenstrahltriebwerken konzipiert, welche eine effiziente Klassifizierung und einen Vergleich zwischen verschiedenen Systemen ermöglicht. Die Ergebnisse, welche in verschiedenen Umgebungen und mit verschiedenen Triebwerken gesammelt wurden, bestätigten die Funktionalität der Plattform und demonstrierten das synergetische Potential welches durch die standardisierte Verbindung verschiedener Diagnostiken erreicht werden kann.

Messungen mit der ATP und einer Langmuirsonde in einem konfokalen Magnetron Sputtering System, welches durch eine zusätzliche elektromagnetische Spule erweitert wurde, zeigten, dass sich die Plasmaeigenschaften und hierdurch auch der Energiestrom auf das Substrat stark in Abhängigkeit des zusätzlichen Magnetfeldes ändern. Durch die Veränderung des externen Magnetfeldes lässt sich die ‚balance‘ der Magnetrons so verändern, dass sich das Verhältnis aus Neutralteilchen zu Ionen bis zu 30-fach erhöhen lässt. Die durchgeführten Testabscheidungen zeigten eine klare Korrelation zwischen der Spannung im Film und der Ionenflussdichte auf das Substrat.

Zur allgemeingültigen Untersuchung der Zusammensetzung des Energiestroms in einem Magnetron Sputtering System wurden umfassende Messungen mit der PTP, einer Quarzkristall-Mikrowaage (QCM) und einer Langmuirsonde (LP) unter Nutzung verschiedener Prozessgas-Kathodenmaterial Kombinationen durchgeführt. Sowohl für die Zusammensetzung als auch für die absolute Stärke des Energiestroms wurden hohe Veränderungen selbst in dem verhältnismäßig einfachen System des dc Magnetron Sputtering mit inerten Gasen festgestellt. In Abhängigkeit von verschiedenen Prozessparametern, wurde der Energiestrom entweder von reflektierten Neutralen, von gesputterten Atomen oder von der Wärmestrahlung eines heißen Targets dominiert.

Eine weniger konventionelle Anwendung von Magnetron Sputtering lässt sich im Bereich der Gasaggregationsquellen (GAS) finden. Hier bilden die atomaren gesputterten Teilchen die Grundlage für den Agglomerationsprozess zur Bildung von nanometergroßen Clustern. Diese Nanopartikel weisen beispielsweise in Form einer funktionellen Beschichtung außergewöhnliche Eigenschaften auf und ermöglichen eine Vielzahl von innovativen Anwendungen. Zur Erlangung eines umfassenden Verständnisses über den Entstehungsprozess im Plasma, ist es nötig die Bedingungen welche in der Aggregationskammer herrschen zu bestimmen. Um dies zu erreichen, wurde der Energiestrom und die Abscheiderate zusätzlich zu den wesentlichen Plasmametern in einer typischen GAS untersucht. Die Ergebnisse zeigen eine vergleichbare Zusammensetzung des Energiestroms wie er auch im konventionellen Druckbereich zu finden ist. Weiterhin deuten die Ergebnisse darauf hin, dass besonders reflektierte Neutrale eine wesentliche Rolle spielen, was insbesondere dann gilt, wenn das Kathodenmaterial Wolfram beinhaltet.

Eine innovative Ergänzung des Magnetron Sputtering ist durch die Kombination von Hochenergieimpulsmagnetronspattern (HiPIMS) mit Plasmabasierter Ionenimplantation (PBII)

gegeben. Die Kombination beider Techniken ermöglicht Reinigung, Beschichtung und Dotieren in einem Prozess darzustellen, wodurch sich vielseitige Anwendungsmöglichkeiten ergeben. Da es sich bei beiden Prozessen um gepulste Techniken handelt, ist insbesondere die Synchronisation der Pulse von Interesse, da sich hierdurch ein weiterer interessanter Parameter zur Einstellung des Prozesses ergibt. Um diesen Parameter und dessen Auswirkung auf den Energiestrom auf das Substrat zu untersuchen, wurde ein spezieller Aufbau entwickelt, welcher durch den Einsatz eines Gitters eine indirekte Messung des Energiestroms auf das Substrat ermöglicht. Mit diesem Aufbau konnten zeitaufgelöste Informationen über die Ionendichte im Bereich des Substrates erhalten werden und die Ergebnisse ließen darauf schließen, dass sich die Ionen in Form einer relativ klar definierten Ansammlung oder Welle von der Kathode zum Substrat bewegen. In einer nachfolgenden Untersuchung wurde der Gitteraufbau durch eine modifizierte Version der PTP ersetzt, welche es ermöglichte das Messsubstrat der PTP direkt als PBII-Substrat zu verwenden. Auf diese Weise konnten absolute Werte für den Energiestrom bestimmt werden und durch Vergleich mit dem Substratstrom Informationen über die Emission von Sekundärelektronen aus dem Substrat erhalten werden. Auch hier wurde die bereits beobachtete Ionenwelle identifiziert und mittels Flugzeituntersuchung konnte bestimmt werden, dass der Transport dieser Welle stark durch Stöße mit dem Hintergrundgas bestimmt ist.

Als Teil dieser Arbeit wurde ein grundlegendes Verständnis der kalorimetrischen Messmethode entwickelt und die Prozesse welche dem Energiestrom in Plasmen zugrunde liegen intensiv untersucht. Die gewonnenen Einsichten wurden unter anderem dazu genutzt die passive Thermosonde weiter zu optimieren indem sowohl die Auswertmethodik als auch der Kalibrierprozess und das Sonden Design an vielen Stellen verbessert wurden.

List of Publications

This thesis is partly based upon the following compilation of peer-reviewed papers which are either already published or submitted for publication.

- [I] C. Bundesmann, C. Eichhorn, F. Scholze, D. Spemann, H. Neumann, D. Pagano, S. Scaranzin, F. Scortecci, H.J. Leiter, **S. Gauter**, R. Wiese, H. Kersten, K. Holste, P. Köhler, P.J. Klar, S. Mazouffre, R. Blott, A. Bult and K. Dannemayer, 'An advanced electric propulsion diagnostic (AEPD) platform for in-situ characterization of electric propulsion thrusters and ion beam sources', *The European Physical Journal D*, vol. 70, p. 212, 2016.
- [II] M. Trant, M. Fischer, K. Thorwarth, **S. Gauter**, J. Patscheider and H.J. Hug, 'Tunable ion flux density and its impact on AlN thin films deposited in a confocal DC magnetron sputtering system', *Surface & Coatings Technology*, vol. 348, p. 159-167, 2018.
- [III] **S. Gauter**, F. Haase and H. Kersten, 'Experimentally unraveling the energy flux originating from a DC magnetron sputtering source', *Thin Solid Films* (submitted), 2018.
- [IV] **S. Gauter**, F. Haase, P. Solar, O. Kylian, P. Kus, A. Choukourov, H. Biederman and H. Kersten, 'Calorimetric investigations in a gas aggregation source', *Journal of Applied Physics* (submitted), 2018.
- [V] **S. Gauter**, M. Fröhlich, W. Garkas, M. Polak and H. Kersten, 'Calorimetric probe measurements for a high voltage pulsed substrate (PBII) in a HiPIMS process', *Plasma Sources Science and Technology*, vol. 26, p. 065013, 2017.
- [VI] **S. Gauter**, M. Fröhlich and H. Kersten, 'Direct calorimetric measurements in a PBII and deposition (PBII&D) experiment with a HiPIMS plasma source', *Surface & Coatings Technology* (article in press), 2018.

Contents

Preface	i
Abstract	iii
Kurzfassung	vii
List of Publications	xi
1 Introduction	3
2 Plasma State	7
2.1 The plasma state of matter	7
2.1.1 Universal plasma properties and definitions	7
2.1.2 Low temperature plasmas	9
2.1.3 Debye shielding	9
2.1.4 The plasma sheath and the Bohm criterion	11
2.1.5 Effect of electric and magnetic fields	14
2.2 Energy Balance and Plasma Surface Interactions	17
2.2.1 The total energy flux	18
2.2.2 Energetic Particles	18
2.2.3 Particles emitted from the surface and surface processes	24
2.2.4 Radiation	28
2.2.5 Conductive and convective energy flux	29
3 Technological Plasmas	33
3.1 Basic mechanisms of plasma generation	33
3.2 Ion Beams and Ion Thrusters	36
3.2.1 The Radio Frequency Ion Thruster	37
3.3 Magnetron Sputtering	38
3.3.1 Direct Current Magnetron Sputtering (DCMS)	38
3.3.2 High Power Impulse Magnetron Sputtering (HiPIMS)	42
3.3.3 Gas Aggregation Cluster Source (GAS)	43
3.4 Plasma Based Ion Implantation and Deposition (PBII&D)	44
4 Plasma Diagnostics	47
4.1 Electrostatic probing - the Langmuir probe	47
4.1.1 The U-I-characteristic	47
4.1.2 Evaluation of the U-I-characteristic	49
4.2 Quartz Crystal Microbalance	50

4.3	Calorimetric Probe	51
4.3.1	Grouping of the energy flux contributions	52
4.3.2	Passive thermal probe (PTP)	52
4.3.3	Active thermal probe (ATP)	60
4.3.4	Comparison of the PTP and the ATP	66
5	Optimization and calibration of the Passive Thermal Probe	67
5.1	Calibration - determination of the heat capacity	67
5.1.1	Calibration with an electron beam	68
5.1.2	Calibration with an ion beam	76
5.1.3	Calibration with equilibrium temperature method	77
5.2	Hardware and software design	78
5.2.1	Software design	79
5.2.2	Hardware design	79
6	Experimental Results	83
	Publication [I]: An advanced electric propulsion diagnostic (AEPD) platform for in-situ characterization of electric propulsion thrusters and ion beam sources	85
	Publication [II]: Tunable ion flux density and its impact on AlN thin films deposited in a confocal DC magnetron sputtering system	99
	Publication [III]: Experimentally unraveling the energy flux originating from a DC magnetron sputtering source	109
	Publication [IV]: Calorimetric investigations in a gas aggregation source	131
	Publication [V]: Calorimetric probe measurements for a high voltage pulsed sub- strate (PBII) in a HiPIMS process	145
	Publication [VI]: Direct calorimetric measurements in a PBII and deposition (PBII&D) experiment with a HiPIMS plasma source	157
7	Conclusion and Outlook	167
	Bibliography	179
	Curriculum Vitae	I
	Acknowledgments	III

1 Introduction

Plasmas are not intuitively understandable to humankind and in fact most people would rather connect the term plasma to the blood plasma instead of an ionized gas. On one hand this is because plasmas, in most of their forms, are not compatible with human life, but more importantly it is due to the fact that they are seldom encountered in everyday life. This is in spite of the fact that more than 99% of the visible universe is in the plasma state. So what is the reason for this apparent contradiction?

Most of the matter in the universe is agglomerated in stars in the state of a thermal plasma created by the immense gravity and the energy supplied by nuclear fusion and additional to that, the interstellar and the intergalactic medium is in the plasma state as well [1]. On earth on the opposite, plasmas seldom appear natural because the average temperature is extremely low compared to the conditions found on the stars in the universe. Due to their exotic nature and apparent randomness of appearance, natural plasmas were typically perceived as the work of gods and often interpreted as a sign of bad fate. Comets were thought to forecast disasters like the outbreak of a plague or a war, lightning was attributed to an angry Zeus and one of the many interpretations of the Aurora Borealis explained it as the reflection or glow from shields and armor of the Valkyrie, see figure 1.1.



Figure 1.1: Examples of natural plasmas observable from earth. From left to right: A comet with a glowing tail made from plasma [1], lightning [2], aurora borealis [2].

Only in the past 200 years mankind has learned to generate and contain plasmas artificially and to use them to their own benefit. This resulted in an exponential increase of the understanding of plasmas and produced a wide field of technological applications. Without some of these applications like microprocessors, our modern digital world would not be possible. A large branch of research in the field of plasma physics was sparked by the desire to reproduce the energy production of the sun. In principle nuclear fusion can be achieved by confining a plasma with a magnetic field in such a way that it will only transfer so little energy to containing walls that it can be effectively heated up to temperatures beyond those present on the stars. However, this task turned out to require research at the forefront of such a variety of different fields of science, that it is still uncertain how much time is needed to

successfully fulfill it. Another traditional domain for plasma applications, which represents a less challenging environment, is the use for lighting. For years, low-pressure discharges in fluorescent tubes were the omnipresent light source associated with any office space or public building, bright high-pressure electric arc lamps lighted the streets and the rise of energy-saving lamps is marked by the flickering and slow increase in brightness when switching on a compact fluorescent lamp. Only recent development in LED technology provided a superior method for lighting and slowly replaces plasma lamps in most applications. Another field of plasma technology which is affecting our modern life in an ever increasing way is related to the semiconductor industry. Without the development of low temperature plasmas, which allow for material processing on the nanometer scale, the production of modern integrated circuits would have not been possible. Nowadays, microprocessors and the products which evolved from this technology, accompany our everyday live in the form of smartphones, computers or even smart home appliances. Parallel to the rise of the application as a processing tool in the semiconductor industry, plasma technology has spread into various industrial fields where it is used for surface cleaning, coating, modification and activation and has been established as one of the predominant processes for the coating with technological thin films. In most of these application the key quality which differentiates it from other methods, is the pronounced non-equilibrium between electrons and the more heavy particles in the plasma. This allows to enhance and trigger chemical reactions which require high energies, without exposing the treated material to high thermal loads. Furthermore, the precise adjustment of the plasma properties through magnetic and electric fields, allows to control plasma based processes at a speed and level of accuracy which is unmatched by comparable thermal or chemical processes.

These advantages have motivated ongoing development and creation of new plasma based thin film deposition techniques. One of the first and most widespread plasma based deposition techniques is direct current magnetron sputtering (DCMS) where material of a solid cathode is evaporated by bombardment with energetic ions. The sputtered atoms can then condense on a substrate positioned close to the evaporation source to build a thin film. One of the most noted enhancement of DCMS is the high-power impulse magnetron sputtering (HiPIMS), where the DC power supply used in conventional magnetron sputtering is replaced by a low frequency pulsed power supply. The reduction of the duty cycle achieved by this technique allows to apply high voltages without overheating the target and consequently generates a more highly ionized plasma. This higher degree of ionization not only creates films with superior properties but also allows the combination with plasma based ion implantation processes (PBII) which are used for doping materials by implantation of atoms. These so-called plasma based ion implantation and deposition (PBII&D) systems can be used to combine multiple process steps into a single system and, thus, create new, or refine present applications. Another innovative application of magnetron sputtering can be found in gas aggregation chambers (GAS), where the magnetron cathode is used as a particle source in the aggregation process of nanometer sized clusters of atoms. This technique has evolved to be one of the most important techniques for the production of nanoparticles and nanoparticle-enhanced thin films.

To fully exploit the advanced techniques for process control available in plasma based technological applications, it is essential to understand the processes in the plasma and the interaction of the plasma with the substrate. This can only be achieved by applying extensive

diagnostics on these processes, which resulted in the development of a vast array of diagnostic tools. These include relatively simple methods like the measurement of plasma parameters with a Langmuir probe or the detection of depositing flux with quartz crystal microbalances but also created a whole field of optical diagnostics or complex diagnostic systems like energy resolved mass spectrometers. One diagnostic which has proven to be particularly useful for thin film deposition processes is the calorimetric probe. This type of probe allows to obtain the energy flux to a substrate exposed to a plasma and, thus, provides critical information regarding the thermal load on the substrate and about the energy available during film formation. The experimental determination of process parameters is not only of central importance for monitoring industrial processes, but is also at the heart of any simulation, either for comparison of the results, or directly as an input parameter to the theoretical model. The collection and evaluation of experimental data and the refinement of diagnostic methods is thus essential to the development of improved systems and for the prediction of the effect of process parameters on the desired outcome.

2 Plasma State

2.1 The plasma state of matter

Plasmas are often called the 'fourth state of matter' which is due to the fact that a plasma can be created by adding a sufficient amount of energy to a substance in the gaseous state. Where for a solid substance to pass into the liquid state, the enthalpy of fusion needs to be provided and for a liquid substance to pass into the gaseous state, the enthalpy of vaporization needs to be added to the system, a similar concept applies for the transition from the gaseous state to the plasma state. For a mono-atomic gas, as more and more energy is added to the system, at some point the energy will be high enough that the ionization energy can be overcome and accordingly the neutral atoms will separate into electrons and ions and a plasma is formed.

The purpose of this chapter is to give a basic introduction into the fundamental concepts of plasma physics. In the first section, some general properties which are common to all types of plasmas are introduced, while in the second section, important phenomena observed especially in low temperature plasmas are described in more detail. For a detailed and exhaustive description of the plasma state of matter the reader is advised to the standard text book literature [3–7].

2.1.1 Universal plasma properties and definitions

Although the roots of plasma physics date back to the 17th century, the ground for modern plasma physics, was only laid in the 20th century by Irving Langmuir and his co-workers [8]. In his work 'Oscillations in ionized gases', Langmuir was the first to introduce the term *plasma* which he described as a region of 'balanced charges of ions and electrons'. Through systematic investigations and proper explanation by mathematical models, they formulated some of the general laws which still define our modern concept of a plasma. In principle, it is characterized using the same terminology as used for a neutral gas, which is primarily described by the number of particles per unit volume n and by their motion which is determined by the temperature T . While the ideal gas consists of a single species only, the plasma must be described as a mixture of two individual gases: the light electrons and the heavy ions. To distinguish between these two, individual densities (n_e , n_i) and temperatures as a measure of the average energy (T_e , T_i) are assigned to electrons and ions.

Quasi neutrality

By definition, a plasma must contain equal numbers of ions and electrons, or more generally speaking, an even number of negative and positive charges:

$$\sum_k q_k n_{i,k} - e_0 n_e = 0. \quad (2.1)$$

Here, q_k depicts the charge of the ion which can be both positive or negative and also includes the possibility of multiply charged ions. For a single ion species of charge $q_k = +e_0$ the quasineutrality condition can be reduced to a condition for equal charge densities $n_i = n_e$. From equation 2.1 it can be seen that the plasma is neutral from a macroscopic point of view, however, as described in the next section this does not have to be true on the microscopic scale. To account for this deviation from neutrality, which in fact is an essential characteristic of the plasma, the supplement *quasi* was added to the term.

Collective behavior

In opposition to a neutral gas where atoms only interact with each other according to the short-range van der Waals forces (r^{-6}), in a plasma, the particle interaction is based on the Coulomb force which decays on a much longer scale (r^{-2}). As a result, each plasma particle interacts with a large number of other particles and, thus, a *collective behavior* is created. This collective behavior is the basis for some of the most fascinating qualities observed in a plasma such as the Debye-shielding or plasma wave phenomena [5].

Classification of plasmas

Plasmas are typically classified according to the density of electrons n_e and their energy as characterized by the electron temperature T_e . The range of these parameters illustrate the diversity of the plasma state with the density scale covering more than 25 decades and the temperature ranging from only a few Kelvin for the interstellar space all the way up to 100 000 000 K for man-made fusion plasmas. This vast field of plasmas can be divided into different regions e.g. into relativistic plasmas, ideal plasmas, degenerate plasmas [9] or according to the coupling between the particles as strongly coupled quantum plasmas, strongly coupled classical plasmas and weakly coupled classical plasmas [5]. For the description of technical plasmas, however, these distinction are too general and, thus, not suited for the distinction between typical technical plasmas. Instead, here, it is more practical to classify plasmas according to the thermodynamic equilibrium between the ions and electrons. Since most technical discharges are electrically driven and the applied power preferentially heats the mobile electrons, these plasmas are typically in thermodynamic non-equilibrium. Due to the weak coupling between heavy particles (ions, neutral atoms) and electrons the energy cannot be efficiently dissipated and in the common case of weakly ionized plasmas, the ions efficiently exchange energy by collisions with the background gas. Accordingly, the electrons T_e depict a much higher temperature than the ions T_i , which in most cases are at a similar temperature to the background gas T_n :

$$T_e \gg T_i \approx T_n. \quad (2.2)$$

Since these plasmas would be relatively cold to the touch, they are commonly referred to as *low temperature plasmas*. The opposite case of *high temperature plasmas* is typically associated with almost completely ionized plasmas such as they are found in the sun or also in some technical applications like arc discharges. Another commonly used classification of technological plasmas is according to their background gas pressure. Here, it is typically differentiated between *high pressure plasma* (HPP), *atmospheric pressure plasma* (APP) and *low pressure plasma* (LPP). While HPP applications can mostly be found in arc discharge lamps, APPs and LPPs are more commonly used in industrial applications with most notable plasma sources of APPs being plasma jets or dielectric barrier discharges and of LPPs being thin film deposition plasmas (magnetron sputtering, plasma-enhanced chemical vapor deposition) or plasmas for etching of semiconductors.

2.1.2 Low temperature plasmas

Low temperature plasmas (LTP) are characterized by a strong thermal non-equilibrium between ions and electrons and are usually generated in a low pressure environment. The artificial state of thermal non-equilibrium has several advantages which can be exploited for technical applications:

- The well defined heating with electric fields allows a controlled and direct method of energy input and even tailoring of the energy distribution in the plasma.
- Due to the strong reduction of thermal losses, the selective heating of electrons allows to create a highly energetic environment with superior efficiency.
- The storage of energy in the electrons allows to initiate chemical processes, which usually require high energies, at background gas temperatures near room temperature and additionally provides improved process control.
- Due to the low temperature of heavy species, treatment of temperature sensitive materials like polymers is possible.

2.1.3 Debye shielding

One of the most important features of a plasma is its ability to shield charges and reduce electric fields. The underlying effect can best be understood by imagining a charge $+Q$ placed in an infinitely large homogeneous plasma. According to Langmuir's definition, the plasma initially is quasineutral and as a LTP the electrons have a significantly higher temperature than the ions. It can be expected, that the electrons are attracted and the ions repelled by this additional charge. As a result, the trajectories of the particles will change slightly towards or away from the charge, resulting in a region with a net negative charge around Q as sketched in figure 2.1. This negative potential effectively screens the electric field of the positive charge and changes the Coulomb potential towards the more rapidly decaying Debye-Hückel potential:

$$\Phi(r) = \frac{Q}{4\pi\epsilon_0 r^2} e^{-r/\lambda_D} \quad (2.3)$$

In this equation $Q/(4\pi\epsilon_0 r^2)$ is the undisturbed Coulomb potential and the exponential term describes the shielding effect of the space charge. As illustrated in figure 2.1, the Debye-Hückel potential decays exponentially and at the distance λ_D the electric field has decreased to e^{-1} of its original strength. The parameter λ_D is called the linearized Debye shielding length which describes the combined shielding action of electrons and ions:

$$\lambda_D^{-2} = \lambda_{D,e}^{-2} + \lambda_{D,i}^{-2}. \quad (2.4)$$

The individual contribution to the shielding can be calculated with Poisson's equation and the Boltzmann factor to yield [5]:

$$\lambda_{D,e} = \left(\frac{\epsilon_0 k_B T_e}{n_e e_0^2} \right)^{1/2}, \quad \lambda_{D,i} = \left(\frac{\epsilon_0 k_B T_i}{n_i e_0^2} \right)^{1/2}. \quad (2.5)$$

These equations confirm, what appears intuitively, that for a lower temperature of the charged species, the shielding is more effective. Since in LTPs $T_e \gg T_i$ this means, that the electrons are the defining species for the size of the Debye sphere and that for LTPs, $\lambda_D \approx \lambda_{D,e}$ can be assumed.

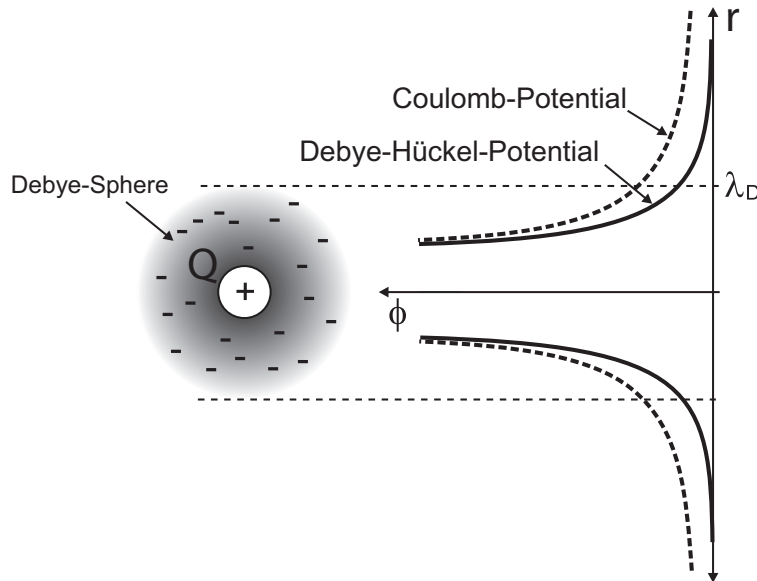


Figure 2.1: Illustration of the Debye shielding for a charge Q immersed in the plasma, along with the unperturbed Coulomb potential and the Debye-Hückel potential. It should be noted that the negative charge around Q is not stationary but that the negative net-charge in this region is due to small changes of the electron trajectories towards the positive charge. Illustration adapted from [9].

Inside of the Debye sphere, a space charge unequal to zero is present and, thus, on this small scale the rule of quasineutrality is breached. Since a plasma, however, by definition must be quasineutral, this observations creates a lower limit of several Debye length $L \gg \lambda_{D,e}$ for the minimal size L of the plasma as it can only restore quasineutrality on this bigger scale. To ensure that the statistical derivation of the Debye length was correct, it is required that many electrons are inside the electron Debye sphere. For this purpose, the plasma parameter $N_{D,e}$ is defined as the number of electrons inside the electron Debye sphere, which must always

be much greater than one:

$$N_{D,e} = \frac{4\pi}{3} \lambda_{D,e}^3 n_e \gg 1. \quad (2.6)$$

From the size of the Debye sphere, a second aspect of the collective behavior can be defined: the electron plasma frequency $\omega_{p,e}$. This parameter describes how fast the plasma can react to an external perturbation i.e. how fast the plasma can compensate any disturbance of its quasineutrality. Since the electrons are much more mobile than the heavier ions, the plasma frequency can be estimated from the ratio between the thermal velocity $v_e \approx \sqrt{k_B T_e / m_e}$ and the typical distance an electron needs to cover for restoring quasineutrality $\lambda_{D,e}$:

$$\omega_{p,e} = \frac{v_e}{\lambda_{D,e}} = \sqrt{\frac{n_e e_0^2}{\epsilon_0 m_e}}. \quad (2.7)$$

Here, m_e stands for the electron mass. The plasma frequency not only defines the minimum lifespan of a plasma $t_{min} \gg \omega_{p,e}^{-1}$ but also represent a descriptive parameter for the understanding of the interaction between electromagnetic waves and the plasma. Longwave radio waves (~ 300 kHz) for example, have a frequency much lower than typical plasma frequencies in the ionosphere (~ 60 MHz) and are thus mostly reflected by the plasma, whereas visible light (~ 500 THz) can pass through relative freely [9]. Another technically relevant example are short wave radio frequencies which are in the range of typical electron plasma frequencies. Due to the similar frequencies, energy can be efficiently transferred to the electrons in the plasma, while the ions with their much lower frequency cannot react to the changes in the electric field and remain at a low energy.

2.1.4 The plasma sheath and the Bohm criterion

The plasma sheath

Since all technical plasmas are necessarily in contact with some containing material such as a vacuum chamber, the transition region between plasma and wall is of specific interest. Because of the action of Debye shielding, even when in contact with a conducting wall, the plasma will remain quasineutral and a space charge sheath will develop close to the surface. This region is called the *plasma sheath*, or simply the *sheath* and the position where quasineutrality is established is called the *sheath edge*. Due to the higher thermal velocity of the electrons, an initially uncharged wall will be hit more often by electrons than ions and if the wall is not connected to any potential, i.e. it is floating, the wall will charge up to a negative potential with respect to the electric potential Φ_{pl} inside the quasineutral plasma. The equilibrium potential of the wall is determined by the balance between ions and electrons, since due to the negative potential, the number of electrons that can reach the wall diminishes as the wall charges up. The resulting equilibrium value is called the *floating potential* Φ_{fl} . Figure 2.2 gives a schematic drawing of the evolution of ion and electron densities and the associated potential for a plasma in contact with a floating wall. For completeness, here, a transition layer called *pre-sheath* is introduced which matches the conditions between the plasma sheath and the unperturbed plasma. The formation of the plasma sheath and the pre-sheath not only explains the charging of surfaces observed for all

materials in contact with a plasma, but also results in a sensitive condition for the velocity of the ions which are able to escape the plasma. This velocity is defined by the Bohm criterion, named after David Bohm who formulated this criterion in 1949 [10].

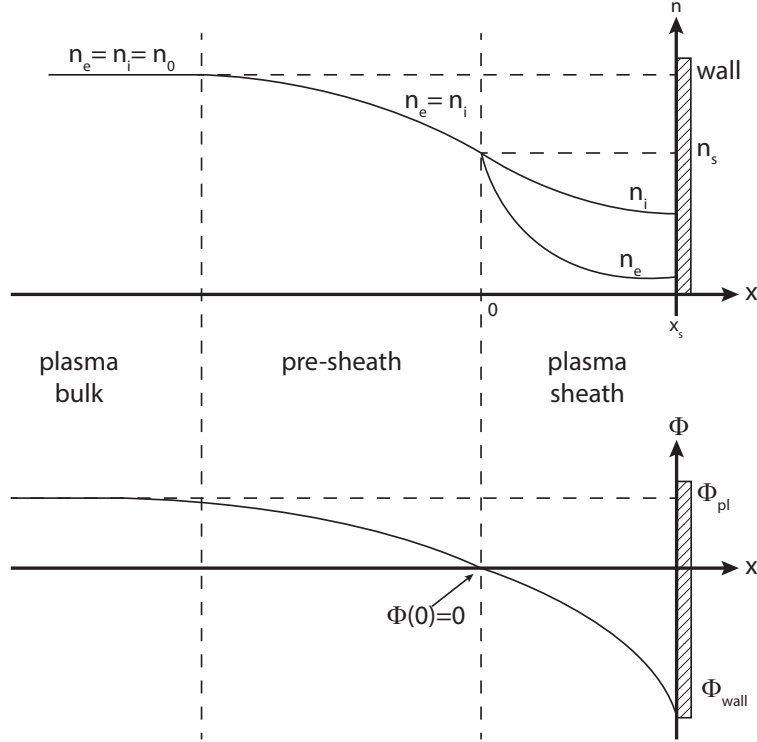


Figure 2.2: Schematic drawing of the plasma-wall boundary layer. The upper picture shows the evolution of the electron and ion densities from the quasineutral plasma through the pre-sheath and the plasma sheath to the floating wall. The lower picture shows the corresponding potential in these regions. Illustration by courtesy of F. Haase, adapted from [3].

The Bohm criterion

The Bohm criterion arises from a stability analysis of the sheath and results in the requirement for a pre-sheath where the ions are accelerated from their thermal velocity to the Bohm velocity v_B [3]. Based on the conservation of ion flux from the plasma to the wall, together with the Boltzmann relation for the electron density, the sheath potential can be obtained by solving Poisson's equation. For a collisionless sheath it can be shown, that the speed v_s of the ions entering the sheath, at the sheath edge must be equal to, or exceed a certain speed called the Bohm velocity v_B :

$$v_s \geq v_B = \left(\frac{k_B T_e}{m_i} \right)^{1/2}. \quad (2.8)$$

If the ions would have a speed smaller than v_B , this would result in an expansion of the pre-sheath into the plasma until the point, where the potential drop in the pre-sheath is big enough to provide sufficient acceleration for the ions to reach v_B . However, from the requirement of an accelerating potential in the pre-sheath, together with the assumption of

quasineutrality in this region, the change of ion velocity v_i as a function of the distance x traveled in the pre-sheath can be calculated as

$$\frac{dv_i}{dx} = \frac{\nu_{mi}v_i^2}{v_B^2 - v_i^2}, \quad (2.9)$$

with ν_{mi} being the collision frequency for momentum loss through collisions with the background gas [5]. From this equation it can be seen that the ions are accelerated for $v_i < v_B$, however not beyond v_B . Accordingly, at the sheath edge, which defines the border between pre-sheath and sheath, the full Bohm criterion must read $v_s = v_B$.

As indicated in figure 2.2, at the sheath edge the potential must be equal to zero, which follows from equation 2.9. From the conservation of energy one can then calculate the potential drop between plasma and sheath edge, which must be equal to the plasma potential Φ_{pl} :

$$\Phi_{pl} = \frac{1}{2} \frac{k_B T_e}{e}. \quad (2.10)$$

From the spatial variation of the potential according to the Boltzmann relation, it is further possible to estimate the ion and electron density at the sheath edge $n_{e,s}$, $n_{i,s}$ with respect to the electron density in the plasma n_e :

$$n_{i,s} = n_{e,s} = n_e \exp\left(-\frac{1}{2}\right) \approx 0.61n_e. \quad (2.11)$$

The matrix sheath

The *matrix sheath* is the simplest plasma sheath which only develops if a step-like high voltage pulse V_0 is applied to the wall in contact with the plasma such as in the case of PBII (see chapter 3.4). Upon application of a high voltage pulse, the mobile electrons are pushed out of the sheath, leaving behind a matrix of ions with uniform density equal to the plasma density n_0 , while the electron density in this type of sheath equals zero. From the Maxwell equations the sheath thickness d_s for the matrix sheath can be calculated as a function of the potential difference V_0 between plasma and wall to be:

$$d_s = \left(\frac{2\epsilon_0 V_0}{en_0}\right)^{1/2} = \lambda_D \left(\frac{2eV_0}{k_B T_e}\right)^{1/2}. \quad (2.12)$$

Using equation 2.5 and with typical values for $e_0/k_B T_e$ in the range of only few eV, it can be directly seen that such a plasma sheath can easily expand over several debye length.

The Child-Langmuir sheath

Although originally formulated to describe the space-charge limited electron flow in a vacuum diode with fixed separation d_s between cathode and anode, the Child-Langmuir law is also applicable to the sheath formed around a wall in contact with a plasma. The space-charge limited current can be derived from the conservation of ion energy and the continuity of ion flux as the ions are accelerated through the sheath [3]. Using Poisson's equation the current

density j_0 for the case of a collisionless ions can be derived as:

$$j_0 = \frac{4}{9} \epsilon_0 \left(\frac{2e}{M_i} \right)^{1/2} \frac{V^{3/2}}{d_s^2}. \quad (2.13)$$

Here, M_i is the ion mass and V the potential difference between cathode and anode. In the case of the plasma sheath, the current is defined by the Bohm velocity v_B and the density of the unperturbed plasma n_0 as

$$j_0 = en_0 v_B. \quad (2.14)$$

Since in the plasma sheath, the current density and the potential difference are defined by the plasma parameters, the sheath thickness must adapt to comply with the Child-Langmuir law. Combining and rearranging equations 2.13 and 2.14 and introducing the electron Debye length defined in equation 2.5, the thickness of the plasma sheath can be calculated to be [3]:

$$d_s = \frac{\sqrt{2}}{3} \lambda_D \left(\frac{2eV}{k_B T_e} \right)^{3/4}. \quad (2.15)$$

If the ions undergo many collisions on their path through the sheath, the assumption of collisionless ions is not valid anymore since the collisions limit the velocity of the ions. The case of the collision dominated sheath is typically described by two extreme cases: the cases of constant mean free path λ_{mfp} and the case of constant collision frequency ν_{mi} . For both assumptions, the ion density cannot reduce as fast as in the case of collisionless ions and accordingly, the current density scales differently with the sheath thickness. For the case of constant λ_{mfp} , the ion current density can be calculated as

$$j_0 = \frac{2}{3} \left(\frac{5}{3} \right)^{3/2} \epsilon_0 \left(\frac{e \lambda_{mfp}}{M_i} \right)^{1/2} \frac{V^{3/2}}{d_s^{5/2}}, \quad (2.16)$$

and for the case of constant collision frequency the current density is given by

$$j_0 = \frac{9}{8} \epsilon_0 \nu_{mi} \frac{V^2}{d_s^3}. \quad (2.17)$$

2.1.5 Effect of electric and magnetic fields

One of the great qualities of a plasma, is the fact that it can be manipulated by electric or magnetic fields. Considering only a single-particle model, the acceleration $\dot{\mathbf{v}}$ of any charged particle in the plasma is determined by Newton's equation of motion and the Lorentz equation. For a particle with mass m and charge q in a three dimensional electric field \mathbf{E} and magnetic field \mathbf{B} , this equation reads

$$m \dot{\mathbf{v}} = q(\mathbf{E} + \mathbf{v} \times \mathbf{B}). \quad (2.18)$$

For the case without electric field $\mathbf{E} = 0$ and with a magnetic field $\mathbf{B} = (0, 0, B_z)$ perpendicular to the initial motion of the charge, the particle follows a periodic circular motion around the magnetic field line. The frequency of this motion is called *cyclotron frequency*

and is defined as [5]

$$\omega_c = \frac{|q|}{m} B_z. \quad (2.19)$$

The corresponding radius r_L of this motion is called *Larmor radius* or *gyration radius* and can be calculated as a function of the perpendicular velocity v_\perp to the magnetic field as

$$r_L = \frac{v_\perp}{\omega_c} \quad (2.20)$$

If the charged particles has an initial velocity not strictly perpendicular to the magnetic field, the orbital path of the charge expands into a helix motion in the direction of the initial motion parallel to the magnetic field line. For the case that the charge can perform a complete gyroorbit before undergoing a collision (with other particles or a wall), the charged particle is called *magnetized* as it is effectively bound to the magnetic field lines. Since the Larmor radius is quite large for ions, in technological plasmas ions can only be magnetized with extremely high magnetic fields, electrons on the opposite, can be easily magnetized even with small magnetic fields.

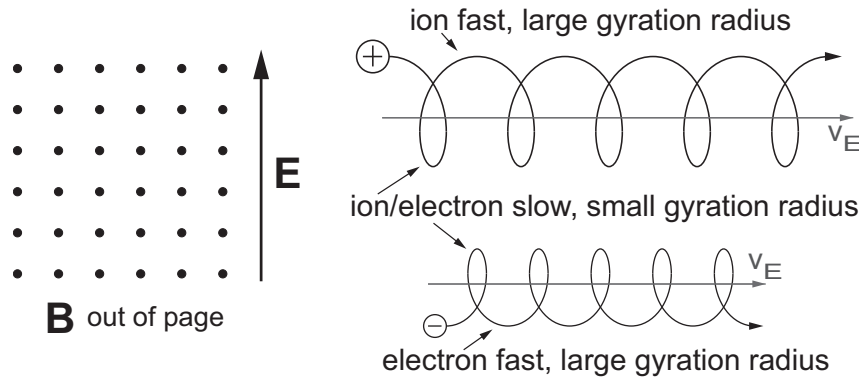


Figure 2.3: Schematic illustration of the cycloidal trajectory resulting from the combined effect of electric and magnetic field.

If any additional force acts on the particles or if the magnetic field is nonuniform, the simple orbital motion becomes more complicated, resulting in complex drift motions. Some examples are the gravitational drift created by the gravitation force, the gradient drift created by inhomogeneous parallel magnetic field lines or the curvature drift created by curved magnetic field lines [5]. One of the most important drift mechanisms is the $E \times B$ -drift which always appears, when both a magnetic and an electric field is present. The superposition of the acceleration by the electric field and the gyration motion created by the magnetic field results in a cycloidal motion with a drift velocity \mathbf{v}_E given by

$$\mathbf{v}_E = \frac{\mathbf{E} \times \mathbf{B}}{B^2}. \quad (2.21)$$

The resulting motion of an electron or an ion is schematically illustrated in figure 2.3. The magnetic field could be replaced by any other external force field such as e.g. the gravitational field. The principal for this motion can be easily understood from equation 2.20, which gives the gyration radius as a function of the particle velocity: As the particle gyrates around the

magnetic field line, its motion will be accelerated on one half of its orbit and decelerated on the other half due to the interaction with the additional force field. Accordingly, the gyration radius changes as well, which results in a drift motion perpendicular to the magnetic and the additional force direction.

Heating mechanisms

The most important application of electric fields to manipulate plasmas is the heating of electrons in the plasma. For a DC-discharge, electrons are accelerated by a potential difference applied between the anode and the cathode. Depending on the applied voltage, the gas pressure and the distance between the electrodes, different discharge modes can develop. In principal, it is differentiated between the Townsend discharge, the subnormal glow, the normal glow, the anomalous glow and the arc discharge. If a magnetic field is added to the discharge region, the path of the electrons passing through the background gas is dramatically extended according to the gyro-motion introduced above. The result for the current-voltage dependence of the discharge is a shift towards smaller voltages i.e. the different discharge regimes are entered at a lower voltage. Due to the more effective plasma generation process achieved in this way, dense plasmas can be generated at lower pressures, which is used in industrially important applications such as magnetron sputtering. For a detailed description of the different discharge modes found in DC-discharges, the reader is referred to standard literature such as [5] or [11].

Even higher charge densities can be achieved through heating with AC-current in the radio frequency range (typically a frequency of 13.56 MHz is used). If an alternating potential is applied to a parallel plate discharge, a high-voltage capacitive sheath builds up between the electrode and the plasma. In such a capacitive RF-discharge, two principal mechanisms for heating the plasma must be considered: the ohmic heating and the stochastic heating [3]. Due to the high frequency of the RF-power and the high mass of the ions, only the electrons can respond to the fast changes in the potential while the ions only see the time-averaged potentials. Accordingly the electrons can gain high energies from the field and transfer it by collisions with neutrals from the background gas. As the electron-neutral collisions represent a resistance, this process is called ohmic heating. The stochastic heating on the opposite is a collisionless heating mechanism, where momentum is transferred to the electrons from interaction with the high-voltage sheath. As a result of the movement of the electrons in the bulk plasma, which oscillate at the frequency of the RF-power, the sheath oscillates in the opposite direction. When the electrons collide with the sheath edge, they are reflected by the electric field, built up by all the ions inside the sheath, much like a tennis ball is reflected by a tennis racket [5]. To create a net energy gain from this reflection, the phasing of the electron after the reflection needs to be different from the oscillating electric field. Therefore, the electrons must have a random phasing when they collide with the sheath edge, which is the reason why this type of heating is called stochastic heating.

Besides the heating mechanisms for simple DC- or capacitive RF-discharges, many other mechanisms for plasma heating, such as used in inductive discharges or wave-heated discharges, exist. A more complete theoretical description of the heating mechanisms mentioned here and other common alternatives can be found in the text book literature such as [3, 5, 6].

2.2 Energy Balance and Plasma Surface Interactions

As already mentioned above, all technological plasmas are, up to a certain extend, in contact with surrounding surfaces. In most cases these are necessary to either introduce energy or simply, to create the right environment as in the case of the vacuum chamber. Thus, independent of the specific branch of plasma physics, the understanding and investigation of plasma surface interactions (PSI) are among the most important fields of research in plasma physics. Since both the parameters of the plasma and the parameters of the surface have a significant impact on each other it is not possible to fully describe the system by just looking at one side of this interaction. However, to allow experimental investigations, it is necessary to break down the complex interactions into smaller parts which can be investigated separately. A common approach to do this, is to look only at one direction of this interaction, while the other is minimized through appropriate design of the experiment. In this way the effect of changes in the surrounding surfaces onto the plasma parameters can be investigated separately from the effect of changes in the plasma parameters onto the surrounding surfaces.

The effects the plasma has on the surface can be divided into three categories: The chemical modification of the surface, the physical modification of the surface and the effect of energy flux towards the surface. The chemical modification describes the chemical reactions which are enhanced by the plasma, like chemical cleaning or activation of the surface [12], while the physical modification covers e.g. implantation, sputtering or secondary electron emission. The third category describes the energy balance at the surface taking into account the energy fluxes associated with the chemical (endothermic/exothermic reactions) and physical processes (momentum flux, released particles etc.) as well as any other processes resulting in energy exchange between plasma and the surrounding surface.

This group is of specific importance to technological plasmas since it can be directly correlated to important parameters such as longevity (plasma jets), thrust (ion thrusters), etch rate (plasma etching) or film structure and film properties (plasma assisted film growth). The effect on film growth can be described by so called *structure zone diagrams*. In figure 2.4 a recent version of such a diagram is presented which clearly displays the influence of energy flux and associated substrate temperature onto film structure and deposition rate. In the following sections the most important processes contributing to the energy balance at the surface will be described in greater detail, including equations which allow us to perform absolute calculations. For most of these processes, in reality, certain additional coefficients need to be taken into account. These usually describe the probability or the efficiency of a specific process and range from 0 to 1. The sticking coefficient e.g. describes the probability that a particle sticks to the surface and the energy transfer coefficient, describes the percentage of energy transmitted in a collision between an impinging particle and the surface. For ease of understanding these coefficients are assumed to be 1 in the following description and are thus neglected. The effect of this is, that the energy flux calculated with these equations, should always overestimate the actual energy flux. For a detailed analysis and for comparison with absolute values, however, these coefficients need to be taken into account and adjusted to the specific case at hand.

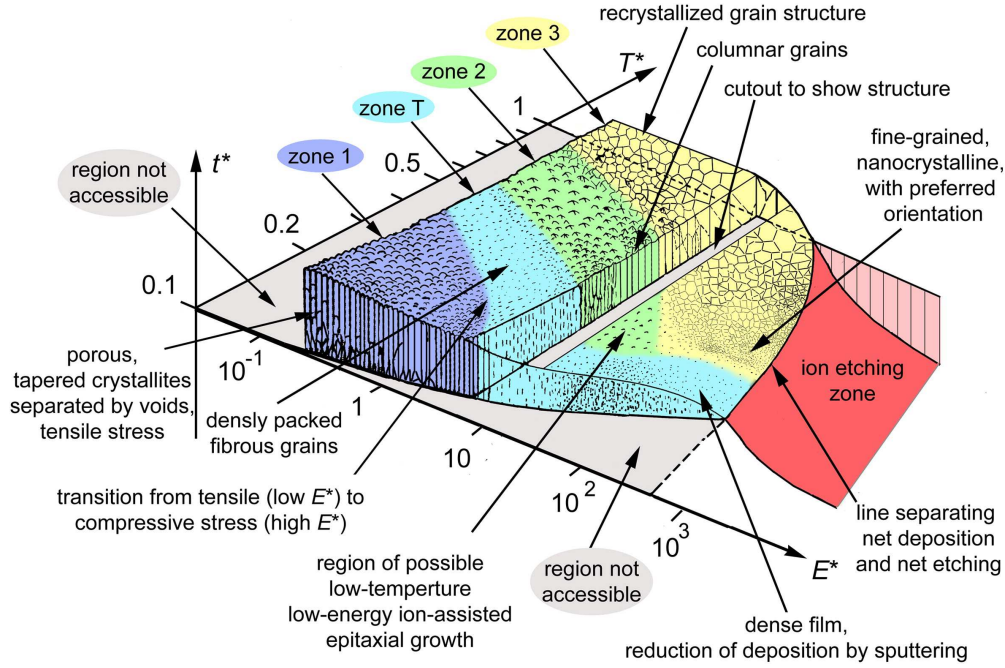


Figure 2.4: Structure zone diagram for energetic deposition. T^* is the generalized temperature, E^* the normalized energy flux and t^* represents the net thickness of the film. The numbers on the axes are for orientation only and depend on the material and the deposition conditions. Graphic taken from [13].

2.2.1 The total energy flux

The energy balance of a substrate or any other surface in contact with the plasma, is the result of the total energy flux to the surface. This total energy flux J_{total} can coarsely be divided into the energy flux from energetic particles $J_{particles}$, surface processes $J_{surface}$, radiation $J_{radiation}$, conduction and convection J_{con} and energy flux resulting from emitted particles $J_{emitPart}$:

$$J_{total} = J_{kin} + J_{surface} + J_{radiation} + J_{con} + J_{emitPart} \quad (2.22)$$

Since calorimetric investigations (see section 4.3) allow for measuring of the total energy flux only, understanding the different contributions is essential to permit more detailed interpretation of the obtained results.

2.2.2 Energetic Particles

Energetic particles which hit a surface can either stick to this surface and transfer their kinetic energy to the bombarded material or be reflected, transferring only part of their kinetic energy. Under the assumption of a sticking probability of 100%, the general term for the energy flux J_{kin} which is transferred by the kinetic impact of particles can be written as

$$J_{kin} = \Gamma_{kin} \bar{E}_{kin}, \quad (2.23)$$

with Γ_{kin} being the flux density of the impinging particles and \bar{E}_{kin} the mean kinetic energy. In almost all cases, the actual energy of the impinging particles varies according to a complex energy distribution, however, due to the vast amount of particles impinging on the surface, the use of an average energy provides a good approximation. The influence of the impact of heavy kinetic particles such as ions, neutrals or clusters is known to have an important effect on film growth [13–17]. On the one hand, the associated energy transfer can lead to changes of the film structure, resulting in changes of e.g. optical or mechanical properties. On the other hand, energetic particle bombardment can also result in implantation of unwanted species, reduction of deposition rate, or even ablation due to sputtering processes. Hence, for most technical plasmas, the knowledge and control of the kinetic energy transferred to the substrate, is very important to allow a better understanding and tuning of the system. In the next paragraphs the sum of the energy flux from kinetic particles is broken down into the contributions from the most relevant particles as they appear in typical plasma systems:

$$J_{kin} = J_e + J_i + J_n, \quad (2.24)$$

with J_e being the contribution to the energy flux due to energetic electrons, J_i due to energetic ions and J_n due to energetic neutrals.

Both, the contribution from electrons as the well as the one from ions can be easily determined from the plasma parameters acquired from Langmuir probe measurement. To determine the contribution from energetic neutrals can be much more tricky, since both the energy of the fast neutrals as well as the flux are often difficult to determine.

Electrons

The free electrons take an important role in all non-isothermal discharges. They are not only the most efficient channel of energy transfer from external electric and magnetic fields, but also determine the basic plasma properties like e.g. degree of ionization or plasma potential. One of the key properties of technological plasmas is the energetic difference between electrons and other heavier particles. Due to the effective heating of electrons and their small collision cross section these can reach very high temperatures while the background gas remains at a comparatively low temperature. This combination of high energies and low thermal stress allows for energetic modification of heat-sensitive material like e.g. plastics or even human tissue.

For electrons equation 2.24 can be rewritten as

$$J_e = \Gamma_e \bar{E}_{kin,e}, \quad (2.25)$$

where the electron particle flux density $\Gamma_e = j_e/e_0$ is given as the electron current density j_e divided by the electron charge e_0 . Both j_e and $\bar{E}_{kin,e}$ depend on the electron energy distribution function (EEDF) applicable for the investigated system. Common cases which can be described analytical are Maxwellian, Druyvesteyn or the mono-energetic EEDF which

result in the following energy fluxes [18]:

$$J_e = \begin{cases} n_e \sqrt{\frac{T_e k_B}{2\pi m_e}} k_B T_e \cdot 2 \exp(-\xi) = \frac{j_e}{e_0} 2 k_B T_e & \text{Maxwellian} \\ n_e \sqrt{\frac{T_e k_B}{2\pi m_e}} k_B T_e (-\xi \cdot \exp(-0.25\xi) + (1.79 + 0.89\xi^2) \operatorname{erfc}(0.5\xi)) & \text{Druyvesteyn} \\ n_e \sqrt{\frac{T_e k_B}{2\pi m_e}} k_B T_e \cdot 2\pi(1 - \xi)^2 & \text{Mono-energetic} \end{cases} \quad (2.26)$$

Here $\xi = (\Phi_{pl} - \Phi_s)/(T_e k_B)$ and describes the potential difference between the plasma Φ_{pl} and the substrate Φ_s in relation to the electron temperature T_e , k_B is the Boltzmann constant, e_0 is the electron charge and m_e is the electron mass. The Maxwellian distribution is based on

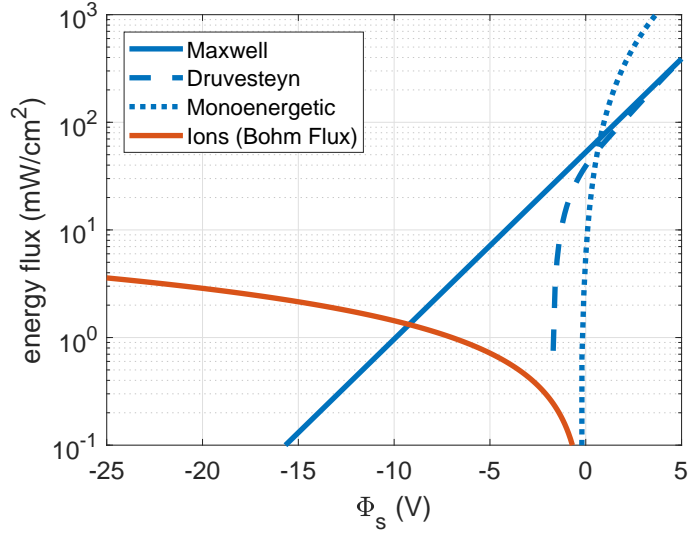


Figure 2.5: Calculated energy flux as a function of substrate bias for electrons from three different EEDFs and for ions as calculated from the Bohm flux. The input parameters ($n_e = 6 \cdot 10^{15}/m^3$, $k_B T_e/e_0 = 2.5eV$, $\Phi_{pl} = 2.2V$) are typical parameters found in the Titanium DC Magnetron sputtering experiment described in publication [III].

the assumption of thermodynamic equilibrium and a velocity independent, constant collision frequency, which is the case in discharges with high ionization degree where electron-electron collisions are dominant. The Druyvesteyn distribution on the opposite is based on a constant cross section, which results in stronger depletion of the high energy tail and a shift of the maximum to higher energies [19, 20]. A comparison of the resulting energy flux for the different EEDFs for the same plasma parameters is plotted in figure 2.5.

Ions

Quasi-neutrality demands that the number of ions in the plasma must be approximately the same as the number of electrons and according to the theory presented in 2.1.4, an equal flux of both species to any substrate at floating potential is expected. Due to the

higher mass of the ions, they deliver energy in a more focused way as compared to the relatively isotropic energy flux from electrons. This localized energy transfer is known to be particularly important for deposition processes [21, 22].

Analog to the electrons, the basic equation for the energy flux delivered by ions is given by

$$J_i = \Gamma_i \bar{E}_{kin,i}. \quad (2.27)$$

Here, $\Gamma_i = j_i/e_0$ is the ion particle flux density and $\bar{E}_{kin,i}$ is the mean kinetic energy. Both Γ_i and $\bar{E}_{kin,i}$ depend on a complex set of parameters and can change strongly dependent on the investigated system. The current density j_i can for most cases be described by the following expressions [18]:

$$j_i = \begin{cases} n_e \sqrt{\frac{T_e k_B e_0}{m_i}} \exp(-0.5) & \text{Bohm-flux} \\ \frac{4}{9} \frac{\epsilon_0}{e_0} \sqrt{\frac{e_0}{m_i}} \frac{\Phi_{sh}^{3/2}}{d_{sh}^2} & \text{Child sheath without collisions} \\ \frac{1}{4} n_i v_i & \text{thermal flux} \\ n_i v_{amb} & \text{ambipolar diffusion} \end{cases} \quad (2.28)$$

Here, m_i is the mass of the ions, n_i the ion density, d_{sh} the sheath width, v_i and v_{amb} ion velocities and ϵ_0 the electric permittivity constant. For low-pressure conditions, as they are found in typical process plasmas, either the Bohm equation ($p \leq 10 Pa$) or the Child law ($\leq 1 Pa$) give the most applicable descriptions for the ion current.

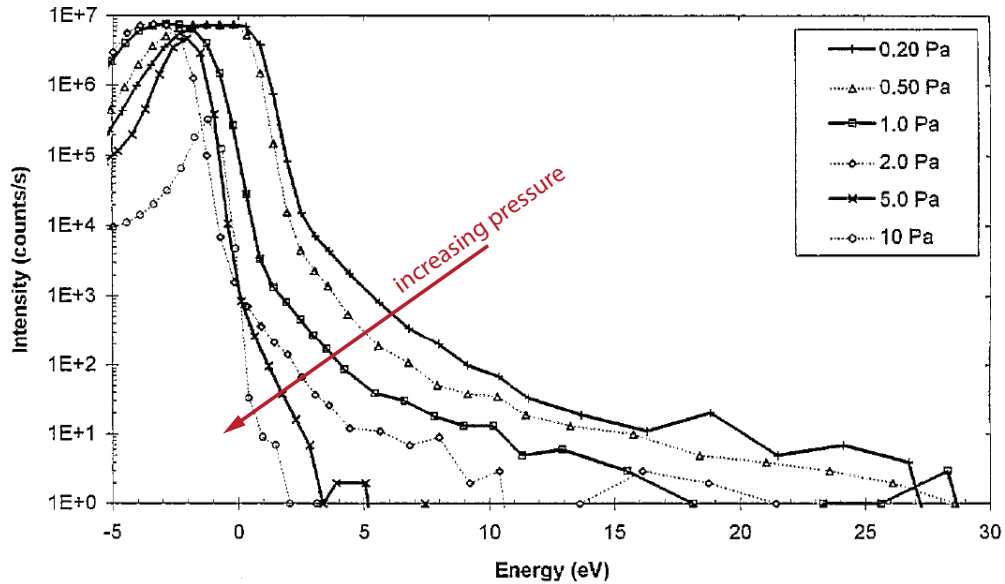


Figure 2.6: Effect of the Ar gas pressure on the energy distribution function (IEDF) for different Ar pressures in a DC magnetron sputtering system with a copper target at 400 mA. Graphic taken from [23].

For positive ions, the kinetic energy is mainly determined by the voltage drop over the sheath in front of the substrate $\Phi_{sh} = \Phi_{pl} - \Phi_s$. In this case the kinetic energy of the ions

is simply given by

$$\bar{E}_{kin,i} = \Phi_{sh}e_0. \quad (2.29)$$

However, using this simple description, the actual energy flux is usually overestimated as it does not take into account the effect of collisions, which gain importance as the mean free path is in the same order of, or shorter than the sheath thickness. The collisions can significantly alter the IEDF and lead to reduction of high energy ions and a general decrease of ion current as can be seen in figure 2.6. For the special case of an ion beam, the kinetic energy as well as the ion current is defined by the utilized extraction and acceleration mechanism which, in the example of a gridded ion source, results in an almost monoenergetic ion energy with the current density being defined by the space-charge limited current law (Child-Langmuir).

For negative ions, as they appear in electro-negative plasmas or processes using oxygen admixture, the acceleration process is of a different origin. If they are produced close to a cathode, e.g. the target of a magnetron, they can gain high kinetic energies in the order of several 100 eV. And, although they are decelerated as they pass through the sheath of a floating substrate, they will only lose little energy compared to their initial kinetic energy. Accordingly, this contribution can be expected to be strong in all environments where negative ions can be produced in the vicinity of a highly negative electrode.

Besides with Langmuir probes, $\bar{E}_{kin,i}$ and j_i can be effectively determined by various other diagnostics such as Faraday cups, energy resolved mass spectrometers, retarding field analyzers or $E \times B$ -probes.

Neutrals

The description of the energy flux from energetic neutral particles is theoretically less complicated. Compared to electrons or ions the flux density is independent of the substrate potential, however, since they do not carry any charge the detection can also be more complicated and error prone (see section 4.2). The energy flux is again calculated with equation 2.23 as the product of particle flux density Γ_n and kinetic energy $\bar{E}_{kin,n}$:

$$J_n = \Gamma_n \bar{E}_{kin,n}. \quad (2.30)$$

In technological plasmas, the origin for kinetic neutral particles can mostly be attributed to three different processes: sputtering, reflection of ions from the cathode and collisions between fast ions and slow neutrals. Depending on the exact origin, the values for $\bar{E}_{kin,n}$ and Γ_n can vary strongly.

Sputtering is the basis for plasma based physical vapor deposition (PVD) techniques and is also the key process for plasma etching. In general, sputtering is the evaporation of a solid material through bombardment by kinetic heavy particles. Upon impact of a particle, its energy and momentum is transferred to the material, initiating a 'billiard-like' collision cascade which eventually results in the evaporation of one or several atoms from the bombarded surface. The number of evaporated particles and their initial energy depend on various parameters of the impinging particle (e.g. energy, angle of incidence, mass) as well as on the properties of the bombarded material (e.g. temperature, structure, mass) [26]. Figure 2.7a

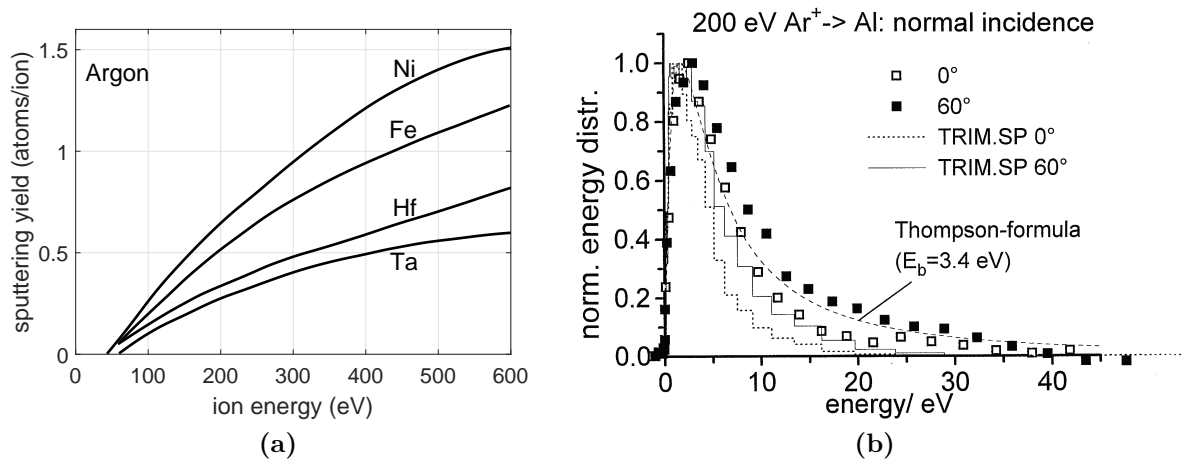


Figure 2.7: (a) Sputtering yield curves as a function of the incident ion energy for different materials bombarded with argon ions. The curves show a fit according to data from [24]. (b) Energy distribution of sputtered aluminum atoms for 200 eV argon ions for normal incidence, compared with the Thompson distribution and TRIM simulations, graphic taken from [25].

illustrates the dependence on incident ion energy and surface material for an energy range as it is typically found in magnetron sputtering experiments [24]. The amount of evaporated particles is characterized by the *sputtering yield* Y which can be understood as the efficiency of the sputter process:

$$Y = \frac{\text{number of sputtered particles}}{\text{number of incident particles}}. \quad (2.31)$$

In typical magnetron sputtering processes, the yield is in the range of 0.1 to 2, depending mostly on the incident ion energy and mass as well as on the used target material [24]. The energy of the sputtered particles can be described by the Thompson formula which expresses the sputtering yield as a function of the ejected energy E_{spu} for a fixed incident ion energy E_{inc} as

$$Y(E_{spu})dE_{spu} \propto \frac{1 - \sqrt{(U_s + E_{spu})/\gamma E_{inc}}}{E_{spu}^2(1 + U_s/E_{spu})^3} dE_{spu}, \quad (2.32)$$

where U_s is the surface binding energy of the target material, $\gamma = 4M_1M_2/(M_1 + M_2)^2$, with M_1 and M_2 being the masses of incident ion and target atom [27, 28]. For the assumption $\gamma E_{inc} \gg U_s$, equation 2.32 can be approximated by:

$$Y(E_{spu})dE_{spu} \propto \frac{E_{spu}}{(E_{spu} + U_s)^3} dE_{spu} \quad (2.33)$$

The kinetic energies of the sputtered particles $\bar{E}_{kin,n}$ calculated with this formula, are typically in the range of only few eV up to several 10 eV for most process plasmas. An example of the measured energies and comparison with different models for 200 eV argon ions impinging on aluminum is given in figure 2.7b.

Another common approach to calculate the sputter yield and the energy of the sputtered particles is through simulations of the sputtering cascade in the material. The most widely used simulation software to for this task, is the 'Stopping and Range of Ions in Matter'

(SRIM) [29]. This code uses Monte Carlo methods to simulate the particle impact and resulting changes of the bombarded material and outputs relevant parameters such as the number and energy of reflected and sputtered particles.

Reflection of ions from the cathode appears alongside sputtering and is of specific importance if the mass of the incident ion M_1 is smaller than that of the target material M_2 [30]. Although the yield for reflection is typically lower than the sputter yield, the resulting energy flux can often be in the same range or even higher due to the higher kinetic energy of these particles. Although, in reality the energy of the reflected particles is described by a complex energy distribution function, an approximate relation between the velocity of the incident ion v_{inc} and the velocity after reflection v_{refl} can be given as [27]:

$$v_{refl} \approx \left(\frac{M_1 - M_2}{M_1 + M_2} \right) v_{inc} \quad (2.34)$$

Winters et. al [30] investigated the energy per sputtered atom for different target materials and incident ion species and found energies ranging from a few eV for a high ratio M_1/M_2 , up to several 100 eV for a low ratio as found for helium on copper.

Collisions between fast ions and neutrals can either be elastic or with charge exchange, in both cases giving rise to energetic neutrals. For an elastic collision up to 100% of the momentum of the incident ion can be passed on to the collision partner. The exact percentage varies as a function of the mass ratio of the colliding particles and the impact angle [31]. Charge exchange or charge transfer describes the exchange of charge upon collision between ions and neutral particles. According to this process, a kinetic ion can be neutralized without losing its kinetic energy and, thus, creating a neutral particle with the kinetic energy of the initial ion.

Both mechanisms become of special importance for pressures higher than $\sim 10^{-2}$ Pa where the mean free path reaches dimensions of typical vacuum chambers. In the case of an ion beam operated in this pressure regime this can result in a percentage of more than 70% neutralized particles in the beam [32, 33]. For even higher pressures as found in magnetron or RF discharges, this effect also becomes of importance for the energy distribution in the sheath. Both, for self-biased, powered electrodes or externally biased substrates, collisions between ions and neutrals in the sheath can create neutral particles with high energies equivalent to the ions accelerated by the sheath potential.

2.2.3 Particles emitted from the surface and surface processes

In general, the contribution of particles leaving the substrate can be treated equivalent to those impinging on the target. However, since these particles take away energy from the target, the corresponding energy flux has a negative sign. The emission of particles can be caused by e.g. particle impact, by energetic photons (UV) or by chemical etching. The most common emission processes in technological plasmas are due to particle impact which results in sputtering of target atoms and emission of secondary electrons.

Besides the particle emitting processes the bombardment with charged particles or film building species is associated with additional energy-relevant processes taking place on the surface of the substrate. On top of that, for the special case of a reactive plasma, a complex set of chemical processes have to be considered as well. Since a complete analysis of all of these processes would not be feasible, this subsection aims to describe the most important surface processes found in technological plasmas in a general manner.

Sputtering

As described in section 2.2.2, the impact of heavy particles on a surface can result in evaporation of material. Accordingly, for every impinging heavy particle on the substrate, there is a chance that an atom is sputtered from the surface and leaves the substrate with a kinetic energy higher than zero. As described by the Thompson distribution (equation 2.32), however, this energy is always much smaller than the incident energy of the impinging particle. Therefore, even for materials with a high sputtering yield, the effect on the energy flux of particles being sputtered from the substrate is negligible compared to the integral energy flux.

Secondary electron emission (SEE)

Secondary electron emission has been closely studied due to its importance in different appliances such as cathode ray tubes or electron multipliers but also due its essential role in most plasma environments. While sputtering is only observed for bombardment of heavy particles like ions or neutrals, secondary electron emission can be created by impact of electrons and photons as well [6].

For the negative energy flux created by secondary electrons, only true secondary electrons have to be considered. Reflected electrons are usually neglected as they transfer approximately the same energy to the surface as they take away, resulting in a negligible net-energy flux. Independent of the origin, the energy flux for secondary electron emission is given by

$$J_{see} = -\Gamma_{see}\bar{E}_{see,kin}, \quad (2.35)$$

as the product of particles flux density Γ_{see} of secondary electrons emitted from the surface and the average kinetic energy of the emitted electrons $\bar{E}_{see,kin}$. Analog to the negative contribution from sputtering, the contribution of energy taken away by secondary electrons will always be relatively small and can be neglected in most cases. However, a more significant effect can appear in the current measurement as it is falsified by SEE. As an electron is released from the surface this will lead to an increased current in the case of positive net-current and to a decrease in the case of negative net-current. In cases with high SEE, as found in plasma based ion implantation (see chapter 3.4), this can result in significant deviations between the energy flux estimated from electrical current measurements and the experimentally determined energy flux, see publication [VI].

Electron work function (EWF)

Whenever an electron is emitted from the surface or added to the surface from vacuum level, the energy from the electron work-function Φ_{wf} is released or needs to be overcome (see figure 2.8). The electron work-function describes the energy necessary to raise the electron from Fermi level to vacuum level which needs to be overcome to release the electron from the surface. For nonmetals (semiconductors and dielectrics) the electron work-function can be replaced by the minimum binding energy of a valence electron [27]. The energy flux resulting

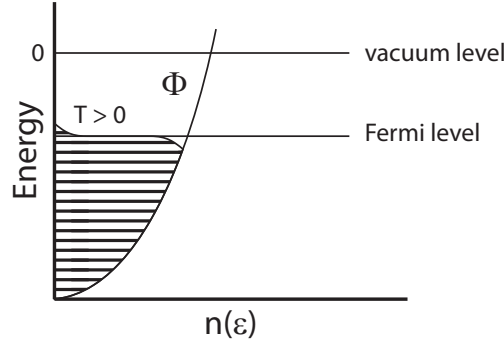


Figure 2.8: Density of states $n(\epsilon)$ curve for the conduction band of a free electron metal. The Fermi level is marked with $\mu = \epsilon_F$ and the electron work-function is given by Φ . Graphic taken from [34]

from the electron work function depends on the electrical net-flux to the substrate, which is composed from the electron fluxes Γ_{see}, Γ_e and the ion flux Γ_i :

$$J_{wf} = \Phi_{wf}(\Gamma_e - \Gamma_{see} - \Gamma_i). \quad (2.36)$$

In the case of a floating substrate and for zero Γ_{see} , electron flux and ion flux are equal and the contribution due to the electron work function disappears. However, for the case of a substrate, which is positively biased with respect to the floating potential, the contribution from the electron work function is important, as Φ_{wf} often is in the range or even higher than the kinetic energy of the electrons in the plasma, see equation 2.25.

Electron-ion recombination

Every ion arriving at a surface recombines with an electron and is neutralized. As described in the section above, in a conductive surface connected to ground, the electron usually comes from the conduction band and for dielectric surfaces a valence electron is removed from the material. The energy necessary to overcome the electron work-function is already covered by the contribution J_{wf} , so the energy flux from electron-ion recombination on the surface is simply given by the product of ion flux Γ_i and the ionization energy of the impinging ion E_{ion} :

$$J_{rec} = \Gamma_i E_{ion}. \quad (2.37)$$

Since typical ionization energies are in the range of 10-25 eV ($E_{ion,Ar} = 15.76$ eV), the energy flux due to electron-ion recombination for a floating substrate, is in most cases more significant than the energy flux due to kinetic impact of ions or electrons.

Film formation

Upon impact of a sputtered particles or precursor fragments on a surface, the impinging particle usually condenses on the surface and leads to film formation. As the impinging particle bonds to the surface the enthalpy of sublimation E_{sub} is released. Additional to the energy flux from the kinetic impact, film forming particles are associated with the energy flux due to sublimation:

$$J_{sub} = \Gamma_n E_{sub}, \quad (2.38)$$

with Γ_n being the particle flux density of neutral film-building particles. The most practical way to determine Γ_n is by determination of the effective growth rate of the film. This is usually achieved either by in-situ detection of the mass of the growing film (QCM) or by measurement of the film thickness and deposition time (profilometer, X-ray techniques), see chapter 4.2 for more details on the determination of Γ_n .

Typical sublimation energies are in the range of a few eV up to almost 10 eV and are therefore comparable to the typical energies of sputtered atoms. This makes the energy flux due to film formation just as important as the energy flux due to kinetic impact of sputtered particles.

Chemical reactions

Plasma processes which purposefully include chemical reactions are usually referred to as reactive plasma processes. The reactions in such processes start from simple molecule formation or oxidation of certain species and can become arbitrarily complex as mixtures of reactive species or complex molecules are introduced into the plasma. What makes these processes specifically complex, is that a plasma does not give an environment where chemical reactions happen in thermodynamic equilibrium. Instead, due to the high energies available from electrons, reactions can appear which are only associated with very high temperatures under thermodynamic equilibrium. These reactions in turn have a significant influence on the plasma properties itself, which results in a complex, highly sensitive, dynamic equilibrium. Any surface in contact with such a reactive plasma will also be exposed to those reactions and depending on whether the reactions are endothermic or exothermic, a negative or positive energy flux can be the result.

A simple example is the case of a pure hydrogen plasma. Here, the molecular hydrogen can be dissociated in the plasma, leaving single hydrogen atoms. Due to momentum conservation, the most efficient channel for re-formation into a molecule is by three body collision. As a result of the long mean free path, such a collision is unlikely to happen in the bulk of a low pressure plasma. Instead, it can be expected to take place at a surface, like the chamber wall or a substrate, where the surface can act as a third collision partner. During the formation of the molecule, the binding energy will be released and partially transferred to the surface, resulting in a positive energy flux which is proportional to the binding energy and the rate at which this process happens. Other, more complex examples can be found for plasma etching or plasma cleaning processes. For these applications, the fundamental processes are chemical sputtering (CS) and surface film reactions (SFR) in combination with physical sputtering (PS) [18]. Both CS and SFRs involve at least one chemical reaction before the resulting molecule can desorb from the surface. Depending on whether the reaction is endothermic

or exothermic, this reaction can both result in a positive or a negative energy flux and accordingly heating or cooling of the substrate.

2.2.4 Radiation

The glow associated with any plasma is one of the most striking features and always holds a certain fascination. It is obvious that this glow must also be associated with a significant energy flux to any surface exposed to it.

Line-radiation can be in the ultra violet, the visible or also in the infra-red, depending on the composition of the plasma. The resulting energy flux depends on the photon energy E_{ph} and the flux of photons arriving at the surface Γ_{ph} :

$$J_{rad,ph} = \Gamma_{ph} E_{ph}. \quad (2.39)$$

It is relatively difficult and error prone to obtain an absolute measure for the photon flux, since any detection system will always have to deal with numerous assumptions and approximations. These are for example, assumptions regarding the comparability between light detector and the substrate or the approximation of the absorption coefficients of different optic fibers and long term changes of detector sensibility.

A famous example for a model of the energy flux which includes the contribution from line radiation is given by Thornton in 1978 [35]. In this work Thornton investigated the substrate heating in cylindrical magnetron sputtering sources and compared experimental results with a simple theoretical model. For this model Thornton calculated the line radiation with the following assumptions:

- I. The average energy spent by an electron in making an ion is nearly constant at about 26.4 eV for argon.
- II. Since the ionization energy is 15.75 eV, the remaining 10.65 eV are used in excitation and are ultimately radiated with a cosine distribution, allowing half of the energy (5.33 eV) to arrive at the substrate.
- III. Each sputtered atom requires the production of $1/Y$ ions (Y - sputter yield).

This results in an energy flux of $5.33/Y$ eV per deposited atom and yielded contributions in the same range as the contribution from condensation. It is difficult to prove whether this method actually provides reliable results for calculating the contribution from line radiation, however, it illustrates nicely that also any theoretical model requires numerous critical assumptions.

Heat radiation describes the thermal radiation (IR) emitted from any surface. Depending on the temperature and the distance to the investigated surface this contribution can be quite significant, see publication [III]. In general the energy transfer between two surface due to thermal radiation is described by the Boltzmann radiation law:

$$J_{rad,boltz} = \sigma(\epsilon_{rad} T_{rad}^4 - \epsilon_s T_s^4), \quad (2.40)$$

with the Stefan-Boltzmann constant $\sigma = 5.67 \cdot 10^{-8} \text{ W}/(\text{m}^2 \text{K}^4)$, ϵ_{rad} , ϵ_s the emissivity of the hot surface and the substrate and T_{rad} , T_s the temperature of the corresponding surfaces. Since this equation describes the complete energy transfer, it is necessary to add a geometrical factor which compensates for the geometrical configuration of the investigated surfaces.

2.2.5 Conductive and convective energy flux

Any substrate in a plasma process will always be in physical contact with some kind of holder and the back ground gas. This results in a contribution which is typically negative, although it can also become positive, depending on the temperature difference between substrate and gas or heat reservoir at the end of the conductor [36].

Conductive energy flux is described by Fourier's law of heat conduction:

$$J_{cond} = \frac{1}{A_s} \frac{\lambda_c A_c}{d_c} (T_c - T_s), \quad (2.41)$$

with T_s and A_s being the temperature and area of the substrate, T_c the temperature of the heat reservoir at the end of the conducting material and A_c , d_c and λ_c the cross section, length and heat conductivity of the conducting material. Although simple in theory, for most systems this contribution is difficult to calculate in reality. This is mainly due to the difficulties associated with the definition of the heat reservoir for conductive cooling, which must be at a constant temperature during the investigated period and connected through a well-defined connection. The latter aspect creates difficulties since the thermal conductivity depends strongly on the contact between the substrate and the conducting material, which is oftentimes only clamped or screwed on. In figure 2.9 an exemplary calculation of the energy flux according to equation 2.41 for the conductive cooling of the passive thermal probe used in this thesis is shown alongside some curves for gas cooling. Conduction also takes place in gas, however, since the dominant mechanism for energy transport in gases is actually associated with the physical transport of particles, the energy transfer in gas is more appropriately labeled as convective energy flux as described in the following paragraphs.

Convective energy flux due to interaction with the background gas is in general of less importance in low-pressure plasma systems, however, under conditions of higher pressures where the molecular flow is replaced by Knudsen flow or viscous flow, it must be considered [18].

For the **free molecular regime** (up to ~ 10 Pa) the mean free path of a gas atom λ_g is greater or comparable to the sheath thickness of the boundary layer in front of the substrate d_{bl} . In this regime the energy flux is proportional to the difference between substrate temperature T_s and gas temperature T_g as well as the free molecular heat conductivity χ , the accommodation coefficient α_g and the gas pressure p [40]:

$$J_{mol,conv} = \alpha_g \chi p (T_g - T_s). \quad (2.42)$$

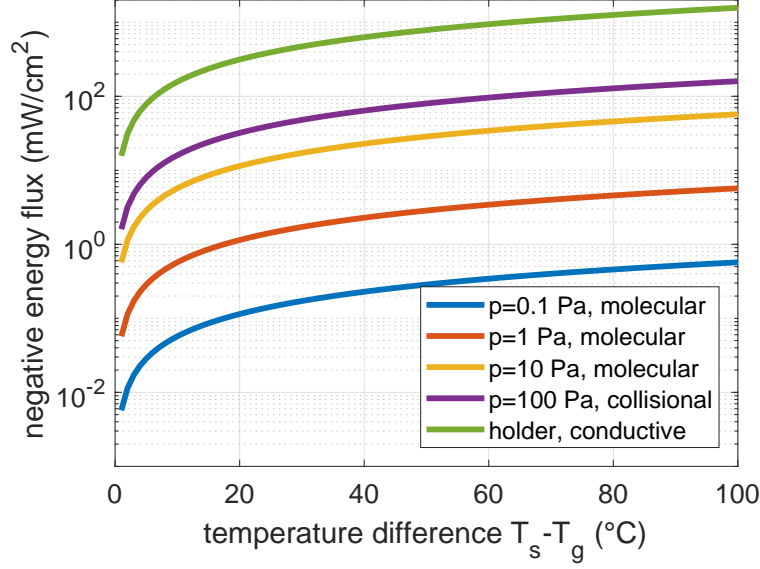


Figure 2.9: Conductive and convective energy flux values as a function of temperature difference between substrate and surrounding gas or heat reservoir. To calculate the values for the free molecular regime, an accommodation coefficient of $\alpha_g = 0.85$ (Ar on W) and a free molecular heat conductivity of $\chi = 0.67 \text{ W}/(\text{m}^2 \text{KPa})$ ($c_p/c_v = 5/3$, $T_g = 293 \text{ K}$, $M_g = 39.948 \text{ g/mol}$) [37, 38] were used. For the curve at 100 Pa, the energy flux was calculated according to equation 2.45 and with $N_u = 1$, $\lambda_g = 1.6 \cdot 10^{-4} \text{ W}/(\text{cmK})$ and $d_{bl} = 1 \text{ mm}$ [39]. The conductive cooling through a substrate holder is described by equation 2.41. For the displayed curve, the heat conductivity was chosen to be $\lambda_c = 380 \text{ W}/(\text{mK})$, $A_c = 7.8 \cdot 10^{-7} \text{ m}^2$ (1 mm copper wire), $d_c = 2 \text{ cm}$ and the probe surface to be $9.5 \cdot 10^{-5} \text{ m}^2$ (11 mm diameter circular platelet).

According to Knudsen theory the free molecular heat conductivity is given by

$$\chi = \frac{c_p/c_v + 1}{c_p/c_v - 1} \sqrt{\frac{R}{8T_g\pi M_g}}, \quad (2.43)$$

where c_p/c_v marks the adiabatic coefficient and M_g the atomic mass of the gas atom and R the universal gas constant. The accommodation coefficient is defined as

$$\alpha_g = \frac{E_{in} - E_f}{E_{in} - E_s}, \quad (2.44)$$

with E_{in} and E_f being the initial and final energy of the gas atom and E_s the thermal energy per atom of the substrate surface.

Conditions with higher pressure are usually described by the **collisional regime**, where the mean free path is much smaller than the thickness of the boundary layer. Here, the energy flux is described analog to Fourier's law as

$$J_{col,conv} = N_u \lambda_g \frac{T_s - T_g}{d_{bl}}, \quad (2.45)$$

with the Nusselt number N_u and the thermal conductivity of the gas λ_g .

As it can be seen from figure 2.9 the energy flux from to the background gas can become

a significant contribution especially for higher pressures and big differences between gas and substrate temperature, however, in most setups the energy flux through conductive cooling will be the dominant process.

3 Technological Plasmas

For a laboratory plasma or any technological plasma the loss processes of charge carriers are much higher due to the necessary confinement by surrounding walls. To compensate these losses and keep the discharge running, it is essential to provide a continuous supply of power to the system. Since the development of the first dedicated plasma discharges, a variety of different methods have been developed to efficiently transfer energy to the plasma [3, 5]. The vast majority of these applications use electromagnetic waves which couple to the free electrons in the plasma. To further increase the efficiency of these systems by creating a higher rate of ionization, in many cases additional magnetic fields were added to the setup. This chapter gives a brief introduction into the fundamental principles of plasma generation and the types of plasma systems investigated in this thesis. Since all of the investigated systems are technological applications, the plasma is not created for its own sake but rather as a tool to achieve a specific goal. While in the case of ion thrusters, the goal is to propel a space craft, for magnetron sputtering the goal is to coat a substrate with a precisely defined thin film condensed from sputtered atoms. These two examples alone, give a good idea of the diversity of applications and the versatility associated with the specific features of a plasma.

3.1 Basic mechanisms of plasma generation

For the majority of all technical plasmas the initial generation mechanism is based on ionizing collisions between energetic electrons e and neutral background gas atoms A :



To start the process of plasma generation, it is thus an initial condition for free electrons to be available in the system. Thanks to ionizing cosmic or natural nuclear radiation, free electrons are present in any neutral gas and in some cases they are created by thermionic emission, field emission or other technical generation mechanisms to kick-start the plasma generation process. Due to their electrical charge, these free electrons can be efficiently accelerated by electromagnetic fields. Once their kinetic energy is high enough to allow ionization of neutral particles from the background gas ($E_{kin} > E_{ion}$), an avalanche effect is initiated as more and more electrons can contribute to the ionization process [5].

As illustrated in figure 3.1, this so-called *volume ionization* results in an exponential growth of the electron density n_e according to

$$n_e(x) = n_e(0)e^{\alpha x}. \quad (3.2)$$

Here, x is the distance, the electron has traveled through the background gas and α is the first

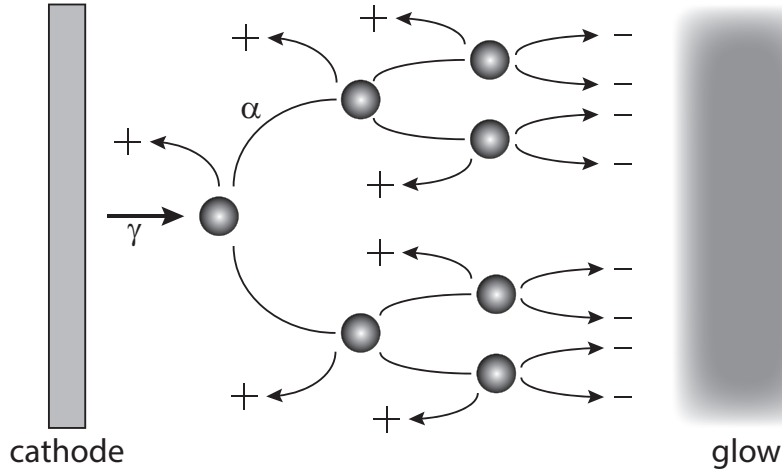


Figure 3.1: Illustration of the basic plasma generation process by the electron avalanche effect. A free electron or one which is generated by secondary electron emission, initiates a cascade of electron-ion pairs resulting in an exponential growth of the electron density. Illustration by courtesy of F. Haase, after [5].

Townsend coefficient which describes the number of ionization processes per unit length [11]:

$$\alpha = \frac{\nu_{ion}}{v_D}. \quad (3.3)$$

The volume ionization is, thus, primarily defined by the frequency of the ionization events ν_{ion} and by the mean drift velocity of the electron v_D .

Opposing the generation processes, are the loss mechanisms, which, when a steady state is reached, exactly balance the ionization of the gas. The dominant loss mechanism in technical plasmas is usually the recombination at the wall. Here, either single charge carriers recombine and neutralize upon collision with the wall or electrons and ions recombine in a three-body collision with the wall. However, as described in section 2.2.3, the impact of electrons and ions on a surface is also associated with the emission of so-called secondary electrons. The wall does, thus, not only represent a source for losses but also for generation of the essential free electrons. The efficiency of the secondary electron emission is described by the amount of released electrons per impinging ion, the so-called *secondary electron yield*:

$$\gamma = \frac{\text{released electrons}}{\text{impinging ion}}. \quad (3.4)$$

An analogous coefficient δ is defined for electron impact, but since it is typically one order of magnitude smaller than that for ions, it is usually neglected.

For an idealized DC-discharge where only volume ionization according to the α -process and secondary electron emission by ion impact on the cathode are present, a simple balance equation for breakdown between two electrodes at a distance d from each other can be obtained:

$$\gamma (e^{\alpha d} - 1) = 1, \quad (3.5)$$

This equation can be understood as the requirement for the secondary electron yield to be high enough, so that the released electrons can create enough ions by the α -process, to

compensate the loss of ions at the cathode. For the volume ionization coefficient α , Townsend formulated an empirical law which gives its dependence on the electrical field E and the gas pressure p [5]:

$$\frac{\alpha}{p} = A \exp\left(-\frac{B}{E/p}\right), \quad (3.6)$$

with A and B being characteristic constants for the used gas. Combining this equation with equation 3.5, the *Paschen law* is obtained, which gives a condition for the breakdown voltage $U_{bd} = E_{bd}d$ for a DC-discharge:

$$U_{bd} = \frac{Bpd}{C + \ln(pd)} \quad \text{with} \quad C = \ln\left[\frac{A}{\ln(1 + 1/\gamma)}\right]. \quad (3.7)$$

In figure 3.2 the Paschen curves for the breakdown voltage as a function of the pressure-distance product in different gases are plotted. The minimum is the result of too few atoms for ionization being available on the left side of the minimum and too little energy being gained per mean free path on the right side.

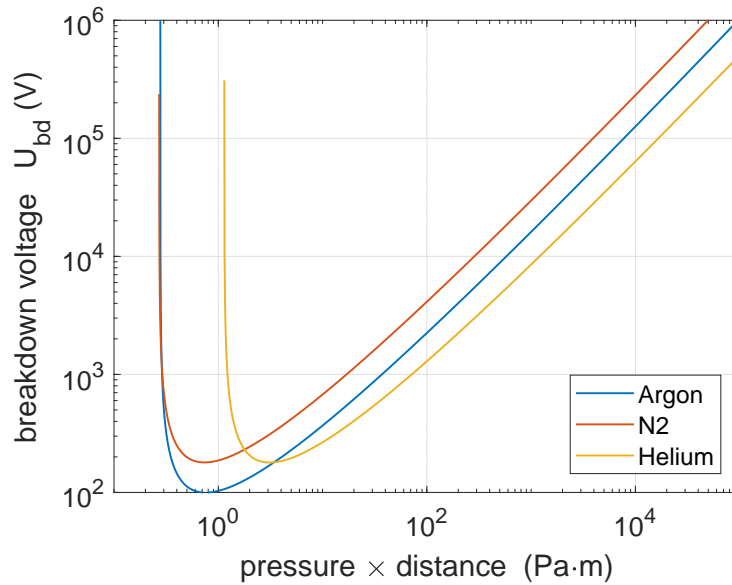


Figure 3.2: Breakdown voltages according to the Paschen Law for Argon, Nitrogen and Helium with constants from [3] and a secondary electron emission coefficient of $\gamma = 0.1$.

Although, the above described processes are fundamental to any technological discharge, in reality many other processes like metastable-metastable ionization, charge exchange collisions or stepwise ionization need to be considered too. A more complete description of the processes involved in generating and maintaining a stable plasma can be found in the textbook literature, see e.g. [3, 5, 6].

3.2 Ion Beams and Ion Thrusters

Ion beams have been developed independently in a number of separate fields of scientific research and application, however, especially in the early days, the development was mainly driven by two mostly unrelated fields: atomic and nuclear physics and space propulsion [11]. Nowadays ion beams are commonly used in many fields of research and are well established in industrial processes for material processing, surface analysis or thin film coating processes [41]. Due to the multitude of applications, numerous different setups have been developed over the years, many of which are described in textbooks such as [11] or [41]. A method for the efficient and standardized comparison between the different ion beam models and concepts would be of great use to help the future development of ion beams, independently of their application. Exactly this also gives the motivation for the 'advanced electric propulsion diagnostics' (AEPD) platform which is described in publication [I].

The main principle of an ion beam is to combine an ion source (e.g. a plasma) with an acceleration method to create an energetic beam of ions. For space propulsion the force which is created as the ions are accelerated, is used to create thrust while in e.g. microelectronics the energetic ions are used for implantation. Figure 3.3 gives two typical examples of ion thrusters which illustrate the main acceleration principles used in most ion beams. In a

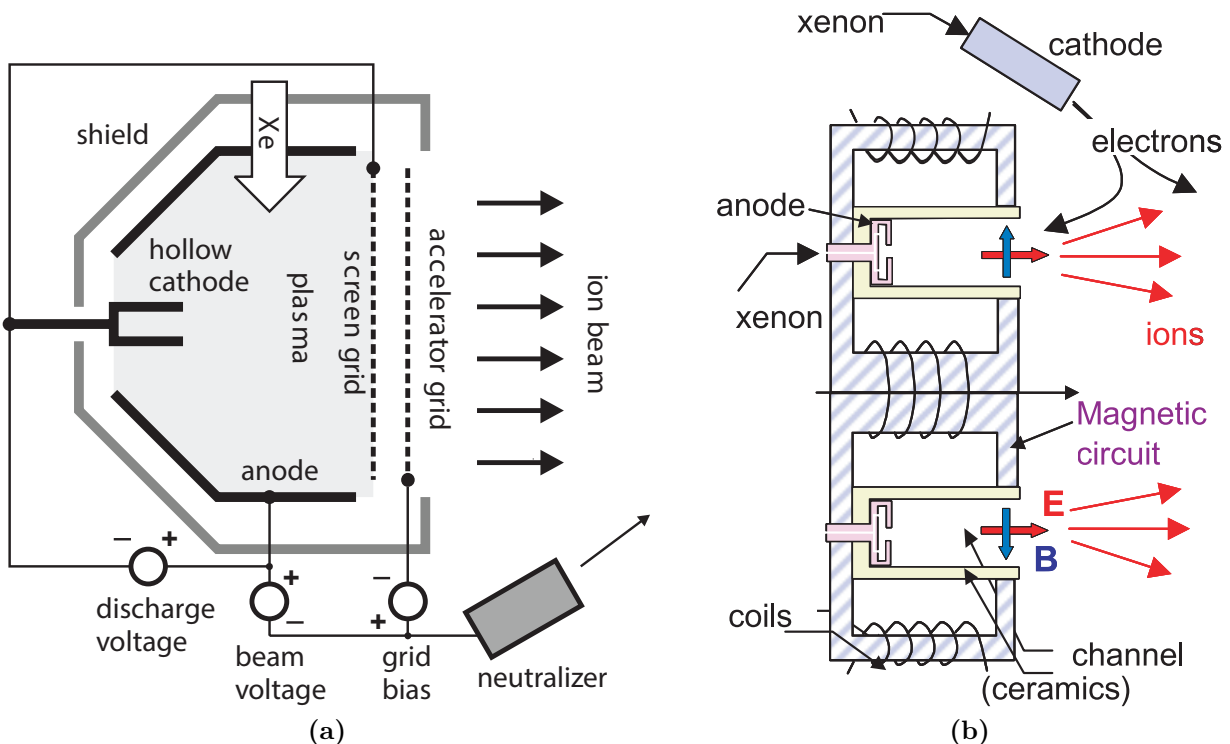


Figure 3.3: (a) schematic drawing of a typical gridded thruster with a combination of a dc discharge with a hollow cathode, taken from [5]. (b) schematic drawing of a typical Hall-effect plasma thruster where the ions are accelerated by the sudden potential drop in front of the discharge gap, taken from [42].

gridded thruster, such as the one shown in figure 3.3a, the plasma is confined by a screen grid and the walls of the plasma chamber. By applying a high voltage (~ 1000 V) between

the neutralizer and the anode, the ions can be extracted from the plasma and accelerated to a high monoenergetic energy. Any ion beam which is operated as an ion thruster includes a neutralizer which is typically positioned close to the extracted beam outside of the source. The neutralizer emits electrons into the beam and is necessary to prevent charging of the space craft and problems associated with space-charge limited flow. While the development of ion beams in the USA was mainly focused on gridded sources, in the Soviet Union a different type of thruster called Hall-effect thruster was favored. A schematic drawing of a typical Hall-thruster is shown in figure 3.3b. The plasma is created inside an annular gap with insulated walls which contains a metallic anode through which the propellant gas is introduced. The cathode is positioned at the open end of the plasma gap and creates a plasma bridge which defines the attractive electrostatic potential for the ions from the plasma gap. The magnetic circuit which creates a localized, transverse magnetic field near the exit of the plasma channel, traps the electrons by forcing them onto an azimuthal path in the $E \times B$ direction. The resulting electron drift is the origin for the name of this type of thruster as it is described by the Hall current [5]. Due to the higher mass of the ions, they are not as effectively bound to the magnetic field and can thus be accelerated by the electric field between the anode and the cathode while the electrons are left behind.

3.2.1 The Radio Frequency Ion Thruster

The radio frequency ion thruster (RIT) is a gridded thruster much like the one shown in figure 3.3a, however, instead of generating the plasma as a dc discharge, here, the energy is inductively coupled into the plasma using radio frequency waves in the MHz regime. In

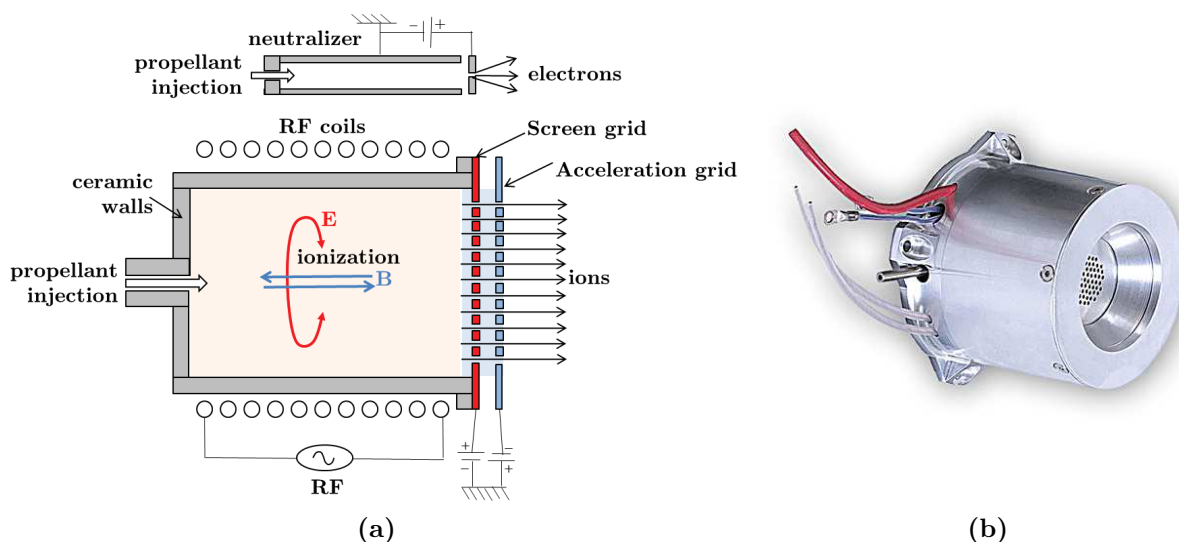


Figure 3.4: (a) schematic drawing showing the generic operation principle of an RF-Ion thruster, taken from [43]. (b) photograph of the RIT- μ X, taken from [44].

figure 3.4a a schematic drawing, showing the general operation principle for a RIT along with a photograph (figure 3.4b) of the RIT- μ X which has been investigated as a part of this thesis (see publication [I]) is shown. The schematic drawing can be divided into three parts: In the 'ion production' part, the propellant gas is ionized in a radio frequency (RF)

plasma. The alternating current in the RF coils generates an alternating magnetic field resulting in an azimuthal, circular electric field [43], which accelerates the free electrons to energies high enough to ionize the neutral gas. In the 'ion acceleration' part, the extracted ions are accelerated in exactly the same way as with all gridded thruster: by a potential difference between the neutralizer and the screen grid. Typically in gridded thruster at least one additional grid is used for control of the beam form for earth-based ion beams the acceleration potential is created between an anode in contact with the plasma and the grounded chamber walls [45]. The third part is the 'beam neutralization', which again is used to create the attractive pole for the acceleration potential and emits electrons to neutralize the beam. The RIT- μ X represents a special branch in ion thruster development which is motivated by the requirements for micro propulsion, which is typically associated with precise thrust modulation in the μ N to low mN range. Such low thrusts are required for the precision positioning of e.g. space craft in formation flying observatories like the 'Laser Interferometer Space Antenna' (LISA) [46].

3.3 Magnetron Sputtering

Magnetron sputtering is the most common and also oldest plasma based coating technique. Its basic idea is to evaporate material from a target by ion bombardment, which allows to deposit a film on a substrate which is exposed to the evaporated material. Due to the high quality of the deposited films and their finely adjustable properties, it is nowadays the process of choice for the deposition of a wide range of industrially important coatings [47]. The introduction of the 'conventional' or 'balanced' magnetron in the 1970s marks an important step in the evolution of sputter deposition techniques and in many ways can be understood as the starting point for the development of modern magnetron sputtering systems. Based on this original design, over the years many different variations evolved with a key point being the optimization of the magnetic field, resulting in 'unbalanced' magnetrons or 'closed-field' multi-source systems. The more recent development of 'High Power Impulse Magnetron Sputtering' (HiPIMS) further expands the possible fields of application and made magnetron sputtering feasible for the combination with other surface treatment processes like 'Plasma-based ion implantation' (PBII). The sources investigated in this thesis include both conventional magnetron sputtering systems as well as more advanced systems. The following section gives a brief description of these systems and their most relevant qualities.

3.3.1 Direct Current Magnetron Sputtering (DCMS)

The conventional magnetron combines a glow discharge with a magnetic field configured parallel to the target surface. In figure 3.5 the alignment between the fields is illustrated along with a schematic setup. As it can be seen, the electric field is generated between a surrounding anode and the cathode which is made of the material which will be used to form the coating. The magnets are arranged in such a way, that the magnetic field lines are perpendicular to the electric field for a region close to the target surface. The magnetic field prevents the electrons from simply following the electric field lines and instead, as a result of the Lorentz force, they gyrate around the magnetic field lines. For the region of

perpendicular fields, this means that the electrons are trapped in the plasma and gyrate around the magnetic field lines with a characteristic radius called the Larmor radius r_L :

$$r_L = \frac{v_{e,\perp} m_e}{e_0 B_\perp} \quad (3.8)$$

Here, $v_{e,\perp}$ is the velocity of the electron perpendicular to the magnetic field B_\perp and m_e and e_0 are the mass and charge of the electron. This gyration dramatically increases the path an electron covers before it reaches the anode and proportionally increases the probability for ionization.

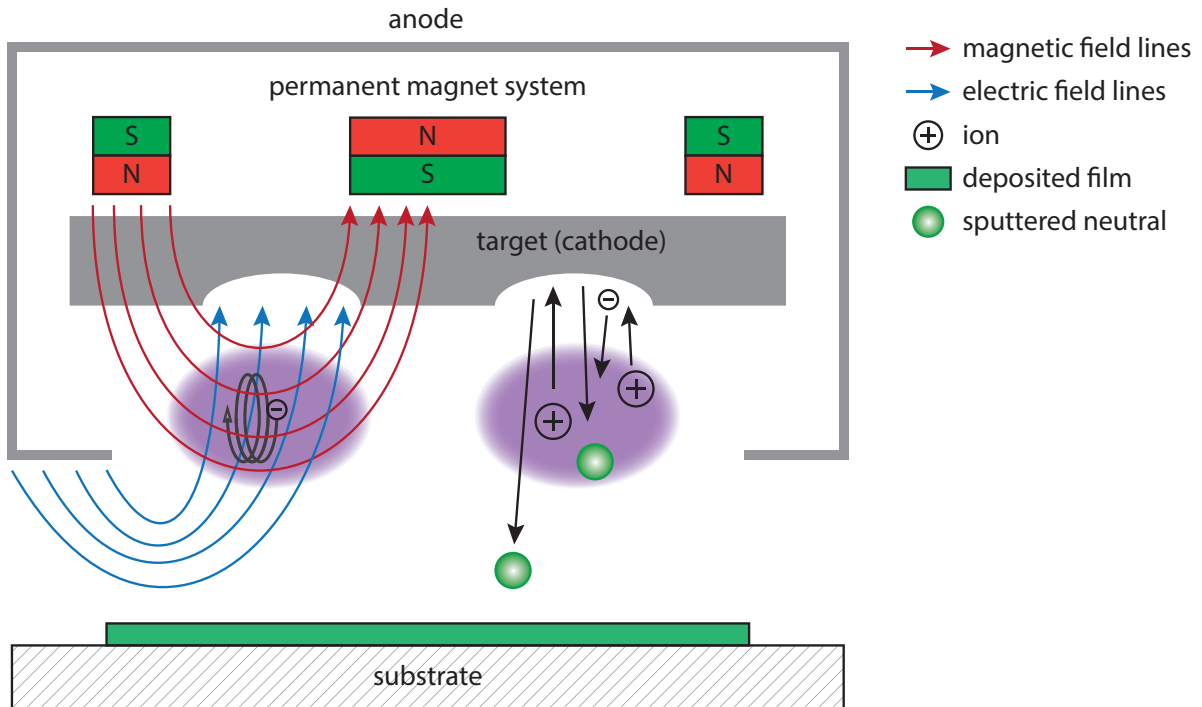


Figure 3.5: Illustration of a typical planar circular magnetron, showing a cross section of the setup. On the left side the field configuration is shown with the region of most effective electron trapping indicated by the purple color. On the right side the motion of electrons and ions together with the flux of sputtered atoms are indicated. Illustration by courtesy of F. Haase.

In a circular planar magnetron such as the one used in this thesis, the target is a disk with a typical radius of 5 to 10 cm and the magnetic field is created by two separate packs of magnets positioned behind the target. One magnet pack is positioned in the center and the other around the perimeter of the disc as visible in the cross-section of figure 3.5. Since the impinging ions create a high energy flux to the cathode, the magnets and the cathode is cooled with water to prevent demagnetization of the magnets or damage to the cathode. Due to the radial symmetry, this type of magnetron forms a 'donut-shaped' plasma torus above the cathode, which is clearly visible and results in a circular erosion zone on the target surface, called the race track. To allow for comparison between different magnetron systems, the current-voltage-characteristic is a good indicator. Based on the physics of an abnormal glow discharge, which is the typical operation regime for a magnetron, Thornton [48] derived

an empirical law which is applicable for most planar magnetrons:

$$I \propto U^n \quad (3.9)$$

The parameter n is characteristic for the specific system and describes the efficiency of the electron trapping which is primarily dependent on the working pressure, the target material and the magnetic field strength. Typical values for n can range from 7 to 14 [49].

As argued above it was well known that the strength of the magnetic field is critical to the magnetron operation but it was only in 1986, almost 20 years after the invention of the conventional magnetron, that Window and Savvides investigated the effect of unequal inner and outer magnet packs [50], see figure 3.6. They found that, by using an 'unbalanced' magnetic field with stronger magnets on the perimeter, the ion density in the substrate region can be effectively increased without sacrificing the high flux of coating atoms associated with the conventional setup. Ions play a critical role in the deposition process of magnetron

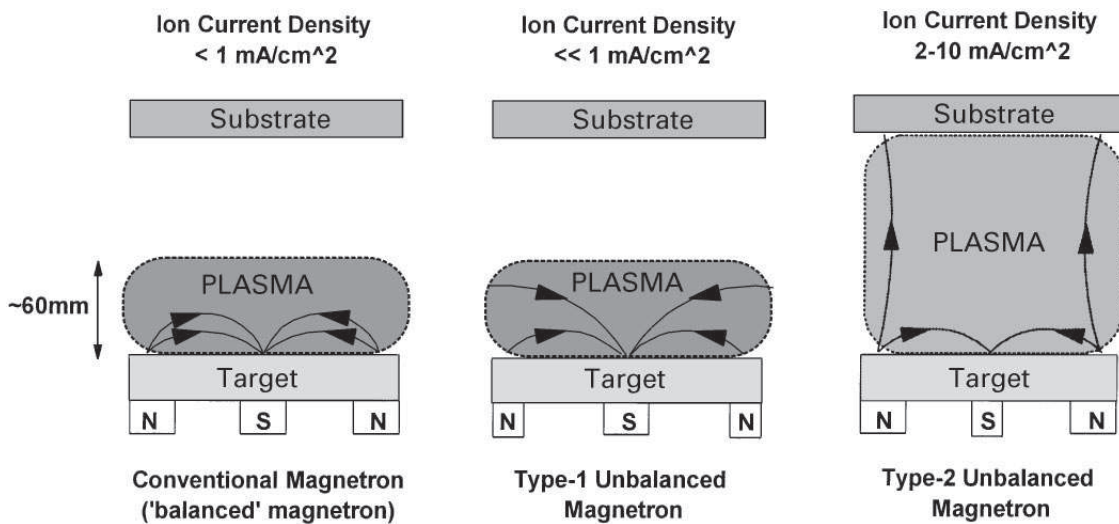


Figure 3.6: Comparison of magnetron systems with different magnetic configurations. The difference in plasma confinement between the conventional and unbalanced magnetrons is schematically shown by the gray plasma region.

sputtering films. As a heavy species, the ions can transfer energy more localized to the growing film than the electrons or e.g. radiation [49]. This localized energy transfer was found to strongly influence the structure and properties of the growing film and the observed changes were found to be both a function of the amount of ions impinging on the substrate as well as of their energy. In figure 3.6 the effect on the plasma confinement for different magnet configurations is shown. For the conventional case, with a 'balanced' magnetic field, the trapping of the electrons is very efficient. As the electrons gyrate along the magnetic field lines, they can only drift towards the target where they will eventually change direction due to the negative potential and start drifting back into the plasma. For 'Type-1 Unbalanced' magnetrons, the inner magnet pack is stronger than the outer one, which results in some of the B-field lines not ending on the cathode but instead, being directed towards the chamber walls. This results in a slightly lower plasma density in the main plasma as electrons can escape towards the wall. However, if the outer magnets are chosen to be stronger than

the inner ones, again, the field lines are not closed, but in this case the open field lines are directed towards the substrate. This configuration is called 'Type-2 Unbalanced' and is associated with ion current densities in the range of an order of magnitude higher than those obtained in the conventional magnetron. The reason why the ion density changes so dramatically as a function of the magnetic field, is not the direct interaction according to the Lorentz force (ion gyration radii are usually bigger than discharge dimensions) but because of their coupling to the electrons. As explained above, the electrons are effectively bound to the B-field and accordingly, for type-2 magnetrons, more electrons can escape from the main plasma region towards the substrate. Since the escape of electrons along the field lines would lead to unequal densities of electrons and ions, the plasma reacts by forming a space charge electric field E . This field reduces the electron motion away from the center of the plasma and accelerates the ion movement towards the substrate [5]. The resulting drift of coupled electrons and ions is called 'ambipolar diffusion' and can be understood as a 'dragging along' of the ions by the flux of the electrons.

A typical approach for compensation of the low flux of ions in conventional magnetrons is the negative biasing of the substrate. This however, can lead to defects and increased stress in the film caused by the higher energy of the accelerated ions. Instead, a high flux of relatively low energy ions is generally preferred [51], which are conditions readily provided by the type-2 unbalanced setup.

DCMS with additional magnetic field

One of the experimental setups used to change the balance of the magnetic field, is the combination of a magnetron with an additional magnetic field provided by an electromagnetic coil. This coil can e.g. be placed outside of the chamber [52] or as shown in figure 3.7 be integrated in the substrate holder [53]. The idea of such a setup is, that it can flexibly

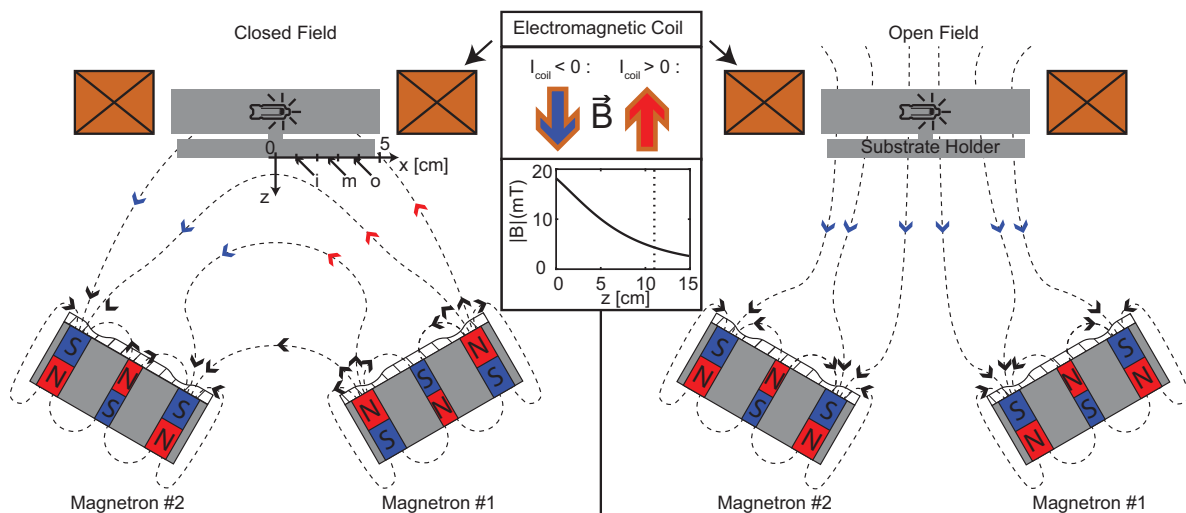


Figure 3.7: Schematic setup of an advanced magnetron sputtering system with two confocal magnetrons with unbalanced magnet configurations. Here two configurations of the confocal system are shown: closed field (the magnetrons have opposing magnetic polarity) and open field (both magnetrons have the same magnetic polarity). The additional magnetic field created by the coil allows to flexibly change the balance of the magnetic field and accordingly the number of ions on the substrate. Taken from [53].

change the flux of ions onto the substrate by adjusting the current of the electromagnetic coil. Additionally it is an effective tool to investigate the effect of different magnetic field configurations.

3.3.2 High Power Impulse Magnetron Sputtering (HiPIMS)

One of the most important process parameters in magnetron sputtering is the plasma density. Since a higher plasma density results in both higher deposition rates as well as a higher fraction of ionization in the sputtered material flux, it is desirable to maximize this parameter. This resulted in the development of a branch of magnetron sputtering called ionized physical vapor deposition (IPVD), which defines systems with more than 50% of ions in the sputtered vapor [54]. These systems usually include a secondary discharge which provides additional ionization of the sputtered atoms and thus allows for e.g. improved deposition in trenches of high aspect ratio. However, since these techniques cannot be easily incorporated into existing magnetron sputtering systems, they create relatively high cost and complexity compared to DCMS.

In DCMS a higher plasma density can be achieved by simply increasing the power density supplied to the target. However, this also leads to overheating and eventually melting of the target which creates an upper limit for this approach. In 1999 Kouznetsov et al. [55] introduced a novel approach to overcome this limit by applying a high power unipolar pulse of low frequency and low duty cycle to the cathode. This method is called *high power pulsed magnetron sputtering* (HPPMS) or *high power impulse magnetron sputtering* (HiPIMS). The low duty cycle (0.5 - 5%) allows to use much higher cathode voltages (500-2000 V) resulting in peak power densities in the order of 0.5-10 kW/cm² without overheating the target.

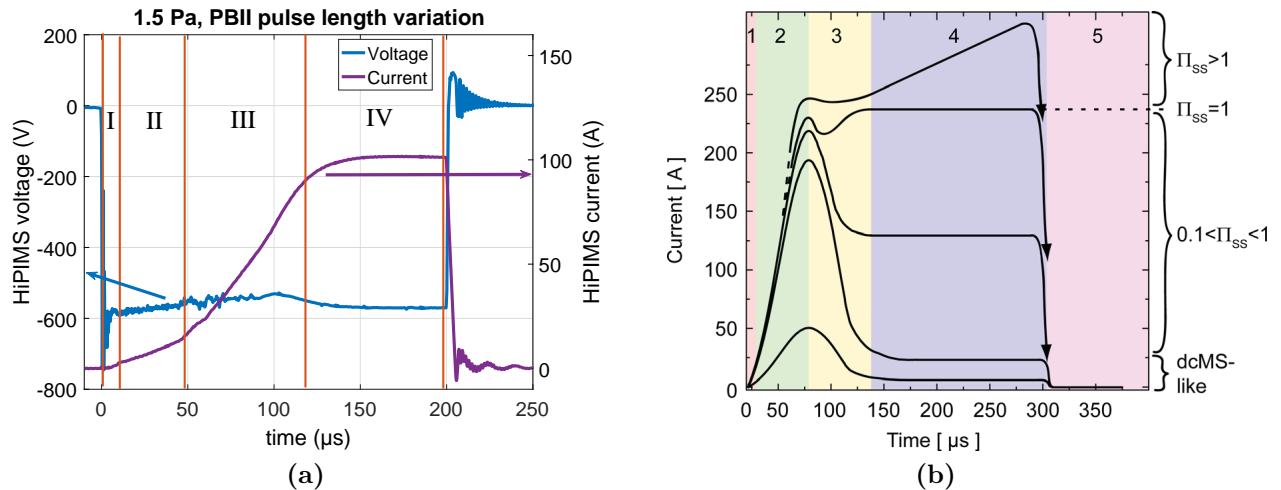


Figure 3.8: (a) voltage and current signal for an exemplary HiPIMS pulse with a frequency of 100 Hz and 200 μs on-time. The roman numerals indicate the phases introduced in (b) with a more detailed description given in [56]. (b) schematic illustration of the HiPIMS current pulse divided into five different phases and three regimes according to the self-sputtering parameter Π_{ss} . Plots taken from [57] and [54].

In figure 3.8 typical ion and voltage signals for a HiPIMS discharge are shown. The current can be divided into five different regions, which each represents a different phase of

the discharge:

1. *ignition* - short period with negligible plasma in the bulk volume which leads to the ignition of the plasma.
2. *current rise* - initial current increase after the bulk plasma breakdown, with the development of a dense plasma torus above the race track. In this phase the plasma mainly consists of background gas ions.
3. *gas depletion* - the current and plasma density reach a maximum which creates a strong reduction of the working gas atom density. The density reduction is mainly a result of the high electron impact ionization and momentum transfer from the sputtered atoms.
4. *plateau/runaway* - for the plateau case, a stable current develops as the result of a balance between gas-rarefaction, refilling with background gas and self-sputtering. If the self-sputtering is efficient enough, the discharge current continues to rise (runaway) as a result of further depletion of the background gas and replacement by ions of the sputtered species.
5. *afterglow* - after the HiPIMS pulse is switched off, the current drops sharply, followed by a slower decay of the plasma density, which in some cases can result in a weak plasma being present for the entire off-time of the pulse.

A particularly interesting case appears, when the sputtered vapor is created at a high enough rate that the ions of the working gas are not further needed to sustain the plasma. This case is called sustained self-sputtering and the threshold to this regime is defined by the self-sputtering parameter Π_{ss} :

$$\Pi_{ss} = \alpha\beta_t Y_{ss} = 1. \quad (3.10)$$

Here, α is the ionization probability for the sputtered atom, β is the probability for an ion created by ionization from the sputter vapor to return to the target, and Y_{ss} is the self-sputter yield of this ion. In the regime of sustained self-sputtering, it is possible to reduce the amount of background gas pressure and in some cases the discharge can be run without additional working gas [58]. The absence of working gas allows to create films with very high purity and superior properties due to fewer collisions of the sputtered atoms on their path to the substrate.

Compared to DCMS, HiPIMS systems present a comparable complexity as the only difference is the power supply, while providing two orders of magnitude higher electron densities in the range of $10^{18} - 10^{19} \text{ m}^{-3}$. The main disadvantage is a reduction of the deposition rate by up to 50% [59], which is typically associated with ionized particles of the sputter vapor returning to the target, also known as the 'returning ion effect' [54].

3.3.3 Gas Aggregation Cluster Source (GAS)

The first magnetron based cluster source was introduced by Haberland [60] in 1991 as an alternative to the existing cluster sources which usually involved a laser or thermal evaporation process. While the original idea was to grow strongly adherent films, in recent

years this type of cluster source has been majorly used to produce complex nanoparticles or nanoparticle-films [61]. Figure 3.9 shows a schematic setup of a typical magnetron-based gas aggregation cluster source. A magnetron sputtering source is positioned in a relatively small water-cooled chamber. The high gas pressure in the aggregation chamber (>10 Pa) and the cooled walls, allow to efficiently cool the sputtered target atoms by collisions with the background gas. The cooling is necessary to increase the probability for the formation of dimers as a result of three-body collisions. Once the dimer is formed it can further grow by attachment of single atoms or by coagulation with other dimers or bigger particles. Since the aggregation chamber is connected with a small nozzle to the differentially pumped deposition chamber, the particles are transported by the resulting gas flow from the aggregation chamber into the deposition chamber where they arrive as a beam of nanoparticles.

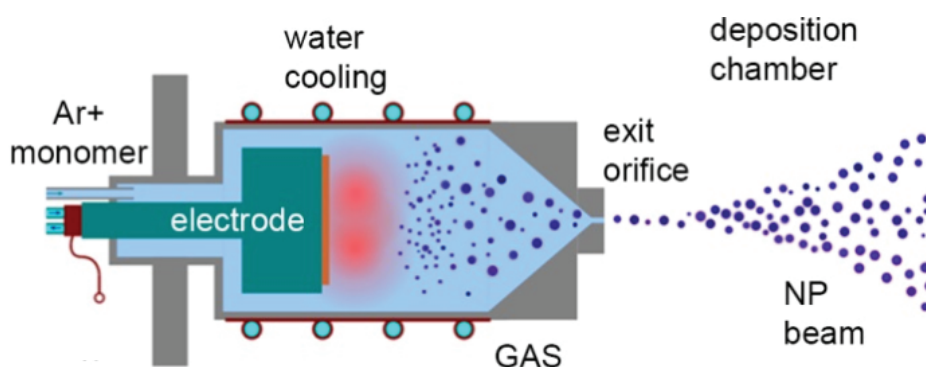


Figure 3.9: Schematic drawing of the setup for cluster generation in a typical Haberland type aggregation source. Taken from [62].

3.4 Plasma Based Ion Implantation and Deposition (PBII&D)

Plasma based ion implantation and deposition is a hybrid process which combines plasma based ion implantation (usually known as *plasma based ion implantation* (PBII) or *plasma immersion ion implantation* (PIII)) with a plasma based deposition process. The idea here is, that through the combination of both processes, almost any desirable elemental composition profile can be created [63]. To combine the two systems, a deposition plasma with a high degree of ionization in the depositing species is needed. For this reason, in most cases cathodic arcs, also known as vacuum arcs, are used as a deposition source, however other sources have also been used such as IPVD sources with post-ionization or more recently HiPIMS [64].

Plasma based ion implantation (PBII)

PBII or PIII was developed as an alternative process to ion beam based ion implantation which is a line-of-sight process and, thus, does not allow practical treatment of three-dimensional objects. In PBII the highly kinetic ions are not supplied by an external ion

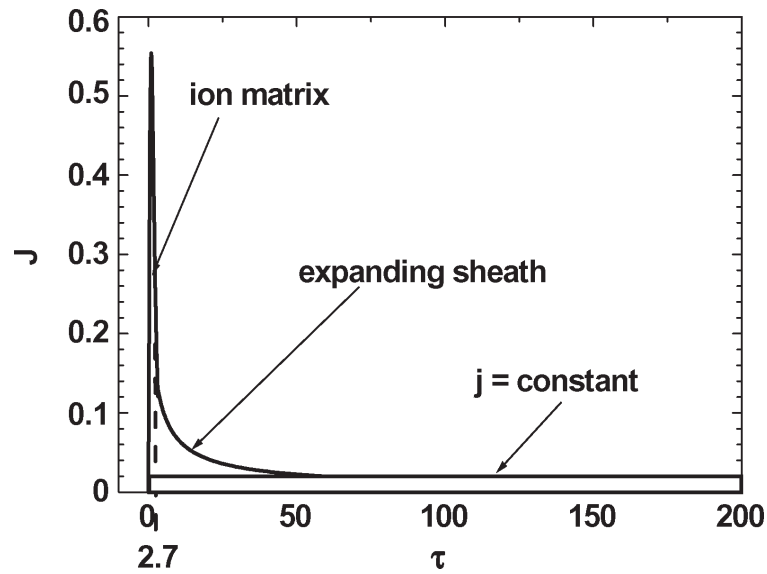


Figure 3.10: Theoretical evolution of the normalized ion current density J as a function of the normalized time τ , according to the Lieberman model for application of a negative voltage step to a planar substrate. The time is normalized on the inverse ion plasma frequency and the current density on $e_0 n_i v_0$, where n_i is the ion density and v_0 the characteristic ion velocity. Graph taken from [63] with data from [65]

beam, but instead, the substrate is immersed in a plasma and becomes part of the ion acceleration scheme itself. By biasing the object, ions from the plasma are accelerated in the plasma sheath, which uniformly develops around the immersed object.

As it can be seen in figure 3.10, the development of the sheath effectively shields the potential from the plasma, resulting in a short burst of high ion current followed by a much lower constant current. The experimentally observed current signal is in good agreement with the theory and can be explained by the Lieberman model as followed [65]: Upon application of the bias voltage, first, the electrons are repelled according to the time scale of the inverse electron plasma frequency ($\omega_{p,e}^{-1} \approx 10^{-9} s$, see equation 2.7). Since the ions are too massive to respond as quickly as the electrons, a matrix of ions is exposed, which is also called the *ion matrix sheath*. Next, on the slower timescale of the inverse ion plasma frequency ($\omega_{p,i}^{-1} \approx 10^{-6} s$, see section 2.1), the ions in the matrix sheath are accelerated towards the substrate and create a sharp maximum in the current as visible in figure 3.10. As more and more ions are extracted from the plasma, the sheath edge moves into the plasma and on a longer time scale of typically tens of $\omega_{p,i}^{-1}$, the sheath and the current density evolve towards a steady-state configuration according to the Child-Langmuir law [63]. To utilize the high current from the matrix sheath, the bias voltage is typically operated in a pulsed mode with frequencies of a few Hz up to several MHz.

HiPIMS as a source for PBII&D

HiPIMS with its high fraction of ions in the sputtered atom flux and advantages regarding implementation into DCMS systems, scalability and advanced techniques such as 'gasless' self-sputtering is an intuitive candidate as a deposition source for PBII&D [64]. Figure 3.11 shows a typical arrangement for implementation of such a system. Compared to other

sources usually employed in PBII&D, such as laser ablation plasmas or (filtered) cathodic arc evaporation, HiPIMS has the advantage of producing fewer multiply charged ions which allows a more monoenergetic processing and, thus, more precise control of the interface and film texture. Additionally it is characterized by a much higher accompanying flux of neutrals which makes it particularly useful for the deposition part of PBII&D.

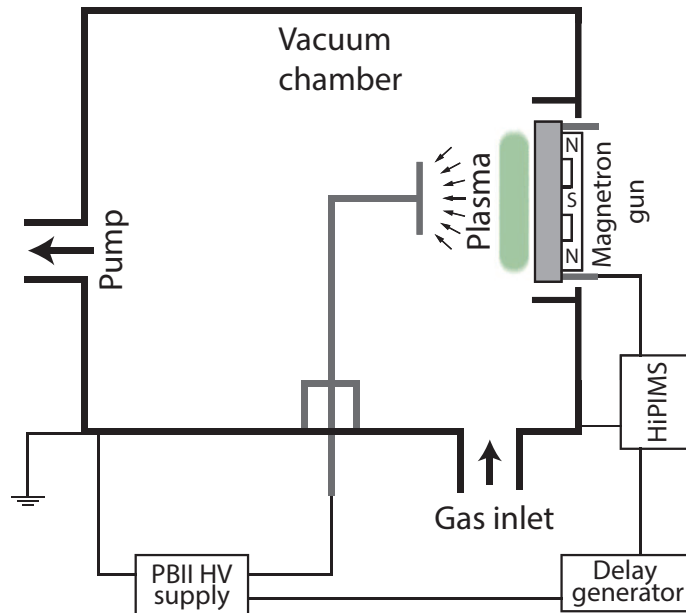


Figure 3.11: Schematic drawing of a typical arrangement for PBII&D with HiPIMS. Adapted from [66].

4 Plasma Diagnostics

This chapter gives an introduction into the theory and design of the diagnostic tools used for the measurements in this thesis, with a particular focus on the calorimetric probes used to measure the energy flux from a plasma.

4.1 Electrostatic probing - the Langmuir probe

The original article which introduced the concept of electrostatic probing in gaseous discharges and still builds the theoretic foundation for modern Langmuir probe (LP) measurements, has been published by Mott-Smith and Langmuir in 1926 [67]. Due to its experimental simplicity and richness of information regarding critical plasma parameters, the Langmuir probe evolved to be the most successful diagnostic method for plasma characterization. It is beyond the scope of this work to fully describe this method and its underlying theory, instead, this section will describe the basic ideas and focus on the methods used to obtain the plasma parameters for the measurements presented in this thesis. More detail on different probe geometries, electronic measurement procedures and specialized probes can be found in the references [4, 5, 68].

4.1.1 The U-I-characteristic

In figure 4.1b a typical Langmuir curve as measured in a magnetron sputtering experiment along with the sketch of a planar probe (4.1a) similar to the one used to obtain the data is shown. Since both ions and electrons are not mono-energetic, but are described by a complex energy distribution function, the amount of ions and electrons being able to reach the probe gradually changes as a function of the probe potential. As described in chapter 2.1, at the floating potential Φ_{fl} , the current of electrons and ions are equal, resulting in a net current of 0 A. Due to the higher energy of the electrons, this potential must always be more negative compared to the plasma potential Φ_{pl} .

The form of the Langmuir curve, starting from a very negative potential (-50 V in figure 4.1b), can be explained as follows: If the probe is biased negative enough that even the electrons from the highly energetic tail of the energy distribution cannot reach the probe surface, the current on the probe is solely produced by ions. For potentials even more negative than this, the resulting ion-saturation current $I_{i,sat}$ in theory stays on a constant level. The slight decrease, which is typically observed in real measurement curves, is solely an effect of increasing sheath thickness and, accordingly, greater collection surface for the ion current. The region where the probe current is solely created by ions is called the

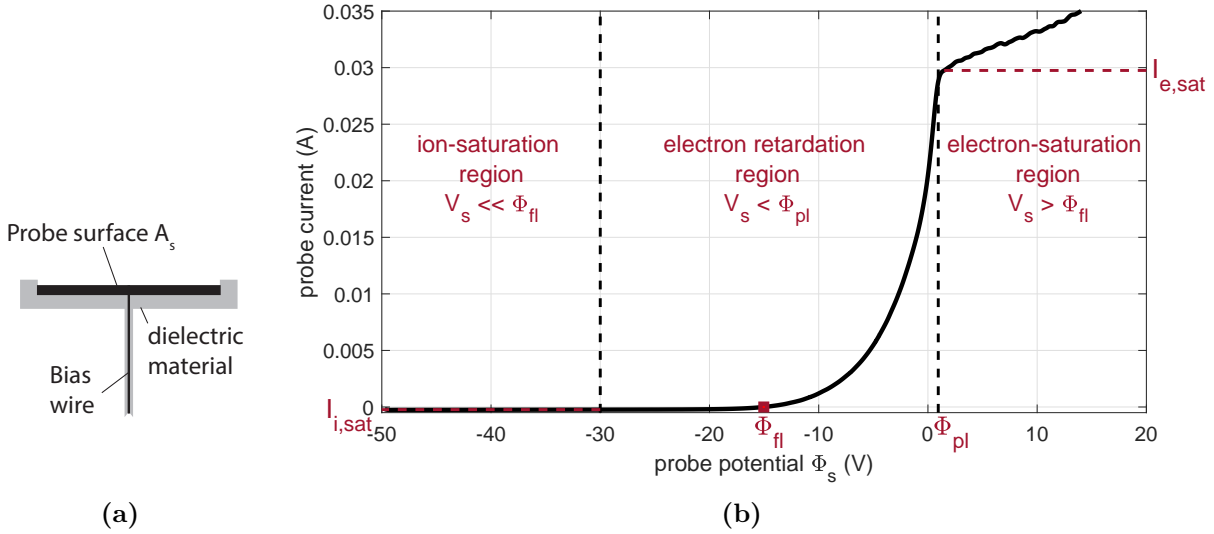


Figure 4.1: (a) schematic drawing of a planar Langmuir probe. (b) exemplary Langmuir measurement curve for a planar probe with 11 mm diameter. The relevant regions and obtained parameters are marked in red. It should be noted that, by tradition, the negative probe current is plotted.

ion-saturation regime and the current in this region is given by

$$I_{i,sat} = n_i e_0 A_s v_B \approx 0.61 n_i e_0 A_s \sqrt{\frac{k_B T_e}{m_i}}. \quad (4.1)$$

As it can be seen from the equation, the ion-saturation current is only defined by the ion density n_i , the Bohm velocity v_B and the surface area of the probe A_s . Through the definition of the Bohm velocity (section 2.1), it can also be expressed by the energy which the ions gain in the presheath, which results in the relation $v_B = 0.61 \sqrt{k_B T_e / m_i}$. Here, m_i is the ion mass, k_B the Boltzmann constant and T_e the electron temperature. Using this relation, a direct connection between ion saturation current, electron temperature and ion density is given, and, if both T_e and $I_{i,sat}$ are known the ion density can be calculated.

If the probe potential is increased to higher values, the electron retardation region is entered. Here, more and more electrons are able to reach the probe surface and due to the Maxwellian energy distribution, the current rises exponentially, resulting in a total current I_{tot} of

$$I_{tot} = n_e e_0 A_s \sqrt{\frac{k_B T_e}{2\pi m_e}} \left(0.61 \sqrt{\frac{2\pi m_e}{m_i}} - \exp\left(-\frac{e_0(\Phi_{pl} - \Phi_s)}{k_B T_e}\right) \right), \quad (4.2)$$

with the electron charge e_0 , the electron mass m_e and the probe potential Φ_s .

At the plasma potential Φ_{pl} , the probe is at the same potential as the plasma and no electric field and, accordingly, no sheath is present around the probe. Here, all ions and electrons can reach the probe. If the probe potential is increased to even higher values, the current shows a characteristic kink and stays at an almost constant level afterwards. Any further increase is only due the fact of an increasing collision parameter described by the OML model [5]. In the so-called electron-saturation regime, analogous to the ion-saturation regime, the ions cannot reach the probe and the current is solely defined by the density n_e

and energy of the electrons:

$$I_{e,sat} = -\frac{1}{4}n_e A_s e_0 \sqrt{\frac{8k_B T_e}{\pi m_e}}. \quad (4.3)$$

4.1.2 Evaluation of the U-I-characteristic

According to the theory introduced above, the basic information of electron and ion density, floating potential, plasma potential and electron temperature can be obtained from the measurement curve with relative simple methods. While the floating potential and the saturation currents, can be directly observed, the electron temperature is calculated from a linear fit to the logarithmic plot of the current in the retardation regime (see figure 4.2a and 4.2b). As it can be easily seen from equation 4.2, such a semilog-plot will result in a linear function with a slope equal to $e_0/k_B T_e$. From the ion saturation current and the electron temperature, the ion and electron density ($n_i = n_e$) can be directly obtained from equation 4.1. The plasma potential is either obtained as the inflection point of the current or as the intersection of linear fits in the semilog-plot to the electron current in the retardation region and in the electron-saturation region, see figure 4.2b.

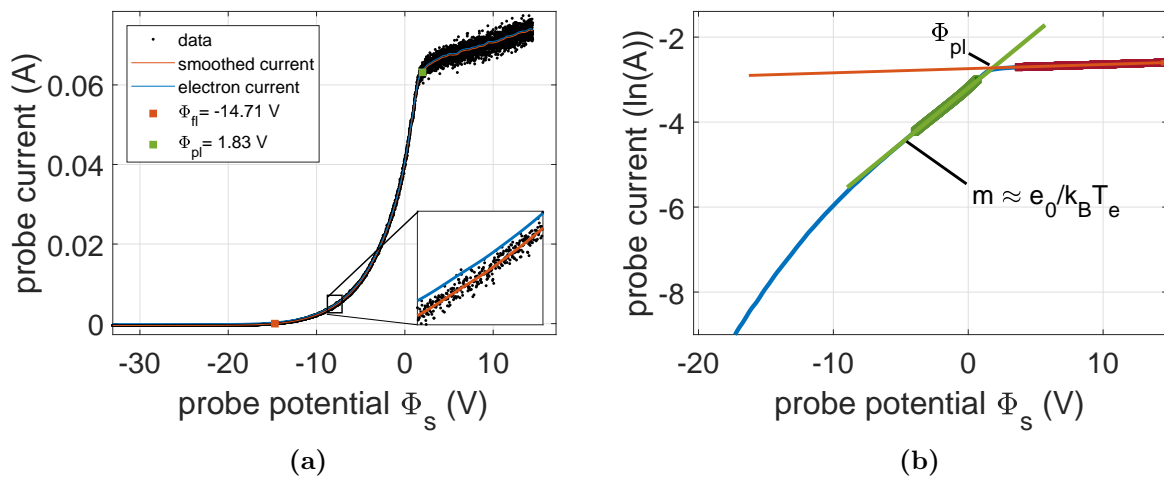


Figure 4.2: (a) exemplary measurement data of a planar Langmuir probe obtained in a magnetron sputtering experiment. The calculated values for the floating and the plasma potential are marked and along with the raw data, a smoothed fit and the electron current obtained after subtraction of $I_{i,sat}$ from the measured current, is given. (b) semilog-plot of the electron retardation and electron-saturation region of the data shown in (a). The two linear fits are used to calculate the electron temperature (slope m of green line) and the plasma potential (intersection of fits).

These basic methods give reasonably good results in most plasma environments, however, to reach higher accuracy and obtain more detailed results, sophisticated methods for the exact evaluation of the U-I-characteristic are advisable [68]. For example, in the case that the electron distribution function significantly deviates from a Maxwellian distribution, some of the assumption, which are made for deriving the above equations, do not apply anymore. In these cases the most common method for evaluation of the Langmuir data is the *Druyvestyn*

method. Using this method, the electron distribution function can be directly derived from the second derivative of the I-V-curve, which allows a more accurate determination of the electron temperature and gives additional information regarding e.g. secondary electron populations in the plasma [5].

All LP measurements presented in this thesis, including the one shown in figure 4.2a, are obtained using a National Instruments acquisition card in combination with *LabVIEWTM* software. Analog to the improvements made to the thermal probe measurement software (see chapter 5.2.1), the LP software was also majorly overhauled as a part of this thesis. The software optimization was done in close collaboration with Fabian Haase and the reader is advised to his PhD thesis for a more detailed description of the improved software.

4.2 Quartz Crystal Microbalance

For most deposition systems it is of fundamental importance to know the deposition rate, so that the thickness of the deposited film can be effectively adjusted. The basic technique to obtain this parameter is by measurement of the deposition time and subsequent measurement of the sheath thickness using e.g. profilometers or microscopes. The biggest disadvantage of this methods is that it only gives a time-averaged value and that it does not allow in-situ measurements. In 1959 Sauerbrey solved both of these problems by introducing an elegant method for the in-situ measurement of the deposition rate: the Quartz Crystal Microbalance (QCM) [69]. The basic idea of this method is to measure the mass m of a deposited film using the eigenfrequency f_0 of a piezoelectric crystal. By treating the deposited film as an extension of the crystal thickness, Sauerbrey derived the following relation between the change of eigenfrequency Δf , crystal area A , density and shear modulus of the quartz ρ_q, μ_q and the change of the mass Δm :

$$\Delta f = \frac{2f_0^2}{A\sqrt{\rho_q\mu_q}}\Delta m. \quad (4.4)$$

By using the crystal as part of a resonant circuit, the oscillation frequency can be determined with a resolution below 1 Hz and since typical AT-cut piezoelectric crystals have eigenfrequencies in the range of a few MHz, even small changes of mass can be detected accurately.

In this thesis, the commercially available QCM *IL150* produced by *Intelmetrics Global Ltd.* with 6 MHz AT-cut crystals (14 mm diameter, 3 mm thickness) have been used. As in all modern QCM's, the crystal has a plano-convex shape, which results in most of the oscillations to occur in the central exposed region of the crystal and allows firm clamping on the sides. To increase the life cycle of the crystals by allowing thicker films than originally intended by Sauerbrey, the *IL150* employs a more rigorous acoustic analysis of the loaded crystal as a one dimensional composite resonator [70]. Using this model, the thickness T_f of the deposited film can be calculated from

$$T_f = \frac{D_q}{D_f} \frac{N_q T Z_f}{3.14 Z_q} \arctan \left(\frac{Z_q}{Z_f} \tan \left(3.14 \left(1 - \frac{T_q}{T} \right) \right) \right), \quad (4.5)$$

with D_q , D_f and Z_q , Z_f the density and the acoustic impedance of the crystal and the deposited film, respectively, N_q the frequency constant for an AT-cut quartz crystal and T and T_q the period of the loaded and the unloaded crystal, respectively. However, it should be noted, that this more complicated calculation of the film thickness only results in appreciable deviations from those predicted with equation 4.4 for heavily loaded crystals. Therefore, for most cases, the original assumption that the film can be treated as an extension of the crystal ($Z_f = Z_q$) is valid and equation 4.5 can be reduced to

$$T_f = \frac{N_q D_q}{D_f} (T - T_q). \quad (4.6)$$

Since the primary measurement value of the QCM, in accordance with equation 4.4, is the mass of the deposited film, any derived values like film thickness or deposition rate necessarily include assumptions regarding the density of the deposited material. As especially the density can vary greatly depending on various parameters in the thin film deposition process, it needs to be chosen with great care and the resulting measurements have to be analyzed accordingly.

4.3 Calorimetric Probe

The measurement of energy flux with calorimetric probes, also known as thermal probes, is a well established method which originates from the measurement of radiation coming from the sun or other radiation sources [71]. It was notably introduced to plasma environments for measuring the energy balance of surfaces in 1978 by Thornton [35] and has been since proven as a versatile and robust diagnostic [17, 72–77]. Over the years a variety of different methods have been developed like the Gardon sensor which deduces the energy flux from increased temperature in the center of an exposed membrane [17, 78] or a method which deduces the energy flux from the temperature gradient over a partially exposed substrate [79, 80]. A refined version of the temperature gradient method is utilized in the thermopile sensor, which combines a cooled PT100 element with an array of 1600 thermocouple junctions [77].

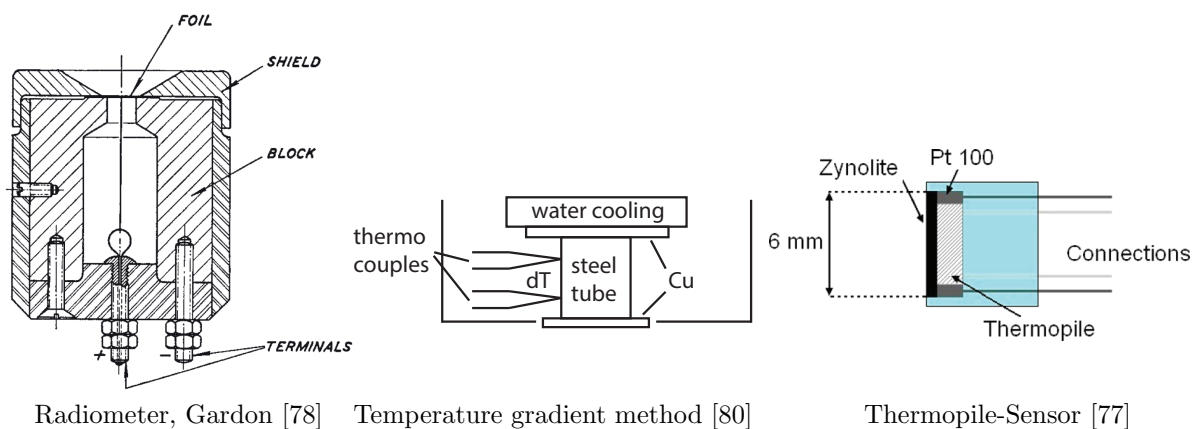


Figure 4.3: Schematics of different calorimetric probes.

The calorimetric probes used in this thesis are commonly known as passive thermal probe

(PTP) and active thermal probe (ATP). The passive thermal probe was introduced by Thornton [35] in 1978 and is essentially based on the relation between net-power to the substrate and temperature gradient of a substrate exposed to a plasma. The active thermal probe is a much newer development [81] and is based on the balance between external energy flux and supplied energy flux through active heating of the probe substrate. The detailed construction and underlying principles of those probes are described in greater detail in the following sections.

4.3.1 Grouping of the energy flux contributions

In section 2.2 the different contributions to the integral energy flux for a substrate in contact with a plasma were introduced theoretically. To understand which of those contributions are actually measured by the calorimetric probe, it is helpful to sort these into different groups. An intuitive way to do this is to group them into positive and negative contributions, or, from the perspective of the substrate, incoming and outgoing energy fluxes:

$$J_{in} = J_{kin} + J_{radiation,line} + J_{+surface} \quad (4.7)$$

$$J_{out} = J_{con} + J_{radiation,heat} + J_{emitPart} \quad (4.8)$$

Here it is assumed, that the probe is cooled by the gas, the substrate holder and heat radiation and that the surface reactions result in a positive energy flux. Although this grouping is very useful to understand the nature of the energy balance, a different sorting is necessary to understand the integral energy flux which is detected by the thermal probe. In their primary operating mode both thermal probes give a differential measure of energy flux. This means that actually not the absolute energy flux is measured, but the difference between the energy flux with the plasma switched on and that with the plasma switched off. Therefore, it is necessary to sort the different contributions according to their typical time constants, by dividing them into continuous and switchable contributions:

$$J_{meas}(t) = J_{kin} + J_{radiation,line} + J_{+surface} + J_{emitPart} \quad (4.9)$$

$$J_{cont}(T_s, t) = J_{con} + J_{radiation,heat} \quad (4.10)$$

The continuous contribution J_{cont} changes only weakly as a function of time t and more directly as a function of the substrate temperature T_s , while the switchable contributions J_{meas} change abruptly once the plasma is shut off. Due to the short time period which is used for evaluation, the continuous contributions can be assumed to be constant and thus disappear due to the differential measurement method. The remaining switchable contribution J_{meas} yields the measurement value.

4.3.2 Passive thermal probe (PTP)

In the first two parts of this section the measurement principle and design of the passive thermal probe used in the majority of the experiments in this thesis are described. In the

last part, common methods for evaluation of the obtained temperature curves are presented.

Physical probe design

The passive thermal probe used in the majority of the experiments in this thesis is based on the original Thornton design [35] and was developed and refined in the plasma technology group of Prof. Kersten at Kiel University [32]. An improved version of this design which was developed as a part of this thesis is described in chapter 5.2. Figure 4.4 gives a photograph

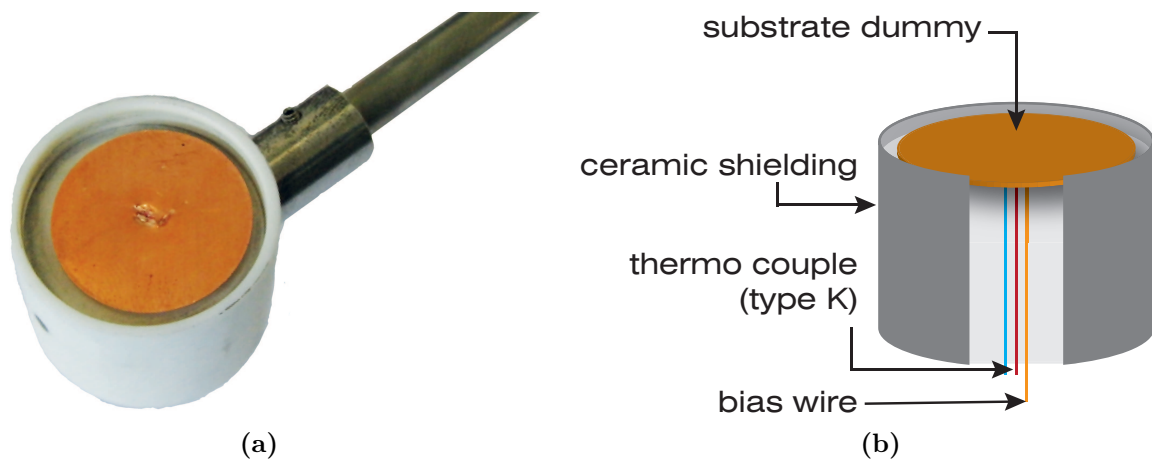


Figure 4.4: (a) Photograph of the PTP sensor head with dummy-substrate made of copper, in the middle the indentations from spot welding are visible. (b) Schematic drawing of the sensor head of the PTP.

and schematic drawing of the sensor head which uses a circular dummy substrate made of a copper sheet. The substrate has a diameter of 2 cm, a thickness of $70 \mu\text{m}$ and a high thermal conductivity of $\lambda_{Cu} = 390 \text{ W}/(\text{m} \cdot \text{K})$. The high thermal conductivity is necessary to create a homogeneous temperature over the whole substrate and ensures fast heat transfer to the back of the substrate. Here the temperature is detected with a Type K thermocouple ($40 \mu\text{V}/\text{K}$) which is spot welded to the middle of the probe. Additional to the two thermocouple wires, a copper wire is spot welded to the back of the probe, which allows biasing of the probe and measurement of electrical current or potential.

The copper plate is shielded by a ceramic housing made of Macor[®] which minimizes energy flux to the back of the probe resulting in an exposed substrate area of $A_s = 3.12 \text{ cm}^2$. Additionally, the ceramic insulates the substrate electrically from the metallic holder and has a high heat capacity of $C_h = 18.2 \text{ J}/\text{K}$. The copper substrate on the opposite, is optimized to have a small heat capacity of typically $C_h = 0.1 \text{ J}/\text{K}$ which results in fast changes of the substrate temperature upon exposure to energy flux. The big difference in heat capacity ensures, that any energy transfer between substrate and holder changes on long timescales and can thus be neglected according to equations 4.15 and 4.16.

In figure 4.5 a schematic drawing of the main components of the measurement setup is shown, a detailed description can be found in [82]. The temperature-dependent voltage, resulting from the Seebeck effect, is amplified by a circuit outside of the vacuum chamber (AD595, [83]). This circuit together with an additional amplifier increases the voltage to $15 \text{ mV}/\text{K}$ and integrates a cold-junction compensation and reference zero-point (0°C). The

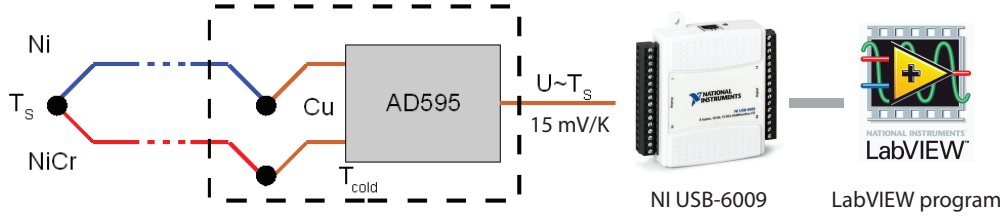


Figure 4.5: Schematic drawing of electronic measurement setup for the passive thermal probe.

thermocouple wires are connected with copper wires to the measurement electronics. At the junctions between thermo- and copper wire, other, unequal, temperature-dependent voltages are created which are compensated according to the temperature at this junction by the cold-junction compensation. The cold-junction temperature is measured by a PT100 element in the integrated circuit and since the cold-junction in the measurement setup is actually at the vacuum feed through it can result in erroneous absolute temperature values. However, since for the measurement of the energy flux only relative changes in the temperature are relevant, one only has to make sure that the cold-junction is at a constant temperature for the period relevant to the evaluation.

The resulting signal is detected by a National Instruments multifunction I/O device 'USB-6009' which has a resolution of 14 bit and maximum acquisition rate of 48 kHz. Due to the thermal inertia of the copper plate, time resolutions above 100 Hz do not give any extra information. However, to reduce statistical noise the acquisition card is always operated at its maximum frequency, which allows for averaging over 480 temperature values for each data point acquired at 100 Hz. A more detailed description of the acquisition algorithm developed in *LabVIEWTM* is given in section 5.2.1.

Measurement principle

The energy of a thermodynamic system can be described by its enthalpy, which is a measure for the total amount of energy or heat stored in the system. The change of the enthalpy of a substrate \dot{H}_s is equal to the product of its heat capacity C_s and the time derivative of its temperature dT_s/dt :

$$\dot{H}_s = C_s \frac{dT_s}{dt} = P_{in} - P_{out}. \quad (4.11)$$

Under the assumption that no processes take place inside the substrate which lead to a change of enthalpy, a change can only be the result of interaction with its environment. This interaction can be characterized by the power coming to the substrate P_{in} and the power leaving the substrate P_{out} . To obtain a measure which is independent of the size of the substrate, it is common to normalize these powers with the area of the substrate A_s . This results in the energy fluxes J_{in} and J_{out} which have been introduced in section 4.3.1:

$$J_{in} = \frac{P_{in}}{A_s} \quad \text{and} \quad J_{out} = \frac{-P_{out}}{A_s} \quad (4.12)$$

The minus before P_{out} is inserted because the power is defined as an absolute value, while the energy flux going out from the substrate already is negative. If we are now able to switch

P_{in} off, we get two equations to describe the change of enthalpy:

$$\begin{aligned} \text{Heating: } \dot{H}_h &= C_S \dot{T}_h = P_{in} - P_{out,h} \\ \text{Cooling: } \dot{H}_c &= C_S \dot{T}_c = -P_{out,c} \end{aligned} \quad (4.13)$$

Under the assumption that the power leaving the substrate during the heating phase $P_{out,h}$ equals the power leaving the substrate during the cooling phase $P_{out,c}$ at the same temperatures, these two equations can be combined to calculate the incoming power from the temperature gradients:

$$P_{in} = C_s (\dot{T}_h - \dot{T}_c). \quad (4.14)$$

As argued in section 4.3.1, in our typical plasma environment we do have contributions to the energy flux which can be switched off and others, which mainly change as a function of the substrate temperature and only weakly as a function of the time. Using this grouping, 4.13 can be rewritten as:

$$\begin{aligned} \text{Heating: } \frac{\dot{H}_h}{A_s} &= \frac{C_s}{A_s} \dot{T}_h = J_{meas} + J_{cont,h}, \\ \text{Cooling: } \frac{\dot{H}_c}{A_s} &= \frac{C_s}{A_s} \dot{T}_c = J_{cont,c}. \end{aligned} \quad (4.15)$$

Since the contributions collected in J_{cont} only change slowly as a function of time, the assumption $J_{cont,h} = J_{cont,c}$ can safely be made for short time periods. This results in a simple relation for the energy flux which is detected by this method:

$$J_{meas} = \frac{C_s}{A_s} (\dot{T}_h - \dot{T}_c). \quad (4.16)$$

To allow precise and reliable determination of J_{meas} it is thus crucial to first obtain accurate values for the heat capacity and the exposed area of the probe and then precisely measure the evolution of the substrate temperature. The heat capacity for metallic probes can best be obtained by electron beam calibration described in chapter 5.1 and the effective probe area A_s is usually defined by the physical probe design. For the measurement of the probe temperature two aspects are of specific importance: the acquisition rate and the resolution. A high acquisition rate is necessary to minimize the evaluation times. This allows for taking advantage of small-heat-capacity-probes and strengthens the assumption of equal J_{cont} for the evaluated times. A good resolution is necessary to reduce the statistical error and lower the detection limit for a small energy flux.

Methods of evaluation

All evaluation methods for the temperature data acquired with the PTP are based on the theory presented in 4.3.2 and 2.2.5. In the following section, three methods for PTP evaluation are described in descending order regarding its versatility. These methods are the basis for PTP evaluation in most environments and need only slight modification even for extreme cases like the high energy flux from a hot plasma jet [84]. The *kink method* and

the *dT-method* are the most commonly used approaches and are closely related, as both are used to obtain the derivative of the temperature. The *equilibrium temperature method* is less practical for application with classical passive thermal probes of the 'Thornton-type', however a modified probe design would allow for efficient measurement without the necessity for a calibrated heat capacity.

According to section 4.3.2, it can be easily shown that heating and cooling of the substrate follows an exponential course if conductive cooling of the probe is dominant:

$$\left. \begin{aligned} T_{s,heat}(t) &= T_{eq} + \frac{P_{in}}{\alpha} - \left(\frac{P_{in}}{\alpha}\right) \exp\left(-\frac{\alpha}{C_s}t\right) \\ T_{s,cool}(t) &= T_{eq} + (T_{st} - T_{eq}) \exp\left(-\frac{\alpha}{C_s}t\right) \end{aligned} \right\} \text{temperature curve} \quad (4.17)$$

Here α is a constant which describes the efficiency of the conductive cooling and T_{st} denotes the probe temperature at the start of the cooling process. For better reliability when fitting this exponential course and especially for better understanding of any deviation from it, it is useful to analyze the time derivative of the temperature dT_s/dt as a function of the substrate temperature T_s . From equation 4.17 this so-called *dT-curve* can be calculated to be

$$\left. \begin{aligned} \frac{dT_{s,heat}}{dt} &= -\frac{\alpha}{C_s} \cdot T_{s,heat} + \frac{\alpha T_{eq} + P_{in}}{C_s} \\ \frac{dT_{s,cool}}{dt} &= -\frac{\alpha}{C_s} \cdot T_{s,cool} + \frac{\alpha}{C_s} \cdot T_{eq} \end{aligned} \right\} \text{dT-curve} \quad (4.18)$$

From these equations two things become obvious: the time derivative of the probe temperature as a function of the substrate temperature is a linear function and the slope of the linear function is only a function of the conduction coefficient α and the heat capacity C_s . It should be noted that equations 4.17 and 4.18 change for more complex environments as cooling by gas or radiation becomes more relevant. However, in most vacuum processes, the simple model presented here represents a viable description.

The kink method requires a high measurement frequency and little noise since only a short time-period of the graph is evaluated. For such small t , equations 4.17 can be approximated as linear functions using the Taylor series:

$$\left. \begin{aligned} T_{s,heat}(t) &= \frac{P_{in}}{C_s}t + T_{eq} \\ T_{s,cool}(t) &= \frac{\alpha}{C_s}(T_{eq} - T_{st})t + T_{eq} \end{aligned} \right\} \text{linear approximation} \quad (4.19)$$

In principle, using these equations, $(\dot{T}_h - \dot{T}_c)$ can be easily determined for any point with the same temperature on the heating- and the cooling-curve and according to the equations 4.18, $(\dot{T}_h - \dot{T}_c)$ will always yield the same value for $T_{s,heat} = T_{s,cool}$. As it can be seen from the measurement data shown in figure 4.6b, we do get parallel linear functions for the dT-curve and thus we indeed obtain the same value all along the curve. However, as illustrated in 4.6a, for the kink method, the curves are just evaluated at short time periods around the point where the energy flux initially starts (heating kink) and where it stops (cooling kink). The reason for this is, that in many measurement environments the conditions are not as ideal

as in the example measurement or in the model introduced above. Instead, warmup effects, which influence the energy flux due to e.g. conductive cooling or heat radiation, can disturb the measurement and make the assumption of approximately equal P_{out} during heating- and cooling-phase become less and less true. As argued in section 4.3.1 this erroneous influence can be minimized by comparing heating- and cooling-curves which are measured in a short time period. Evaluating only the time period around the kinks minimizes this time period and makes it more likely, that the temperature of the substrate holder or the vacuum vessel can be assumed to be constant. The main advantages of this method are

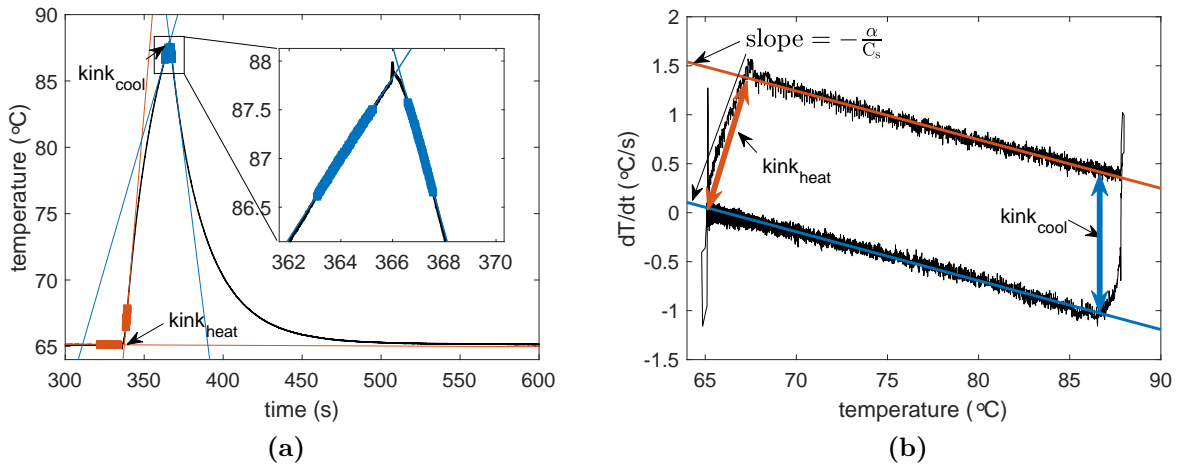


Figure 4.6: Demonstration of the *kink method* on an example measurement. (a) temperature curve as a function of time with marked evaluation areas around the two kinks, resulting in determined energy fluxes of $J_{kink,heat} = 39.15 \text{ mw/cm}^2$ and $J_{kink,cool} = 40.2 \text{ mw/cm}^2$. (b) dT -curve of the temperature data from (a) with linear fits of the heating and cooling period and the red and the blue arrow indicating the points which were used to build the difference in derivatives at the kinks.

short measurement times, no necessity for complex fitting or calculating of derivatives and negligible influence of temperature changes in the probe vicinity. The main disadvantage is, that an efficient mechanism for switching of the power source is necessary to allow for short evaluation periods.

The dT -method or exponential method determines the derivatives from an exponential function according to equation 4.17. The coefficients of the exponential function can either be obtained directly by an exponential fit algorithm or indirectly from the linear fits in the dT -curve as demonstrated in figure 4.7.

The advantage of this method is, that the measurement frequency can be much lower as compared to the kink method since a comparatively long time period is used for the evaluation. However, this also makes it necessary to have a very stable measurement environment, where no significant temperature change in the probe vicinity appears during this period.

The equilibrium temperature method is based on the balance between cooling and heating of the probe at the maximum temperature. For the simple case of solely conductive cooling of the probe, we can obtain the maximum temperature T_{max} for the heating phase

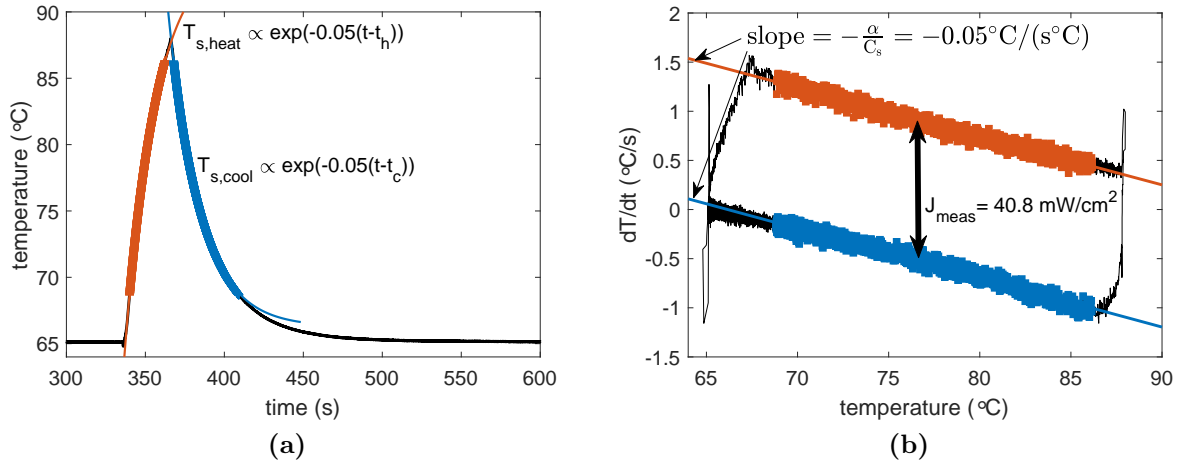


Figure 4.7: Demonstration of the *dT-method* on the same exemplary measurement data shown in figure 4.6. **(a)** temperature curve as a function of time with marked evaluation areas for obtaining the exponential fit resulting in a determined energy flux of $J_{meas} = 40.8 \text{ mW}/\text{cm}^2$. **(b)** *dT-curve* of the temperature data from (a) with linear fits of the heating and cooling period. The slope of the fits can be used to determine the coefficients of the exponential fit in (a). The differences in the derivative used for obtaining the energy flux is indicated by the black double arrow.

from equation 4.17 as

$$T_{max} = T_{eq} + \frac{P_{in}}{\alpha}. \quad (4.20)$$

Rearranging this equation and replacing P_{in} by $J_{in}A_s$, we get an expression for the energy flux which is independent of the heat capacity:

$$J_{in} = \frac{\alpha}{A_s}(T_{max} - T_{eq}). \quad (4.21)$$

To obtain the energy flux in this way, it is not only mandatory to know the conduction coefficient α , but it is also necessary to determine both the maximum temperature the probe will reach and the temperature of the heat sink which is relevant for the conductive cooling of the probe.

If the heat capacity of the probe is known, α can in principal be determined from any *dT-curve* measured for any unknown constant energy flux. This is due to the fact, that in the case of solely conductive cooling, the *dT-curve* consists of two parallel linear functions with a negative slope equal to $-\alpha/C_s$, see figure 4.6 and equation 4.18. For a known heat capacity, α can thus be directly determined from the negative tilt of the slope. The determination of the two temperatures T_{max} and T_{eq} can be achieved in two different ways. The classic approach is to observe the whole system for a sufficient time without energy flux, so that the equilibrium temperature can be determined. Then, the energy flux is switched on and the system is observed until it reaches thermal equilibrium, so that the maximum temperature can be determined. The *dT-curve* of such a measurement performed with a conventional thermal probe of the 'Thornton-type', is shown in figure 4.8a. For this measurement, the probe was exposed to the energy flux of an electron beam for 7 h and subsequently the

cooling of the probe was monitored for another 7 h. The figure clearly illustrates the main problem of this approach: as the probe is heated up, the probe housing and connection wires also start heating and therefore falsify the result on this long time scale. This problem can be avoided by implementing a cooling system into the probe as it has been successfully demonstrated for a specially designed sensor introduced by Thomann et al. [85].

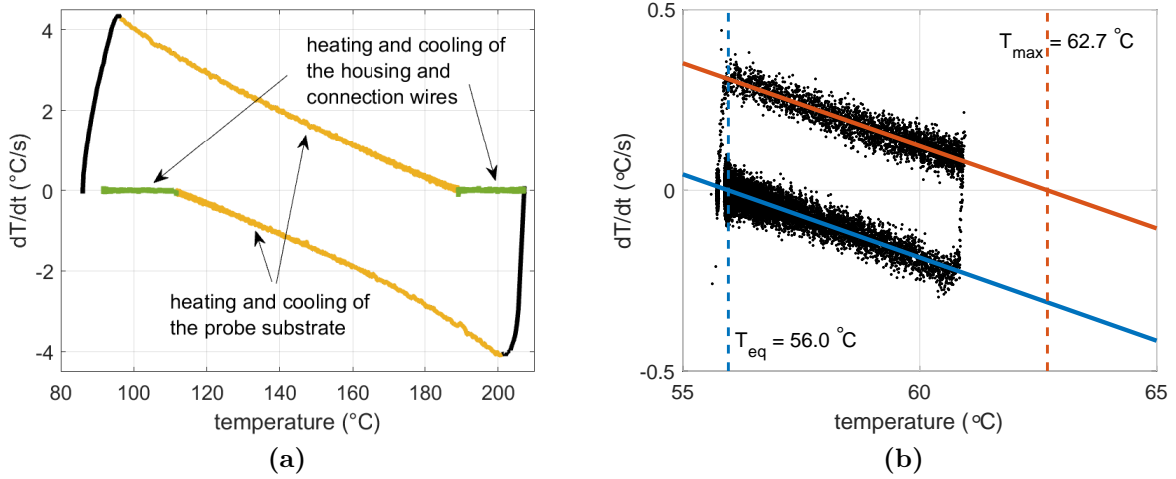


Figure 4.8: (a) dT-curve of a conventional PTP for 7 h hour exposure to a constant energy flux from an electron beam. (b) illustration of the extrapolation used to determine the maximum temperature and the equilibrium temperature from the dT-curve. The exemplary measurement curve is from an electron beam experiment with a heating time of 30 s.

A different approach to avoid this problem, which does not require modifications of the conventional setup, is to obtain the maximum and equilibrium temperature from an extrapolation of the linear functions in the dT-curve. From equations 4.17 and 4.18 it can be easily shown, that the linear functions in the dT-curve intersect the x-axis at the maximum temperature T_{max} and at the equilibrium temperature T_{eq} , for the heating and cooling curve, respectively. As presented in figure 4.8b, using this procedure, much shorter measurement times similar, or even shorter than those used for the exponential method can be used. Depending on the design of the probe, parallel measurement of the temperature of the heat sink for short-term conductive cooling would even allow measurements without the necessity of a cooling curve i.e. without the necessity for switching of the power source. Using this approach, the slowly changing temperature of the heat reservoir for conductive cooling becomes irrelevant, since it is determined at the time of measurement. Consequently, any long term change of T_{eq} becomes irrelevant and thus the need for a water cooling system to keep T_{eq} at a constant value, is eliminated.

The main drawback of this method is that the cooling by gas is disregarded. As described in section 2.2.5, however, gas cooling can be quite significant for pressures above ~ 1 Pa. Although this drawback cannot be principally overcome, the erroneous influence can be minimized by designing the probe in such a way, that the cooling due to gas can be disregarded compared to the conductive cooling through the holder. Without these optimizations, the applicability of this method is limited to systems with very low background gas pressure. Since the calibration experiment used in this thesis operates at such a low gas

pressure, one possible application of this method is the recalibration of probes which have been coated with a dielectric film. The procedure to achieve this, is presented in section 5.1.3.

Evaluation of PTP data for non-ideal measurement conditions can best be achieved by careful analysis of the dT-curve for the recorded temperature data. In the dT-representation (see e.g. figure 4.7b) changes of the measurement conditions can be understood much more easily. Some examples for this are:

- A deviation from the linear course expected for the heating curve indicates that either the energy flux is not constant during the heating phase, or that the efficiency of the cooling changes strongly. This can be observed for example if close walls heat up strongly during the measurement.
- If both cooling and heating have a linear course, but with a different slope, this indicates, that the cooling terms change abruptly when the power is shut off as the slopes are defined by the efficiency of the cooling. Such an effect can appear for example, if the probe is turned to shut off the energy flux and is then exposed to gas with a different temperature.

Once the deviations during the measurement are understood, they can typically be compensated by a customized evaluation method. A good example for this can be found for the measurement in a plasma jet by Kewitz et al. [84]. Here, the main difficulties arose from a slow starting mechanism of the jet and from severe heating of the probe housing and environment caused by the high energy flux. The authors showed the effect of these difficulties in the dT-curve and developed a solution based on the extrapolation of the heating curve which allows to compensate the erroneous influences.

4.3.3 Active thermal probe (ATP)

Analog to the description of the PTP, the first two parts of this section describe the measurement principle and the design of the active thermal probe. In the last part, the two different approaches for evaluation of the acquired measurement data are presented.

Physical probe design

The basic principle for measurement of energy flux with the ATP is to maintain a substrate which is exposed to an energy flux at a constant temperature. The power which is necessary to achieve this, can then be correlated to the energy flux to the substrate. The active thermal probe used in this thesis was originally developed in the ZIM-Project 'E-Impact' in collaboration with the INP-Greifswald and has first been introduced by Wiese et al. in 2008 [86]. The main components are the temperature regulated dummy substrate and a measurement electronic which is used to acquire the data and regulate the substrate temperature. The sensor is manufactured by *UST Umweltsensortechnik* and consists of a 630 μm ceramic substrate with a conducting paths on its upper surface. The probe in its typical configuration with the ~ 20 cm holder and 8-pin custom connector is shown in figure 4.9.

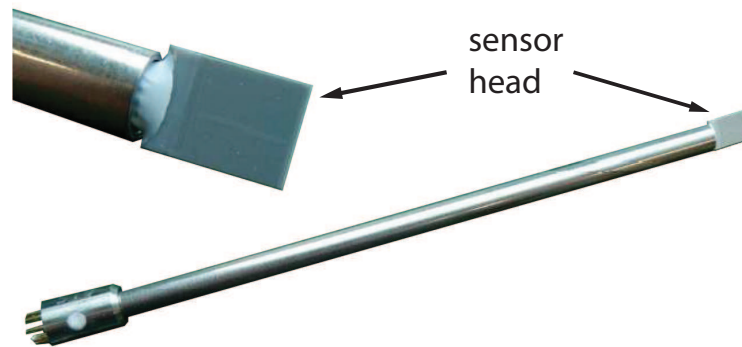


Figure 4.9: Photograph of the active thermal probe used in this thesis.

As visible in figure 4.10, two separate circuits are imprinted on the substrate. On the left side is the measurement circuit which covers an area of 0.47 mm^2 and next to it on the right, the much smaller and more dense compensation circuit is visible. Both of these circuits are made from platinum and have a resistance of $R_0 = 100 \Omega$ at $0 \text{ }^\circ\text{C}$ and have similar temperature dependence as a typical PT100 element. Through these circuits, the sensor can be heated by ohmic heating and the temperature T_s can be easily obtained from its relation to the resistance R :

$$R(T_s) = R_0(1 + \alpha T_s + \beta T_s^2), \quad (4.22)$$

with the coefficients $\alpha = 3.9083 \cdot 10^{-3} \text{ K}^{-1}$ and $\beta = -5,755 \cdot 10^{-7} \text{ K}^{-2}$. Both circuits are connected via four wires to the measurement electronics to allow four-terminal sensing which is necessary to allow accurate voltage and current measurement independent of the length of the connecting cables. The measurement electronic developed by *GO-Messtechnik* calculates the resistance from the voltage and current measurement at a rate of 1 Hz and allows regulation of the temperature with $0.1 \text{ }^\circ\text{C}$ accuracy. The temperature is held at a constant value by a PI-regulation algorithm which controls the heating power by adjustment of the voltage.

The two-circuit design on the sensor head is necessary to minimize the energy flux from the probe holder and connecting wires to the substrate. Due to the physical connection of the sensor head, conductive cooling creates a constant energy flux which is proportional to the temperature difference between substrate and holder. This conductive energy flux is minimized by the compensation area which is kept at a constant temperature equal to the temperature of the measurement circuit.

Measurement principle

As illustrated above, the sensor head of the active thermal probe is a ceramic substrate which can be heated by two PT100 circuits on its surface. The basis for the measurement principle is to keep the substrate temperature at a constant, defined temperature T_{set} . According to equation 4.11, this requires the power coming to the substrate and the power leaving the substrate to be equal:

$$P_{in} = P_{out} \quad \Leftrightarrow \quad J_{atp,off} = J_{cont}. \quad (4.23)$$

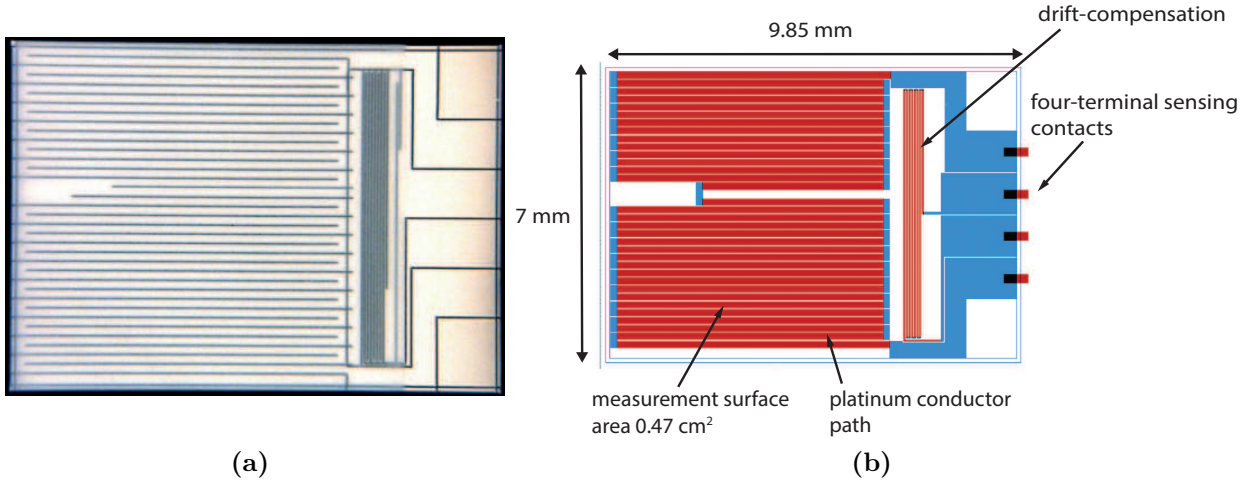


Figure 4.10: (a) photograph of the sensor head with clearly visible circuit path made from laser structured platinum. (b) schematic drawing of the sensor head of the active thermal probe with relevant dimensions and labeling of relevant parts.

If the ATP is not exposed to any additional energy flux, this balance consists only of the energy flux from the ohmic heating $J_{atp,off}$ and the cooling through temperature dependent processes which are summarized according to 4.3.1 in J_{cont} (radiative, convective and conductive cooling).

If an additional energy flux J_{meas} is added to the substrate, the thermal equilibrium of the substrate is disturbed which results in an increase of the substrate temperature. To counteract this, the energy flux from ohmic heating is adjusted by the measurement electronics to a new value $J_{atp,on}$. As visible in figure 4.11, this value is regulated by a PI-algorithm, in such a way that the energy flux is balanced again:

$$J_{atp,on} = J_{cont} + J_{meas}. \quad (4.24)$$

Under the assumption, that the energy flux J_{cont} is equal for both situations, equation 4.23 and 4.24 can be combined to obtain a relation for the sought-after additional energy flux:

$$J_{meas} = J_{atp,off} - J_{atp,on}. \quad (4.25)$$

The power from ohmic heating P_{atp} is simply defined as the product of voltage U and current I through the PT100 element, accordingly the corresponding energy flux is:

$$J_{atp} = \frac{P_{atp}(T_s)}{A_s} = \frac{UI}{A_s}. \quad (4.26)$$

$P_{atp}(T_s)$ is directly detected by the electronics and is used as the primary measurement value. Thus, the measured energy flux can simply be obtained from the difference in power ΔP_{atp} between the situation with and without additional energy flux:

$$J_{meas} = \frac{P_{atp,off} - P_{atp,on}}{A_s} = \frac{\Delta P_{atp}}{A_s}. \quad (4.27)$$

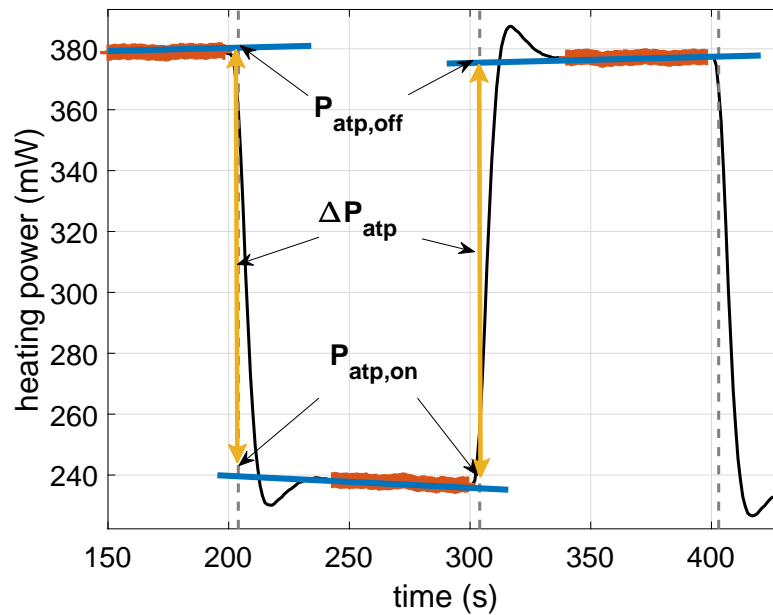


Figure 4.11: Typical measurement data from the active thermal probe acquired in an ion-beam experiment with 700 eV anode current and 60 % pulse width modulation. The differential measurement and evaluation method is exemplified for two measurement points. The values for ΔP_{atp} are obtained as the difference of the linear extrapolation of the power evolution at the switching time. For some of the fit areas a positive or negative drift is visible as the linear fit has a slope unequal to zero.

Methods of evaluation

According to equation 4.27, the energy flux impinging on the probe sensor can be directly obtained from the differences of heating power between a reference measurement and a measurement with additional energy flux. Depending on the time difference between the two measurements, the determined value for the energy flux can differ significantly due to changes in the contributions which are included. If the reference measurement $P_{atp,off}$ was performed e.g. with cold chamber walls and $P_{atp,on}$ was acquired at a later point where the chamber walls were already at a new equilibrium temperature, the resulting energy flux will appear smaller as a result of the change in radiative energy flux. In principle, such a deviation could be compensated if the temperature of the surrounding is constantly recorded. However, since this is not very practical and in most cases even not possible, the slow changes in the continuous contribution J_{cont} can result in systematic errors in the measurement. In the next paragraph a method is presented which allows to effectively minimize this error by a differential measurement and evaluation. In cases of very stable systems or negligible energy exchange with the probe environment, these systematic errors disappear and a continuous measurement can be employed as described in the second paragraph of this section.

Differential evaluation requires switching of the power source for every measurement point. Similar to the kink method of the PTP, only a very short time period is used for the actual evaluation so that the assumption of equal continuous contribution J_{cont} applies for both situations. In the example above, this would mean that the wall is still at the

same temperature for the determination of the measurement power $P_{atp,on}$, as it was for the determination of the reference power $P_{atp,off}$. The determined energy flux only contains the changes in energy flux between the two situations and thus, the continuous contribution and the associated error is eliminated.

As it can be seen from figure 4.11, the slow change in J_{cont} appears directly in the measurement data as a small negative drift for $P_{atp,on}$ and a small positive drift for $P_{atp,off}$. Due to the heat capacity of the probe, the minimal regulation time for adjusting the power is limited to about 60 s and thus, it is not possible to directly obtain the correct values for $P_{atp,on}$ and $P_{atp,off}$ from the measurement data. However, this limitation can be overcome by linear fitting of the data at equilibrium condition and extrapolation into the region of regulation. Since any change of J_{cont} happens on a comparatively long time scale, the resulting change of the heating power of the substrate can be approximated by a linear function. To compensate for the systematic change of J_{cont} the two heating powers $P_{atp,on}$ and $P_{atp,off}$ are obtained from the values of the linear fits at the time of exposure to the energy flux, allowing a comparison for the same values of J_{cont} .

The basic steps for obtaining the correct ΔP_{atp} are thus the following:

- I. Record reference with no additional energy flux for sufficient time to be sure that the probe is in equilibrium; the power must be constant or only change slowly.
- II. After the probe is exposed to the additional energy flux, wait for the regulation to adjust the power to a new equilibrium - again, the power must be constant or only change slowly.
- III. Linearly fit the constant regions of the reference power and measurement power.
- IV. Obtain ΔP_{atp} from the difference of the function values of the linear fits at the time of exposure to the additional energy flux.

Continuous evaluation is based on the same principle as the differential method, however, here, any drifts due to slow-changing contributions are mostly neglected. Accordingly, this technique should only be utilized in very stable environments (big chambers, cooled systems etc.), or in cases where the accuracy of the result is of secondary importance. However, if those conditions are met, this technique has the clear advantage of the reduction of measurement time by 50-90% as compared to the differential method. In figure 4.12 an exemplary measurement from an RF plasma is shown to illustrate the method. As illustrated in figure 4.12a, the principle steps for a parameter variation measured with continuous evaluation are the following:

- I. record reference with no additional energy flux for sufficient time to be sure that the probe is in equilibrium, the power must be constant or only change slowly
- II. expose probe to energy flux and wait for the regulation to adjust to a new equilibrium
- III. change investigated parameter to new value, wait for the probe to adjust to new equilibrium
- IV. repeat step III for all investigated settings

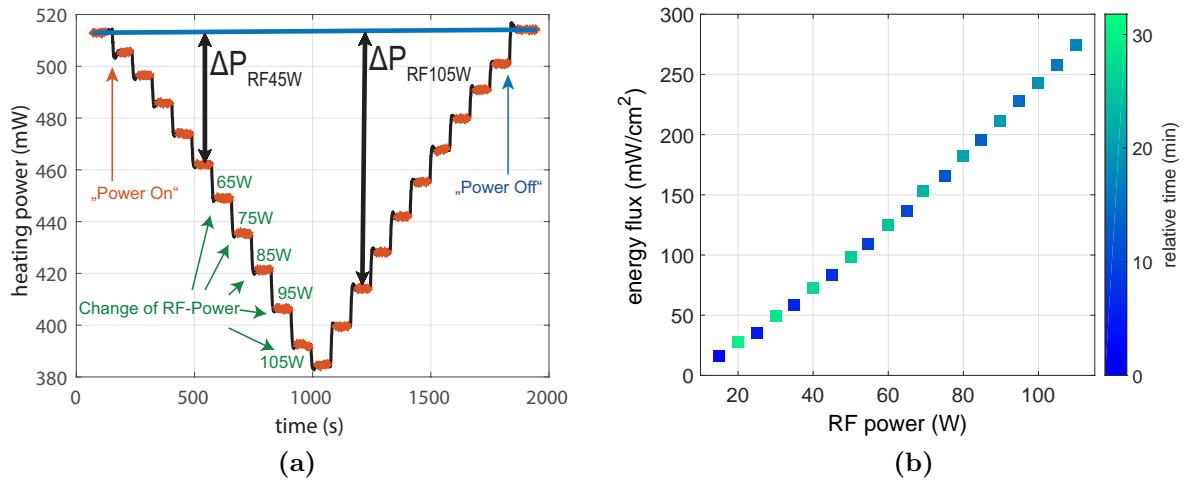


Figure 4.12: Exemplary measurement data from a continuous measurement for variation of the RF power in a capacitive coupled argon RF discharge. In (a) the raw measurement signal is displayed along with the fit of the reference power (blue line) and the red areas which were used for building the respective differences ΔP for the different RF powers. In (b) the resulting energy flux obtained from the evaluation of the data in (a) is shown as a function of the RF power and the relative time.

V. finish the measurement with another reference measurement

With this technique, the reference power is calculated from a linear fit of the reference data recorded at the beginning and the end of the measurement. $P_{atp,on}$ is obtained as the average of the power recorded at equilibrium for each setting and ΔP_{atp} can then be obtained as the difference to the value of the reference function at the corresponding time.

In many cases, a sufficient reduction of the step width of the varied parameter allows to decrease the necessary change in the heating power to such a point, that the temperature regulation is fast enough to keep the probe in equilibrium at all times. This results in a truly continuous measurement with increased detail and in most cases no sacrifice of overall measurement speed. However, as with any version of the continuous method, it is advisable to measure every setting twice at different times to be sure, that no systematic errors due to changes in J_{cont} falsify the measurement.

4.3.4 Comparison of the PTP and the ATP

Both calorimetric probes used in this thesis have certain advantages and limitations, which make them more or less suitable for the application in certain systems. The following points give a short summary of the most relevant features which differentiate the two probes from each other.

PTP	ATP
+ flexible design, easily adjusted to different systems and specifications	+ no calibration required
+ simple in-house manufacturing	+ in-situ measurement possible with continuous measurement
+ measures wide range of energy flux not limited by probe design	+ no switching of the power source necessary with continuous measurement
+ dT-curve provides additional detail	
+ simple biasing and current measurement	

In general, the PTP's biggest advantage is its versatility and its robustness in terms of electronics and hardware. Although, in most situations both probes could be utilized, the more difficult handling of the ATP only makes it preferential in environments such as ion beams where the continuous measurement method can be used.

5 Optimization and calibration of the Passive Thermal Probe

As a part of this dissertation, a revised version of the passive thermal probe was developed in close collaboration with Fabian Haase, a fellow PhD student in our working group. The starting point for the redesign was the PTP introduced in section 4.3.2 which we have both used for the majority of our measurements. This version was developed in 2010 and was optimized for minimal changes of the temperature of the shielding. This was necessary to allow reliable exponential evaluation which was required due to slow acquisition speed and relatively big noise in the temperature. The introduction of an improved acquisition software allowed much faster and more precise measurements, which also allowed the utilization of a different evaluation method - the kink method. The associated, altered requirements together with a better understanding of error sources in the calibration process and the experience gained from working with the original probe allowed us to develop a new and improved version of the passive thermal probe.

5.1 Calibration - determination of the heat capacity

As pointed out in section 4.3.2, the heat capacity plays a central role for measurement with the passive thermal probe. Since the measured energy flux is directly proportional to the heat capacity of the probe C_s (equation 4.16), it is always necessary to accurately determine C_s before being able to obtain absolute measurement results. In principle the heat capacity could be easily calculated from the specific heat capacity (copper: 0.385 J/(gK)) and the mass of the dummy substrate. This would result in heat capacities of 0.0229 J/K and 0.0759 J/K for a circular dummy substrate of 70 μm thickness with 11 mm and 20 mm diameter, respectively. Since the temperature is determined at the junction between thermocouple and copper plate, the relevant heat capacity for measurement with the PTP is given by the volume of material around the junction which changes its temperature at the same rate as the temperature of the junction itself. Accordingly, the heat capacity is majorly made up of the mass of the platelet and to a lesser amount of the connected wires (see figure 5.1). Due to the unknown contribution from the wires and due to eventual errors in the material properties or probe dimensions, it is necessary to calibrate the heat capacity experimentally. Additional to this initial calibration, in environments where coating or sputtering of the probe surface can be expected, further calibration after the measurement are necessary to take into account eventual changes of the heat capacity.

In the first two parts of this section, two proven methods for calibration of the PTP are described. The first method, the calibration with an electron beam, can be described as a primary method as it allows the determination of the heat capacity directly from a power

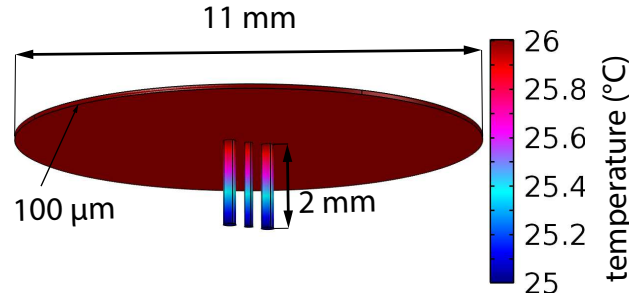


Figure 5.1: Comsol simulation of the temperature gradient in the dummy substrate of the PTP and the connected wires for a temperature difference of 1 °C between upper surface of the platelet and lower surface of the wires. It is clearly visible that, while the platelet itself is in thermal equilibrium, a relatively strong gradient is found in the wires.

source of known energy flux. The second method, where an ion beam is used as the power source, can be understood as a secondary method as it relies on a calibrated reference probe and, thus, gives less accurate results. Due to the higher uncertainty associated with the secondary method, it is always preferable to calibrate with the more direct electron beam calibration. However, in some cases like with a non-conductive coating on the probe surface, the secondary method provides a versatile alternative.

In the third part of this section, an experimental approach for calibration based on the equilibrium evaluation method introduced in section 4.3.2 is presented.

5.1.1 Calibration with an electron beam

The most common method for determination of the heat capacity for a calorimetric probe is by evaluation of the temperature derivative of the probe for exposure to a known energy flux P_{in} . According to equation 4.14, C_s can then be determined according to

$$C_s = \frac{P_{in}}{\dot{T}_h - \dot{T}_c}. \quad (5.1)$$

In principle, the known energy flux could be supplied by different sources like laser light or plasma electrons [74, 87, 88]. However, for these methods the determination of P_{in} involves many uncertainties and requires the experimental determination of other parameters, which decreases the accuracy of the result. By using an electron beam in a specially developed calibration experiment, many of the experimental uncertainties can be avoided and P_{in} can be directly determined from simple voltage and current measurement.

Experimental setup

For the determination of the heat capacity with an electron beam, the known energy flux is supplied by collision-free electrons generated and accelerated in a specially developed calibration experiment shown in figure 5.2 [82]. In comparison to the other power sources, many difficulties which arise from effects like secondary electron emission, non-trivial energy distribution functions or changes in reflectivity are avoided. In this system the electrons are emitted from a heated tungsten wire by thermionic emission described by Richardson's law.

The wire is heated by a current of $I_h \approx 1.3$ A generated by a voltage of $U_h \approx 8$ V across the wire. To avoid accumulation of electrons in front of the wire, it is negatively biased with typically $U_w \approx -70$ V. The free electrons are accelerated onto the probe surface due to the potential difference created by the bias voltage U_s applied to the dummy substrate. The relevant voltage for calculation of the energy of the accelerated electrons can then be calculated from the contribution of the biased tungsten wire, the probe voltage and the average potential across the wire:

$$U_{calib} = \left(U_s - U_w + \frac{U_h}{2} \right) \pm \frac{U_h}{2}. \quad (5.2)$$

U_s and the electrical current I_s arriving at the probe are measured with digital multimeters and from these values the electrical power onto the PTP can be calculated to be

$$P_{el} = I_s \cdot (U_{calib} + \Phi_{wf}). \quad (5.3)$$

Here Φ_{wf} is the energy associated with the work function of the electrons which is released as the electrons become part of the solid, see section 2.2.3. Collisions between electrons and the

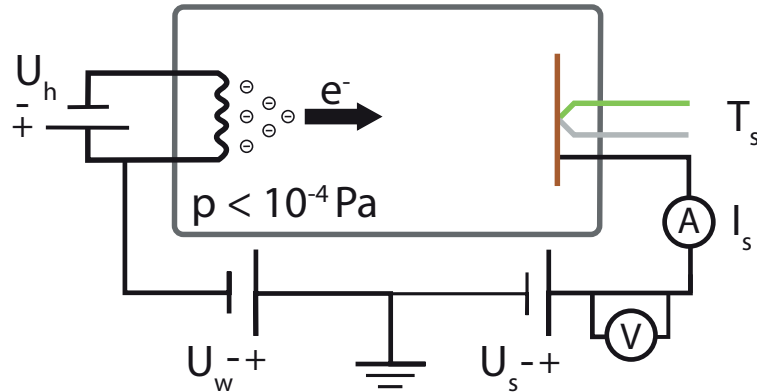


Figure 5.2: Schematic drawing of the calibration experiment for determination of the heat capacity utilizing collision-free electrons. The electrons are emitted by a glowing wire according to Richardson’s law and are then accelerated by the potential difference between wire and probe. It is important, that the current is measured ‘after’ the voltage since the current going through the measurement resistor of the voltage meter can be in the same range as the measurement current I_s .

background gas can lead to ionization of the gas and deviation in the electron energy which could falsify the result. To minimize these erroneous effects, the chamber is evacuated to a pressure below $1 \cdot 10^{-4}$ Pa. Assuming a maximal collision cross section, such low pressures would result in mean free path length for a collision between an electron and a nitrogen molecule of more than 100 m which is much larger than the chamber dimension [89].

Limitations and resulting design rules

The main assumption to allow direct calculation of the energy flux from the current and voltage measurement as shown above, is that all electrons arrive with the same energy at the probe defined by U_{calib} . To achieve this, the electron beam needs to be collisionless

and additionally a well-defined, time independent electrical field between wire and probe substrate is mandatory. While the first requirement is easily fulfilled by pumping the chamber to a very low pressure, the second requirement creates some restrictions for the probe design. The obvious restriction is that dielectric probes can not be calibrated with this method. However, the requirements regarding the electric field also mean that any dielectric materials in the close vicinity of the probe should be avoided. The reason for this is, that electrons can accumulate on the surface of these dielectric materials much like on a capacitor and, thus, not only change the electric field as a function of time, but also contribute to the electric current when they jump from, or flow over the dielectric surface to the probe surface. Since in this case, the electrons arrive with an energy much smaller than $e U_{calib}$, the energy flux calculated from the measurement of voltage and current would overestimate the actual energy flux and, thus, the obtained heat capacity would be too high. In figure 5.3a the resulting effect on the probe current is illustrated with two exemplary measurements recorded in the electron beam calibration experiment. For the blue curve, an optimized probe with no dielectric material exposed to the beam was used and for the red curve, a ceramic block has been positioned in the close vicinity of the probe. The charging of the ceramic is clearly visible as a slowly increasing current throughout the measurement. Additional to the falsified energy of the impinging electrons, the changing current also generates a constantly changing energy flux, which results in erroneous determination of $\dot{T}_h - \dot{T}_c$. The systematic error created from these two effects combined, can easily result in an overestimation of the heat capacity by 100%.

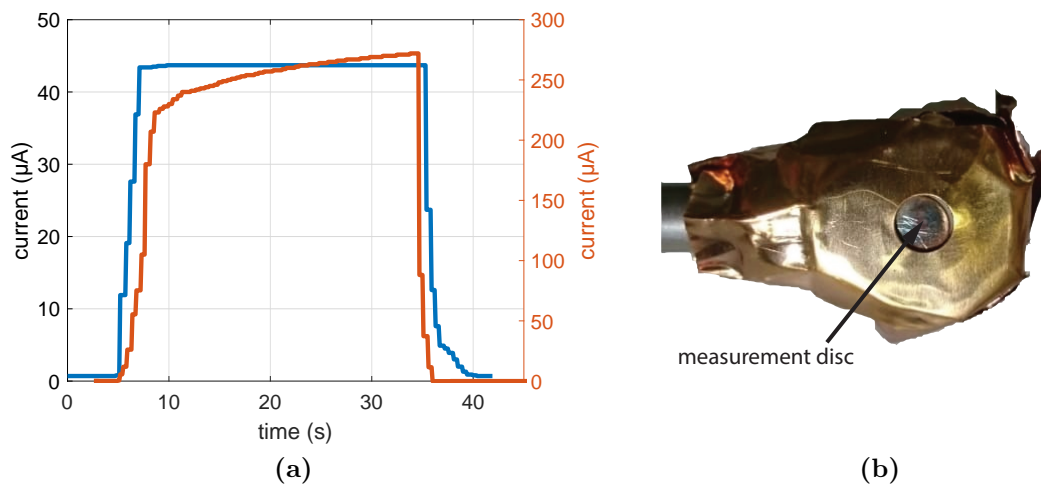


Figure 5.3: (a) typical current curves for the electron beam calibration experiment. The blue curve is recorded for a probe with no dielectric material in the probe vicinity, the red curve is recorded for a calibration where a ceramic block is positioned close to the probe substrate. (b) photograph of an improvised version of a calibration hood which completely covers the ceramic parts of the probe, leaving only the copper measurement disc exposed to the electron beam.

A practical solution to the difficulties associated with surface charges on dielectric materials, is to use a calibration hood. In figure 5.3b, an improvised version of such a hood used to cover the ceramic parts of a thermal probe designed for high energy flux at atmospheric pressure, is shown. By masking the complete ceramic material with a grounded shield, the electrons are effectively hindered to arrive at the ceramic surface and accordingly, the associated erroneous effects are eliminated.

Calibration procedure

According to equations 5.1 and 5.3, the relation between the electrical power and the difference in temperature derivatives in this calibration experiment is given by

$$P_{el} = C_s \cdot (\dot{T}_h - \dot{T}_c). \quad (5.4)$$

To eliminate any constant offsets in P_{el} and to reveal erroneous influences, the probe is successively exposed to different electrical powers by varying the probe bias from typically $U_s = 700 - 1000$ V. The heat capacity can then be obtained from the slope of the linear relation between P_{el} and $\dot{T}_h - \dot{T}_c$. In figure 5.4 this procedure is illustrated for a typical calibration run. The seven heating curves recorded for different P_{el} are evaluated to obtain $\dot{T}_h - \dot{T}_c$ and the heat capacity is then obtained from the linear fit to the obtained data points. In section 4.3.2 it was argued that the kink method usually gives the best results

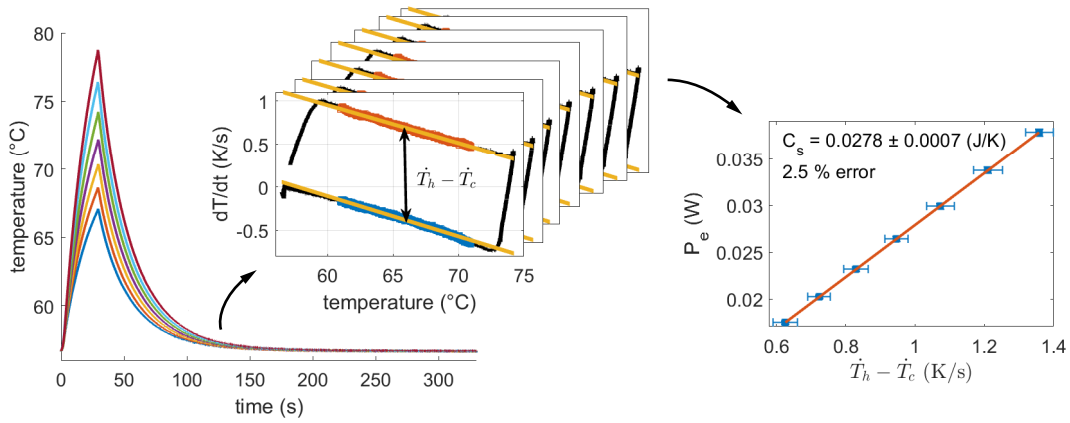


Figure 5.4: Determination of the heat capacity illustrated for a typical calibration run. The difference in temperature derivative is obtained with the exponential method (4.3.2) from the recorded temperature curves for different electrical powers. The heat capacity is obtained as the slope of the linear relation between P_{el} and $\dot{T}_h - \dot{T}_c$.

for evaluation of the temperature curves. However, in this calibration experiment $\dot{T}_h - \dot{T}_c$ is obtained using the exponential method. The reason for this is mainly, that due to limitations of the power supply used to bias the probe, the electrical power P_{el} can not be switched instantaneously. Additionally, the low acquisition frequency of the voltage- and ampere-meter do not allow a reliable determination of P_{el} over a short time period. The advantages associated with the kink method can thus not be exploited here and therefore the exponential method allows more accurate evaluation.

To obtain a better statistic, each probe is usually calibrated over a period of more than 12 hours, resulting in a minimum of 18 calibration runs.

Estimation of the error in the heat capacity

To give more quality to the absolute energy flux measurements obtained with the PTP, it is important to have an accurate estimation of the error in these measurements. While this can be very complex and very much dependent on the investigated system, any error

associated with the system will - according to equation 4.16 - always scale with the error in the heat capacity. Thus, it is necessary to obtain a realistic estimation of the error in the heat capacity as obtained with this calibration experiment.

According to equation 5.4 and the error propagation law, the error in the heat capacity ΔC_s is made up of the error in electrical power ΔP_{el} and the error in difference of time derivatives $\Delta(\dot{T}_h - \dot{T}_c)$:

$$\Delta C_s = (\dot{T}_h - \dot{T}_c) \cdot \Delta P_{el} + P_{el} \cdot \Delta(\dot{T}_h - \dot{T}_c). \quad (5.5)$$

ΔP_{el} can be directly obtained from the accuracy of the digital multimeters. The utilized model 'UT61C' from manufacturer UNI-T is specified to have an accuracy of 0.5 % for voltages up to 600 V and 1 % for voltages above that as well as for the current measurement. Thus, the resulting error for the electrical power is 1.5 or 2 % depending on the utilized voltage range [90].

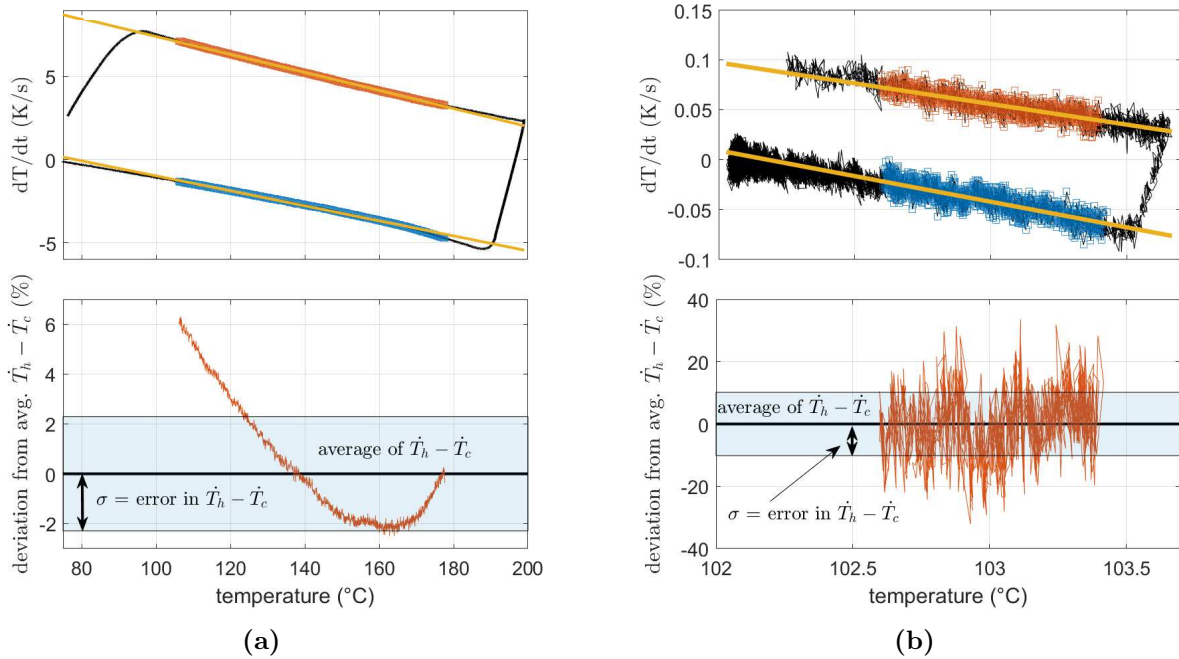


Figure 5.5: Exemplary calibration data obtained for high energy flux (a) and low energy flux (b). The upper figures show the dT -curves with linear fits and marked areas used for evaluation (red for heating and blue for cooling). The lower figures display the deviation from the average difference between the blue and red data points in the upper figures. To allow for better comparison between case (a) and (b), the deviation is given relative to the average difference as a percentage. The standard deviation to this data is marked in blue.

The determination of the error in $\dot{T}_h - \dot{T}_c$ is more complicated as this error is majorly originating from the evaluation method. As described in chapter 4.3.2, in the case of solely conductive losses, the heating and cooling of the probe can be described by a simple exponential function which results in two parallel linear functions in the dT -curve. The deviation from this assumed behavior is the biggest source of error for the determination of $\dot{T}_h - \dot{T}_c$ and is, thus, used to calculate the corresponding error. This error is obtained by calculating

the difference $\dot{T}_h - \dot{T}_c$ for every data point in the evaluated temperature region. Since this theoretically should result in the same value for every data point, the standard deviation of the calculated values can be used as the error for $\dot{T}_h - \dot{T}_c$. In figure 5.5, the procedure is illustrated for two example calibration curves with very high energy flux (a) and very low energy flux (b). For the case of high energy flux, the heating of the probe housing and the connection wires becomes visible as a clear deviation from the linear shape in the dT-curve. This can lead to a systematic error as visible in the lower figure of 5.5a. For the curve in 5.5b on the opposite, the systematic error disappears in the more pronounced statistic error created by the noise in the temperature acquisition. Comparing the relative magnitude of the error, it becomes clear, that the case of high energy flux creates a smaller relative error and should thus also create more accurate results. However, due to the systematic nature of this error it can result in systematically wrong results which appear to have small errors. Thus, for a reliable determination, a compromise between the two extreme conditions presented in figure 5.5 should be chosen: The energy flux should be adjusted, so that the dT-curve is well outside of the statistic domain, while keeping the energy low enough so that the probe housing is not unnecessarily heated. As illustrated in figure 5.4, the heat

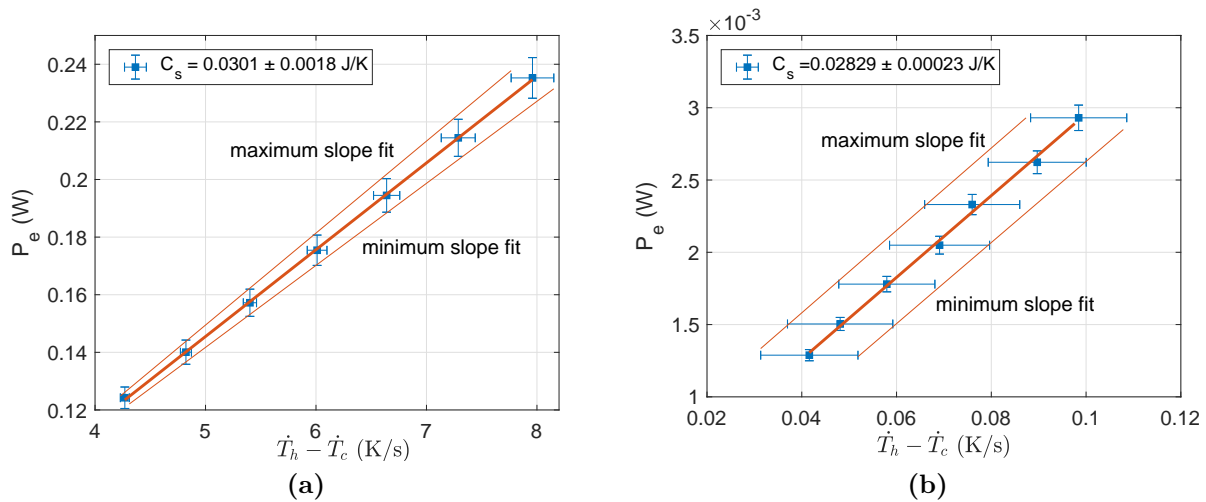


Figure 5.6: Exemplary data from two calibration runs with high energy flux (a) and low energy flux (b). The heat capacity C_s is determined as the slope of the linear correlation between P_{el} and $\dot{T}_h - \dot{T}_c$. The error in C_s is determined from a linear fit with maximum slope and a linear fit with minimum slope.

capacity is determined relatively as the slope of the linear relation between the measured electrical power P_{el} and the difference in derivatives $\dot{T}_h - \dot{T}_c$ determined from the measured temperature curves. In figure 5.6 the results for P_{el} and $\dot{T}_h - \dot{T}_c$ are shown for a calibration run with high energy flux and a calibration run with low energy flux. The data point for the highest P_{el} in each (a) and (b) are obtained from the example curves shown in 5.5. To obtain the error of the heat capacity from the linear fit to the data of P_{el} and $\dot{T}_h - \dot{T}_c$, it is not enough to simply take the error from the linear regression analysis. As described before, the values for $\dot{T}_h - \dot{T}_c$ can show systematic deviations which change depending on the position of the evaluated region. Since all curves are evaluated automatically, using the same evaluation region, this can result in a good linear correlation, which however, gives an erroneous slope. The automation of the evaluation and the origin of the systematic error also ensures, that

the values for $\dot{T}_h - \dot{T}_c$ can only be erroneous in the same way. This means, that in the case of an error, all calculated values will either be too high or all values will be too low. For this reason, the error in the slope of the linear correlation can best be estimated from a linear fit with maximum slope to the data points with maximum negative deviation and from a linear fit with minimum slope to the data points with maximum positive deviation.

Figure 5.8 shows calibration results for a single probe which has been calibrated 430 times over a period of several weeks. As depicted in the figure, the calibration parameters have intentionally been varied up to extreme values to illustrate the robustness of the method and allow an assessment of the errors calculated according to the procedure described above. In figure 5.7 three examples of the obtained dT-curves from the calibrations shown in figure 5.8 are plotted. One trend that can be observed in figure 5.8 is that the calibration with high energy flux generally result in a higher heat capacity and that those with very low energy flux produce a higher variance in the obtained heat capacities. This can be understood from the examples plotted in figure 5.7. For low energy flux (A) the calculated heat capacity is more strongly defined by the statistic error in the temperature measurement as well as in the measurement of current and voltage. For high energy flux on the opposite, the statistic error is negligible but we observe a strong deviation from the linear shape. This deviation results in a systematically lower value of the obtained difference in derivatives (due to the bend in the evaluation region, the curves in the dT-plot are closer together) and therefore in an apparently smaller heat capacity. The most accurate value for the heat capacity can be obtained, if the energy flux is high enough, so that statistical errors become small while keeping it low enough to ensure that the deviation from the linear course in the dT-curve is kept small. An example curve for this case is given in figure 5.7 C.

While for the extreme calibration parameters, a systematic influence can be detected, venting of the chamber or a change of the probe geometry from 0° to 90° (see chapter 5.2) did not show any effect on the determined heat capacity. It can also be noted that under no condition, the calibration showed a deviation higher than 10 % from the average value. Thus, with a reasonable adjustment of the measurement parameters, the error calculated according to the procedure described above, appears to provide a reliable measure for the error associated with the determination of the heat capacity with an electron beam.

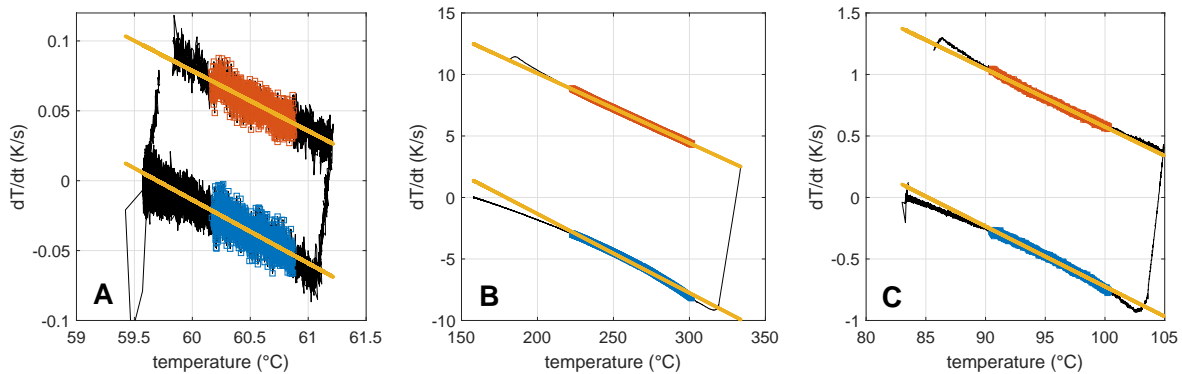


Figure 5.7: Temperature curves plotted as dT-curves representing different calibration parameter sets. The curves correspond to the calibration number 197 (A, low energy flux), 242 (B, high energy flux) and 367 (C, normal energy flux) from figure 5.8.

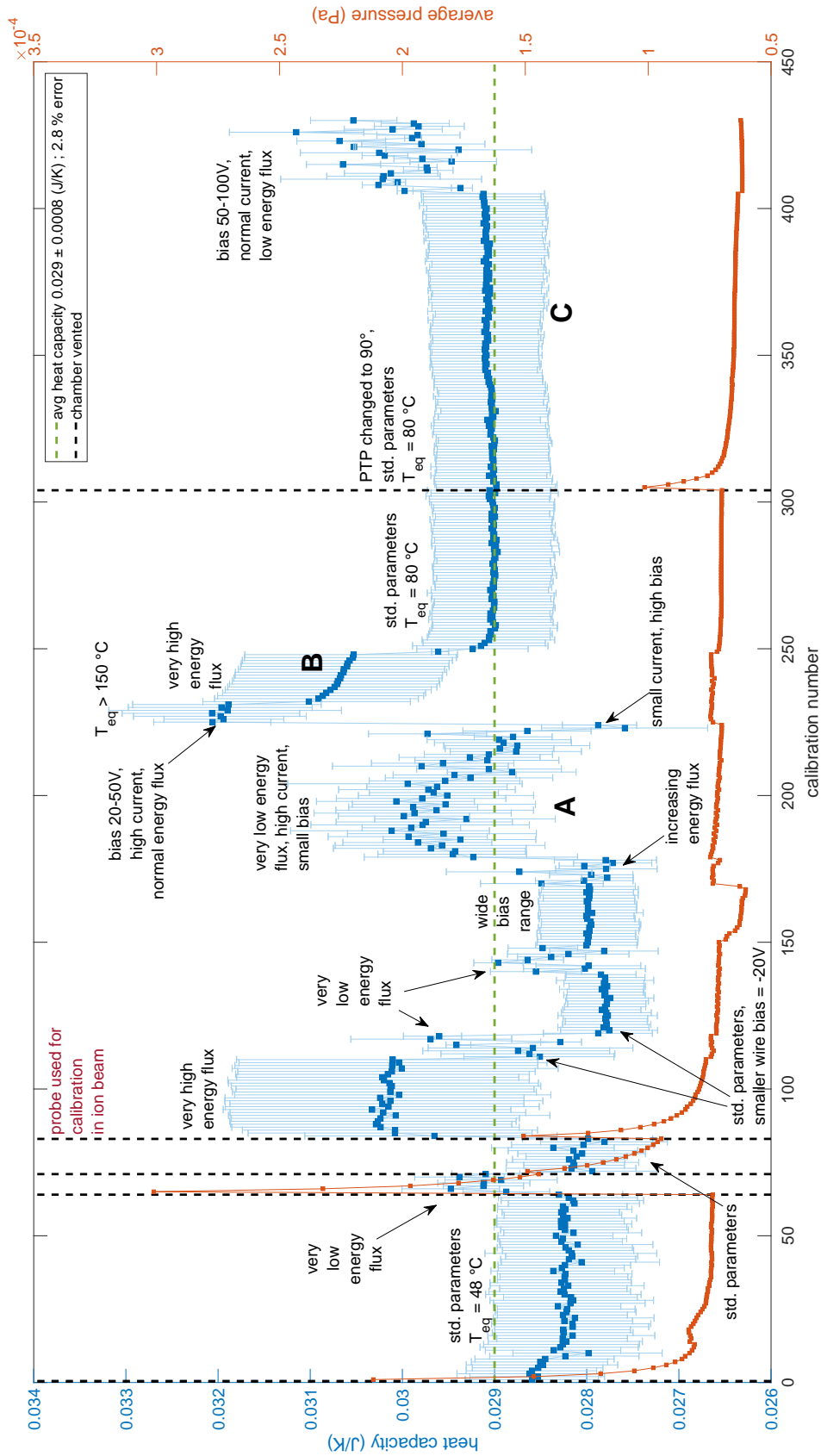


Figure 5.8: Summary of test calibration results obtained for a single probe, calibrated 430 times over a period of 2 months, with the chamber vented five times. After calibration 82 the probe was shortly used as a reference probe for calibration with an ion beam. To obtain a measure for the reproducibility, the probe was calibrated with changes of different parameters resulting partially in extreme configurations. The varied parameters include the bias voltage, the wire bias, the probe geometry, the distance between probe and wire and thus the current and equilibrium temperature. The basic changes for the different calibration sets are denoted in the graphic.

5.1.2 Calibration with an ion beam

Analog to the electron beam calibration, a beam of ions with known kinetic energy can be used to determine the heat capacity of a passive thermal probe. However, to create such a beam entails much bigger experimental challenges and accordingly also bigger uncertainties. Additionally, effects like sputtering and secondary electron emission are more pronounced and could thus further decrease the accuracy.

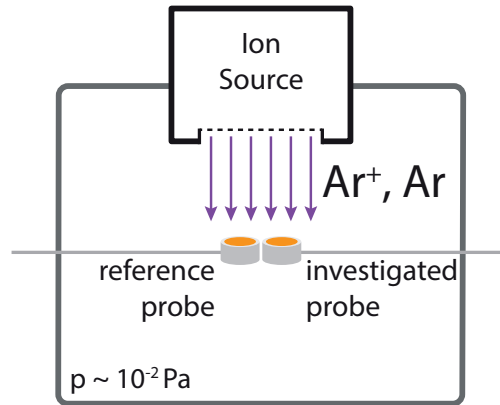


Figure 5.9: Principle sketch for the calibration of the heat capacity using a uniform energy flux supplied by an ion beam and a reference probe to determine the energy flux. The ion source used for calibration in this thesis is the model MW 125 manufactured by Ion-Tech[®].

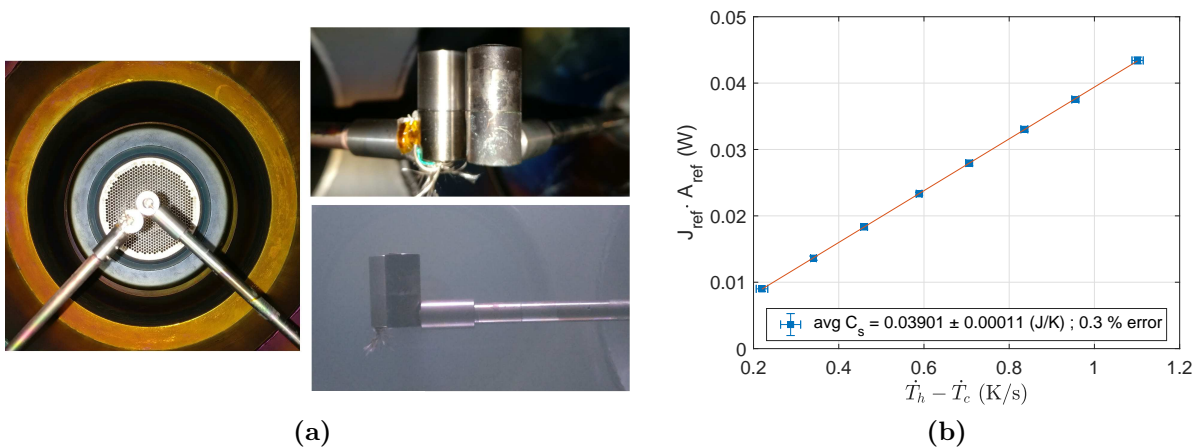


Figure 5.10: (a) photographs from the ion calibration of a copper probe coated with a layer of black non-conductive varnish. (b) plot for the evaluation of the ion calibration results and obtained heat capacity C_s . To allow the determination of C_s from the slope, eight different pulse width modulation settings of the ion beam were used. The grid and anode voltage were set to 300 V, the probes were positioned at a distance of 30 cm and the chamber pressure was $\sim 1 \cdot 10^{-2}$ Pa.

However, as illustrated in the principle sketch 5.9, the ion-beam can be effectively utilized as a constant energy source for a secondary calibration method. This method is based on the comparison of the probe with unknown heat capacity to a reference probe with well-known heat capacity. Upon parallel exposure of both probes to different energy fluxes, the

heat capacity of the investigated probe can be easily determined analog to the procedure for the electron calibration (5.1.1), see figure 5.10. In comparison to the electron beam calibration where the reference power is calculated directly from the measurement of current and voltage, here, the reference power is obtained experimentally using the well calibrated reference PTP.

To allow accurate calibration with this comparative method, it is essential that the energy flux to both probes is equal. In the case of a broad beam ion source like the MW 125 from Ion-Tech, the energy flux is constant within a radius of 2 cm from the axis even at a distance of 30 cm from the beam-grid [91]. Additionally the energy flux is majorly originating from impinging neutrals and ions which has the advantage, that the energy flux can be approximated to be independent of the probe surface and material. A laser in comparison would yield a different energy flux for a different reflectivity of the surface and the calibration with an electron beam has the disadvantage that a an electrically conductive surface is required. The comparative calibration with an ion beam is thus a versatile method which is of specific use where the probe surface is coated with a non-conductive layer.

5.1.3 Calibration with equilibrium temperature method

For both calibration methods introduced above, the heat capacity is obtained from comparison of the change in temperature derivative $\dot{T}_h - \dot{T}_c$ to a known energy flux. In the case of electron beam calibration the value of this energy flux is calculated from the measured current and voltage and in the case of ion beam calibration it is determined by measurement with a reference probe. For the calibration method described in this section, the magnitude of the energy flux is determined through measurement with the equilibrium temperature method introduced in section 4.3.2. Since it is necessary to know α for this method, the

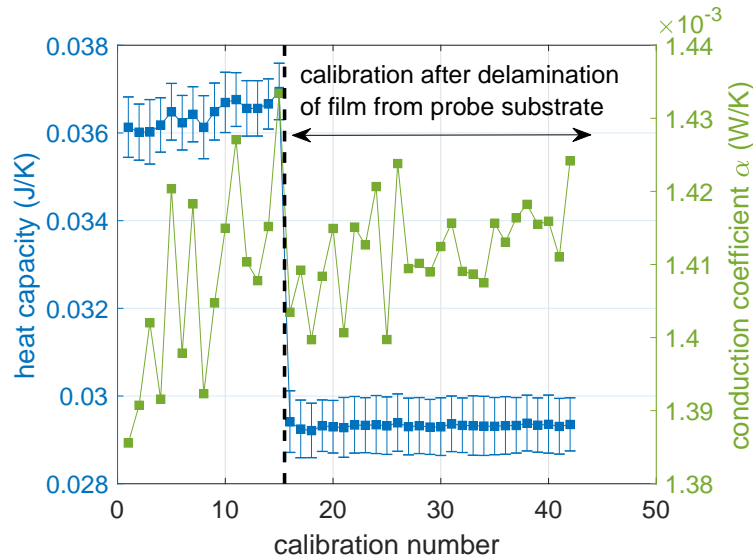


Figure 5.11: Calibration of the heat capacity and the conduction coefficient for the same probe, where for the calibrations left of the dashed line, a metal film covered the probe surface and for the calibrations to the right of the dashed line, this film delaminated and was removed from the probe. While a clear change in heat capacity is detected, α does not show any correlation.

calibration with the equilibrium temperature method is mainly useful as a method for recalibration of initially calibrated probes which have been coated with a dielectric film. Although the non-conductive layer changes the heat capacity of the probe, as can be seen in figure 5.11, the conduction coefficient α does not change. Applying this assumption, the heat capacity can then be determined according to the four following steps. First, the probe is exposed to a constant energy flux of arbitrary quantity in an environment with $p \ll 1$ Pa gas pressure, so that gas cooling can be disregarded. Second, J_{in} is obtained according to the method described in the last part of section 4.3.2. Third, the heating curve used to determine J_{in} is used to determine $\dot{T}_h - \dot{T}_c$ using either the kink method or the exponential method. Fourth, the heat capacity is obtained from equation 5.1 as the ratio between $J_{in}A_s$ and the difference in derivatives $\dot{T}_h - \dot{T}_c$.

5.2 Hardware and software design

As a part of this thesis, the passive thermal probe, the calibration procedure and the associated data acquisition software and evaluation algorithms were fundamentally redesigned and optimized. This process was performed in close collaboration with Fabian Haase, a fellow PhD student in the working group. In figure 5.12 three assembled probes of the new 'PTP2017' design with differently coated probe surfaces are shown. The basis for the hardware redesign was the improved acquisition speed and temperature resolution achieved by the redesign of the acquisition method of the *LabVIEW*TM data acquisition software. Building on this basis, the better understanding of the electron beam calibration method and the importance of surface charges in this experiment allowed to create a more versatile, robust and accurate version of the passive thermal probe. In the following two paragraphs, the essential software improvement and the final result of the hardware redesign will be shortly described.

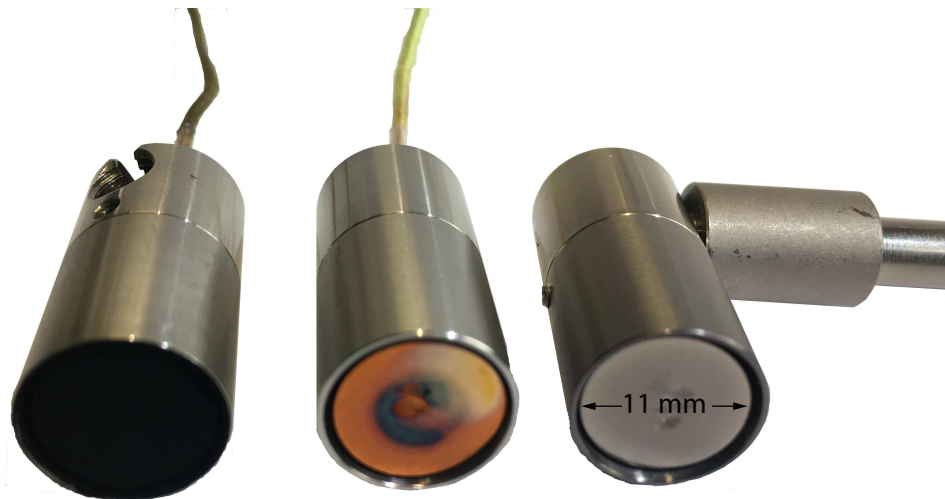


Figure 5.12: Three assembled probes of the new passive thermal probe design 'PTP2017'. The substrate of the probe on the left and the right are coated with carbon and aluminum, respectively, while for the middle one a plain copper substrate is used.

5.2.1 Software design

At the heart of the PTP electronics is the National Instruments data acquisition card USB-6009 [92] which is used to measure the amplified voltage initially created by the thermal junction of the thermocouple. The card can acquire data with a maximum sample rate of 48 kS/s, but since it is connected via USB to the computer, the bottleneck for direct data acquisition is given by the communication frequency of the USB protocol which is in the range of only 20 Hz. This limited the temperature acquisition to a maximum of only 20 Hz in the old version of the acquisition software. However, the acquisition card is also equipped with an on board memory of 512 Byte which allows to exploit the maximum sample rate of the card by temporarily saving data on the micro controller before sending it in bundles to the computer. Based on this method we developed a data acquisition algorithm which utilizes the maximum sample rate and builds the desired measurement frequency by averaging over the acquired samples. The basic steps for a measurement frequency of 100 Hz are illustrated in figure 5.13. Here, the micro controller transfers bundles of 4800 temperature measurements recorded with 48 kHz to the PC every 100 ms. To scale up the frequency from 10 Hz to 100 Hz, these bundles are divided in 10 equal packets consisting of 480 data points. The averaged value of each of these packets then results in the desired measurement frequency of 100 Hz. In this way, acquisition rates as high as the maximum rate of the USB-6009 can be achieved. However, due to the limited heat capacity of the probe, frequencies above 100 Hz do not create additional information. The main advantage of this method is, that it always utilizes the maximum sample rate of the card and decreases the statistic error by averaging the excessive data points.

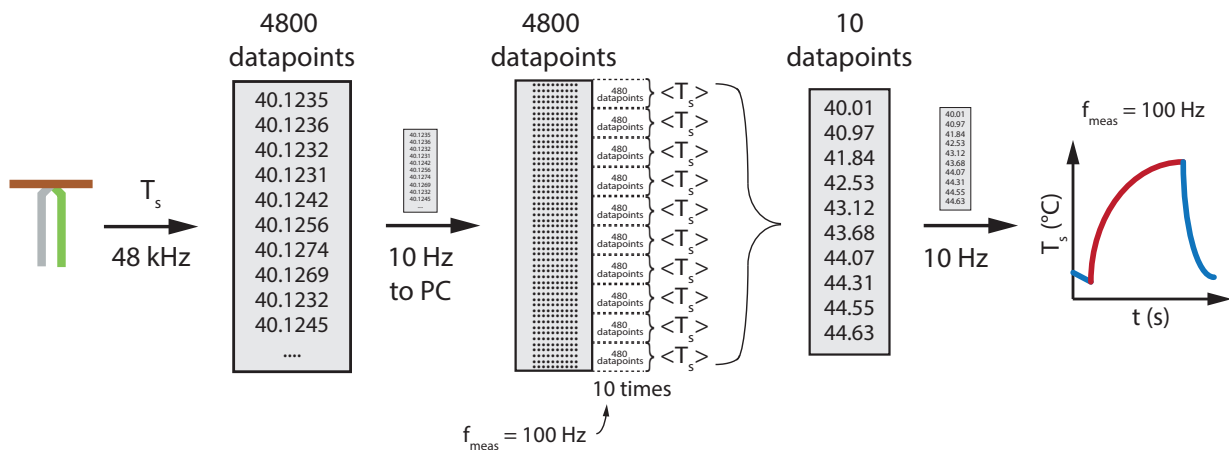


Figure 5.13: Illustration of the data acquisition algorithm used for the temperature measurement of the PTP. For the example of 100 Hz, every final measurement point is the result of the average over 480 single data points.

5.2.2 Hardware design

The motivation for the hardware redesign was principally given by some shortcomings of the old design which are listed below.

- I. ceramic of housing can create errors in the calibration

- II. large probe dimension - high plasma disturbance, low spatial resolution
- III. exchange of probe mount requires recalibration
- IV. assembly process with low reproducibility
- V. short circuit to probe housing for excessive coating with metal

In figure 5.14 a sketch of the newly designed 'PTP2017' is shown together with a legend describing the main elements. One fundamental difference of this probe as compared to

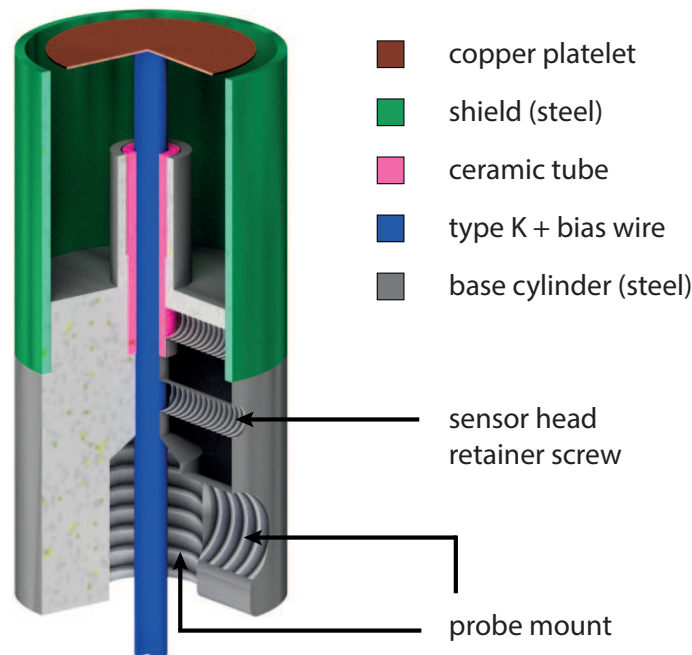


Figure 5.14: Color coded CAD drawing of the PTP2017.

the old one is the replacement of ceramic material with stainless steel. In the old design, ceramic material was chosen due to its low thermal conductivity which was mandatory for the exponential evaluation method used. As a result of the improved acquisition speed and the development of a new evaluation method, the low thermal conductivity was not necessary anymore. The replacement with stainless steel does not only solve the difficulties associated with surface charges in the calibration, but also allows for more delicate manufacturing. This last point allowed to adjust the design to be smaller, more easily and reproducibly assembled and more flexibly incorporated in the experiment. The sensor size was reduced from 20 mm diameter to 11 mm diameter and accordingly the probe housing dimension was reduced as well. The limiting factor for the dimension of the probe housing, is the ratio between the heat capacity of the dummy substrate and the heat capacity of the housing. Since the housing acts both as a primary partner for conductive cooling and radiation exchange, it is mandatory that the temperature of the housing changes on a much slower time scale. For the PTP2017, the housing alone has a heat capacity of 8 J/K, which is 266 times the heat capacity of the sensor plate. The problem of short circuits which appear after excessive coating in

metal depositing experiments has been addressed by isolating the dummy substrate from the housing, using a specially mounted ceramic tube. To prevent coating of the surface of this tube, it is only directly in contact with the metal at its lower part, while the upper part is separated from the housing by a thin slit.

6 Experimental Results

The results discussed and described in this chapter have been obtained in various experiments and in collaboration with many co-authors and partner institutes. All have in common the investigation of the energy flux by thermal probe measurements. To know the energy flux is of key interest for all coating systems, not only to investigate the thermal load on substrates, but also because it has a direct impact on the growth structure and therefore on the properties of the film. For other application like ion beams, the energy flux can provide valuable insights into the geometry and energy of the beam. Through the variety of different investigated plasma environments, it becomes clear that the energy flux changes strongly as the different included contributions are more or less clearly pronounced. Furthermore, by combination with other diagnostics, it is shown that the thermal probe can also be used to gain insights into less directly related processes such as secondary electron emission.

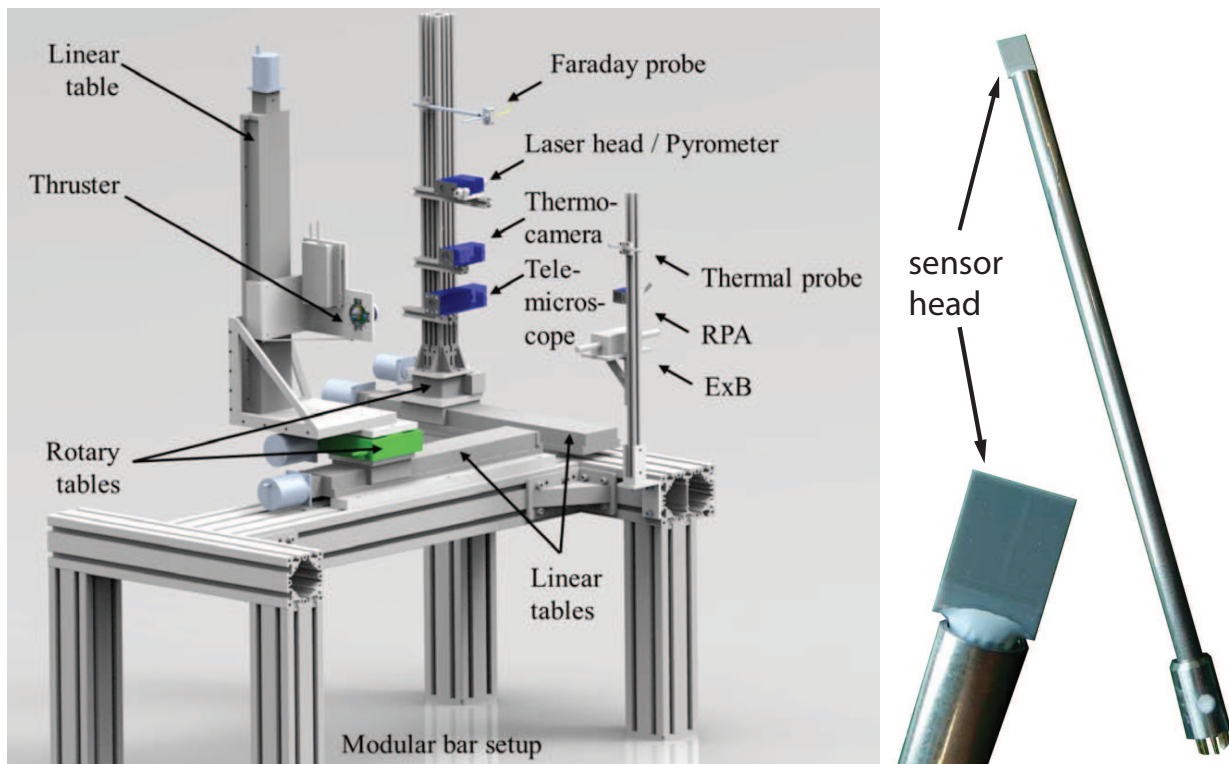
The results are presented in the form of published (or submitted), peer-reviewed publications which are ordered according to two criteria: The first two papers both present results acquired with the active thermal probe, while the last four papers mainly present findings obtained from measurements with the passive thermal probe. The second criteria is given by the type of discharge. The first publication focuses on the diagnostics in an ion beam or ion thruster while the other publications are all performed in systems based on magnetron sputtering. Here, we start from relatively conventional DCMS systems to the case of high pressure magnetron sputtering aimed at the formation of nanoparticles and end with the investigations performed in the exotic combination of HiPIMS and PBII.

Publication I

An advanced electric propulsion diagnostic (AEPD) platform for in-situ characterization of electric propulsion thrusters and ion beam sources

Authors	C. Bundesmann, C. Eichhorn, F. Scholze, D. Spemann, H. Neumann, D. Pagano, S. Scaranzin, F. Scortecci, H.J. Leiter, S. Gauter, R. Wiese, H. Kersten, K. Holste, P. Köhler, P.J. Klar, S. Mazouffre, R. Blott, A. Bulit and K. Dannemayer
Journal	The European Physical Journal D
Technique	Electric propulsion thrusters and ion beam sources
Utilized Probes	Advanced electric propulsion diagnostics (AEPD) platform
Own contribution	approximately 20%

Experimental Setup:



Motivation:

This work was performed in collaboration with partners from Italy, France, the United Kingdom, the Netherlands and Germany as part of the ESA/ESTEC project 'Qualification of the AEPD System as a Standard On-ground Tool for Electric Propulsion Thrusters'. The objective of this project was to further improve the advanced electric propulsion diagnostic

(AEPD) platform [93] and to qualify it with different thrusters in different test environments. The idea of this diagnostic platform is to combine a comprehensive set of diagnostics consisting of different beam diagnostics and methods to characterize the mechanical state of the thruster. The platform is designed to be modular and mobile which allows for easy implementation in different test chambers and characterization of arbitrary ion beams.

Main results:

The publication demonstrates with exemplary measurements from the test-campaigns, that the optimizations regarding vacuum compatibility and reduction of the interaction between diagnostics and thruster, successfully improved the measurement performance. A comparison between the different diagnostic results showed a good agreement. Further, the platform was found to provide a reliable method for comprehensive in-situ characterization of electric propulsion thrusters or ion beam sources for material processing.

An advanced electric propulsion diagnostic (AEPD) platform for in-situ characterization of electric propulsion thrusters and ion beam sources^{*}

Carsten Bundesmann^{1,a}, Christoph Eichhorn¹, Frank Scholze¹, Daniel Spemann¹, Horst Neumann¹, Damiano Pagano², Simone Scaranzin², Fabrizio Scortecci², Hans J. Leiter³, Sven Gauter⁴, Ruben Wiese⁴, Holger Kersten⁴, Kristof Holste⁵, Peter Köhler⁵, Peter J. Klar⁵, Stéphane Mazouffre⁶, Richard Blott⁷, Alexandra Bilit⁸, and Käthe Dannenmayer⁸

¹ Leibniz-Institute of Surface Modification, Permoserstr. 15, 04318 Leipzig, Germany

² Aerospazio Tecnologie s.r.l., Via Provinciale Nord 42a, 53040 Rapolano Terme, Siena, Italy

³ Airbus Defence & Space GmbH, Im Langen Grund, 74239 Hardthausen-Lampoldshausen, Germany

⁴ Christian-Albrechts-Universität zu Kiel, Leibnizstr. 11-19, 24098 Kiel, Germany

⁵ Justus-Liebig-Universität Gießen, Heinrich-Buff-Ring 16, 35392 Gießen, Germany

⁶ ICARE, CNRS, 1C Av. de la Recherche Scientifique, 45071 Orléans, France

⁷ Space Enterprise Partnerships Ltd., Bennetts, Eastergate Lane, Chichester, West Sussex PO20 3SJ, UK

⁸ ESA/ESTEC, Keplerlaan 1, 2201 AZ Noordwijk, The Netherlands

Received 4 April 2016

Published online 18 October 2016 – © EDP Sciences, Società Italiana di Fisica, Springer-Verlag 2016

Abstract. Experimental characterization is an essential task in development, qualification and optimization process of electric propulsion thrusters or ion beam sources for material processing, because it can verify that the thruster or ion beam source fulfills the requested mission or application requirements, and it can provide parameters for thruster and plasma modeling. Moreover, there is a need for standardizing electric propulsion thruster diagnostics in order to make characterization results of different thrusters and also from measurements performed in different vacuum facilities reliable and comparable. Therefore, we have developed an advanced electric propulsion diagnostic (AEPD) platform, which allows a comprehensive in-situ characterization of electric propulsion thrusters (or ion beam sources) and could serve as a standard on-ground tool in the future. The AEPD platform uses a five-axis positioning system and provides the option to use diagnostic tools for beam characterization (Faraday probe, retarding potential analyzer, ExB probe, active thermal probe), for optical inspection (telemicroscope, triangular laser head), and for thermal characterization (pyrometer, thermocamera). Here we describe the capabilities of the diagnostic platform and provide first experimental results of the characterization of a gridded ion thruster RIT- μ X.

1 Introduction

Experimental characterization of electric propulsion (EP) thrusters or ion beam sources for material processing may provide important data both to judge their performance and to achieve a better understanding of physical processes in the plume and in the discharge chamber of such systems. Measurements of plasma parameters and monitoring of possible lifetime limiting alteration of the properties of thruster components, such as, for example, the evolution of the grid hole diameter in gridded ion thrusters, yield valuable information for the development and validation of numerical tools. Those codes, e.g. aiming at plasma and ion beam modeling (examples: particle-in-cell

code XOOPIC for charged particle and plasma simulation [1], IGUN code for simulation of ion trajectories [2]) or thruster lifetime prediction related to the erosion of ion thruster accelerator grids (example: DynaSim code [3]), can help to partially circumvent expensive measurement campaigns with respect to thruster design and performance verification.

In this context, several groups have investigated surfaces of thruster components e.g. by telemicroscopy or thermal imaging methods [4–11]. In order to allow for the in-situ measurement of an extensive set of EP thruster performance parameters, the advanced electric propulsion diagnostic (AEPD) platform was designed and built some years ago [12,13]. The setup was modular and mobile such that it could be easily adapted to vacuum facilities of different size and experimental needs. Several measurement devices for particle beam and mechanical part characterization were implemented: a Faraday probe for thruster

^{*} Contribution to the Topical Issue “Physics of Ion Beam Sources”, edited by Holger Kersten and Horst Neumann.

^a e-mail: Carsten.Bundesmann@iom-leipzig.de

plume characterization, an energy-selective mass spectrometer to collect energy distribution data, a telemicroscope to measure erosion of mechanical parts, a triangular laser head to monitor the surface profile of selected parts of interest, and a pyrometer to measure surface temperature distributions. Most of the sensors consisted of commercially available devices with in-house modifications. Only the Faraday probe was manufactured completely in-house. The AEPD platform was tested successfully with two electric propulsion thrusters: a gridded ion thruster RIT-22 (Airbus Defence & Space, Germany [7,10,12]) and a Hall effect thruster SPT-100D EM1 (EDB Fakel, Russia [8,12]), in two different vacuum facilities.

The previous results demonstrated the capabilities of the first AEPD platform but also some limitations, mainly related to the design but also to financial needs. Therefore, a new activity has been started in order to improve the performance and availability of the diagnostic platform. At present, the activities concentrate on three major topics: (i) the setup and test of additional or alternative plasma-diagnostic tools as extension or redesign of AEPD capabilities, (ii) the implementation of partially new designs of existing sensors in order to reduce the dimension and, hence, the interaction of the diagnostic head and thruster, (iii) qualification of the diagnostic platform as standard on-ground tool for EP thruster characterization.

The first aspect deals with the development and integration of new sensors in the AEPD platform, such as a retarding potential analyzer, an ExB probe or an active thermal probe [13]. The second aspect concerns rather technical issues, such as modifications related to the vacuum compatibility of some diagnostic heads, size reduction and optimization of the respective sensor housings and working distance geometries, but also the protection of the sensor heads from damage due to ion bombardment [14]. The third aspect is not addressed in this paper but will be the focus of future work, because standardization of EP diagnostics is key issue when promoting EP technologies.

In this paper, the most recent implementation of the diagnostic tools is described and first performance characterization results are presented, exemplary, for a gridded ion thruster RIT- μ X (Airbus Defence & Space [15]).

2 Experimental setup

2.1 Positioning system

The AEPD platform (see Fig. 1) consists of a 5-axis positioning system and several diagnostic tools. The positioning system utilizes a modular heavy bar setup, on which three ultra-high-vacuum-specified (UHV-specified) linear tables with a traveling range of 700 mm and a traveling speed of typically 30 mm/s, and two UHV-specified rotary tables are mounted. The positioning system can be easily adapted to chambers of different size. Using the linear and rotary tables, the thruster and the diagnostic heads can be positioned very precisely relative to each other, and even 1- and 2-dimensional mappings or angular-dependent

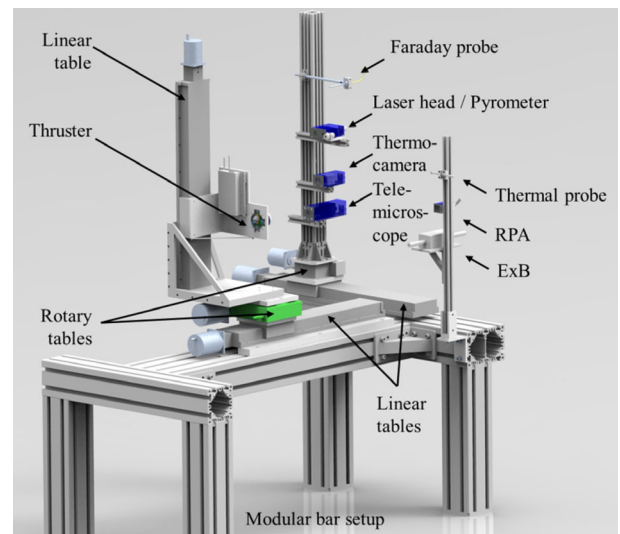


Fig. 1. Drawing of the AEPD platform with modular bar frame, linear and rotary tables, thruster and a possible configuration of diagnostic tools.

measurements can be performed. The current setup requires a minimum chamber diameter of about 2 m and a minimum chamber length of about 2.5 m.

At present, the AEPD platform can be equipped with diagnostic tools for beam characterization (Faraday probe, retarding potential analyzer, ExB probe, active thermal probe), optical inspection (telemicroscope, triangular laser head) and thermal characterization (pyrometer, thermo-camera). Table 1 lists the available diagnostic tools with their measurement principle and possible applications. The main performance parameters of the diagnostic tools are summarized in Table 2. In the following, the diagnostic tools including their design are described in more detail.

2.2 Faraday probe

The Faraday probe has been developed in-house [16]. It uses a graphite ion collector rod, which is embedded in a ceramic tube surrounded by a thin metal cylinder of stainless steel with a length of 101 mm and an outer diameter of 6 mm. The ion collecting diameter is as small as 1.9 mm (area 2.8 mm²) to allow for measurements with high spatial resolution. The ion collector is connected via a shielded BNC cable and a customized vacuum feedthrough to an external board with several high-precision resistors with different resistance. Thus, a large range of signal amplitudes can be covered. Data are recorded using a 12-bit analogue digital converter. With a sampling rate of up to 20 kHz, maximum ion current densities up to 40 mA/cm² with a resolution of 0.05 mA/cm² can be detected.

The Faraday probe is designed as small and compact as possible in order to minimize the interaction with the energetic particle beam. Thus, this probe can also be used to measure the ion current density at a very low distance to the thruster exit plane, which gives access to determining the plasma density inside the discharge chamber.

Table 1. List of diagnostic tools with operation principle and possible measurement applications.

Diagnostic tool	Specifications
Faraday probe	Current density measurements Beam profiling
Retarding potential analyzer	Electrostatic energy analyzer Energy distribution measurements of charged particles
ExB probe	Ion velocity filter Velocity distribution measurements of charged particles Ion species fractions composition
Active thermal probe	Energy flux density measurements Measurement of energy flux density distribution
Telemicroscope	Detection of divergence and irregularities in the beam profile High-resolution optical imaging
Triangular laser head	Inspection and radial erosion measurements of mechanical parts Distance measurements using the triangulation principal
Pyrometer	Surface profiling and axial erosion measurements of mechanical parts Spot measurement of emitted infrared radiation
Thermocamera	Surface temperature measurements of mechanical parts Imaged measurement of emitted infrared radiation Surface temperature images of mechanical parts

The potential of the measuring area is defined by the potential drop at a resistor, whose resistance is, typically, selected such that the potential drop is smaller than 1 V, i.e. it is negligibly small with respect to the beam voltage. The direct calibration of the Faraday probe is not possible because there is no ion current standard. Therefore, the Faraday probe calibration is performed by precisely measuring the resistance and probe area.

2.3 Retarding potential analyzer

The retarding potential analyzer was also developed in-house with the goal to make it as small as possible while keeping the performance (signal-to-noise ratio) sufficiently high. Therefore, a two-grid design with 149 holes has been chosen. The device consists of two grids and an ion collector. The first grid is used for focusing the ion trajectories, the second grid for repelling secondary electrons. The ion collector is used for measuring the ion current and for repelling the ions by applying a repelling voltage U_r . The holes of the first grid have a diameter of 0.4 mm. The first grid could also be used for measuring the ion current density. The measurement area is $24 \times 24 \text{ mm}^2$. The ion collector has cup-shaped cavities, one for each of the 149 ion channels. The repelling voltage can be varied between 0 V and 3000 V with an accuracy better than 0.05%. The collected ion current is transformed by a high-precision resistor into a voltage drop, which is measured by a 14-bit AD converter.

The diameter of the grid holes is chosen such that it is close to the Debye length λ_D . The Debye length of a plasma can be calculated by the following equation:

$$\lambda_D = \sqrt{\frac{\epsilon_0 k T_e}{n_e e^2}} \quad (1)$$

and the continuum equation:

$$j = q_0 n_e v \quad (2)$$

ϵ_0 , k , T_e , n_e , and e are vacuum permittivity, Boltzmann constant, electron temperature, electron density, and elementary charge, respectively. j , q_0 and v are current density, charge and velocity of the ions. Hence, the Debye length depends on current density and ion velocity (or ion energy). In the regime of interest, i.e. for current densities between 1 mA/cm^2 and 10 mA/cm^2 , and ion energies between 100 eV and 2000 eV, the Debye length varies between 0.2 mm and 0.6 mm.

The retarding potential analyzer measures the current I_c at the collector as a function of the repelling voltage U_r . The energy distribution $f(E)$ is then calculated by:

$$f(E) \propto -\frac{dI_c}{dU_r} \quad (3)$$

The maximum of the energy distribution would be a measure for the ion current density. However, quantifying the current density using the current at the collector is impossible, because the transmission of the ions through the grids must not be 100%. Therefore, the energy distribution is normalized to its maximum.

The ion energy distribution is measured with respect to the ground of the vacuum chamber. The ground of the ion thruster and its components is not connected to the vacuum chamber ground. The difference is called secondary star ground (SSG) potential. The SSG potential is negative with respect to the ground of the vacuum chamber and depends on the operation conditions of the thruster.

2.4 ExB probe

The ExB probe exploits the action of a magnetic (B) and an electric field (E) to select ions on the basis of their velocity v_i : only ions whose velocity satisfies the Wien condition (Eq. (4)) are able to pass through the filter and thus being detected [17]. d is the distance between the fixed

Table 2. Summary of selected specifications and performance parameters of the diagnostic tools.

Diagnostic tool	Parameters
Faraday probe	Sensor area diameter: 1.9 mm Measurement range: up to 40 mA/cm ² Accuracy: <0.01 mA/cm ² (depends on dynamic range)
Retarding potential analyzer	Outer dimension: 101 mm (length), 6 mm (diameter) Number / diameter of holes: 149 / 1.8 mm Measurement range: 0 eV–3000 eV Accuracy: <5 eV
ExB probe	Dimension (including housing): 40 × 47 × 84 mm ³ Entrance orifice diameter: 1.6 mm Entrance collimator length: 90 mm Wien filter length: 150 mm Resolution: 1000 m/s Velocity range: up to 100 000 m/s
Active thermal probe	Dimension: 50 × 50 × 280 mm ³ Measurement range: 1 × 10 ⁻³ W/cm ² –4 W/cm ² Sensitivity: ±1 × 10 ⁻³ W/cm ²
Telemicroscope	Sensor dimension: 7 × 10 × 0.3 mm ³ Focal length / extension tube length*: 50 mm/40 mm Image size/working distance: 8.75 × 6.56 mm ² /112.5 mm Resolution*: 1600 × 1200 pixel Radial accuracy: <0.01 mm Depth of field: ±0.5 mm
Triangular laser head	Dimension (including housing): 60 × 70 × 210 mm ³ Spot size*: <0.2 mm (at a working distance of 150 mm) Distance range*: 110 mm–190 mm Repeatability*: <0.001 mm Distance resolution: <0.01 mm
Pyrometer	Dimension (including housing): 95 × 47 × 127 mm ³ Spectral range*: 2.3 μm Spot size*: 1.5 mm (at the focal distance of 110 mm) Temperature range/resolution*: 150 °C–1000 °C/0.1 °C System accuracy*: 0.3% of reading +2 °C Repeatability*: 0.1% of reading +1 °C
Thermocamera	Dimension (including housing): 25 × 30 × 47 mm ³ Spectral range*: 7.5 μm–13 μm Image size*: ~0.05 m × 0.07 m (at a distance of 500 mm) Resolution*: 160 × 120 pixel Lateral resolution*: 1.5 mm (at a distance of 500 mm) Temperature range/resolution*: 0 °C–900 °C/0.1 °C System accuracy*: 2% of reading or 2 °C Dimension (including housing): 56 × 60 × 143 mm ³

*Numbers specified by the manufacturer.

electrodes, where the electric field is created:

$$v_i = \frac{E}{B} = \frac{V_{\text{probe}}}{Bd}. \quad (4)$$

Because the velocity is a function of charge state z_i , mass m_i and ion energy $E_{\text{ion},i}$, different ion species can be separated. Equation (5) expresses the electrodes voltage difference associated with each peak in the spectrum: On one hand a constant magnetic field is used to deflect trajectories of the ions, on the other hand a variable electric field acts for compensating the magnetic force, which allows ions with different velocity to be detected as a function of the voltage applied to electrodes. The retarding potential analyzer measures the current I_c at the collector

in dependence on a repelling voltage U_r , which gives direct access to the energy distribution of energetic ions. In contrast to that, the voltage range to be scanned with the ExB probe depends also on the constructive parameters of the probe (magnetic field intensity, electrodes separation). These constructive parameters affect the performances of the probe in terms of resolution. The probe detector is simply constituted by the collector of a Faraday cup:

$$V_{\text{probe}} = Bd \sqrt{\frac{2z_i E_{\text{ion},i}}{m_i}}. \quad (5)$$

The main aim was to develop a probe, which is able to put together high performances with low invasiveness. These aspects can be considered conflicting because an increase

of the probe resolution can be determined by an increase of the magnetic field, and an increase of the magnetic field is usually associated with larger magnets. This problem was overcome by exploiting a particular magnetic configuration known as Stelter dipole [18] allowing a significant increase of the magnetic field with respect to a traditional dipole with the same overall dimension. In particular, a maximum field of 0.54 T has been obtained for a probe having a $50 \times 50 \text{ mm}^2$ section.

Another important aspect taken into account in the probe design concerns the topology of the magnetic and electric fields at the entrance and the exit of the probe. The different decaying behavior of the fields makes the probe not ideal, thus the Wien condition is no more satisfied in these regions. To overcome this problem the electrodes shape has been optimized in order to make the electric fringing field matching the magnetic one. The spatial resolution of the probe is determined by two collimators at the entrance and exit of the probe selecting ions traveling along a well-defined direction. A modular design approach has been implemented allowing to easily change the collimator length and the orifice diameter.

The probe is mainly used to determine the plasma composition in terms of ion species fraction because of the dependence of the ion velocity on the charge state. Assuming that all ion species are subject to the same accelerating voltage, the separation between the peaks position will be given by $\sqrt{z_i/m_i}$. The area under each peak yields the current carried by each ion species. Therefore, the ratio between this area and the area under the overall spectrum provides the current fraction (neglecting secondary emission effects). On the other hand the position of each peak is connected with the ion velocity through the constructive parameters of the probe: in particular the ion velocity distribution function for each ion species could be determined. This application requires a calibration of the probe providing a correction factor to be applied to the measured ion velocity to obtain the real one.

2.5 Active thermal probe

The active thermal probe (see Fig. 2) was developed as a flexible diagnostic for the measurement of energy flux. For the use as a diagnostic tool for beam characterization as a part of the AEPD platform, it has been further improved and characterized especially regarding its sensitivity towards parasite heat sources.

The physical principle of the measurement method of the active thermal probe is based on the compensation of the incoming energy by decreasing the heating power of a preheated probe. The probe consists of a ceramic dummy-substrate (see Fig. 2a), which is electrically heated to a given set-point temperature. If the probe is exposed to an external energy flux (e.g. by the ion beam) the additional heating of the probe is compensated by a reduction of the electrical heating power, resulting in a constant temperature of the probe. The power of the external energy source is then directly given by the difference in the electrical heating power. In contrast to the other probes, the ATP

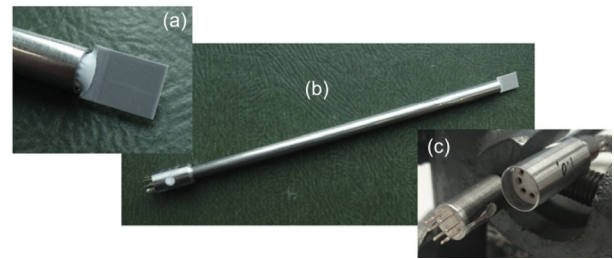


Fig. 2. Active thermal probe: sensor area (a), full image (b) and connector (c).

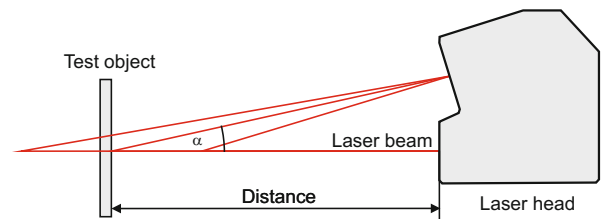


Fig. 3. Measurement principle of the triangular laser head (triangulation effect).

measures both the contribution of charged and neutral particles. A much more detailed description of the working principle of the active thermal probe can be found in references [19–21].

2.6 Telemicroscope and triangular laser head

The telemicroscope is a high-resolution optical camera, which can be used to measure radial (and axial) erosion of mechanical parts. It consists of a CCD camera, an extension tube and a photographic lens. By placing the extension tube between camera and lens, the radial resolution and depth of field is reduced considerably (lateral resolution from formerly 0.15 mm to 0.01 mm; depth of field from formerly 60 mm to 0.5 mm).

The triangular laser head measures the distance to a test object utilizing the triangulation principle, i.e. the fact that the detection angle α depends on the distance between triangular laser head and test object (see Fig. 3). When scanning across the test object, the surface profile can be measured, which gives access to axial (and radial) erosion.

Telemicroscope (The Imaging Source DFK 51AU02) and triangular laser head (Keyence LK-G152) are commercial devices. The triangular laser head is the same one that was used with the previous setup [12]. The telemicroscope has changed slightly with the goal to reduce the overall dimension. Now a smaller lens and a camera with a higher resolution is used. Triangular laser head and telemicroscope are operated inside vacuum. Therefore, some vacuum-sensitive electronic parts (capacitors) had to be replaced. For safety reasons the devices are covered by a small housing each. The overall dimensions could be reduced considerably compared to the previous setup



Fig. 4. Telemicroscope with housing (without metal cover).

with vacuum-sealed housings [12]. The new housings consist of a metal base plate, a front plate made of graphite with sapphire window(s) and a metal cover. The window protects the optics from direct particle impingement. Additionally, the telemicroscope housing is equipped with four high-power LEDs for illumination. Figure 4 shows, exemplary, the housing of the telemicroscope.

2.7 Pyrometer and thermocamera

Pyrometer and thermocamera measure the surface temperature of a test object upon detection of the emitted infrared radiation. The physical principles are described by Planck's law:

$$B(T, \varepsilon, \lambda) = \varepsilon t \frac{2hc^2}{\lambda^5} \frac{1}{\exp\left(\frac{hc}{\lambda kT}\right) - 1} \quad (6)$$

i.e. the intensity of the emitted infrared radiation B depends on the object temperature T , the emissivity ε of the object material, the wavelength λ and, if needed, the transmission t of a window between test object and pyrometer/thermocamera. h , c and k are Planck constant, speed of light and Boltzmann constant, respectively.

When measuring the temperature, the properties of the test object, i.e. the emissivity of the material of interest, and of the setup, i.e. window effects, must be known. Emissivity (graphite of grid area: $\varepsilon = 0.97$) and transmission of the windows (sapphire window for pyrometer: $t = 0.85$; ZnS window for thermocamera: $t = 0.75$) were measured in the spectral region of interest.

Pyrometer (Optris CT 3M) and thermocamera (Optris PI) are commercial devices. Unlike the previous setup [10,12], which contained only a pyrometer, the actual platform uses a pyrometer of different type and additionally a thermocamera. Both devices were chosen because of their small size, which reduces possible interactions with the energetic particle beam. Pyrometer and thermocamera are operated inside vacuum. Therefore, some vacuum-sensitive electronic parts (capacitors) had to be replaced or removed (liquid crystal display). Both diagnostic heads



Fig. 5. Pyrometer sensor head with housing.

Table 3. Summary of operation parameters of the RIT- μ X at operation point 1 (OP1) and 2 (OP2).

Parameter	OP1	OP2
Beam Voltage	1050 V	1700 V
Beam Current	4 mA	8 mA
Accelerator voltage	-200 V	-250 V
Nominal thrust	210 μ N	540 μ N

are placed inside metal housings with appropriate windows (pyrometer: sapphire window; thermocamera: ZnS window) for safety reasons [14]. The housing of the pyrometer is shown in Figure 5, the housing of the thermocamera is similar to that of the telemicroscope in Figure 4.

Operating the diagnostic heads inside vacuum has the advantage that they can be brought closer to the test object. A smaller working distance results in a better lateral resolution, which is especially favorable for the thermocamera.

2.8 Thruster

A gridded ion thruster RIT- μ X [15] was used for the test measurements. Radio-frequency ion thrusters (RITs) generate thrust in two steps: in the first step the propellant is ionized in the oscillating electromagnetic field of a coil (plasma). Once ionized, the propellant is accelerated in the electrostatic field of the thruster's second functional unit called the grid system.

The ionization chamber of the RIT- μ X has an inner diameter of 4 cm at the interface to the grid system and a length of 3 cm. Its inductively coupled plasma is operated with a frequency of 2.5 MHz. The experiments were performed using the standard propellant xenon. The RIT- μ X can be equipped with different sets of grids optimized for specific mission requirements. During the reported tests a configuration with 37 extraction channels was used. It is designed for extraction voltages in the range from 600 V to 2200 V and nominal ion currents between 1 mA and 10 mA. The thruster was operated here at two operation points as summarized in Table 3.

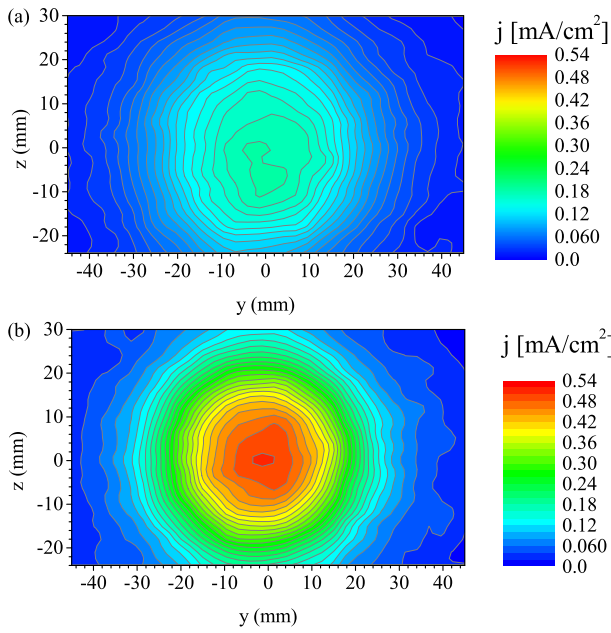


Fig. 6. Current density maps of the RIT- μ X at OP1 (a) and OP2 (b) measured with the Faraday probe at a distance of 120 mm to the exit plane of the thruster.

2.9 Test chamber

The tests were performed in the Jumbo test facility [22]. The tank is of cylindrical shape with a diameter of 2.6 m, a length of 6 m and a volume of 30 m³. It is equipped with turbo and cryo pumps with a total pumping speed of 120 000 L/s for nitrogen or 65.000 L/s for xenon. The base pressure is about 1×10^{-7} mbar.

3 Results

3.1 Faraday probe

Selected current density maps of the thruster at the two operation points are plotted in Figure 6. As expected, rotationally symmetric, Gaussian shaped beam profiles can be seen with a higher maximum current density at operation point 2 ($j_{\max} = 0.52$ mA/cm²) than at operation point 1 ($j_{\max} = 0.18$ mA/cm²). This is related to the higher beam voltage at operation point 2. The full width at half maximum of the beam profiles is 48.0 mm for OP1 and 40.8 mm for OP2.

3.2 Retarding potential analyzer

Measurements with the retarding potential analyzer were performed for both operation points, too. Figure 7 shows the measured current curves and the calculated, normalized energy distributions. Both curves are corrected for the SSG potential U_{SSG} . The energy distributions reveal a single peak with a position slightly higher than the corresponding beam voltage (1078 V for OP1; 1716 V for OP2).

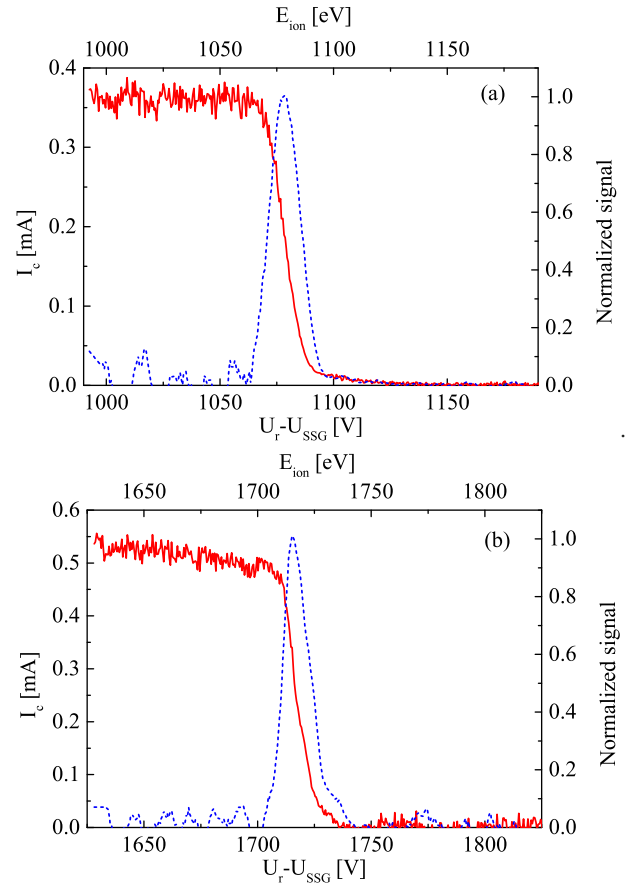


Fig. 7. Current I_c measured with the retarding potential analyzer at the collector (red solid lines) and calculated energy distribution (blue dashed lines) at OP1 (a) and OP2 (b). The curves are corrected for the secondary star ground potential ($U_{SSG} = -42$ V for OP1; $U_{SSG} = -78$ V for OP2).

The difference is related to the plasma potential inside the discharge chamber of the thruster. The full width at half maximum of the peaks is about 16 V for both operation points, which corresponds to less than 2% of the ion energy. Ions with other energies, which could be generated by charge exchange processes, or multiply charged ions were not detected.

3.3 ExB probe

Ion velocity measurements were performed with the ExB probe positioned along the thruster axis at a distance of 350 mm from the thruster exit plane. Figure 8 shows two curves obtained for the two operation points of the thruster. The position of the peaks corresponds to the different ion velocity, which is proportional to the square root of the ion energy. The most pronounced peaks at an electrode voltage difference of ~ 87 eV (OP1) and ~ 111 eV (OP2) can be assigned to singly charged ions (Xe^+). As expected, the ratio of the peak positions is the same as the square root of the ratio of the corresponding ion energies measured with the retarding potential analyzer.

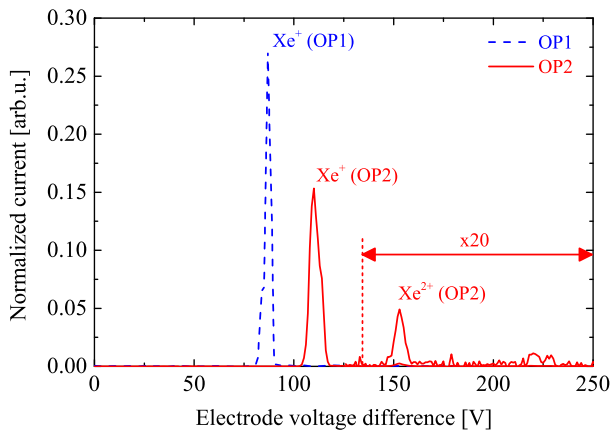


Fig. 8. ExB probe normalized spectra at OP1 (dashed curve) and OP2 (solid curve) at a distance of 350 mm to the exit plane of the thruster.

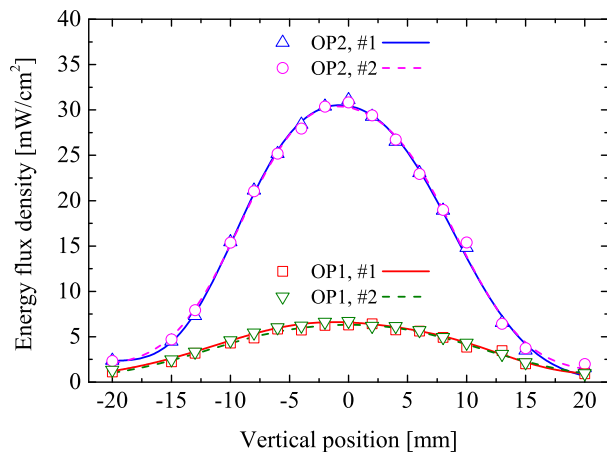


Fig. 9. Energy flux density vs. vertical position for the RIT- μ X running at OP1 and OP2 measured with the active thermal probe. The symbols represent the experimental data, the solid lines give cubic spline interpolations as a guide to the eye. There are two measurements for each operation point.

In the curve for operation point 2 a second peak at an electrode difference voltage of ~ 153 eV can be seen. This peak is related to doubly charged ions (Xe^{2+}). The peak is very small, i.e. the fraction of doubly charged ions is low, as it is typical for gridded ion thrusters.

3.4 Active thermal probe

In Figure 9 selected results for the measurement of the energy flux density under variation of the vertical position relative to the center axis of the thruster are presented. The thruster was aligned in such a way that the beam hits the probe at normal incidence and that the center of the thruster grid has a distance of 490 mm to the probe. Figure 9 summarizes the results of two measurements for the two thruster operation points each. The data illustrate clearly that the measurements show a good reproducibility and give access to the radial distribution of the energy flux density of the beam. Furthermore, it should be pointed out

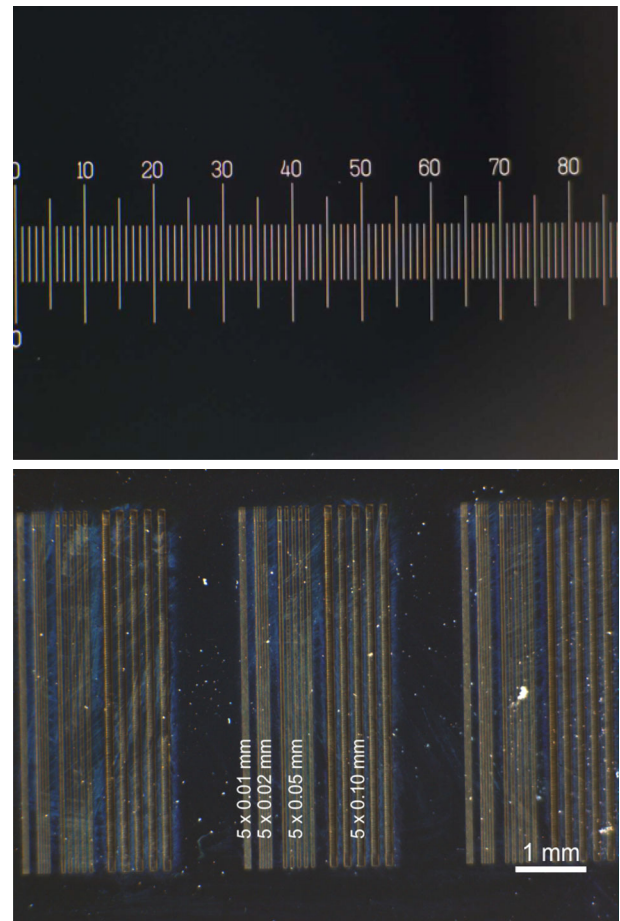


Fig. 10. Telemicroscope image of the test structures: eyepiece graticule (top) and line structure (bottom).

that even close to its lower detection limit of 1 mW/cm^2 the probe gives reproducible results.

3.5 Telemicroscope

The performance of the telemicroscope was investigated using two test structures: a graticule structure and a special line structure. Both test structures are shown in Figure 10. Using the scale of the graticule structure, the field of view can be easily measured. It was found that the field of view is $8.75 \times 6.56 \text{ mm}^2$ at a working distance of 112.5 mm, and the depth of field is smaller than $\pm 0.5 \text{ mm}$. The line structure consists of several pairs of lines, which were laser scribed into a titanium dioxide layer (dark area) on a silicon wafer. Each pair consists of five lines with equal width and spacing of 0.01 mm, 0.02 mm, 0.05 mm or 0.1 mm. It can be seen in Figure 10 that all pairs of lines down to 0.01 mm can be resolved. Hence the lateral resolution of the telemicroscope is better than 0.01 mm. Figure 11 depicts a section of the grid of the thruster (thruster is off). The grid holes can be clearly resolved and grid hole diameter and, hence, the grid hole erosion are accessible. The diameter of the center hole in Figure 11 is $(1.27 \pm 0.02) \text{ mm}$.

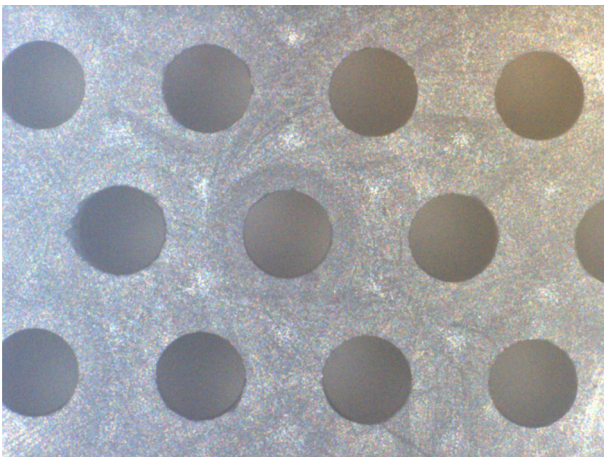


Fig. 11. Telemicroscope image of grid holes of the RIT-μX.

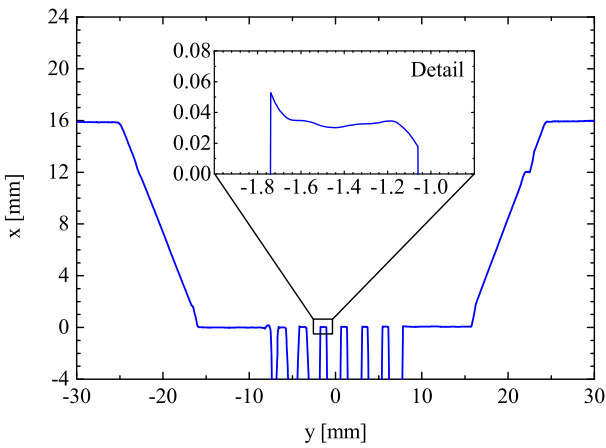


Fig. 12. Surface profile scan across the center of the RIT-μX measured with the triangular laser head. The detail inset shows the measured surface profile scan between two grid holes. The rise of the profile at the left side is a measurement artifact due to the triangulation measurement principle.

3.6 Triangular laser head

Figure 12 shows a surface profile scan of the thruster. Among others, the grid hole area can be identified clearly and the number of holes can be seen. Doing so, the principal shape of the grid including, for instance, its radius of curvature could be measured [7,10]. In case of the RIT-μX the grid is flat. However, there are experimental limitations due to the measurement principle (triangulation effect). Because of that, the triangular laser head might fail in measuring the profile at steep or abrupt edges (see detail inset in Fig. 12).

3.7 Thermocamera

Figure 13 shows thermocamera images of the RIT-μX operated at OP2 and OP1. The surface temperature of almost the whole thruster was imaged. The temperature distribution is nearly homogeneous, apart from the holes. As shown in previous tests, the temperature of the plasma

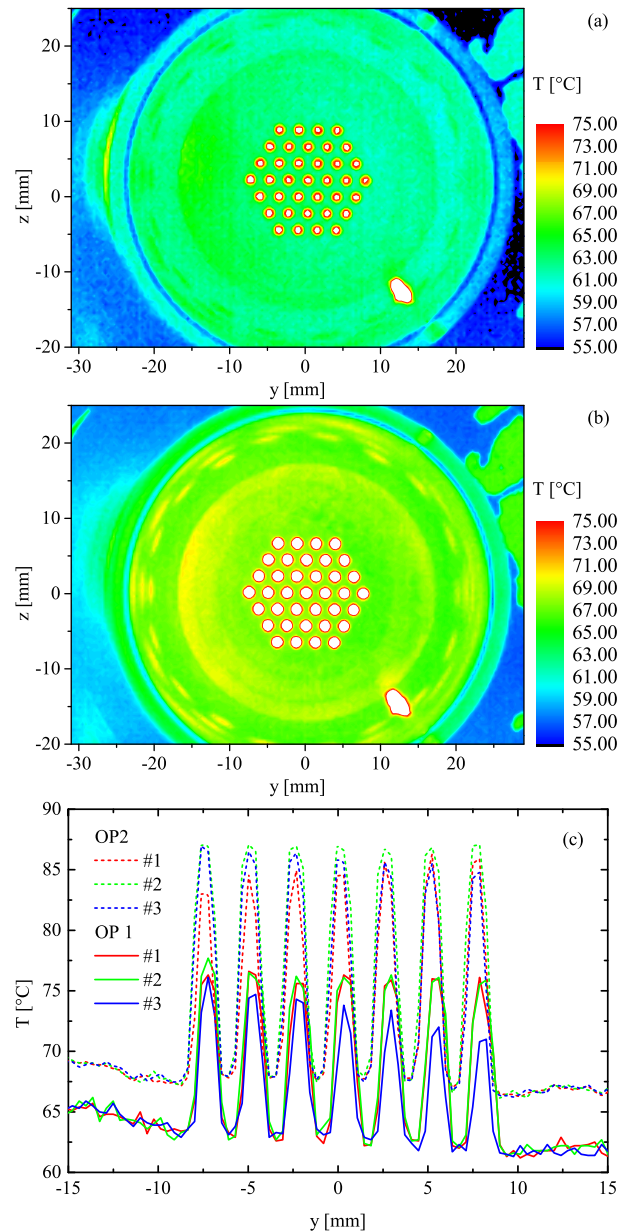


Fig. 13. Thermocamera image of the RIT-μX at OP1 (a) and OP2 (b). (c) Horizontal temperature scans across the center of the thruster extracted from thermocamera images. Please note, the assumed emissivity is that of graphite ($\epsilon = 0.97$). Therefore, the given temperature values are only correct for the grid area.

chamber, which is imaged through the holes is considerably higher than the grid surface temperature [7,10]. In Figure 13c selected temperature line scans for both operation points, which were extracted from thermocamera images, are plotted. There are some interference-like structures. These structures are related to the fact that the sensor pixels of the thermocamera see different fractions of the grid and of the holes. Please note, the height of the maxima differs for the different line scans at the same operation point, whereas the minima and the region on the left and on the right side are the same. Again this is related

to the different fractions of grid and holes seen by the sensor pixels, because the line scans were taken for different z -positions. The grid temperature was found to be $68\text{ °C} \pm 2\text{ °C}$ for OP2 and $63\text{ °C} \pm 2\text{ °C}$ OP1.

No pyrometer data are shown here, because the temperature of all thruster parts is below the lower limit of the measurement range of the pyrometer of 150 °C (see Tab. 2).

4 Conclusion

The experimental data demonstrate impressively the capabilities of the AEPD platform, which allows, for the first time, for a comprehensive in-situ characterization of electric propulsion thrusters or ion beam sources for material processing. Comprehensive characterization is an essential part in the development and optimization process of these devices, and allows to judge the performance with respect to the specific mission or application needs. Furthermore, a standardization of these diagnostics would allow for a reliable comparison of the performance of EP thrusters of different type, which would help promoting EP thruster technologies.

Typically, the main focus lies on investigating beam properties, because the beam provides the thrust or, in material science, the tool for material modification. Important parameters are particle energy or velocity, beam shape and divergence, composition, charge state. All of these parameters can be measured with the current setup. It is not only possible to measure the properties of charged particles (Faraday probe, retarding potential analyzer, ExB probe) but also of energetic neutrals (active thermal probe).

The optical inspection tools (triangular laser head, telemicroscope) provide important information about the shape of mechanical parts and its evolution in time (erosion), which can be life-limiting factors. The triangular laser head is advantageous when measuring axial dimensions, whereas the telemicroscope has its advantage when measuring radial dimensions. However, both devices can be used to measure axial and radial dimensions, though with different accuracy.

Thermal characterization is important, for instance, for evaluating the thermal impact on the performance of satellites (in case of electric propulsion thrusters). Both pyrometer and thermocamera provide similar information. In case of small thrusters, the thermocamera can yield a full thermal image. In case of larger thrusters (with higher power), scanning with the pyrometer seems to be more appropriate because (i) of its smaller dimension and (ii) the smaller time that is needed to perform a line scan instead of taking a thermocamera image.

5 Summary and outlook

We have reported about improvements of our AEPD platform. The activities are focused on modifying the experimental setup in order to reduce possible interactions

between diagnostics and thruster, on implementing additional or alternative diagnostic heads in order to improve the performance or to expand the portfolio of accessible parameters. We have described the main parameters of the new diagnostic tools and presented first experimental results, exemplary, with a gridded ion thruster RIT- μ X.

It can be stated that the improvements on the AEPD platform have improved reliability and repeatability, and, therefore, constitute a major step towards standardization, which is intended to be the final goal. In order to reach this goal, significant effort is still necessary to provide suitable standards.

Author contribution statement

All authors contributed equally to the paper.

The work was performed with financial support provided by ESA/ESTEC (Contract No. 4000107451/12/NL/RA; “Qualification of the AEPD System as a Standard On-Ground Tool for Electric Propulsion Thrusters”). The authors thank R. Woyciechowski, M. Müller, S. Daum (all Leibniz-Institute of Surface Modification), R. Kukies (Airbus Defence & Space), W. Gärtner, U. Bachmann (all Justus-Liebig-Universität Gießen) for technical support.

References

1. J.P. Verboncoeur, A.B. Langdon, N.T. Gladd, *Comput. Phys. Commun.* **87**, 199 (1995)
2. R. Becker, W.B. Herrmannsfeldt, *Rev. Sci. Instrum.* **63**, 2756 (1992)
3. M. Tartz, E. Hartmann, H. Neumann, *Rev. Sci. Instrum.* **79**, 02B905 (2008)
4. M. Crofton, R. Ueunten, L. Harris, E. Yohnsee, R. Cohen, in *Proceedings of the 32nd AIAA Joint Propulsion Conference and Exhibit, Lake Buena Vista, 1996*, Paper AIAA-96-2977
5. S. Mazouffre, P. Echegut, M. Dudeck, *Plasma Sources Sci. Technol.* **16**, 13 (2007)
6. S. Mazouffre, K. Dannenmayer, J. Pérez-Luna, *J. Appl. Phys.* **102**, 023304 (2007)
7. C. Bundesmann, M. Tartz, F. Scholze, H. Neumann, H.J. Leiter, F. Scortecci, D. Feili, P.E. Frigot, J. Gonzalez del Amo, in *Proceedings of the 31st International Electric Propulsion Conference, Ann Arbor, 2009*, Paper IEPC-2009-160
8. C. Bundesmann, M. Tartz, F. Scholze, H. Neumann, F. Scortecci, S. Scaranzin, P.E. Frigot, J. Gonzalez del Amo, R.Y. Gnizdor, in *Proceedings of the 31st International Electric Propulsion Conference, Ann Arbor, 2009*, Paper IEPC-2009-141
9. T. Misuri, A. Milani, M. Andrenucci, in *Proceedings of the 31st International Electric Propulsion Conference, Ann Arbor, 2009*, Paper IEPC-2009-036
10. C. Bundesmann, M. Tartz, F. Scholze, H. Neumann, H.J. Leiter, F. Scortecci, *J. Propul. Power* **27**, 532 (2011)

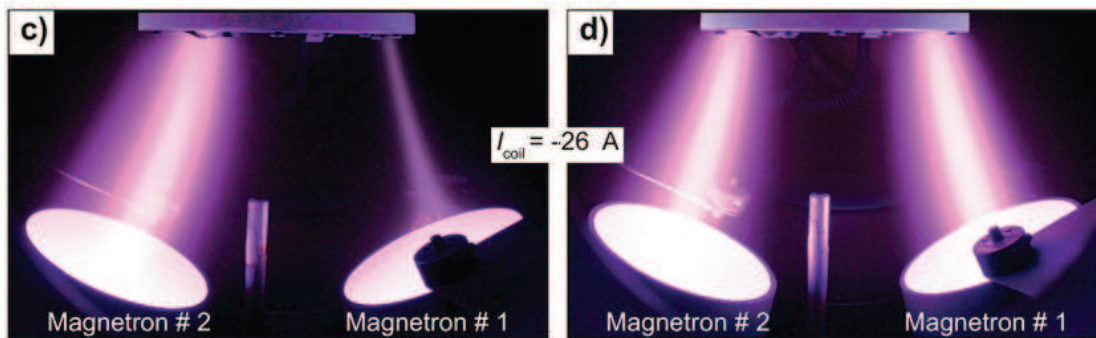
11. T. Misuri, T. Vrebosch, L. Pieri, M. Andrenucci, M. Tordi, E. Marcuzzi, M. Batolozzi, S. Renzetti, J. Gonzalez del Amo, in *Proceedings of the 32nd International Electric Propulsion Conference, Wiesbaden, 2011*, Paper IEPC-2011-129
12. C. Bundesmann, M. Tartz, F. Scholze, H.J. Leiter, F. Scortecci, R.Y. Gnizdor, H. Neumann, *Rev. Sci. Instrum.* **81**, 046106 (2010)
13. D. Pagano, F. Scortecci, C. Bundesmann, C. Eichhorn, F. Scholze, H. Neumann, H. Leiter, H. Kersten, S. Gauter, R. Wiese, R. Blott, P.J. Klar, K. Holste, B. Meyer, S. Mazouffre, A. Bult, J. Gonzales del Amo, in *Proceedings of the 34th International Electric Propulsion Conference, Hyogo-Kobe, 2015*, Paper IEPC-2015-363
14. C. Bundesmann, C. Eichhorn, F. Scholze, H. Neumann, H.J. Leiter, F. Scortecci, in *Proceedings of the 34th International Electric Propulsion Conference, Hyogo-Kobe, 2015*, Paper IEPC-2015-392
15. C. Altmann, H. Leiter, R. Kukies, in *Proceedings of the 34th International Electric Propulsion Conference, Hyogo-Kobe, 2015*, Paper IEPC-2015-274
16. C. Eichhorn, F. Scholze, C. Bundesmann, H. Neumann, in *Proceedings of the 33rd International Electric Propulsion Conference, Washington, 2013*, Paper IEPC-2013-295
17. D. Renaud, D. Gerst, S. Mazouffre, A. Aanesland, *Rev. Sci. Instrum.* **86**, 123507 (2015)
18. K. Halbach, *Nucl. Instrum. Methods* **169**, 1 (1980)
19. R. Wiese, Dissertation, Ernst-Moritz-Arndt Universität, Greifswald, 2008
20. R. Wiese, H. Kersten, G. Wiese, M. Häckel, *Vakuum in Forschung und Praxis* **23**, 20 (2011)
21. R. Wiese, H. Kersten, G. Wiese, R. Bartsch, *Eur. Phys. J. Techniques and Instrumentation* **2**, 2 (2015)
22. P.J. Klar, K. Hannemann, U. Ricklefs, H. Leiter, in *Proceedings of the 34th International Electric Propulsion Conference, Hyogo-Kobe, 2015*, Paper IEPC-2015-89

Publication II

Tunable ion flux density and its impact on AlN thin films deposited in a confocal DC magnetron sputtering system

Authors	M. Trant, M. Fischer, K. Thorwarth, S. Gauter, J. Patscheider and H.J. Hug
Journal	Surface & Coatings Technology
Technique	Confocal magnetron sputtering with additional magnetic field
Utilized Probes	Active thermal probe (ATP), Langmuir probe (LP)
Own contribution	approx. 20%

Experimental Setup:



Motivation:

The main objective of this work was to investigate the performance of a confocal magnetron sputtering system which has been modified by addition of an electromagnetic coil which allows in-situ alteration to the magnetic configuration. By changing the 'balance' of the magnetic field, the amount of ions in the substrate region can be adjusted, resulting in a tunable ion-to-neutral ratio which directly impacts the properties of the deposited film.

Main results:

The measurement results revealed the plasma to create highly inhomogeneous ion and energy flux in the substrate region. Using the in-situ coil, the ion-to-neutral ratio was found to be adjustable up to a factor of 30 compared to operation without the coil. The deposited AlN films showed a correlation between the stress in the film and the ion flux density, with stress changing from tensile to compressive for increasing ion flux density.



Tunable ion flux density and its impact on AlN thin films deposited in a confocal DC magnetron sputtering system

M. Trant^{a,*}, M. Fischer^a, K. Thorwarth^a, S. Gauter^b, J. Patscheider^{c,1}, H.J. Hug^{a,d}

^a Empa, Swiss Federal Laboratories for Materials Science and Technology, Überlandstrasse 129, Dübendorf 8600, Switzerland

^b Institute of Experimental and Applied Physics, Christian-Albrechts-University Kiel, Leibnizstr 19, Kiel D-24098, Germany

^c Evatec AG, Hauptstrasse 1a, Trübbach CH-9477, Switzerland

^d Department of Physics, University of Basel, Klingelbergstrasse 82, Basel 4056, Switzerland



ARTICLE INFO

Keywords:

Magnetron sputtering
Thin films
Aluminum nitride
Plasma
Ion bombardment
Magnetic configuration

ABSTRACT

An in-situ coil implemented in a confocal magnetron sputtering system is used to modify the ion flux impacting the substrate, thereby tuning the ion-to-neutral ratio. Plasma characterization performed at the substrate is used to map the spatial dependence of the ion flux density and the total energy flux density across the substrate holder. In addition, spatially-resolved temperature measurements are performed for different plasma conditions. Aluminum nitride (AlN) thin films were deposited by reactive sputtering in the fully poisoned mode on Si (100) and borosilicate glass substrates using the open field configuration. Texture, growth morphology, and residual stress of the films were determined and correlated with the plasma conditions and substrate temperatures obtained by applying the coil's magnetic field. All AlN films were stoichiometric and showed a hexagonal structure with (001) texture. The film stress was found to change from 0.9 GPa (tensile) to 4 GPa (compressive) with increasing ion flux density. Electron microscopy revealed an evolution from an open grain boundary to a dense film morphology compatible with the observed residual stress dependence of the films on the ion flux. No change in residual stress and film morphology was observed within the 100 °C–500 °C temperature range used here.

1. Introduction

In sputter deposition processes the ion impact on the growing film can be utilized advantageously to control the film microstructure and microchemistry [1–3]. For example, increasing the energy flux of the ions hitting the substrate, a compact film microstructure can be obtained already at a lower deposition temperature.

The ion bombardment processes are governed by the flux of incoming ions j_{ion} and their energy E_{ion} . The ion energy determines the mechanism of momentum transfer and the resulting effects [4]. In the case of low energy ion bombardment ($E_{\text{ion}} < 50$ eV) decremental effects of ion irradiation (e.g. creation of defects or vacancies, implantation) are avoided and the adatom mobility is enhanced collisionally. The latter results in an enhanced surface diffusion and rearrangement for atoms on the surface of the growing film. For a given E_{ion} the flux of incoming ions j_{ion} determines the total amount of energy transferred to the growing film.

It is crucial to control these two parameters independently, as their combination, the average energy per deposited atom, is not a universal parameter [5]. The ion flux and ion energy are also influenced by

pressure and applied substrate bias. The pressure determines the mean free path of both the ions and neutral particles, and thereby influences the energy and flux of both species. The application of a bias controls the ion impact energy but may lead to implantation of the process gas, which leads to strain fields and lattice distortions [6].

The importance of controlling E_{ion} and j_{ion} directly and independently is widely recognized and a variety of approaches to control the plasma flux in deposition systems have been proposed and are still developed further [7]. Petrov et al. used a variable magnetic field generated by a pair of Helmholtz coils placed around the chamber of their single magnetron deposition system to directly control the flux of the ions impacting the sample [8]. Engström et al. adapted the use of a coil to a dual magnetron system designed for the deposition of thin film multilayers [9]. Here we present how this approach can be used for a multiple magnetron system that allows deposition of compound films from elemental targets. Within this work we also compare the open field to the closed field configuration of confocal magnetron sputtering as it was observed that the magnetic orientation of the magnetrons relative to each other has a strong influence on the plasma flux towards the substrate [10]. Confocal reactive sputtering is widely employed in

* Corresponding author.

E-mail address: mathis.trant@empa.ch (M. Trant).

¹ Empa, Swiss Federal Laboratories for Materials Science and Technology, Überlandstrasse 129, 8600 Dübendorf, Switzerland (until 31.10.2017).

<https://doi.org/10.1016/j.surfcoat.2018.04.091>

Received 4 December 2017; Received in revised form 26 April 2018; Accepted 28 April 2018

Available online 24 May 2018

0257-8972/ © 2018 Elsevier B.V. All rights reserved.

research and production for deposition of compound films from elemental targets. As an example we deposited aluminum nitride (AlN) thin films by reactive sputtering, which is the base material for many interesting compounds such as AlSiN for tribological or AlScN for piezoelectric applications [11,12].

AlN thin films have been studied extensively for applications in microelectronic, electroacoustic and optoelectronic devices [13–16]. In order to obtain good piezoelectric properties, polycrystalline wurtzite AlN films with a pronounced c-axis orientation must be achieved [16,13]. For their application in MEMS devices the preferred film properties need to be obtained at low deposition temperatures, and residual stress must be well controlled [17,18]. To achieve these properties appropriately adjusted ion flux and ion energy are advantageous.

2. Experimental setup

The experiments were performed on an AJA ATC 1500F sputtering system with 33 cm in height and a diameter of 37 cm, containing four magnetrons. Two of them were confocally inclined at an angle of 25° with respect to the z-axis and with the center of the targets separated by 15 cm, as schematically shown in Fig. 1, while the other two remained upright along the chamber walls. The magnetrons are unbalanced of type II [19] with an unbalancing factor of $K = \Phi_{mag}^{out} / \Phi_{mag}^{in} = 13$.

Elemental aluminum targets (99.999% purity) with a diameter of 5 cm were used, and the power supplies (Advanced Energy MDX 500) were operated in direct current constant power mode at 200 W and connected to a common ground. The heatable substrate holder, with a diameter of 89 mm, was oriented face down and its center located at a distance of 12 cm from the center of the targets.

Argon (6.0 purity) was used as a process gas and nitrogen (5.0 purity) was added for the case of reactive sputtering. Purifiers (Alphagaz O₂-free) were installed on both gas lines to further reduce the remaining oxygen concentration and moisture. The chamber is equipped with a turbomolecular pump (210 ls) and the base pressure of the chamber was better than 5×10^{-7} mbar.

A water-cooled coil was built and installed inside the vacuum chamber around the substrate holder. The coil consists of Kapton insulated copper wire with a core diameter of 1.7 mm. A total of 149 turns fit over a length of 58 mm and an inner and outer diameter of 176 mm

and 244 mm respectively. The magnetic field of the coil (\vec{B}_{coil}) reaches 180 mT at the substrate holder surface for a coil current (I_{coil}) of 26 A. The magnetic field strength along the z-axis for $I_{coil} = 26$ A is included in the schematic of the setup shown in Fig. 1.

2.1. Plasma diagnostics

Several methods were employed to measure selected plasma parameters in the open field (OF) and closed field (CF) configurations, and for varying \vec{B}_{coil} (see Fig. 1).

The substrate holder was used as an electrical probe to measure the floating potential (V_{float}) and the ion saturation current (I_{sat}). For the latter, a bias of $V_{bias} = -60$ V was applied to the substrate holder.

A commercial Langmuir probe (LP) acquisition system (ALP, Impedans LTD) was used to acquire current-voltage data (I–V data). A cylindrical tungsten wire, with a diameter $r_{LP} = 50$ μm and a length $l_{LP} = 10$ mm, was used as a probe tip. The probe was installed on a linear positioner to measure the ion current density (j_p), the plasma potential (V_p) and V_{float} as a function of the x-position (see Fig. 1).

An active thermal probe (ATP) was alternatively installed onto the same positioner to measure the total energy flux to the substrate. The ATP consist of a Pt100 resistor embedded in an insulating ceramic 7 mm wide and 10 mm long [20].

The LP and ATP were positioned about 13 mm below the substrate holder. The measurements mentioned above were conducted in a pure Ar atmosphere to avoid the problem arising from the formation of an insulating layer on the probes' surfaces. The Ar flow was set to 15 sccm and the pumping speed was adjusted to obtain a working pressure of approximately 5 μbar.

2.2. Depositions

AlN thin films were deposited onto Si (100) and borosilicate glass substrates, both 6×6 mm², using the open field configuration. The samples were mounted close to the center (position x_i in Fig. 1), at a middle radius (x_m) and at the outer rim (x_o) of the substrate holder. Note that the substrate holder was not rotated during the deposition process. Prior to the deposition process, the substrates were ultrasonically cleaned for 10 minutes in a mixture of acetone and ethanol.

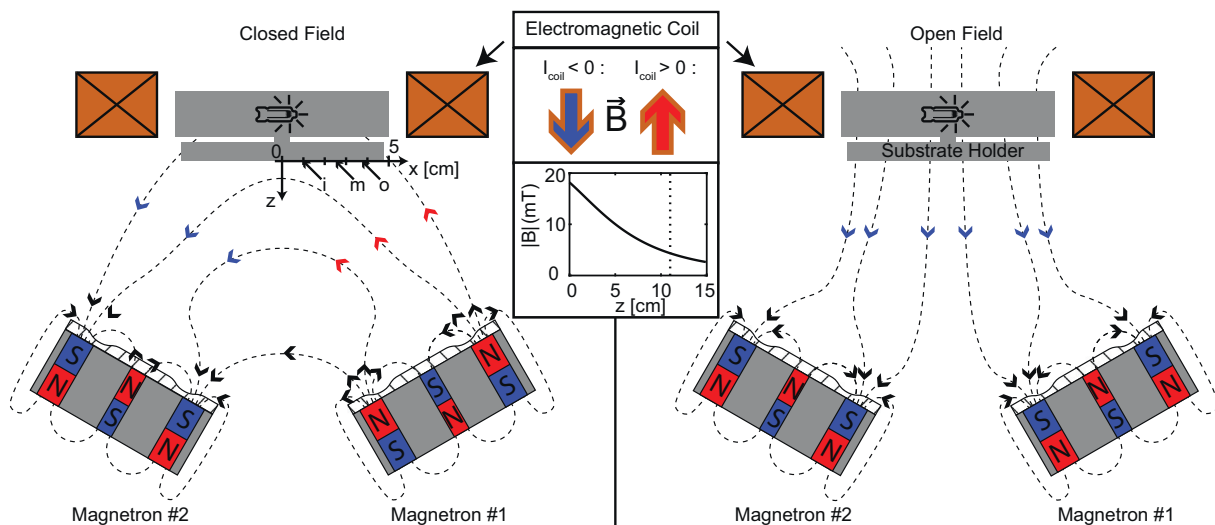


Fig. 1. Schematics of the experimental setup showing the closed field (left side) and open field (right side) configuration with a qualitative representation of the magnetic field lines arising from the magnetrons ($I_{coil} = 0$ A). The substrates were placed at three different positions along the x-axis ($x_i = 1$ cm, $x_m = 2.5$ cm, $x_o = 3.75$ cm). By inverting the current inside the electromagnetic coil the direction of the magnetic field can be reversed. The graph shows the magnetic field strength as a function of the vertical position along the central axis of the coil for $|I_{coil}| = 26$ A. Position $z = 0$ corresponds to the substrate holder surface position and the dotted line indicates the z-position of the target. (For interpretation of the references to color in this figure, the reader is referred to the web version of this article.)

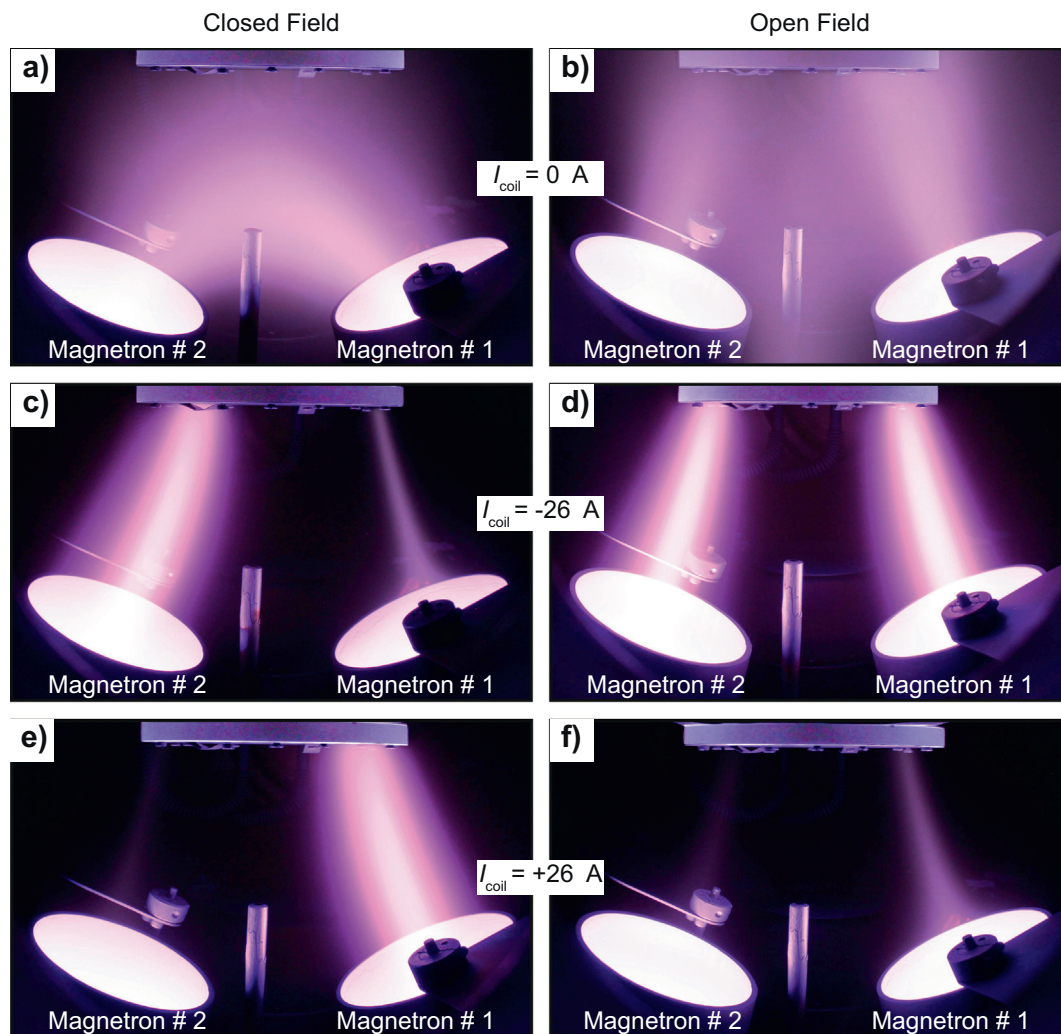


Fig. 2. Photographs of the plasma for different magnetron configurations and coil currents I_{coil} . The magnetrons were operated in a pure Argon atmosphere with conditions as described in Section 2.2. The photographs were taken with fixed aperture, shutter speed and ISO setting for comparability.

After transfer to the process chamber the samples were plasma cleaned by applying a 13.56 MHz RF bias of -75 V to the substrate holder for 2 minutes in an argon atmosphere. This was followed by a target cleaning step (3 minutes), to initially bring the target into its metallic state, and a target poisoning step (2 minutes), both performed with closed magnetron shutters. Depositions were carried out in the fully poisoned state with a flow of $\phi = \phi_{\text{Ar}} + \phi_{\text{N}_2} = 15$ sccm + 12 sccm, and the pumping speed was adjusted to obtain a pressure of approximately $5 \mu\text{bar}$.

To determine the working point in the fully poisoned state, a hysteresis curve was recorded and a nitrogen flow rate in the reactive mode well beyond the transition region was chosen.

The deposition time was kept constant at 120 minutes, and the substrate holder was left at floating potential. After deposition the target was again brought into its metallic state by an additional target cleaning step (3 minutes).

I–V data were also recorded at $t = 30$ min and $t = 90$ min during film deposition at the positions x_i , x_m and x_o with a Langmuir probe length $l_{\text{LP}} = 5$ mm, smaller than the width of the substrates (6 mm). One LP data acquisition cycle was performed within less than a minute. For the rest of the process the probe was retracted from the deposition chamber. Before each data acquisition cycle the probe was cleaned by application of a positive bias of 100 V, leading to electron bombardment and consecutive heating of the probe.

The deposition system is equipped with a substrate heater to vary

the temperature of the substrates during film growth. The temperature of the latter can, however, become considerably higher, if the plasma conditions lead to an additional energy influx to the sample surface. To calibrate the substrate surface temperature we used silicon wafer pieces with type K thermocouples attached to the surface facing the plasma. The thermocouples were attached with an electrically insulating and thermally conducting ceramic glue (Omega CC). Temperature measurements were performed at the locations x_i , x_m and x_o .

2.3. Thin film characterization techniques

The film thickness was measured with a stylus profiler (DektakXT, Bruker). The residual stress of the thin films was determined for the borosilicate glass samples using the Stoney equation and the radius of curvature, measured with a confocal microscope (DCM8, Leica) [21].

Atomic composition was determined by Rutherford Backscattering (RBS) with 2 MeV He for the Si substrates. Additionally, elastic recoil detection analysis (ERDA) with 13 MeV ^{127}I was used to refine the oxygen concentration. More details about the RBS and ERDA analysis are described elsewhere [22]. The crystalline texture was analyzed for the Si substrates by X-ray diffraction (XRD), set up in a symmetric $2\theta - \theta$ geometry with a parallel beam, using Cu $K\alpha$ radiation (D8, Bruker). A nickel filter was used to eliminate the Cu $K\beta$ radiation.

SEM micrographs of the film cross sections were taken for the Si substrates to analyze the growth morphology. The SEM (Hitachi, S-

4800) was operated at 1 keV and a magnification of 60×10^3 .

3. Results and discussion

3.1. Plasma characterization

The CF and OF setup are displayed in Fig. 1. For the CF case the arrangements of the magnets of magnetrons #1 and #2 are antisymmetric to each other, leading to closed field lines between the magnetrons. For the symmetric OF case the magnets of both magnetrons have the same orientation. This results in parallel magnetic field lines in the region between the magnetrons and the substrate holder (called far field region in the following). In our specific setup the far field of magnetron #2 is parallel to the field generated by the coil for negative currents for the OF and CF configuration. For magnetron #1 this is true for the OF configuration only, since its magnets are reversed in the CF configuration and its far field then becomes anti-parallel to \vec{B}_{coil} for $I_{\text{coil}} < 0$ (colored arrows).

Fig. 2 displays photographs of the plasma for different operating conditions. Panels a) and b) show the plasma without an additional applied field for the CF and OF configuration, respectively. The bright areas indicate regions of high plasma density, and their geometry resembles that of the field lines (Fig. 1). Panels c), d), e) and f) show the plasma in an applied field. For $I_{\text{coil}} = -26$ A the applied field is parallel to the far field of magnetron #2 for the CF configuration, and parallel to both magnetrons for the OF configuration (Fig. 1). The plasma then extends from the magnetron(s) to the substrate. In the closed field configuration the plasma of magnetron #1 remains localized at the magnetron. For $I_{\text{coil}} = +26$ A the applied field is now parallel only to the far field of magnetron #1 for the CF configuration.

3.1.1. Ion saturation current and floating potential measured with the substrate holder

For magnetron sputtering the floating potential (V_{float}) of the substrate and the ion saturation current (I_{sat}) flowing into the substrate are often used for plasma characterization.

The floating potential is related to the plasma potential (V_p) as

$$V_{\text{float}} = V_p + \frac{k_B T_e}{e} \ln \left[0.61 \sqrt{2\pi \frac{m_e}{m_i}} \right], \quad (1)$$

where T_e is the electron temperature, k_B is the Boltzmann constant, e is the elementary charge, and m_i and m_e are the ion and electron mass, respectively.

The ion saturation current is given by

$$I_{\text{sat}} = 0.61 \int_{A_{\text{probe}}} n_{i0} \sqrt{\frac{k_B T_e}{m_i}} dA \quad (2)$$

where n_{i0} is the ion density of the plasma (without mutual perturbations arising from the presence of the measurement probe), and the integral is carried out over the entire probe area (A_{probe}) [23].

In this study, we use these quantities to characterize the dependence of the plasma state on the coil current in the closed field and open field configuration, and for single and dual magnetron operation.

Fig. 3 displays the measurement results for the floating potential and the ion saturation current as a function of coil current. Data was taken for single and dual magnetron operation, and in OF and CF configuration. Both, V_{float} and I_{sat} , were measured with the substrate holder as an electrical probe.

First we discuss the results obtained for the operation of a single magnetron (#2, Fig. 1). For increasing negative coil currents, V_{float} saturates at approximately -18 V. For positive coil currents, V_{float} becomes less negative and rises to about -7 V. The additional magnetic field generated by the coil does not significantly affect the discharge current and voltage of the magnetrons. Therefore the electron temperature, which is given by the local plasma conditions at the

magnetron, remains unaffected, and we conclude from Eq. (1) that V_p drops together with V_{float} for increasing coil currents.

The ion saturation current remains small for positive coil currents (c), in agreement with the visual appearance of the plasma at magnetron #2 for positive coil currents (Fig. 2 e), f). For increasing negative coil currents I_{sat} rises and then saturates at about 25 mA. The difference between the OF and CF setup is minute, indicating that \vec{B}_{coil} dominates the fields arising from the interactions of the magnetrons in both configurations.

Panels b) and d) of Fig. 3 show the results for dual magnetron operation. The dependence of V_{float} on I_{coil} for the OF configuration is the same as that obtained during single magnetron operation (a), open symbols). The same is observed for the CF configuration for negative coil currents. However, for positive coil currents V_{float} is dominated by magnetron #1 with its far field then parallel to that of the coil. Consequently the dependence of V_{float} is symmetric with respect to the current direction. The symmetric behavior of the CF configuration is also observed for the ion saturation current (d), filled circles). In the OF configuration I_{sat} is doubled in every point compared to the single magnetron operation (c), open symbols). This increased current becomes apparent from Fig. 2 d) showing the extension of the plasma of each magnetron at the substrate holder, and Eq. (2) relating the ion saturation current to an integration over the substrate holder area.

The results demonstrate that with the field generated by the coil, I_{sat} can be varied by more than one order of magnitude. The consequences for the film growth will be discussed in Section 3.2. However, panels b) and d) in Fig. 2 show that the plasma density depends on the position on the substrate holder, which prevents a homogeneous deposition over a wide area of the substrate holder. At the same time, it provides us with the opportunity to deposit samples simultaneously under different plasma conditions. With our position-dependent measurement of the plasma conditions a correlation of plasma parameters and films properties becomes possible.

3.1.2. Ion and energy flux distributions

The photographs of the plasma shown in Fig. 2 suggest that the spatial distribution of the ion current density, and with it the energy flux provided by the plasma, is localized near the outer rim of the substrate holder ($\pm x_0$) for $I_{\text{coil}} = -26$ A.

The ion current density distribution and the total energy flux density for $x > 0$ (above magnetron #1), while powering both magnetrons in the closed field configuration, are shown in Fig. 4 a). As expected both show nearly Gaussian distributions with centers on the outer part of the substrate holder and almost identical widths. The small differences of the center position of the two distributions is believed to arise from the limited precision of the linear positioner and from the size of the probes. For $I_{\text{coil}} = 15$ A, the ion current density is reduced to about half of that obtained at $I_{\text{coil}} = 26$ A, and the centers position is shifted slightly towards the center of the substrate holder. For negative coil currents the ion current density becomes smaller than 2 mA m^{-2} .

The dependence of the ion current density on the coil current at position $x = 3$ cm is displayed in Fig. 4 b). For $I_{\text{coil}} > 0$ the ion current density increases rapidly, whereas it remains small for negative I_{coil} . This is consistent with the results of the ion saturation current data shown in Fig. 3 c). Note that the Langmuir and thermal probe measurements are performed above magnetron #1, whereas the ion saturation current measurements shown in Fig. 3 c) were performed operating magnetron #2 that has the opposite polarity than magnetron #1 for the closed field configuration. For this reason the dependence on the direction of the coil current is reversed.

The partial energy flux density from ions impacting on the electrically floating substrate (J_{ions} in W m^{-2}) is given by

$$J_{\text{ion}} = E_{\text{ion}} j_{\text{ion}}, \quad (3)$$

where j_{ion} is the ion flux in $\text{s}^{-1} \text{ m}^{-2}$ and $E_{\text{ion}} = e \cdot (V_p - V_{\text{float}})$ the ion

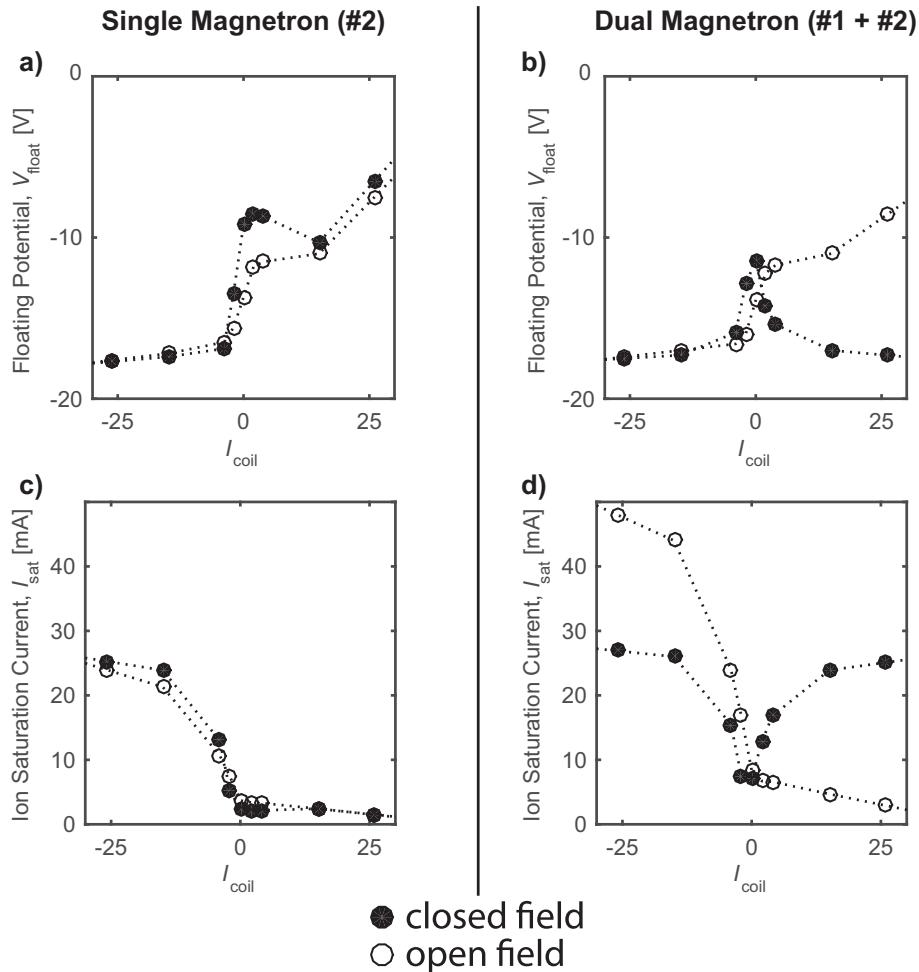


Fig. 3. Ion saturation current and floating potential as a function of the current in the coil for open field and closed field configuration. Here, the substrate holder was used as an electrical probe. Graphs a) and c) show the results of measurements performed powering a single magnetron. Note that in both cases magnetron #2 was used, which has the same magnetic arrangement for both configurations. Graphs b) and d) show the results of measurements where both magnetrons were powered simultaneously.

energy [24]. With the measured ion current density $j_p = j_{ion} \cdot e$ Eq. (3) becomes

$$J_{ion} = j_p (V_p - V_{float}), \tag{4}$$

where V_p and V_{float} are the measured plasma and floating potentials. We find that the ratio of J_{ion} to the total energy flux density (J_{tot} in $W\ m^{-2}$) is smaller than 0.1 for all data points. Hence, we conclude that most of the energy flux arises from electrons, radiation, and neutral atoms hitting the substrate [25].

3.2. Dependence of film properties on plasma parameters and temperature

The maximum achieved ion saturation current measured over the entire substrate holder is two times higher for the open field configuration than for the closed field configuration (see Fig. 3 d)). For applications where a high sample throughput or the use of different target materials requires a rotation of the substrate holder the open field configuration is more attractive, and we therefore choose this configuration for the depositions.

Aluminum nitride thin films were grown by reactive sputtering in the open field configuration with two magnetrons, each operated at 200 W constant power. All depositions lasted 120 min, and the substrate holder was left floating. The samples were clamped onto the substrate holder, which results in a rather high thermal resistance between them. The actual sample temperature can thus be different from that of the

substrate holder. Therefore the sample temperatures arising from the sputter process were determined for all sample position and conditions in separate sputtering experiments. The ion current densities were measured at $t = 30$ min and $t = 90$ min during the thin film deposition by moving the Langmuir probe to the corresponding positions. Measuring at all three positions consecutively took less than 1 minute. Further details on the deposition conditions, Langmuir and temperature measurements are described in Section 2.2.

Table 1 shows the temperatures and ion current densities obtained at the three sample positions for the different deposition conditions. With the heater turned off, a sample temperature of 259 °C was found at the position x_o for $I_{coil} = -24$ A, where the highest ion current density of 74 $A\ m^{-2}$ was obtained. A significant increase of the sample temperature to 349 °C was also observed at x_o , with a substrate heater setpoint of 250 °C.

The ion current densities vary about a factor of two across the substrate holder for $I_{coil} = 0$ A. For larger coil currents a substantial spatial variation of the temperatures and ion current densities across the substrate holder is observed. Those observations are compatible with the visual appearance of the plasma depicted in Fig. 2 b) and d).

We found that the dependence of the total energy flux and ion current density on the x-position is comparable to that measured for the closed field configuration (Fig. 4 a)), but that the position and the value of the maximum ion current density is slightly different. The position x_o matches with the maximum of the ion current density distribution of

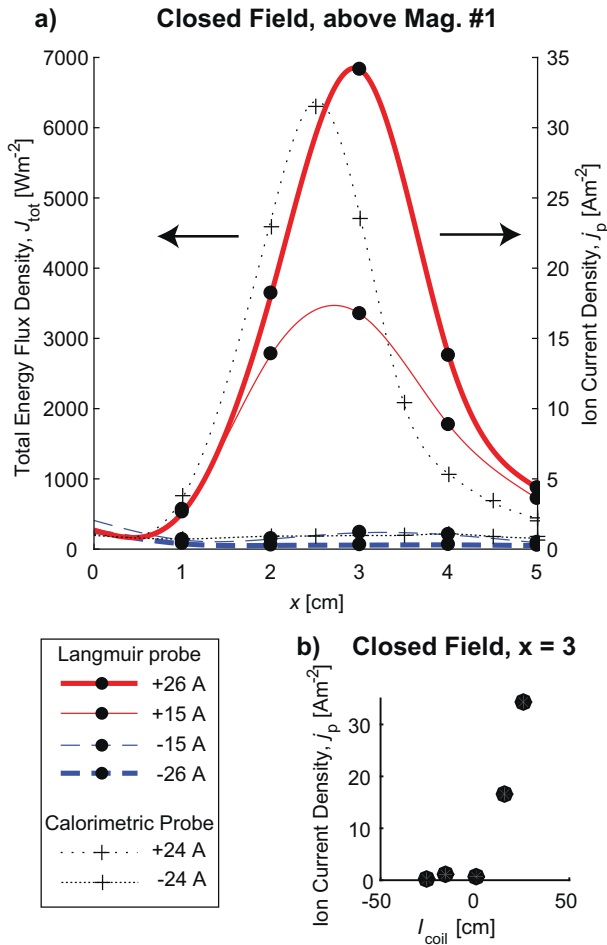


Fig. 4. Panel a) shows the total energy flux density (crosses, left axis) and ion current density (bullets, right axis) as a function of the x-position in the closed field configuration for various coil currents. The measurements were performed above magnetron #1 with the calorimetric and Langmuir probe. Panel b) shows the ion current density as a function of the coil current at position $x = 3$.

the open field configuration.

The film thicknesses were all in the range of 770 ± 100 nm, with a correlation between increasing film thickness and target consumption (race track depth). No dependence on the substrate temperature or on the ion current density was observed. From the latter we conclude that the applied magnetic field changes the ion to neutral ratio, while the flux of film-forming atoms to the substrate remains constant.

All films showed a stoichiometric AlN composition with a metal to non-metal ratio of 1:1. The oxygen content was below 2 at%. The argon concentration was found to be smaller than 0.07 at% for all films, independent of the ion flux density.

To analyze the dependence of the film properties on the different conditions observed at the sample positions x_i , x_m and x_o , the residual stress σ and XRD-diffractograms were measured for all samples, and the cross sections of selected samples were inspected.

Fig. 5 a) displays the dependence of the residual stress on the sample temperature for the position x_i (open circles), x_m (open squares), and x_o (open stars), respectively, without an external field ($I_{coil} = 0$). The residual stress of the films was found to depend on the ion current density, but not on the substrate temperature: The residual stress changes from 0.7 GPa (tensile) to -0.3 GPa, and -1.8 GPa (compressive) with the ion current densities of 2.5 A m^{-2} , 3.9 A m^{-2} and 5.5 A m^{-2} for the positions x_i , x_m and x_o respectively. The fact that the stress is independent of the sample temperature (for the temperature range covered here) can be attributed to the low homologous temperature. The

Table 1

Sample temperature (T) and ion current density (j_p) at the sample positions x_i , x_m and x_o for different experimental conditions. The letters in parentheses indicate the corresponding samples presented in Fig. 7.

Heater Setpoint	I_{coil} [A]	Position	T [°C]	j_p [A m^{-2}]
Heater Off	0	x_i (a)	108	2.4
		x_m	108	4
		x_o	108	5.9
	-12	x_i	141	2.7
		x_m	165	6.3
		x_o	245	56
140°C	-24	x_i (d)	145	1.5
		x_m (e)	171	6.4
		x_o (f)	259	74
	0	x_i	187	2.5
		x_m	187	4
		x_o	187	5.7
250°C	0	x_i (b)	250	2.5
		x_m	250	4.0
		x_o	250	5.7
	-12	x_i	-	-
		x_m	-	-
		x_o	-	-
500°C	-24	x_i	275	2.6
		x_m	312	6.3
		x_o	349	72
	0	x_i (b)	500	2.3
		x_m	500	3.7
		x_o	500	5.2

latter is defined as the deposition temperature normalized by the melting temperature of the deposited film material, and is smaller than 0.3 for all deposition temperatures used here.

Fig. 5 b) depicts the dependence of the residual stress σ on the ion current density j_p for all deposited samples. The residual stress changes linearly from 0.9 GPa (tensile) to -1.93 GPa (compressive) for $0 \leq j_p \leq 7 \text{ A m}^{-2}$ with

$$\sigma(j_p) = a \cdot j_p + b \quad (5)$$

and

$$\begin{aligned} a &= (-0.47 \pm 0.13) \text{ GPa m}^2 \text{ A}^{-1} \\ b &= (+1.56 \pm 0.6) \text{ GPa}. \end{aligned} \quad (6)$$

For larger ion current densities, $7 \text{ A m}^{-2} \leq j_p \leq 75 \text{ A m}^{-2}$, the compressive residual stress increases at a lower rate to about -4 GPa with

$$\begin{aligned} a &= (-0.03 \pm 0.15) \text{ GPa m}^2 \text{ A}^{-1} \\ b &= (-1.49 \pm 9.9) \text{ GPa}. \end{aligned} \quad (7)$$

The dashed lines show the linear fits to the data points.

The dependence of the residual stress and the ion energy on the ion current density appear to be correlated (see Fig. 5 b) and c)). The ion energy was calculated as for Eq. (4) and increases linearly from 10 eV to 18 eV for $0 \leq j_p \leq 7 \text{ A m}^{-2}$ with

$$E_{ion}(j_p) = c \cdot j_p + d \quad (8)$$

and

$$\begin{aligned} c &= (+1.6 \pm 0.3) \text{ eV m}^2 \text{ A}^{-1} \\ d &= (+6.8 \pm 1.3) \text{ eV}. \end{aligned} \quad (9)$$

For ion current densities above 7 A m^{-2} it reaches a saturation at 22 eV. The intersection between the dashed lines indicate a change of slope at an ion current density of 10 A m^{-2} , close to that observed for the dependence of the residual stress on ion current density. This suggests that the steep decrease in residual stress for $0 \leq j_p \leq 7 \text{ A m}^{-2}$ can be attributed to an increase in both, the ion energy and the number of impacting ions (corresponding to an increasing ion current density). For higher ion current densities only the number of impacting ions changes and the decrease in residual stress becomes less steep.

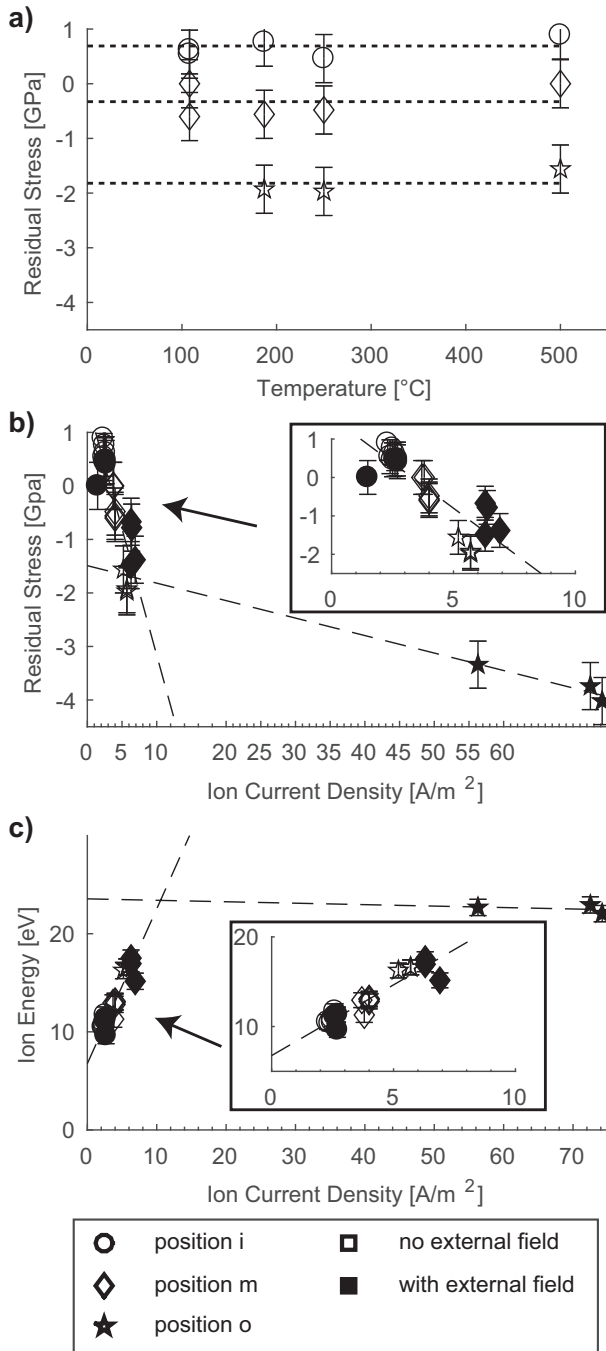


Fig. 5. Dependence of the residual stress on temperature (a) and ion current density (b). Graph c) shows the dependence of the ion energy ($E_{ion} = V_p - V_f$) on the ion current density. The dashed lines are linear fits to selected data points.

Our observations regarding the residual stress are in accordance with results from other groups. A change from tensile to compressive stress is commonly observed with increasing bombardment by energetic particles (neutrals or ions) for sputtered thin films [10,17]. This behavior is also found for the case of AlN depositions when the pressure, bias potential or the N₂/Ar ratio is varied in order to change the bombardment of the growing film [17, 18, 26, 27]. However, variation of the before mentioned parameters might entail changes in other process parameters (i.e. IV-characteristics) or film composition (i.e. argon incorporation), which can be excluded in our work.

To study the crystallinity of the films XRD measurements were

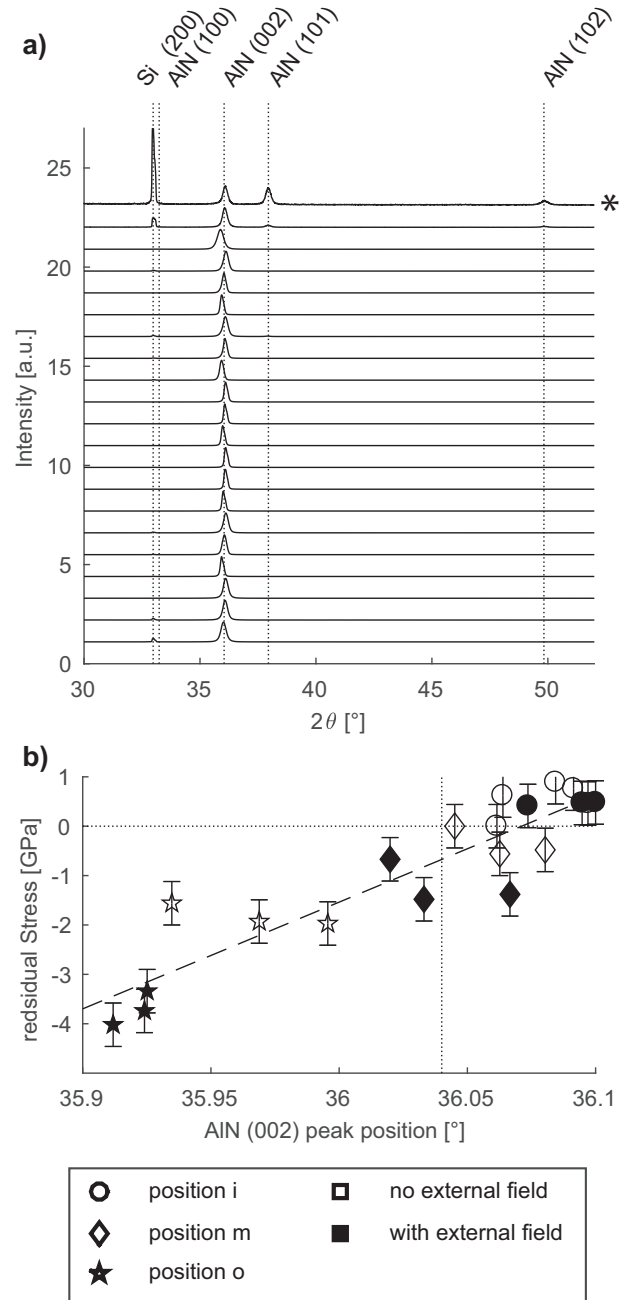


Fig. 6. Panel a) shows normalized XRD spectra of samples deposited under the conditions listed in Table 1 and are presented in the same order as therein. The sample at position x_i (position of lowest energy influx) deposited with the heater and the coil switched off (see Table 1) is marked by the *. The dotted lines indicate the peak position of Si and hexagonal wurtzite [33,34]. Panel b) shows the residual stress measured on the borosilicate glass samples plotted versus the AlN (002) peak position obtained from the $2\theta - \theta$ scans of the silicon samples. The dashed line shows the linear fit to the data, and the dotted lines indicate 0 residual stress and the AlN (002) peak position from literature respectively.

performed. The $2\theta - \theta$ scans, shown in Fig. 6 a), revealed that all films exhibit only the hexagonal wurtzite structure. In combination with rocking curves it was found that the c-axis is oriented perpendicular to the sample surface, except for the sample at position x_i (position of lowest energy influx, marked by the * in Fig. 6 a)) deposited with the heater and the coil switched off (see Table 1). This specific sample shows several XRD peaks of considerable intensity in the $2\theta - \theta$ scan which can be attributed to other planes of the AlN wurtzite phase,

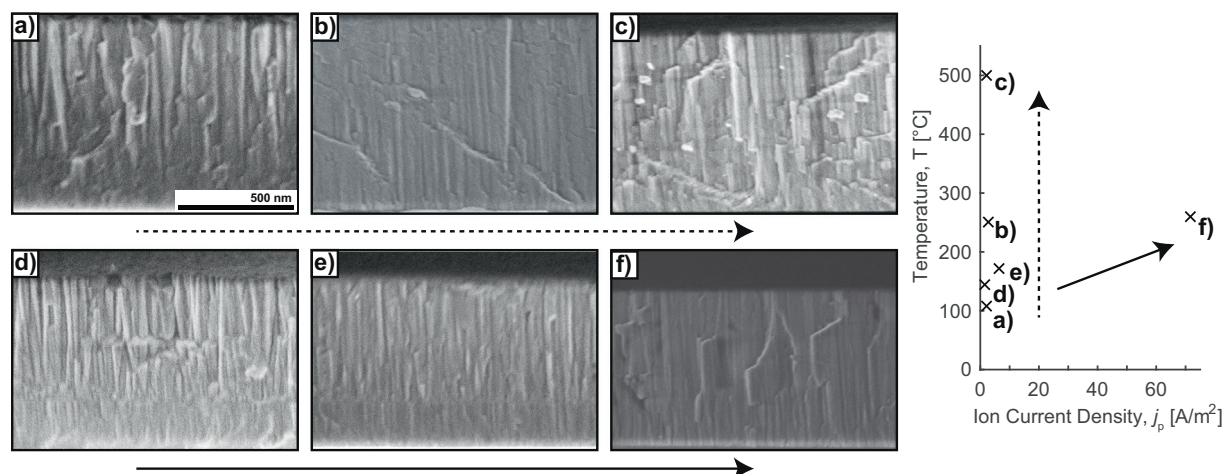


Fig. 7. Cross section morphology of selected samples imaged by SEM. Samples a), b) and c) were exposed to almost identical ion current densities but deposited at different temperatures. For the images d)–f) the ion current density increases, which is accompanied by a change in the substrate temperature because of the plasma heating. The values corresponding to the different deposition conditions are plotted in the graph on the right side, and are also listed in Table 1.

indicating that the preferential (001) orientation is lost. A pole figure analysis of a selected sample (sample f) in Fig. 7) showed the fibre texture typical for polycrystalline AlN. The (002) texture is commonly observed in literature for AlN thin films deposited by magnetron sputtering [28–31]. For a detailed discussion about the influence of the growth conditions on the texture we refer to previous work [32].

Fig. 6 b) shows the residual stress measured on the borosilicate glass samples plotted versus the AlN (002) peak position obtained from the $2\theta - \theta$ scans of the silicon samples. An in plane compressive stress of a thin film leads to a shift towards lower angles of the peak position, which is reflected by the negative slope of the data-fit (dashed line). The data-fit crosses the 0 residual stress line almost at the position of the literature value for the AlN (002) peak (dotted vertical line) confirming the good agreement of the data obtained by the different techniques and on different substrates.

Fig. 7 shows film cross sections of selected samples, where different growth morphologies can be observed. Panels a) to c) show samples grown at different temperatures and low ion current densities ($< 2.5 \text{ A m}^{-2}$). They exhibit well-oriented elongated crystalline grains with pronounced grain boundary contrast. This morphology is compatible with open grain boundaries leading to tensile film stress observed at low ion current densities (see Fig. 5 b)). The growth morphology is not affected by the temperatures used within this study, which is compatible with the residual stress that was also found to remain constant for these conditions. Panels d) to f) show the evolution of the morphology with increasing ion current density. At an ion current density of 1.5 A m^{-2} a film morphology similar to those visible in panels a) to c) is observed. For higher ion current densities (e) and f)) a vanishing grain boundary contrast is observed. This indicates an increase of the film density, and is compatible with the observed transition from tensile to compressive film stress with increasing ion current densities (Fig. 5 b)). Because the growth morphology did not change at increased temperatures, the observed densification at higher ion flux can be solely attributed to the change in ion bombardment. The above presented observations are in agreement with the extended structure zone diagram proposed by André Anders [1]. The observed transitions in the stress state and growth morphology are compatible with the transition from zone 1 to zone T with the pathway along the normalized energy axis.

4. Conclusion

An in-situ coil installed in a confocal magnetron sputtering system was used to tune the ion-to-neutral ratio by a factor of 30. Our present experimental setup did, however, not permit a homogeneous ion flux

over the whole area of the substrate holder. Yet, for an experimental deposition system this inhomogeneity can be advantageous, because it allows the simultaneous deposition of samples exposed to different plasma conditions, and hence a study of the film properties on the plasma parameters, in a single run.

The stress of the deposited AlN films changes from 0.9 GPa (tensile) to -4 GPa (compressive), with increasing ion flux density, but was found to be independent on the sample temperature between $100 \text{ }^\circ\text{C}$ and $500 \text{ }^\circ\text{C}$. All films showed a (001)-texture with columnar grains. The observed evolution from an open to a closed grain boundary morphology with increasing ion flux is compatible with the observed stress evolution. From this we conclude that a well-designed magnetic field generated by a coil is an experimental parameter that allows a precise control of the film properties in a confocal magnetron sputtering system.

Acknowledgments

Support from the Swiss National Science Foundation (project Nr. 200021_150095), and Empa is hereby gratefully acknowledged. We thank S.M. Vranjkovic for designing the in-situ coil and the Langmuir probe holder, and for his help in installing these systems in our sputter deposition chamber.

We thank Max Döbeli from the Laboratory for Ion Beam Physics of ETHZ for the ERDA and RBS measurements and analysis, as well as Erwin Hack from the Laboratory for Transport at Nanoscale Interfaces at Empa for the ellipsometry measurements and the helpful discussions.

References

- [1] A. Anders, A structure zone diagram including plasma-based deposition and ion etching, *Thin Solid Films* 518 (15) (2010) 4087–4090, <http://dx.doi.org/10.1016/j.tsf.2009.10.145>.
- [2] A. Anders, *Handbook of Plasma Immersion Ion Implantation and Deposition*, Wiley, 2000.
- [3] T. Itoh, *Ion Beam Assisted Film Growth*, Elsevier B.V., 1989.
- [4] M. Nastasi, M. Wolfhard, W. Ensinger, Ion implantation and thin-film deposition, in: A. Anders (Ed.) *Handb. Plasma Immers. Ion Implant. Depos.*, in: Wiley, 2000, pp. 125–242.
- [5] I. Petrov, F. Adibi, J.E. Greene, L. Hultman, J.-E. Sundgren, Average energy deposited per atom: a universal parameter for describing ionassisted film growth? *Appl. Phys. Lett.* 63 (1) (1993) 36–38, <http://dx.doi.org/10.1063/1.109742>.
- [6] I. Petrov, L. Hultman, U. Helmerson, J.-E. Sundgren, J. Greene, Microstructure modification of TiN by ion bombardment during reactive sputter deposition, *Thin Solid Films* 169 (2) (1989) 299–314, [http://dx.doi.org/10.1016/0040-6090\(89\)90713-X](http://dx.doi.org/10.1016/0040-6090(89)90713-X).
- [7] O. Baranov, K. Bazaka, H. Kersten, M. Keidar, U. Cvelbar, S. Xu, I. Levchenko, Plasma under control: advanced solutions and perspectives for plasma flux

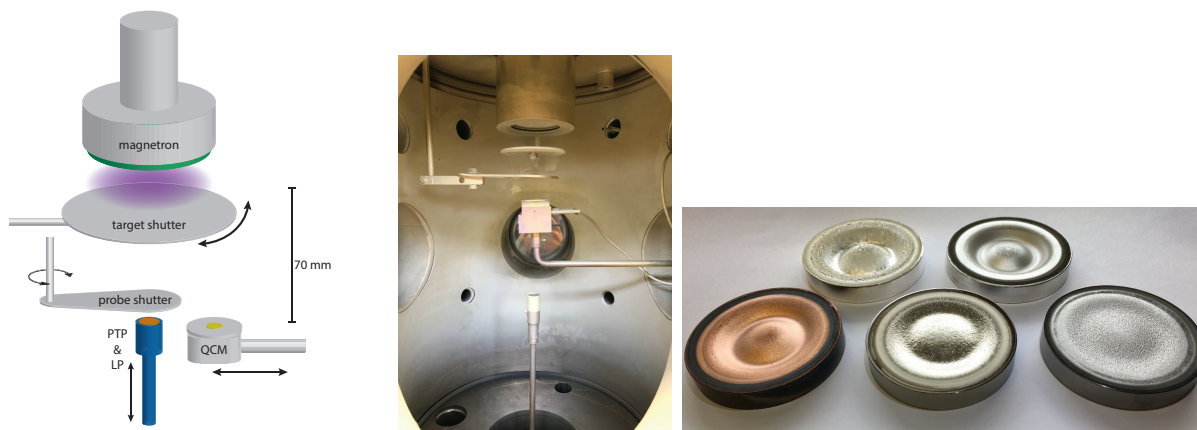
- management in material treatment and nanosynthesis, *Appl. Phys. Rev.* 4 (4) (2017) 041302, <http://dx.doi.org/10.1063/1.5007869>.
- [8] I. Petrov, F. Adibi, J.E. Greene, W.D. Sproul, W. Münz, Use of an externally applied axial magnetic field to control ion/neutral flux ratios incident at the substrate during magnetron sputter deposition, *J. Vac. Sci. Technol. A Vacuum, Surfaces, Film.* 10 (5) (1992) 3283–3287, <http://dx.doi.org/10.1116/1.577812>.
- [9] C. Engström, T. Berlind, J. Birch, L. Hultman, I. Ivanov, S. Kirkpatrick, S. Rohde, Design, plasma studies, and ion assisted thin film growth in an unbalanced dual target magnetron sputtering system with a solenoid coil, *Vacuum* 56 (2) (2000) 107–113, [http://dx.doi.org/10.1016/S0042-207X\(99\)00177-3](http://dx.doi.org/10.1016/S0042-207X(99)00177-3).
- [10] J. Musil, Flexible hard nanocomposite coatings, *RSC Adv.* 5 (74) (2015) 60482–60495, <http://dx.doi.org/10.1039/C5RA09586G>.
- [11] E. Lewin, D. Loch, A. Montagne, A.P. Ehiasarian, J. Patscheider, Comparison of AlSiN nanocomposite coatings deposited by HIPIMS and DC magnetron sputtering, *Surf. Coatings Technol.* 232 (2013) 680–689, <http://dx.doi.org/10.1016/j.surfcoat.2013.06.076>.
- [12] M. Akiyama, T. Kamohara, K. Kano, A. Teshigahara, Y. Takeuchi, N. Kawahara, Enhancement of piezoelectric response in scandium aluminum nitride alloy thin films prepared by dual reactive cosputtering, *Adv. Mater.* 21 (5) (2009) 593–596, <http://dx.doi.org/10.1002/adma.200802611>.
- [13] M.-A. Dubois, P. Mural, Properties of aluminum nitride thin films for piezoelectric transducers and microwave filter applications, *Appl. Phys. Lett.* 74 (20) (1999) 3032–3034, <http://dx.doi.org/10.1063/1.124055>.
- [14] R. Elfrink, T.M. Kamel, M. Goedbloed, S. Matova, D. Hohlfeld, Y. van Andel, R. van Schaijk, Vibration energy harvesting with aluminum nitride-based piezoelectric devices, *J. Micromech. Microeng.* 19 (9) (2009) 094005, <http://dx.doi.org/10.1088/0960-1317/19/9/094005>.
- [15] J. Bjurström, V. Yantchev, M. Moreira, I. Katardjiev, Efficient RF voltage transformer with bandpass filter characteristics, *Electron. Lett.* 49 (3) (2013) 198–199, <http://dx.doi.org/10.1049/el.2012.3982>.
- [16] M. a. Moreira, T. Törndahl, I. Katardjiev, T. Kubart, Deposition of highly textured AlN thin films by reactive high power impulse magnetron sputtering, *J. Vac. Sci. Technol. A Vacuum, Surfaces, Film.* 33 (2) (2015) 021518, <http://dx.doi.org/10.1116/1.4907874>.
- [17] M.-A. Dubois, P. Mural, Stress and piezoelectric properties of aluminum nitride thin films deposited onto metal electrodes by pulsed direct current reactive sputtering, *J. Appl. Phys.* 89 (11) (2001) 6389–6395, <http://dx.doi.org/10.1063/1.1359162>.
- [18] S. Fichtner, T. Reimer, S. Chemnitz, F. Lofink, B. Wagner, Stress controlled pulsed direct current co-sputtered Al $1 \times$ Sc \times N as piezoelectric phase for micro-mechanical sensor applications, *APL Mater.* 3 (11) (2015) 116102, <http://dx.doi.org/10.1063/1.4934756>.
- [19] B. Window, N. Savvides, Charged particle fluxes from planar magnetron sputtering sources, *J. Vac. Sci. Technol. A Vacuum, Surfaces, Film.* 4 (2) (1986) 196–202, <http://dx.doi.org/10.1116/1.573470>.
- [20] R. Wiese, H. Kersten, G. Wiese, R. Bartsch, Energy influx measurements with an active thermal probe in plasma-technological processes, *EPJ Tech. Instrum.* 2 (1) (2015) 2, <http://dx.doi.org/10.1140/epjti/s40485-015-0013-y>.
- [21] M. Ohring, *Materials Science of Thin Films*, Elsevier Science, 2001.
- [22] D.A. Jaeger, Interface Investigations on Titanium Nitride Bilayer Systems, Ph.D. thesis (2012) <http://infoscience.epfl.ch/record/181534http://dx.doi.org/10.5075/epfl-thesis-5509>.
- [23] A. Piel, *Plasma Physics*, vol. 1, Springer Berlin Heidelberg, Berlin, Heidelberg, 2010, pp. 1689–1699, <http://dx.doi.org/10.1007/978-3-642-10491-6>.
- [24] K.M. Pollock, T. Kaufman-Osborn, J. Hiltrop, J.R. Doyle, Effects of temperature and near-substrate plasma density on the structural and electrical properties of DC sputtered germanium thin films, *J. Vac. Sci. Technol. A Vacuum, Surfaces, Film.* 29 (5) (2011) 051301, <http://dx.doi.org/10.1116/1.3607410>.
- [25] H. Kersten, H. Deutsch, H. Steffen, G. Kroesen, R. Hippler, The energy balance at substrate surfaces during plasma processing, *Vacuum* 63 (3) (2001) 385–431, [http://dx.doi.org/10.1016/S0042-207X\(01\)00350-5](http://dx.doi.org/10.1016/S0042-207X(01)00350-5).
- [26] G. Este, W.D. Westwood, Stress control in reactively sputtered AlN and TiN films, *J. Vac. Sci. Technol. A Vacuum, Surfaces, Film.* 5 (4) (1987) 1892–1897, <http://dx.doi.org/10.1116/1.574480>.
- [27] F. Medjani, R. Sanjinés, G. Allidi, A. Karimi, Effect of substrate temperature and bias voltage on the crystallite orientation in RF magnetron sputtered AlN thin films, *Thin Solid Films* 515 (1) (2006) 260–265, <http://dx.doi.org/10.1016/j.tsf.2005.12.145>.
- [28] J. Lin, R. Chistyakov, C-axis orientated AlN films deposited using deep oscillation magnetron sputtering, *Appl. Surf. Sci.* 396 (2017) 129–137, <http://dx.doi.org/10.1016/j.apsusc.2016.11.025>.
- [29] A. Pelisson, M. Parlinska-Wojtan, H. Hug, J. Patscheider, Microstructure and mechanical properties of AlSiN transparent hard coatings deposited by magnetron sputtering, *Surf. Coatings Technol.* 202 (4-7) (2007) 884–889, <http://dx.doi.org/10.1016/j.surfcoat.2007.05.094>.
- [30] C. Duquenne, P.Y. Tessier, M.P. Besland, B. Angleraud, P.Y. Jouan, R. Aubry, S. Delage, M.A. Djouadi, Impact of magnetron configuration on plasma and film properties of sputtered aluminum nitride thin films, *J. Appl. Phys.* 104 (6) (2008) 063301, <http://dx.doi.org/10.1063/1.2978226>.
- [31] M. Ishihara, S. Li, H. Yumoto, K. Akashi, Y. Ide, Control of preferential orientation of AlN films prepared by the reactive sputtering method, *Thin Solid Films* 316 (1-2) (1998) 152–157, [http://dx.doi.org/10.1016/S0040-6090\(98\)00406-4](http://dx.doi.org/10.1016/S0040-6090(98)00406-4).
- [32] A. Pelisson, Al-Si-N Transparent Hard Nanostructured Coatings, Ph.D. thesis University of Basel, 2009, https://edoc.unibas.ch/1000/1/Dissertation-Pelisson_Volltext_Unibas09.pdf.
- [33] H. Schulz, K.H. Thiemann, Crystal structure refinement of AlN and GaN, *Solid State Commun.* 23 (11) (1977) 815–819, [http://dx.doi.org/10.1016/0038-1098\(77\)90959-0](http://dx.doi.org/10.1016/0038-1098(77)90959-0).
- [34] D.M. Többsen, N. Stüßer, K. Knorr, H.M. Mayer, G. Lampert, E9: the new high-resolution neutron powder diffractometer at the Berlin neutron scattering center, *Mater. Sci. Forum*, vol. 378, Trans Tech Publ, 2001, pp. 288–293.

Publication III

Experimentally unraveling the energy flux originating from a DC magnetron sputtering source

Authors	S. Gauter, F. Haase and H. Kersten
Journal	Thin Solid Films (submitted)
Technique	DC magnetron sputtering (DCMS)
Utilized Probes	Passive thermal probe (PTP), Quartz crystal microbalance (QCM), Langmuir probe (LP)
Own contribution	approx. 50%

Experimental Setup:



Motivation:

This work concludes an extensive investigation of the contributions to the energy flux in a DC magnetron sputtering system. Since the calorimetric measurement method provides an integral value of the energy flux, it is of specific importance to understand the different contributions which are included. These contributions are in no way universally comparable and change strongly depending on the combination of target material and background gas. The idea of this study is to provide results for a wide range of combinations and, thus, create a ground for extrapolation into other systems.

Main results:

Combining different diagnostics and simulation results, allowed to gain insights into the contributions to the integral energy flux in a variety of target process gas systems. Three contributions were identified which can dominate the energy flux to a floating substrate: For combinations which produce a high sputter rate the highest energy flux is created by

the condensation and kinetic impact of the sputtered atoms. If the mass ratio between process gas and target atoms is very small, a high amount of ions is reflected from the target and results in a dominating contribution from reflected neutrals in the energy flux. For materials which have a low thermal conductivity such as titanium, the target heats up to high temperatures and creates a dominant energy flux by radiation.

Experimentally unraveling the energy flux originating from a DC magnetron sputtering source

Sven Gauter¹, Fabian Haase¹, and Holger Kersten¹

¹Institute of Experimental and Applied Physics, Kiel University, Kiel, Germany

Abstract

We present investigations of the energy flux in DC magnetron sputtering for 15 different target-gas combinations. The utilized gases were Ar, Kr and He which were studied using targets made of Ag, Al, Cu, Ti and W. The effect of parameter variations (distance, pressure and discharge power) was investigated by calorimetric measurements utilizing a passive thermal probe. For the variation of discharge power, supplementary measurements of plasma parameters and deposition rate were performed using a planar Langmuir probe and a quartz crystal microbalance. The obtained results were used to gain better insight into the different contributions to the integral energy flux. The measurements illustrate clearly that, depending on the target material and on the target gas combination, the main mechanisms generating the energy flux can vary dramatically. For small gas-target mass ratios, reflected neutrals were identified as the main contribution of the energy flux while for combinations with high sputter yield, condensation and kinetic impact of sputtered particles were found to be the most relevant. For thermally poor conducting targets as in the case of titanium, the target can heat up significantly resulting in a strong energy flux from heat radiation which dominates the otherwise modest energy flux.

1 Introduction

One of the major applications present in the large field of plasma technology are plasma-wall interactions such as etching, film deposition and surface modification. In these processes, thermal conditions at the substrate surface are of key interest since they play a dominant role in the final properties of the product. The surface temperature influences elementary processes like adsorption, desorption, diffusion as well as chemical processes like chemical sputtering and surface reactions [1–3]. Especially in the case of thin-film deposition the morphology and stoichiometry of the layers are highly dependent on the thermal surface conditions and on the impact of kinetic particles [1, 4, 5]. As a widespread thin-film deposition technique, magnetron sputtering has been thoroughly investigated and over the years many variations such as reactive sputtering, pulsed DC or high-power im-

pulse magnetron sputtering (HiPIMS) have been developed. In spite of these new developments, the classic metal deposition using DC magnetron sputtering systems is still of high relevance to research and industry alike. Starting from the well noted study by Thornton in 1978 [6] many investigations of the energy flux in these systems have been performed resulting in extensive literature on the topic. Since calorimetric probes provide energy and time integrated values which include a complex mix of different contributions (e.g. from charged particles, neutrals, surface processes, radiation etc.), a persistent point of discussion is the distinction between the several contributions to the integral energy flux. An approved method to obtain more detailed information is the combination of calorimetric measurements with Langmuir probe (LP) and deposition rate measurements. The determined values can be combined to give a simple model of the energy flux and also al-

low the normalization of the measured energy flux on the amount of deposited atoms. Thornton et al. used this procedure in a subsequent study [7] investigating various materials in cylindrical-post and planar magnetron sputtering systems. The same approach was picked up by Drüsedau et al. [8] who additionally combined their experimental results with Monte Carlo simulations. Incorporating the results obtained by Drüsedau, Ekpe et al. [9] developed a sophisticated model to predict deposition rates and calculate the energy per deposited atom. Later, innovative experimental approaches have been presented by e.g. Harbauer et al. [10] who developed a combined sensor of different plasma diagnostics or by Bornholdt et al. [11] who combined energy flux measurements with the bias sweep of a Langmuir probe measurement. Besides the here introduced studies which only represent a small selection and are limited to the area of inert-gas DC magnetron sputtering (DCMS), numerous other studies regarding the energy flux for complex material systems or innovative magnetron sputtering sources have been published, e.g. [12–15]. The work presented here ties in with the basic DCMS studies and seeks to provide a broader overview using a wide range of target-gas combinations investigated for essential parameter variations. Furthermore, the different contributions to the energy flux are analyzed using showcasing examples.

2 Experimental Setup

The experiments were performed in a vacuum vessel (volume of 26 litres) with a top mounted planar DC magnetron sputtering system by *Angstrom sciences* equipped with a water cooled two inch target driven by an *Advanced Energy* MDX 500 power source. The chamber was evacuated by a two stage pumping system consisting of a *Pfeiffer Vacuum* MVP 040-2 membrane pump and a *HiPace* 300 turbo pump which was able to pump the chamber to a base pressure of 10^{-3} Pa. The gas flow was controlled by a *MKS* 647C multi-channel gas flow controller with a pressure control system regulated by a PID controller, which was used for the pressure variations. The pressure was monitored with a Baratron pressure gauge.

For the power and distance variations a constant gas flow value was set. The passive thermal probe (PTP) was mounted on a linear drive inserted at the bottom of the chamber to allow variation of the axial distance between PTP and target. The quartz crystal microbalance (QCM) was introduced from the side through a KF-40 feedthrough mounted on a movable rod (figure 1). The standard distance to the target for all probes was 70 mm, the standard pressure was 2 Pa and the standard magnetron power was chosen to be 50 W. The experimental parameters are summarized in table 1.

For the lower and upper limits in the variations, no stable discharge conditions were reached for He and Kr with some targets and it should be noted that the measurements with helium were performed at a pressure of 2.8 Pa instead of 2 Pa.

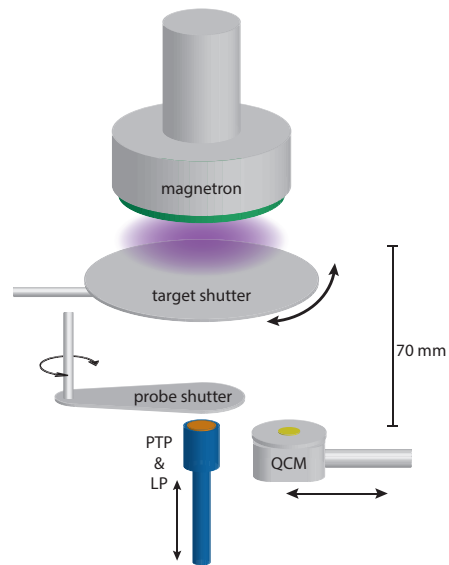


Figure 1: Sketch of the utilized experimental setup with the passive thermal probe, which was also used as a planar Langmuir probe, as well as the QCM which could be moved to the center position.

The magnetron was shut off during the cooling phase of the PTP measurements using the target

Table 1: Experimental parameters used for the parameter variations performed for five targets (Ag, Al, Cu, Ti, W), with the varied values printed **bold**. All experiments were performed with helium, argon and krypton with the magnetron in power regulated mode. The standard condition was chosen to be at 70 mm distance to the target, 50 W power and 2 Pa pressure, however, some extreme values could not be reached when using He or Kr for some targets.

	variation of power	variation of distance	variation of pressure
power (W)	30 - 190	50	50
distance (mm)	70	30 - 160	70
pressure (Pa)	2	2	0.5 - 12

shutter. To minimize the erroneous effect on the calorimetric measurements created by a hot target shutter, an additional shutter close to the probe (probe shutter) was used. Specific test measurements and temperature measurements confirmed that this second shutter remains at a low temperature during the experiments, while a considerable energy flux was detected from the target shutter.

In a subsequent investigation, IR heat camera recordings using an *Optris* PI-D2009-11-A camera were performed to study the effect of target heat radiation. Selected samples of sputter deposited thin films were prepared for analysis with a scanning electron microscope (SEM). A sketch of the discharge chamber is presented in figure 1 illustrating the utilized probes and shutter.

3 Diagnostic tools and simulations

All measurements were performed successively with three different probes (PTP, QCM, LP) centered on the chamber axis at approximately the same distance to the target. For the parameter variations all values were measured twice in a back-and-forth approach to allow a simple estimation of the statistical error and reveal potential effects from e.g. hysteresis. The corresponding plasma parameters and deposition rates were primarily determined to allow an estimation of the energy flux associated with ions, electrons and depositing particles and are, thus, only discussed in these terms.

3.1 Quartz crystal microbalance

For the measurement of the deposition rate, a commercially available quartz crystal microbalance (QCM) IL150 from *Intelmetrics Global Ltd* with a gold coated, 14 mm diameter, 6 MHz crystal has been used without water cooling. Since the QCM primarily detects the change of mass on the quartz crystal, it is necessary to provide material specific constants to allow the calculation of the deposition rate in nm/min [16]. For the different investigated materials, the density and impedance of the bulk material [16] have been used and, thus, the obtained results of the deposition rate may have a tendency to overestimate the actual rate according to the actual density of the deposited film [17].

Deposition rate measurements due to helium sputtering have proven to be difficult since the IL150 was not able to calculate applicable results. Therefore, the deposition rates for helium sputtering were estimated by normalizing the obtained results from argon using the sputter yields for argon and helium obtained from *SRIM* simulations. Later comparison with deposition rates calculated from the sheath thickness measured with the SEM confirmed that this procedure provides reliable values.

3.2 Passive thermal probe

A detailed description of the PTP and the evaluation of the measurement is presented here as the understanding of the procedure is important for the discussion of the results in section 5. The probe utilized in the experiments consists of a sensor plate (substrate dummy) made of copper with a diameter of 11 mm

and a thickness of $70 \mu\text{m}$. Spot-welded to the back of it is a Type K thermocouple and a copper wire for biasing and current readings [18]. For all PTP measurements the probe was not connected to any external potential and was therefore at floating potential. The sensor plate is surrounded by a metallic shielding to make sure, that only contributions from the upper half-space are included in the measurement. A schematic drawing of the PTP design is shown in figure 2.

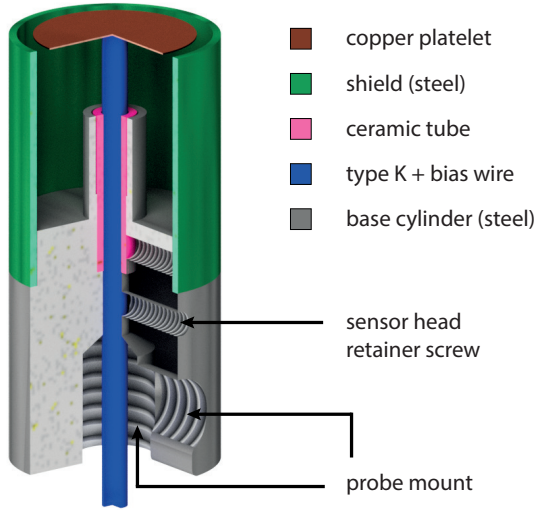


Figure 2: Schematic drawing of the PTP sensor head. The Type K thermocouple and the wire for biasing are spot-welded to the back of the copper platelet that represents the substrate. The whole sensor is housed in a stainless steel cylinder to shield it from any surrounding influences other than the ones coming from the upper half-space.

It should be noted that the PTP measures a time and energy integrated value of the energy flux that is created by various energy sources and processes such as charged and neutral particles, surface processes like film formation or radiation from a hot target or chamber walls, respectively. The basic idea of the PTP is to determine the energy flux from the relation between the time derivative of the enthalpy (\dot{H}) and the time derivative of the temperature (\dot{T}_s) of a well defined substrate dummy. During the heating (T_h - energy source on) and the cooling (T_c - energy source

off) of the substrate dummy this relation yields:

$$\text{Heating: } \dot{H}_h = C_s \dot{T}_h = P_{in} - P_{out,h} \quad (1)$$

$$\text{Cooling: } \dot{H}_c = C_s \dot{T}_c = -P_{out,c} \quad (2)$$

Here C_s is the heat capacity of the probe, P_{in} gives the power from the source and $P_{out,h}$ and $P_{out,c}$ denote the power leaving the probe during heating and cooling, respectively. Assuming that the negative cooling terms of equation 1 and 2 are equal for the same substrate temperatures ($P_{out,h}(T_s) = P_{out,c}(T_s)$), the equations for heating and cooling can be combined to calculate the energy flux J_{in} :

$$J_{in} = \frac{P_{in}}{A_s} = \frac{C_s}{A_s} (\dot{T}_h - \dot{T}_c), \quad (3)$$

There are various methods of evaluating calorimetric temperature curves, however, if the power source is capable of fast switching between off- and on-states or if fast shut-off of the source can be realized due to a shutter system, the most desirable method is the so-called *kink method*, see figure 3. The main reason

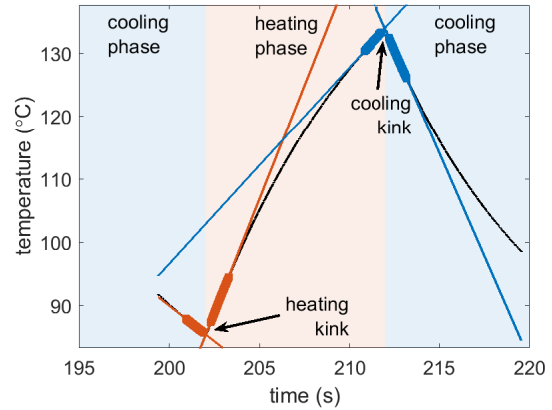


Figure 3: Exemplary evaluation of a PTP curve with heating and cooling kink. The highlighted data points in red and blue denote the data points used for the linear fits.

for this is that for the assumption of equal cooling terms during the heating and the cooling phase, any energy flux originating from secondary heat sources has to be constant for the investigated time period.

When evaluating with the *kink method*, as described in [19], only a short time period of about 2 s around the kinks between the cooling and heating phases are evaluated. This means, that the above-mentioned assumption also only needs to apply in this short time frame. Accordingly, any contribution to the energy flux which is relatively constant during this time period does not significantly influence the measured energy flux. This makes the PTP measurement a truly differential method and efficiently minimizes the influence of parasitical energy flux contributions which change on a slower time scale.

The kink that evolves when switching the power source on from an off-state is referred to as heating kink and the kink the power source is switched off again (start of the next cooling phase) is referred to as cooling kink. From both kinks an accurate measurement of the energy flux at these times is obtained and any potential discrepancy between those two results can already be a valuable hint for the stability of the investigated process and the reliability of the measurement method. In figure 3 an exemplary temperature curve with clearly labeled cooling and heating phases as well as evaluated points and corresponding linear fits around the kinks are presented.

By subtracting the slopes of the two linear fits around the kinks, $\dot{T}_h - \dot{T}_c$ can be easily obtained and the energy flux can be calculated from equation 3, using the heat capacity C_s and surface area A_s of the probe. Since the heat capacity of the probe changes with increasing film thickness, two different PTP probes were used in rotation to minimize the effect of the film which is continuously deposited during the extensive investigations. Using the calibration experiment introduced in [18], the probes were being recalibrated several times throughout the measurements.

3.3 Langmuir probe

The design of the PTP also allows to use the copper plate as a planar Langmuir probe (LP), which is achieved by using an additional wire to apply a bias voltage and measure the resulting current. The measurements were performed using an in-house developed electronics based on a *National Instruments*

USB-6002 card with a sample rate of 50 kHz. A typical measurement takes 4 s, resulting in a total of up to almost 20k data points with a step width of 4.6 mV, depending on the investigated interval. The electron temperature T_e was derived from the slope of the semi-logarithmic current-voltage plot [20]. The plasma potential Φ_{pl} was determined as the intersection between the linear fit used to obtain T_e and the linear fit to the electron saturation regime. In figure 4, two exemplary Langmuir curves are shown for silver in argon and helium, respectively.

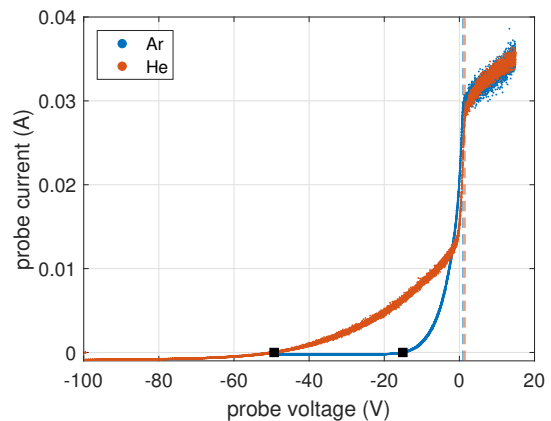


Figure 4: Exemplary Langmuir curves for Ag in Ar (blue data points) and He (red data points) for a discharge power of 90 W at a distance to the target of 70 mm and a gas pressure of 2 Pa and 2.8 Pa for Ar and He respectively. The black square indicates the determined floating potential and the dashed lines the corresponding plasma potentials for Ar and He, respectively.

It can be recognized that for He the LP curve strongly deviates from the typical shape expected for Maxwell distributed electrons, while for Ar a more characteristic planar LP curve is observed. For He, more energetic electrons are present which result in an increase of the current for more negative probe voltages. For argon the floating potential was $\Phi_{fl} = -15.0$ V and the plasma potential $\Phi_{pl} = 1.0$ V, whereas helium exhibited values of $\Phi_{fl} = -49.3$ V and $\Phi_{pl} = 1.5$ V. The more pronounced population of high energy electrons for helium results in a more negative floating potential and a wider gap to Φ_{pl} . The electron temperature T_e was determined for the

population with lower energies as it accounts for the majority of the current, however, it must be noted that this may result in an underestimation of the average electron temperature and correspondingly an underestimation of the calculated electron contribution to the energy flux (see section 4).

3.4 TRIM simulations

TRIM simulations were performed using SRIM-2013 to obtain sputter yields Y_{sp} and the yield of backscattered/reflected particles Y_{refl} as well as the average energy of sputtered and reflected particles E_{sp} and E_{refl} , respectively [21]. The ion acceleration voltage, which is one of the input parameters of TRIM, was derived from averaged values of the recorded power supply readings during the PTP measurements at the standard power setpoint of 50 W. Incident ion angles of 0° up to 30° in a step width of 10° were chosen with 10^5 simulated ions each. The results were corrected by subtracting the surface binding energy of the target material from the energy component of the sputtered particle that is perpendicular to the target since this aspect is not included in the simulation. For further calculations, an average over the values obtained by TRIM simulations for 0° up to 30° was used since we estimate the majority of the incident ions to impact within these angles. Ions with greater incident angles will most likely result in sputtered or reflected particles with such a small angle of emission that they are unlikely to arrive at the substrate (probe) position. We decided to simulate a wider range of incident angles as a method to compensate for the surface roughness. However, it must be noted that the calculated values are taken as a rough estimate only and, therefore, do not claim to quantitatively reflect the real conditions.

From the yields (Y_{sp} and Y_{refl}) and the average energies (E_{sp} and E_{refl}) of the sputtered and reflected particles we also calculated the amount of energy per incident ion which is carried away from the target by sputtered and reflected particles, respectively:

$$\begin{aligned} E_{sp,norm} &= Y_{sp} E_{sp} \\ E_{refl,norm} &= Y_{refl} E_{refl}. \end{aligned}$$

Especially the comparison between these two values can be a useful indicator for the relevance of the sputter or the reflection process for the integral energy flux.

4 Contributions to the energy flux

As described in section 3.2, the energy flux obtained with the PTP is always a time- and energy integrated quantity which reflects the energy flux originating from a complex set of processes [22, 23]. In 1978 Thornton introduced an approximate model to calculate the energy flux for the case of magnetron sputtering with inert gases [24]. This model was based on the contributions from kinetic energy of the sputtered particles J_n , the heat of condensation J_{cond} and the plasma radiation $J_{rad,pl}$. Since then, this model was verified in numerous studies and further refined by additional contributions and sophisticated methods of theoretical calculations. In the following paragraphs the common methods for calculation of the most important contributions relevant for this study alongside some of their limitations are presented. For most of these processes, in reality, certain additional coefficients need to be taken into account. They usually describe the probability or the efficiency of a specific process and range from 0 to 1. The sticking coefficient e.g. describes the probability that a particle sticks to the surface and the energy transfer coefficient describes the percentage of energy transmitted in a collision. For ease of understanding, these coefficients are chosen to be 1 in the following description and also in the absolute calculations presented in this study. As a result, the calculated energy flux represents an 'upper limit estimation' and could, thus, overestimate the actual energy flux. A more generic and detailed description can be found in [22, 23].

4.1 Electrons and ions

The contribution from charge carriers, also called the electric contribution, includes the kinetic energy which is transferred upon impact of electrons or ions on the substrate and the potential contribution which

is released as they recombine. At the floating potential the kinetic contribution is characterized by the equal current densities of ions and electrons j_{fl} and their respective kinetic energies. The kinetic energy of the ions is given by the difference between plasma and floating potential $\Phi_{pl} - \Phi_{fl}$ and in the case of a Maxwellian electron energy distribution function (EEDF) the contribution from electrons can be estimated by the electron temperature T_e . The contribution due to recombination is calculated by the difference between ionization energy Φ_{iniz} and the electron work function Φ_{ewf} . The resulting energy flux can thus be calculated as

$$J_{electric} = \frac{j_{fl}}{e_0} [(\Phi_{pl} - \Phi_{fl}) + 2k_B T_e + (\Phi_{iniz} - \Phi_{ewf})], \quad (4)$$

with the Boltzmann constant k_B and elementary charge e_0 . The variables in equation 4 can be directly obtained from Langmuir measurements and accordingly the errors and uncertainties which are typically associated with Langmuir measurements appear in the calculated electric contribution as well.

4.2 Sputtered particles

Similar to the electric contribution, the contribution from sputtered particles includes a kinetic portion and a potential portion which are both proportional to the flux of sputtered atoms Γ_n . As the sputtered atoms hit the surface of the probe, their kinetic energy E_{kin} is transferred to the probe and as they bind to the film, the surface binding energy E_{bin} is released. The energy flux associated with the sputtered flux can thus be calculated to be:

$$J_{sputter} = \Gamma_n (E_{kin} + E_{bin}). \quad (5)$$

As described in section 3.1, the particle flux can be obtained from QCM measurements. The values for the surface binding energy are taken from literature and are summarized in table 2 for the investigated materials.

The kinetic energy of the arriving sputtered particles is associated with much greater uncertainty. The initial kinetic energy obtained from the sputter process is typically calculated according to the

Table 2: Relevant material properties for the investigated target materials as taken from [25]. E_{bin} gives the surface binding energy, A the atomic mass number, ρ the density of the bulk material and k the thermal conductivity.

	A	E_{bin} (eV)	ρ (g/cm ³)	k (W/(m K))
Ag	108	2.9	10.50	429
Al	27	3.4	2.70	237
Cu	64	3.5	8.96	401
Ti	48	4.9	4.51	22
W	184	8.8	19.30	174

Thompson-formula [26], Monte Carlo simulations or it is determined experimentally [27]. For this study the initial energy is calculated using SRIM [21] as described in section 3.4. The greatest uncertainty, however, arises from the energy loss due to collisions with the background gas which is discussed in section 4.4.

4.3 Reflected neutrals

Reflected neutrals are created as process gas ions get neutralized and reflected from the target cathode. Accordingly, these particles can carry high energies up to the cathode potential, with average energies in the range of ~ 100 eV. The importance of this contribution, especially for the sputtering of heavy targets, was already recognized by Hoffmann and Thornton in 1980 [28] and has since been discussed in numerous works [7–9, 22, 23, 29, 30]. Even though some work has been done to experimentally investigate these fast neutrals by e.g. Rosnagel [31], quantitative measurements are coming with many experimental challenges. Due to this fact, and due to the difficulty of distinction from other energy flux contributions, the effect of reflected neutrals is often neglected or underestimated in the discussion of measured energy flux values. In this work, we consider this contribution by elimination of other contributions which is supported by SRIM simulations as described in 3.4.

4.4 Energy loss due to collisions with the background gas

To understand the energy deposited at the substrate (PTP), one has to take energy losses into account which occur along the way from the target to the substrate surface. These energy losses are governed by the mean free path for collisions between the energetic particles and the background gas λ_{mfp} and by the fraction of energy lost in each collision. The reduction of the initial energy from the sputter process E_{sp} as a function of the distance to the target d can be approximated by

$$E_{kin}(d) = E_{sp} \cdot \exp(-R_{re} d / \lambda_{mfp}), \quad (6)$$

with R_{re} being the remaining fraction of kinetic energy of the colliding particle after one collision. To obtain a rough estimation of this parameter, we calculated an average value as a function of the mass-ratio between impinging sputtered metal atom and the background gas atom. This procedure is inspired by Westwood [32] who integrated the collision equation over all possible collision angles and averaged the result assuming the same probability for each collision angle. However, due to the curvature of the hard sphere, the collision angle does not change linearly with the collision parameter b and, therefore, collision angles close to 90° are overestimated for the assumption made by Westwood. To obtain a more realistic estimation, we calculated the average energy exchange and average angle of deflection for a collision in three dimensions by assuming the probability of the collision parameter to scale with its value. The further from a central collision, the more collision possibilities exist along the radius defined by the collision parameter b . In figure 5 the resulting curves along with calculated values for the gas target combinations investigated in this study are shown together with a small sketch to illustrate the main variables of the collision model. Comparing to Westwood's approach, we obtain the same average angle of deflection and the same values for R_{re} at very uneven masses but smaller energy losses for more similar masses ($0.1 < M_g/M_t < 10$).

Providing a realistic estimation of the mean free path is associated with much greater difficulty and

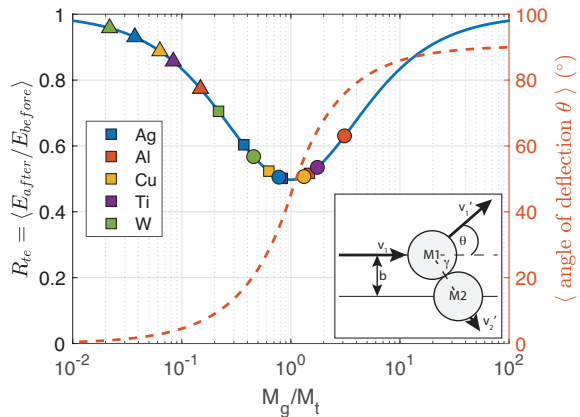


Figure 5: Average remaining energy and average angle of deflection for a collision between two hard spheres as a function of their mass ratio. M_g depicts the mass of the background gas atom and M_t the mass of the sputtered target atom. The values relevant for this study are marked by colored squares (Ar), circles (Kr) and triangles (He) with the different colors representing the different target materials. The values were derived from a simple, elastic 3D hard-sphere collision model.

uncertainty for three principle reasons: (i) as first recognized by Robinson in 1979 [33] the cross section is reduced strongly as a function of the particle energy, (ii) reliable data for cross sections between sputtered atoms and noble gases is rare and usually interpolations from noble gas collision cross sections are used, although one may expect significant discrepancies [29,34,35], (iii) the temperature of the gas can increase strongly as a result of collisions with sputtered particles and reflected neutrals, resulting in a significant increase of the mean free path [36,37]. These points are difficult to resolve experimentally and even though detailed simulations allow to calculate the reduction of the energy of the sputtered atoms and reflected neutrals, they still lack absolute accuracy due to estimated collision cross sections and are furthermore limited to a specific geometry [29]. For our system at standard conditions we estimate that with a pressure-distance product of 140 Pa mm, the sputtered flux is partly thermalized with a smaller fraction of ballistic particles [29,38]. The specific percentage, however, is expected to vary strongly as a

function of the mass ratio i.e. for tungsten in helium the momentum exchange is minimal and almost no deflection of the particles is expected while for silver in argon on average half of the energy is lost in every collision and the direction is changed by 45° , see figure 5.

Although collisions primarily represent a loss mechanism in terms of energy flux, a part of the energy transferred to the gas will also arrive at the substrate as directed background gas atoms - or more isotropic - as thermal energy transferred from the heated gas. As pointed out by Somekh [29] and experimentally shown by Rosnagel [31], the elongated mean free path for faster particles (see figure 6) will also lead to an increased importance of fast reflected neutrals for the energy flux, as they can more efficiently transfer energy from the target to the substrate.

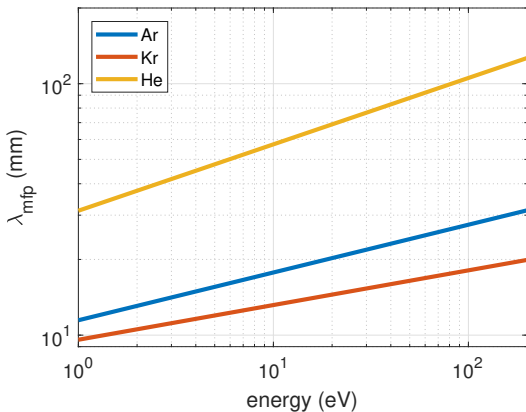


Figure 6: Mean free path for fast noble gas atoms passing through the same noble gas background as calculated according to the Variable Soft Sphere (VSS) model from Koura and Matsumoto [39]. The pressure and temperature used for calculation of the plotted λ_{mfp} are 2 Pa and 350 K.

4.5 Radiation

Energy flux by radiation can principally come from two sources: (i) line radiation from the plasma and (ii) black-body radiation from hot elements in the plasma chamber. Especially the role of line radiation

is difficult to estimate and in most cases it is assumed to be negligible. For our experiment, prior measurements based on the comparison between a modified PTP and OES measurements confirmed that this contribution does not significantly influence our integral energy flux. However, it should be noted that Thornton on the opposite obtained values of several eV per deposited atom from calculations based on the ionization and sputter mechanism [6].

The second source for radiative energy flux is much easier to understand and to investigate. In the case of magnetron sputtering, the primary origin for significant black body radiation is the magnetron target or the anode. In case of poor thermally conducting target materials or insufficient cooling, these parts can get extremely hot and generate a strong energy flux to the substrate. This energy flux can be calculated according to the Boltzmann radiation law:

$$J_{rad} = \nu F_{ts} \sigma (T_t^4 - T_s^4). \quad (7)$$

Here T_t and T_s are the temperatures of the target and the substrate, σ the Stefan-Boltzmann constant, F_{ts} a geometrical factor for parallel discs [40] and ν the radiation exchange rate which compensates for the emissivities being smaller than 1 [41]. In figure 7 an exemplary calculation of the energy flux from a hot magnetron according to equation 7 is shown. Here it is clearly visible that this contribution is small compared to typical integral energy flux values for temperatures below roughly 400°C and can increase to values in the range of 100 mW/cm^2 for high temperatures and higher emissivities.

5 Results

The calorimetric measurements as obtained by the PTP are presented in figure 8. The errors are estimated from repeated measurements obtained by the applied back-and-forth measurement principle.

The first row shows the results for the power, distance and pressure variation in argon. The second row displays the corresponding results for krypton and the third row those for helium. A general order of the energy flux is observed with Ti and W yielding the highest energy flux values, Ag and Cu showing

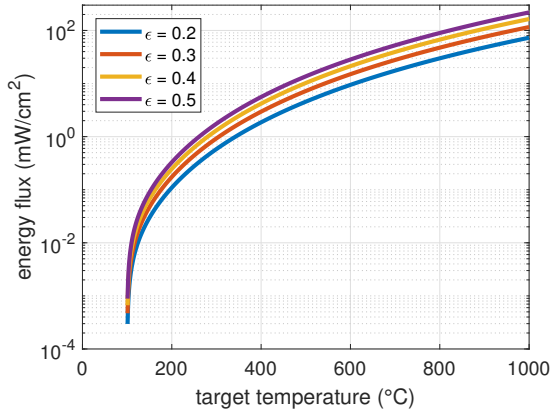


Figure 7: Calculated energy flux according to equation 7 for two parallel discs with diameters $d_t = 5.08$ cm, $d_s = 11$ mm, distance 70 mm and a temperature of 100 °C of the substrate surface. The different graphs are calculated for different emissivities of $\epsilon = 0.2 - 0.5$ for both surfaces.

relatively similar values with moderate energy flux and Al showing the smallest values. Merely in helium there is a more pronounced difference between Ag and Cu and the lightest material aluminum yields a higher energy flux relatively to the other materials. This is likely caused by the more effective sputtering of Al in He resulting from the more akin masses between sputtering gas and target material as compared to the heavier materials. This hypothesis is in good agreement with the SRIM simulations which calculated significantly higher sputter yield for He on Al as compared to Cu.

The power variations show an almost linear increase for all gases and target materials. Since the energy flux can primarily be understood as power transfer from the cathode to the substrate such a linear increase can intuitively be expected. The only outlier regarding this trend is Ti in Ar and Kr which shows a clear deviation as a result of the role of increasing target radiation (see section 6.3). The distance variation shows an expected overall trend for all investigated target-gas combinations with decreasing energy flux values for increasing distance to the target. The observed exponential decrease can be understood as a result of the increased number of collisions

the sputtered and reflected particles undergo as they transit from the target towards the probe. Except for the case of Ti in He, the results of the pressure variation show much less pronounced trends. The energy flux remains relatively constant and in most cases exhibits a weak maximum in the investigated pressure region. The trends can be understood as the result of a balance between the amount of particles being sputtered and reflected from the target and the interaction of these particles with the background gas. For increasing pressure we observed an increase in magnetron current and, accordingly, a decrease of the magnetron voltage due to the constant power mode. In terms of energy flux, the most relevant effect of increased current is the increased amount of sputtered particles and reflected neutrals, while the decrease of the voltage results in a smaller sputter- and reflection yield and smaller kinetic energies of sputtered and reflected particles. In most cases these effects alone would result in an increase of energy flux as the proportional increase with current is not fully compensated by the attenuating effects associated with the decreasing voltage. However, the decreasing mean free path at higher pressures yields another weakening factor for the energy flux as more energy is dissipated in the background gas and, accordingly, less energy flux arrives at the substrate. As observed, these effects mostly balance the integral energy flux in the investigated pressure regime and the observed maximum likely marks the pressure where the attenuating effect of increased collisions start to dominate the energy flux.

6 Discussion

In the following section we will discuss in greater detail three cases where different mechanisms dominate the measured integral energy flux. In figure 9 the different contributions to the integral energy flux at the standard condition are illustrated using a stacked bar plot. Along with the measured energy flux, the calculated values for the electric contribution and the sputter contribution are presented. For the difference to the measured energy flux a placeholder contribution denoted as 'others' is introduced. In the case of small

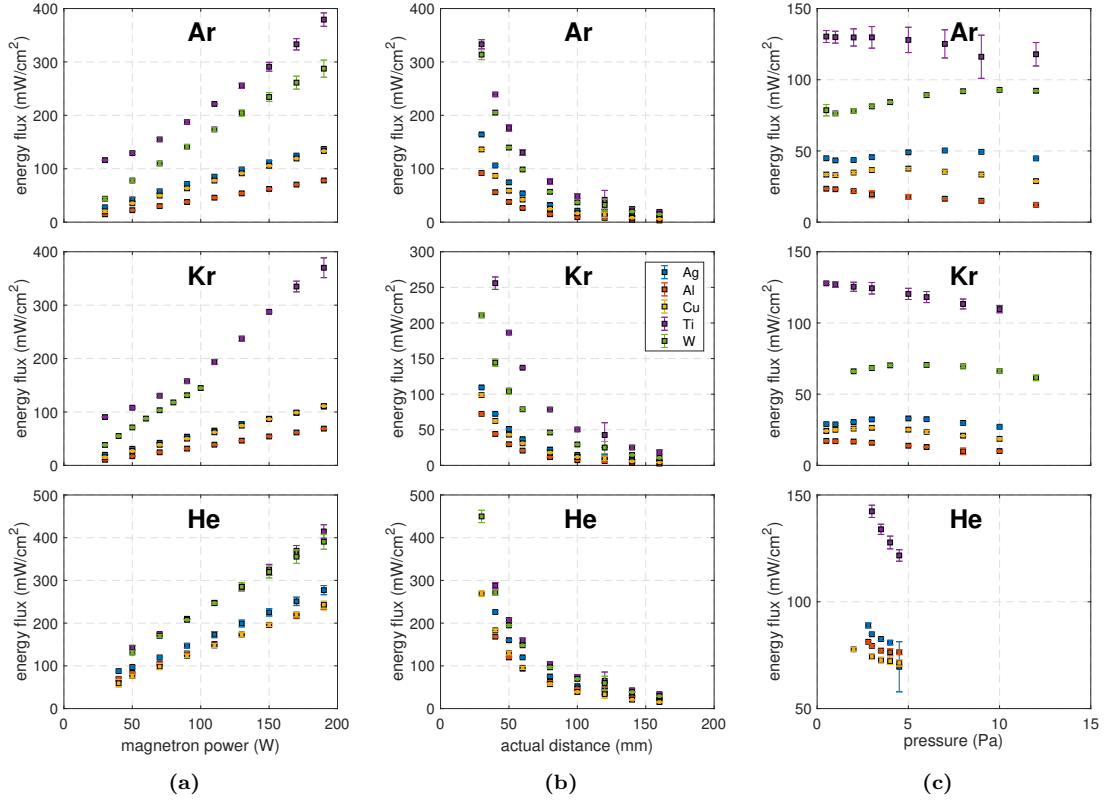


Figure 8: PTP results in argon, krypton and helium for (a) power variation, (b) distance variation and (c) pressure variation. The variations were performed according to the parameters summarized in table 1. The first row shows the results for argon, the second row the investigations for krypton and the last row for helium. While most of the displayed values are obtained as an average from repeated measurements, the results of the power variation with Ti only include the values for the systematic increase of the power from 30 W to 190 W. The values of the systematic decrease of the power from 190 W back to 30 W have been excluded for clarity since a strong hysteresis due to excessive target radiation was detected.

gas-target mass ratios (all He and all W) the contribution from 'others' is expected to be dominated by reflected neutrals which is in good agreement with results obtained from SRIM simulations (plotted in blue). In the case of titanium the target was found to heat up to high temperatures which suggests that the high contribution of 'others' is caused by excessive target radiation. These two extreme cases are discussed in more detail in the last two paragraphs of this section while the first paragraph will focus on the case that the energy flux is dominated by the contribution of thin-film growing particles as observed for

high sputter yield materials like copper or silver.

6.1 Deposition dominated energy flux (Ag, Cu)

For those target materials which exhibit a high sputter yield, usually the contribution from film growing particles dominates the integral energy flux. As an exemplary case, in figure 10 the integral energy flux for a copper target as measured by the PTP during the power variation in argon is presented. In addition, the calculated contributions according to the

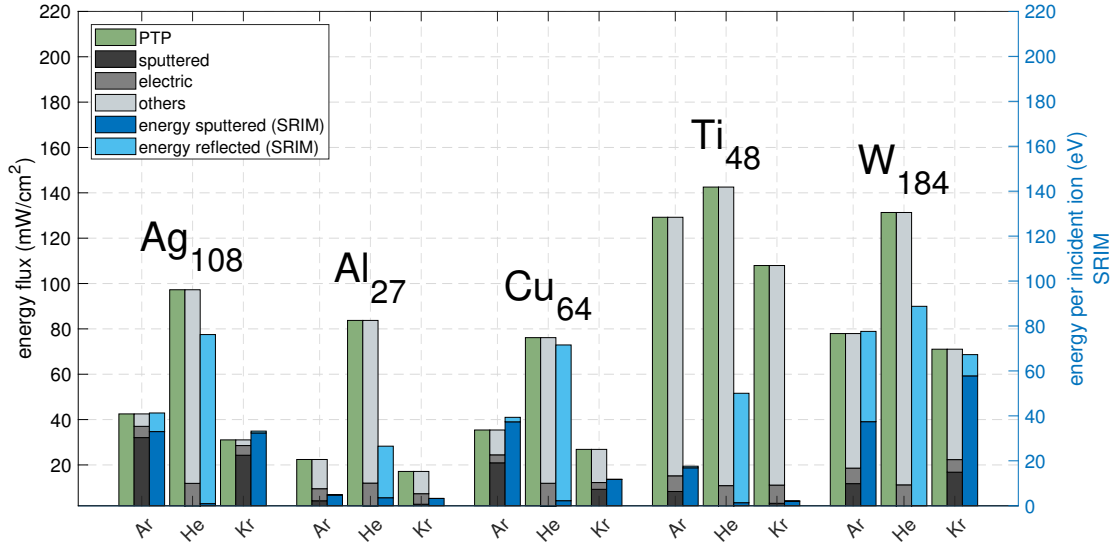


Figure 9: Illustration of the different contributions to the integral energy flux at standard conditions (50 W, 70 mm, 2 Pa) for all investigated target-gas combinations along with simulated data of energy carried away from the target by sputtered and by reflected particles. The values are displayed using a stacked bar graph. The green bar depicts the total energy flux as measured by the PTP (green bar). In three shades of gray, the calculated contributions for the sputtered particles using QCM and TRIM data, the electric contributions by electrons and ions calculated from the Langmuir data and the contributions from 'others' as calculated by subtraction of the combined sputtered and electric contributions from the PTP values. As discussed in the text, the contribution from others can likely be assigned to radiation in the case of titanium and to reflected neutrals in the other cases. The blue bars show the energies calculated from TRIM simulations as described in section 3.4 for sputtered and reflected particles.

equations presented in section 4 and the sum of these calculated values (labeled as 'calc') are shown. Here it can be seen that the neutrals are the biggest contributions to the energy flux as the calculated sum of 'neutr' and 'cond' accounts for ~60 % of the measured energy flux independent of the magnetron power. The 'electric' contribution from ions and electrons on the opposite is relatively small and adds up to only ~10 %. As visible from figure 9, similar percentages are observed for silver with the calculated contribution from neutral particles representing an even bigger portion of the overall energy flux. Due to the aforementioned 'upwards estimation' the percentage of energy flux which is not related to the sputtered particles or electric contribution is expected to be even higher than the calculated difference to the mea-

sured energy flux. In the cases of copper and silver the target surface remained at relatively low temperatures and no significant contribution from radiation was detected (<1 mW/cm²). Therefore, it can be assumed that even in the cases of high sputter yield materials a considerable portion of the energy flux can be attributed to reflected neutrals. This observation is in good agreement with those made by Rosnagel in his study investigating reflected neutrals [31].

6.2 Reflected neutrals dominated energy flux (He, W)

As it is clearly visible in figure 8 the energy flux is persistently among the highest values for all measurements with helium or in the case of tungsten as target

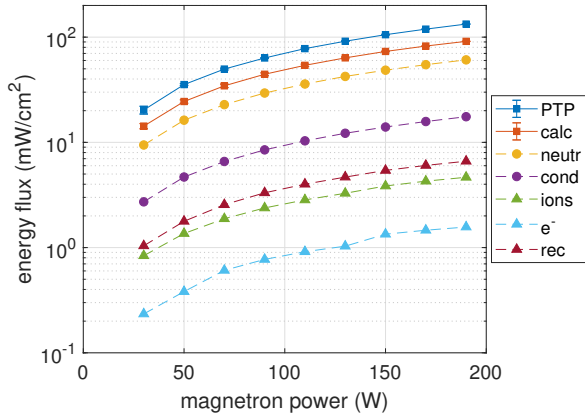


Figure 10: Measured integral energy flux of Cu in Ar during power variation as well as the calculated contributions derived from Langmuir, QCM and SRIM data. The errors presented in the PTP results originate from repeated measurements and the errors displayed in the sum of the calculated contributions ('calc') are obtained by summing up all standard deviations of the individually calculated values.

material. In figure 9 it is shown, that these high energy flux values can not be explained alone by the electric contribution or by that of sputtered atoms. Instead, it is likely a result of the high percentage of particles being reflected from the target. This can be intuitively understood from the simple model of a 2-body collision where we have a high probability for reflection if the incoming particle has a much smaller mass than the other collision partner. However, as shown in [42] even for a gas-target ratio significantly higher than 1, reflection can appear as a result of implanted gas ions in the target material. The results of the SRIM simulations further support the significance of backscattered particles as for almost all cases where He or W is involved we calculate a higher amount of energy being carried away from the target as reflected neutrals compared to that carried away by sputtered particles. Taking into account the more pronounced influence of background gas collisions for the sputtered particles as compared to the reflected ones (see section 4.4), it can be expected that the observed integral energy flux is strongly dominated by reflected neutral particles in these showcasing exam-

ples. As argued in section 6.1, the contribution from reflected neutrals is expected to have a significant influence also in cases where it is much less distinguishable and likely masked by other effects of comparable magnitude and it is further expected to become more relevant for increasing pressure [31].

6.3 Radiation dominated energy flux (Ti)

One striking observation from the various materials studied, is that Ti seems to be the outlier not only in terms of the magnitude of the resulting energy flux but also in terms of the reproducibility of the measurements. Especially in the power variation, Ti exhibited a strong hysteresis of the measurement values obtained at the beginning of the measurement set and the values obtained at the end. For the same parameters we observed a discrepancy in the order of up to ~ 50 mW/cm² and obtained strongly changing values for a repetition of the whole measurement run. Since Ti yields one of the lowest thermal conductivity of all metals (see table 2) one can assume that the heating of the target can have a significant effect. To investigate this, additional measurements were performed using an extended measurement procedure while additionally monitoring the target temperature using an infrared camera. These measurements revealed a direct correlation between the changes in the measured energy flux and the target temperatures. During the measurement, the temperature of the target exceeded the maximum temperature range of 900°C of the IR camera and when the plasma was turned off, a faint orange glow from the target was visible with the naked eye. Following this measurement, the energy flux solely originating from the hot target was measured directly using the PTP. This was achieved by simply shutting off the radiation from the target using the 2-shutter system if the plasma switched off. In figure 11 the resulting energy flux values and the corresponding target temperatures as a function of time along with an exemplary image from the IR camera are presented. Here it can be seen that the target cooled down relatively slow, indicating a weak thermal connection of the target surface to the water-cooled copper holder which remained below 20

°C. Additionally, it can be noted that the measured energy flux values are in good agreement with the calculated values in section 4.5.

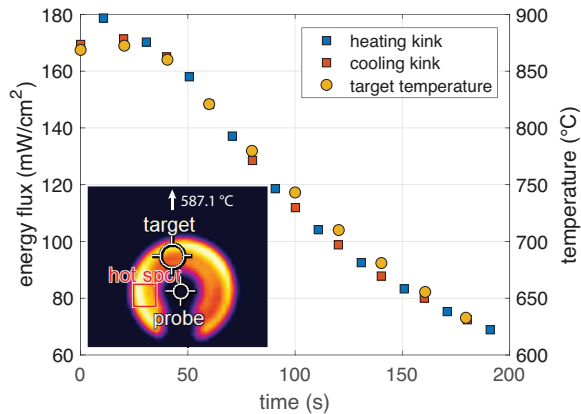


Figure 11: Energy flux due to target radiation as measured with the PTP during cool-down after an extended variation of the magnetron power, along with the corresponding target temperature detected with the IR camera. Additionally an exemplary image obtained with the IR camera indicating the three measurement spots is presented. During the investigations the temperature of the target exceeded 900°C, resulting in a faint orange glow visible to the naked eye.

Since the target temperature changes relatively slow, the energy flux from the plasma excluding the target radiation can be detected using a different switching mechanism for the shut off of the energy flux. By switching off the magnetron voltage instead of closing the shutters, the same background of radiation from the target is present in the small investigated time frame, both during heating and cooling phase. This way, according to the theory presented in section 3.2, the measurement includes all contributions but no target radiation (n.t.r.). In figure 12, measurements for the power variation with Ti using this measurement method alongside with the measurements from figure 8 using the 2-shutter method are presented. The measurements without radiation (source switching) exhibit the same linear dependence as observed for all other metals and show excellent reproducibility. On the other hand, the poor reproducibility for Ti using the shutter system and the resulting increased energy flux values and,

accordingly, the large contribution from 'others' in figure 9 can thus be clearly attributed to the radiation from the target. From the difference between the values obtained from the two measurement methods, a direct determination of the energy flux due to radiation is possible. E.g. for 50 W in argon, the contribution from radiation can be determined to be ~ 100 mW/cm², which correspond to 90 % of the calculated contribution from 'others' in figure 9.

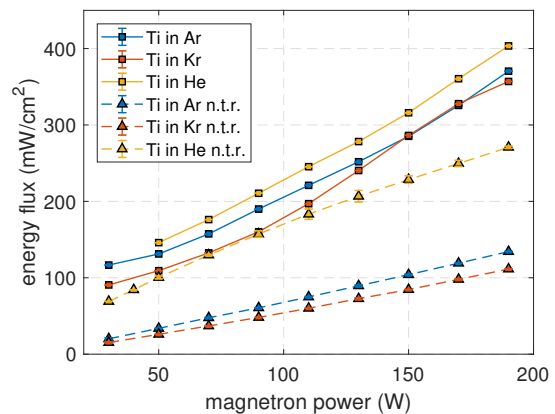


Figure 12: Energy flux measurements of titanium in Ar, Kr and He utilizing two different measurement principles. The data points (squares) connected with the solid lines are produced with the 2-shutter method (see figure 8a), whereas the points (triangles) connected with the dashed lines were obtained using no shutters but instead switching of the power source. Since in the latter case the target radiation is present as a background during both the heating and cooling phase, these measurements are obtained with no target radiation (n.t.r.) contribution in the integral energy flux.

To exclude the possibility of poor thermal conductivity caused by an uneven target backside or improper mounting, we performed additional measurements with a freshly machined target backside to guarantee a smooth surface. This optimization only slightly improved the cooling of the target, so that the obtained results should apply to other comparable systems as well. This is in agreement with recent observations for hot target sputtering of titanium [43,44] or nickel [45] and could also explain high energy flux values observed by Cormier et al. [12]. Additional measurements with gadolinium, which has an

even lower thermal conductivity of $10.5 \text{ W}/(\text{m K})$, exhibited similar characteristics as Ti and, thus, further underline the impact of the targets thermal conductivity. However, it must be noted that the contribution from target radiation is highly dependent on a variety of uncertain factors such as the target history (e.g. how long was the target exposed to high power) or on the efficiency of the target cooling system (e.g. thinner targets would dramatically decrease the target heating).

Although no significant hysteresis during the measurements presented in figure 8 was observed for the other target materials, the same additional investigations were performed with silver, aluminum and tungsten. In all cases the target temperature did not exceed values above 300°C and accordingly, the radiation from the target resulted in energy flux values below $2 \text{ mW}/\text{cm}^2$. It can thus be concluded that the absence of a hysteresis and, accordingly, good reproducibility is a sufficient indicator for a negligible effect of target radiation.

6.4 SEM investigations

The influence of process parameters on the thin film growth can be graphically described by a so called structure zone diagram (SZD). For magnetron sputtering the most referred to SZD is the one introduced by Thornton in 1974 [1] or the updated version presented by Anders in 2010 [46]. For DC magnetron sputtering with no additional substrate heating or biasing, films are typically assigned to the Zone 1 or in some fewer cases to the transition region Zone T. To allow a comparison to these models and, thus, create a connection between the presented energy flux measurements and the actual deposited film, samples were deposited at selected parameter combinations. The copper films were deposited onto silicon substrates placed at a distance of 70 mm to the target surface. For each condition samples were prepared for both, a grounded substrate and an isolated substrate at floating potential. The films were examined using a *Zeiss GeminiSEM* scanning electron microscope (SEM) producing top view images of the surface morphology of the films as well as cross sections revealing the structural growth. Images of the

surface for the floating substrates and cross sections for both the grounded and the floating substrates are summarized in figure 13. Although the substrate is heated much stronger by electrons if it is connected to ground, the images show very similar structures for both the floating and grounded case. Although the substrate is warmer during the deposition on a grounded substrate, the homologous temperature stays within the lower regime as the temperature is not expected to reach a significant fraction of the melting temperature of the material. Therefore no significant effect on the film formation is expected.

In principle, two distinctively different structures, which are best visible in the cross sections, can be observed in figure 13. *A* exhibits a columnar growth structure with clear crystal boundaries which extend throughout the complete film. These crystal boundaries are also visible in the top view image where they create a grain-like structure. The same structure is also visible in the top view of *D*, however, due to the small thickness of the deposited film, the cross section images do not exhibit clear details. Only in a close examination, an indication for domed crystallites with bigger diameter compared to the ones seen in *A* is present. In both cases the bombardment by reflected neutrals is comparatively low and while the depositing atoms are expected to be partly thermalized for 2 Pa, they are likely completely thermalized in the case of 12 Pa. For samples *B*, *C* and *E* the clear columnar structure is disrupted in favor of a more dense growth pattern with smaller crystallites which do not extend through the complete film thickness. The disruption of the columnar morphology is somewhat comparable to that observed for biased sputtering [47, 48]. Here the kinetic impact of highly energetic ions disrupts the columnar growth which is typically attributed to resputtering and additional nucleation sites. In the same way, in our case the formation of smaller crystallites can be associated to the increased energy of reflected neutrals and depositing atoms arriving at the substrate. In the case of the increased discharge power (*B*) the energy increases mostly as a result of stronger rarefaction and increased magnetron voltage. For the significantly reduced pressure (*C*), the dominant parameter is the increased mean free path which directly results in fewer collisions and, accord-

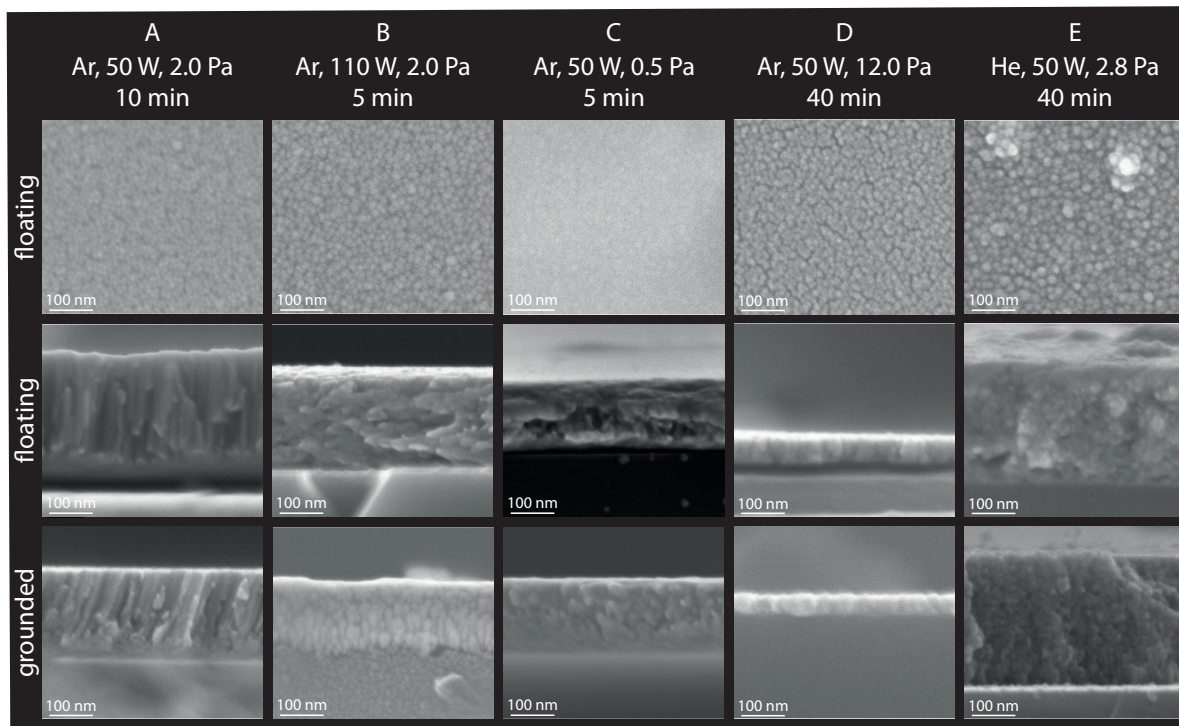


Figure 13: SEM images of a copper film deposited on a silicon wafer in Ar and He at selected discharge parameters. The top row shows the surface morphology for films deposited on a floating substrate, the second and third row show cross sections of the corresponding films with a floating and grounded substrate, respectively.

ingly, higher energies. The extreme case with helium as a sputter gas (*E*) results in a strong neutral bombardment combined with a low deposition rate. The strong neutral bombardment could explain the finely grained structure visible in the cross sections and the comparatively rough surface observed in the top view is likely a result a resputtering.

7 Conclusions

Detailed investigations of the energy flux in DC magnetron sputtering with fifteen gas-target combinations examined for essential parameter variations have been presented. Additional measurements using Langmuir probe, QCM and IR imaging combined with SRIM simulations were used to allow a more detailed analysis of the different contributions to the

integral energy flux. In spite of the apparent simplicity of the investigated system (DCMS of metals using inert gases), fundamentally different compositions of the integral energy flux were observed. The three dominant mechanisms were identified as the energy flux originating from sputtered particles, from reflected neutrals and from a hot target surface. While the first mechanism is of essential nature to the film deposition process and is especially dominant for materials with a high sputter yield, the mechanism attributed to reflected neutrals was found to be of equal importance. In the case of a small gas-target mass ratio the energy flux from reflected neutrals can even be the leading factor. For target materials with a low thermal conductivity, such as titanium, the target surface can heat up to high temperatures resulting in a significant radiative energy

flux which can easily surpass the contribution from other mechanisms. However, in systems with a biased substrate the contribution of charged particles becomes more and more significant and in many cases dominates the energy flux.

The understanding of the driving mechanisms behind the different contributions and on how they transfer the energy to the substrate and the growing film can in principal be used to tailor the composition of the energy flux. While the energy flux from radiation, condensation or electrons represents a relatively anisotropic contribution, the kinetic impact of ions, sputtered particles and especially reflected neutrals dissipates energy much more localized into the film. Changing e.g. the gas-target mass ratio by using a different background gas could, thus, be used to change the amount of highly kinetic particles impinging on the film during deposition. The copper samples investigated by SEM illustrated the principal changes of the film structure from columnar growth to a more dense film with smaller crystallites. In spite of the expected increase in energy flux associated with electron heating, no clear difference of the film structure for samples deposited at floating potential compared to those using a grounded substrate were observed.

Acknowledgements

The authors would like to thank Dr. Oleksandr Polonskyi from the Technical Faculty of the Christian-Albrechts-University in Kiel, Germany, for his dedicated work in acquiring the SEM images.

References

- [1] J. A. Thornton, "Influence of apparatus geometry and deposition conditions on the structure and topography of thick sputtered coatings," *Journal of Vacuum Science and Technology*, vol. 11, no. 4, p. 666, 1974.
- [2] H. Deutsch, H. Kersten, S. Klagge, and A. Rutscher, "On the Temperature Dependence of Plasma Polymerization," *Contrib. Plasma Phys.*, vol. 28, pp. 149–155, 1988.
- [3] H. Deutsch, H. Kersten, and A. Rutscher, "Basic Mechanisms in Plasma Etching," *Contributions to Plasma Physics*, vol. 29, no. 3, pp. 263–284, 1989.
- [4] H. Kersten, H. Deutsch, H. Steffen, G. M. W. Kroesen, and R. Hippler, "The energy balance at substrate surfaces during plasma processing," *Vacuum*, vol. 63, pp. 385–431, aug 2001.
- [5] H. Kersten, R. J. M. M. Snijkers, J. Schulze, G. M. W. Kroesen, H. Deutsch, and F. J. De Hoog, "Energy transfer from radio frequency sheath accelerated CF+3 and Ar+ ions to a Si wafer," *Applied Physics Letters*, vol. 64, no. 12, pp. 1496–1498, 1994.
- [6] J. A. Thornton, "Substrate heating in cylindrical magnetron sputtering sources," *Thin Solid Films*, vol. 54, no. 1, pp. 23–31, 1978.
- [7] J. A. Thornton and J. L. Lamb, "Substrate heating rates for planar and cylindrical-post magnetron sputtering sources," *Thin Solid Films*, vol. 119, pp. 87–95, sep 1984.
- [8] T. P. Drüsedau, T. Bock, T.-M. John, F. Klabunde, and W. Eckstein, "Energy transfer into the growing film during sputter deposition: An investigation by calorimetric measurements and Monte Carlo simulations," *Journal of Vacuum Science & Technology A: Vacuum, Surfaces, and Films*, vol. 17, pp. 2896–2905, sep 1999.
- [9] S. D. Ekpe and S. K. Dew, "Theoretical and experimental determination of the energy flux during magnetron sputter deposition onto an unbiased substrate," *Journal of Vacuum Science & Technology A: Vacuum, Surfaces, and Films*, vol. 21, no. 2, p. 476, 2003.
- [10] K. Harbauer, T. Welzel, and K. Ellmer, "A combined sensor for the diagnostics of plasma

- and film properties in magnetron sputtering processes,” *Thin Solid Films*, vol. 520, no. 20, pp. 6429–6433, 2012.
- [11] S. Bornholdt and H. Kersten, “Transient calorimetric diagnostics for plasma processing,” *The European Physical Journal D*, vol. 67, p. 176, aug 2013.
- [12] P.-A. Cormier, A. Balhamri, A.-L. Thomann, R. Dussart, N. Semmar, J. Mathias, R. Snyders, and S. Konstantinidis, “Measuring the energy flux at the substrate position during magnetron sputter deposition processes,” *Journal of Applied Physics*, vol. 113, p. 013305, jan 2013.
- [13] M. Čada, J. W. Bradley, G. C. B. Clarke, and P. J. Kelly, “Measurement of energy transfer at an isolated substrate in a pulsed dc magnetron discharge,” *Journal of Applied Physics*, vol. 102, p. 063301, sep 2007.
- [14] F. Haase, D. Lundin, S. Bornholdt, and H. Kersten, “On the Impact of Electron Temperature in Magnetron Sputtering Benchmarked with Energy Flux Measurements,” *Contributions to Plasma Physics*, vol. 55, pp. 701–713, dec 2015.
- [15] D. Lundin, M. Stahl, H. Kersten, and U. Helmersson, “Energy flux measurements in high power impulse magnetron sputtering,” *Journal of Physics D: Applied Physics*, vol. 42, no. 18, p. 185202, 2009.
- [16] Intelmetrics Global Ltd, “Model IL150 Thickness Monitor - Instruction Manual.”
- [17] M. Samuelsson, D. Lundin, J. Jensen, M. A. Raadu, J. T. Gudmundsson, and U. Helmersson, “On the film density using high power impulse magnetron sputtering,” *Surface and Coatings Technology*, vol. 205, pp. 591–596, oct 2010.
- [18] M. Stahl, T. Trottenberg, and H. Kersten, “A calorimetric probe for plasma diagnostics,” *Review of Scientific Instruments*, vol. 81, no. 2, pp. 1–5, 2010.
- [19] S. Gauter, M. Fröhlich, W. Garkas, M. Polak, and H. Kersten, “Calorimetric probe measurements for a high voltage pulsed substrate (PBII) in a HiPIMS process,” *Plasma Sources Science and Technology*, vol. 26, p. 065013, may 2017.
- [20] R. Hippler, *Low Temperature Plasmas : fundamentals, technologies, and techniques. Volume 2*. Weinheim: WILEY-VCH Verlag, 2008.
- [21] J. F. Ziegler, M. Ziegler, and J. P. Biersack, “SRIM – The stopping and range of ions in matter (2010),” *Nuclear Instruments and Methods in Physics Research Section B: Beam Interactions with Materials and Atoms*, vol. 268, pp. 1818–1823, jun 2010.
- [22] H. Kersten, H. Deutsch, H. Steffen, G. Kroesen, and R. Hippler, “The energy balance at substrate surfaces during plasma processing,” *Vacuum*, vol. 63, pp. 385–431, aug 2001.
- [23] D. Depla and S. Mahieu, eds., *Reactive Sputter Deposition*, vol. 109 of *Springer Series in Materials Science*. Berlin, Heidelberg: Springer Berlin Heidelberg, 2008.
- [24] J. A. Thornton, “Magnetron sputtering: basic physics and application to cylindrical magnetrons,” *Journal of Vacuum Science and Technology*, vol. 15, pp. 171–177, mar 1978.
- [25] W. M. Haynes, *CRC Handbook of Chemistry and Physics*. Boca Raton, FL: CRC Press, 2014.
- [26] M. W. Thompson, “II. The energy spectrum of ejected atoms during the high energy sputtering of gold,” *Philosophical Magazine*, vol. 18, pp. 377–414, aug 1968.
- [27] A. Goehlich, D. Gillmann, and H. Döbele, “Angular resolved energy distributions of sputtered atoms at low bombarding energy,” *Nuclear Instruments and Methods in Physics Research Section B: Beam Interactions with Materials and Atoms*, vol. 164-165, pp. 834–839, apr 2000.
- [28] D. W. Hoffman and J. A. Thornton, “Compressive stress and inert gas in Mo films sputtered

- from a cylindrical-post magnetron with Ne, Ar, Kr, and Xe,” *Journal of Vacuum Science and Technology*, vol. 17, pp. 380–383, jan 1980.
- [29] R. E. Somekh, “The thermalization of energetic atoms during the sputtering process,” *Journal of Vacuum Science & Technology A: Vacuum, Surfaces, and Films*, vol. 2, pp. 1285–1291, jul 1984.
- [30] R. Wendt, K. Ellmer, and K. Wiesemann, “Thermal power at a substrate during ZnO:Al thin film deposition in a planar magnetron sputtering system,” *Journal of Applied Physics*, vol. 82, pp. 2115–2122, sep 1997.
- [31] S. M. Rossnagel, “Energetic particle bombardment of films during magnetron sputtering,” *Journal of Vacuum Science & Technology A: Vacuum, Surfaces, and Films*, vol. 7, pp. 1025–1029, may 1989.
- [32] P. Sigmund, “Theory of Sputtering. I. Sputtering Yield of Amorphous and Polycrystalline Targets,” *Physical Review*, vol. 184, pp. 383–416, aug 1969.
- [33] R. S. Robinson, “Energetic binary collisions in rare gas plasmas,” *Journal of Vacuum Science and Technology*, vol. 16, pp. 185–188, mar 1979.
- [34] D. Lundin, C. Vitelaru, L. D. Poucques, N. Brenning, and T. Minea, “Ti–Ar scattering cross sections by direct comparison of Monte Carlo simulations and laser-induced fluorescence spectroscopy in magnetron discharges,” *Journal of Physics D: Applied Physics*, vol. 46, p. 175201, may 2013.
- [35] Y. Yamamura and M. Ishida, “Monte Carlo simulation of the thermalization of sputtered atoms and reflected atoms in the magnetron sputtering discharge,” *Journal of Vacuum Science & Technology A: Vacuum, Surfaces, and Films*, vol. 13, pp. 101–112, jan 1995.
- [36] D. W. Hoffman, “A sputtering wind,” *Journal of Vacuum Science & Technology A: Vacuum, Surfaces, and Films*, vol. 3, pp. 561–566, may 1985.
- [37] S. M. Rossnagel, “Gas density reduction effects in magnetrons,” *Journal of Vacuum Science & Technology A: Vacuum, Surfaces, and Films*, vol. 6, no. 1, p. 19, 1988.
- [38] I. Petrov, I. Ivanov, V. Orlinov, and J. Sundgren, “Comparison of magnetron sputter deposition conditions in neon, argon, krypton, and xenon discharges,” *Journal of Vacuum Science & Technology A: Vacuum, Surfaces, and Films*, vol. 11, pp. 2733–2741, sep 1993.
- [39] K. Koura and H. Matsumoto, “Variable soft sphere molecular model for air species,” *Physics of Fluids A: Fluid Dynamics*, vol. 4, pp. 1083–1085, may 1992.
- [40] F. P. Incropera, D. P. DeWitt, T. L. Bergman, and A. S. Lavine, *Fundamentals of Heat and Mass Transfer*. Hoboken, NJ, USA: John Wiley & Sons, Inc., 2007.
- [41] Massachusetts Institute of Technology, “Radiation Heat Transfer Between Planar Surfaces,” <http://web.mit.edu/16.unified/www/FALL/thermodynam/>, 2018.
- [42] R. Feder, C. Bundesmann, H. Neumann, and B. Rauschenbach, “Ion beam sputtering of germanium – Energy and angular distribution of sputtered and scattered particles,” *Nuclear Instruments and Methods in Physics Research Section B: Beam Interactions with Materials and Atoms*, vol. 334, pp. 88–95, sep 2014.
- [43] A. A. Komlev, E. A. Minzhulina, V. V. Smirnov, and V. I. Shapovalov, “Influence of argon pressure and current density on substrate temperature during magnetron sputtering of hot titanium target,” *Applied Physics A*, vol. 124, p. 48, jan 2018.
- [44] E. A. Minzhulina, V. I. Shapovalov, V. V. Smirnov, A. V. Zav’aylov, and V. S. Levitskiy, “Thermal processes during reactive sputtering of

hot titanium target,” *Journal of Physics: Conference Series*, vol. 857, p. 012031, may 2017.

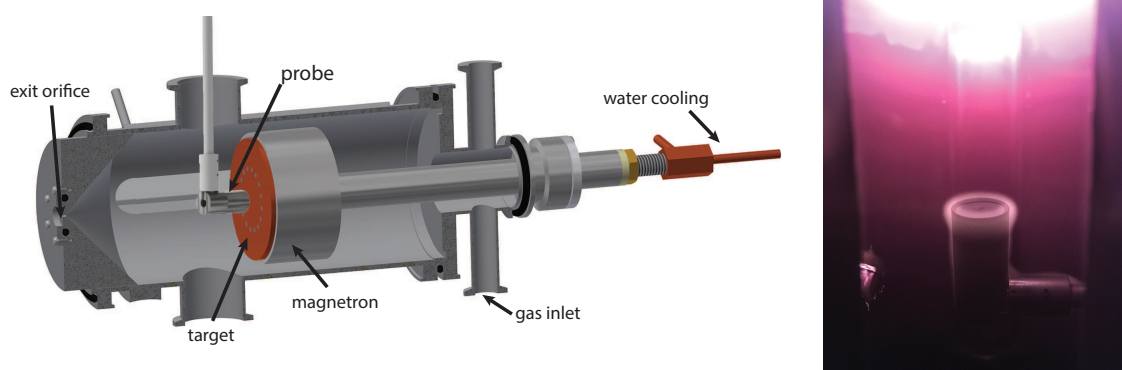
- [45] A. Caillard, M. El’Mokh, N. Semmar, R. Dusart, T. Lecas, and A.-L. Thomann, “Energy Transferred From a Hot Nickel Target During Magnetron Sputtering,” *IEEE Transactions on Plasma Science*, vol. 42, pp. 2802–2803, oct 2014.
- [46] A. Anders, “A structure zone diagram including plasma-based deposition and ion etching,” *Thin Solid Films*, vol. 518, no. 15, pp. 4087–4090, 2010.
- [47] D. M. Mattox and G. J. Kominiak, “Structure Modification by Ion Bombardment during Deposition,” *Journal of Vacuum Science and Technology*, vol. 9, pp. 528–532, jan 1972.
- [48] J.-W. Lim, Y. Ishikawa, K. Miyake, M. Yamashita, and M. Isshiki, “Influence of Substrate Bias Voltage on the Properties of Cu Thin Films by Sputter Type Ion Beam Deposition,” *MATERIALS TRANSACTIONS*, vol. 43, no. 6, pp. 1403–1408, 2002.

Publication IV

Calorimetric investigations in a gas aggregation source

Authors	S. Gauter, F. Haase, P. Solar, O. Kylian, P. Kus, A. Choukourov, H. Biederman and H. Kersten
Journal	Journal of Applied Physics (submitted)
Technique	DC magnetron sputtering (DCMS)
Utilized Probes	Passive thermal probe (PTP), Quartz crystal microbalance (QCM), Langmuir probe (LP)
Own contribution	approx. 45%

Experimental Setup:



Motivation:

To create a better understanding of the formation processes for particles and clusters in a magnetron sputtering gas aggregation source, it is mandatory to gather detailed information about the conditions inside the aggregation chamber. To achieve this, measurements of the plasma parameters, the deposition rate and the energy flux can provide fundamental information. This applies both to the case of single element particles as well as more complex systems created from composite targets. In these systems, it is of special interest to understand the different contributions in the energy flux and how they can be attributed to the different elements in the target.

Main results:

In the higher pressure regime used in gas aggregation sources (20 - 210 Pa), the main mechanisms responsible for the energy flux to a floating substrate were found to be comparable to those observed in the conventional DCMS pressure regime (0.5 - 2 Pa). While the contribution from electrons and ions is negligible, especially the contribution from fast reflected

neutrals and that from the sputtered atoms was found to dominate the energy flux. Furthermore, the effect of gas-rarefaction appeared to be of specific importance in this comparably high-pressure environment.

Calorimetric investigations in a gas aggregation source

Sven Gauter,¹ Fabian Haase,¹ Pavel Solař,² Ondřej Kylián,² Peter Kůš,³ Andrei Choukourou,² Hynek Biederman,² and Holger Kersten¹

¹*Institute of Experimental and Applied Physics, Kiel University, Kiel, Germany*

²*Department of Macromolecular Physics, Faculty of Mathematics and Physics, Charles University, Prague, Czech Republic*

³*Department of Surface and Plasma Science, Faculty of Mathematics and Physics, Charles University, Prague, Czech Republic*

(Dated:)

A gas aggregation source based on DC magnetron sputtering was investigated using a passive thermal probe and supplementary diagnostics (Langmuir probe and quartz crystal microbalance). Parameter variations of pressure, axial distance and magnetron current have been performed for three different targets (pure Cu, pure W, composite Cu/W) in argon discharge. The measurements showed the energy flux to be significantly higher for the case of the pure tungsten and the composite target compared to the copper target, which is likely a result of the strongly increased amount of neutrals being reflected from the heavier targets. Furthermore, gas rarefaction by the sputtered atoms was found to be essential for the understanding of the observed energy flux and that the dominant contributors to the energy flux in the higher pressure regime are comparable to those observed in the conventional lower pressure regime. Selected deposited films have been investigated ex-situ by scanning electron microscopy, which allowed to gain insight into the nanoparticle formation in relation to the observed energy conversion.

I. INTRODUCTION

Metal nanoparticles (NPs) produced by means of gas aggregation cluster sources (GAS) represent an ever growing field in nanoscience¹⁻⁵. In the past, the major focus was laid upon construction of GAS themselves^{6,7}, to understand the basic principles of the nanoparticle formation process^{1,2,8,9}, the properties of single-phase particles and their transport to substrates¹⁰⁻¹². Recent developments shift the focus from single material to composite nanoparticles, which resulted in a variety of different approaches to achieve complex nanoparticle formation. Some methods employ multiple steps such as in-flight coating or subsequent coating of single-metal NPs by a thin film of another material^{13,14}. Although the formation of the core is in this case completely decoupled from the deposition of the shell the produced shell is usually very thin (typically several nm). Another method utilizes simultaneous sputtering of two or more metals from several magnetrons in one aggregation chamber¹⁵ allowing for the production of multi-component NPs. Although control of the component ratio can be well achieved with this method, the control of the overall homogeneity is not straightforward. The same problem arises when a single magnetron is used with a target composed from two halves consisting of two different metals^{16,17}. Other studies with different forms of composite targets like a silver target with a concentric thin gold wire inserted in the erosion track¹⁸ or various alloyed targets¹⁹⁻²¹ were found to reliably produce nanoparticles with varying results regarding particle size distribution, composition and structure. A similar approach, which is investigated in this study is based on small pellets of different material located in the erosion track. Although the possibility to produce core-shell NPs using this method was already demonstrated²², the formation and growth of such NPs

is still not well-understood. This is partially due to insufficient knowledge of the processes occurring inside the aggregation chamber, such as heating/cooling of growing NPs. To gain insight on the energy flux inside the aggregation chamber and, thus, also on the energy conversion relevant for the formation process of the particles, energy flux measurements using a passive thermal probe (PTP) were performed for different settings of discharge power, gas pressure and distance to target. Supplementary to the measurement of the power density (energy flux) with the PTP, the deposition rate was measured using a quartz crystal microbalance (QCM) and plasma parameters were monitored with a Langmuir probe (LP). To correlate the obtained experimental values to the formation process of the particles, these test films were deposited for selected parameter sets and analyzed using a scanning electron microscope (SEM).

II. EXPERIMENTAL SETUP OF THE GAS

The investigated system represents a typical gas aggregation cluster source consisting of an indirectly cooled 3 inch magnetron inserted on the axis of a cylindrical vacuum chamber of 100 mm diameter. The distance between the target and the exit orifice (2 mm diameter) was 131 mm for the standard magnetron position (distance magnetron to PTP: 16 mm). To allow extraction of particles, the aggregation chamber is connected to the main, differentially pumped vacuum chamber ($p < 1$ Pa, 210 l/s from turbo pump). The operation pressures of 20 - 210 Pa inside the aggregation chamber were obtained with a gas flow of 2 - 40 sccm of argon introduced at the top of the chamber (see figure 1). Differential pumping creates a pressure gradient directed from the gas input of the aggregation chamber towards its exit orifice, allow-

ing efficient transport of clusters and particles. Both the magnetron and the chamber walls were cooled with water. The position of the magnetron in the chamber was adjustable via a sliding vacuum feedthrough, see figure 1. The magnetron was powered by an *Advanced Energy MDX500* DC power supply operated in constant current mode. The magnetron voltage, current and power were continuously recorded to monitor the process. Pure Ar was used as a process gas.

For all measurements, the probes were side-mounted to the aggregation chamber facing the magnetron target. Since the probes could not be moved along the vertical axis of the magnetron, the distance variation was performed by moving the magnetron to the most distant position ($d_{max} = 66$ mm) and then successively moving it closer to the probes with intermittent measurements until reaching the minimum distance of $d_{min} = 16$ mm.

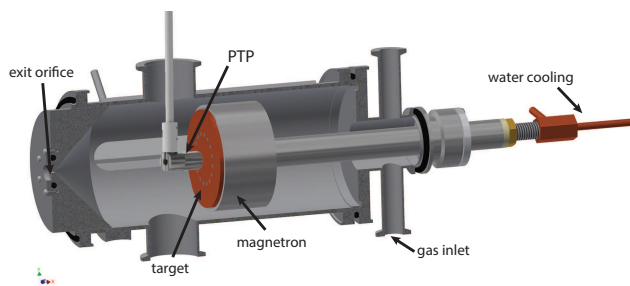


Figure 1: Schematic drawing of the aggregation chamber. The probes were mounted inside the aggregation chamber at a standard distance of 16 mm from the magnetron.

Identical parameter variations as summarized in table I have been performed for three different targets: a pure tungsten target, a pure copper target and a composite target made from copper with 37 tungsten pellets of 3 mm diameter distributed over the race track (see figure 2). All targets were 3 mm in thickness and exhibited similar erosion depths in the race track area. To identify systematic errors such as time-dependent changes in the surface condition of the target, several parameter settings have been measured twice at different times during the variation. The resulting deviation is represented as error bars in the presented measurement results.

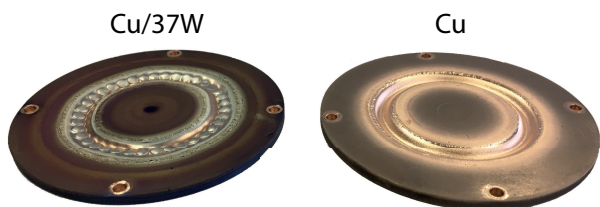


Figure 2: Photograph of the utilized Cu/37W (left) and pure Cu (right) 3 inch targets used in the gas aggregation source. The pure W target is not shown.

III. UTILIZED PROBES

All measurements were performed subsequently with three different kind of probes centered on the chamber and magnetron axis at approximately the same distance to the target. The Langmuir probe measurements were performed using the PTP substrate as a planar Langmuir probe which was biased using a copper wire. The corresponding plasma parameters were primarily calculated to allow an estimation of the energy flux by ions and electrons and are, thus, not discussed in greater detail in this study.

A. Quartz crystal microbalance

For the measurement of the deposition rate, a commercially available quartz crystal microbalance (QCM) *IL150* from *Intelmetrics Global Ltd* with a gold coated 14 mm diameter crystal without water cooling has been used. As described in section II, the QCM was introduced to the chamber using the same mount as used for the PTP. Due to the different probe geometry, the QCM sensor was positioned at a slightly farther distance of 20 mm to the target surface at standard position. Since the QCM detects the change of mass on the quartz crystal, it is necessary to provide material specific constants to allow the calculation of the deposition rate in nm/min ²³. Since, the determined deposition rate calculated from the change of mass is directly proportional to the assumed film density that has been set as an input parameter in the IL 150, it is necessary to obtain realistic densities for the different utilized targets. This was achieved by performing test depositions at different parameters allowing to deduce effective densities from thickness and weight measurements. The resulting densities which were used for the determination of the deposition rates presented in section IV A are summarized in table II. It should be noted that the measured densities are lower as compared to the values of bulk metals which is due to the highly porous character of deposited nanoparticle films.

Although the determined densities from these test depositions showed relatively small errors, later depositions with different substrate holder configurations or substrate material showed strongly deviating results. For this reason, the results of the QCM are only evaluated regarding their relative changes for each investigated target. Here it should be noted, that the change of film density for the different investigated conditions will result in somewhat erroneous deposition rates. However, this effect is expected to be small compared to the general trends and is not further considered for sake of simplicity.

B. Passive thermal probe

For the energy flux measurements inside the aggregation chamber a passive thermal probe was side-mounted

Table I: Experimental parameters used for the parameter variations performed for three different targets, with the varied values printed **bold**. All experiments were performed with argon and the magnetron in was operated in current regulated mode. The standard condition was chosen to be at 16 mm distance to the target, 500 mA current and 60 Pa pressure.

	variation of distance	variation of current	variation of pressure
distance (mm)	16 - 66	16	16
current (mA)	500	50 - 500	500
pressure (Pa)	60	60	20 - 210

Table II: Experimentally determined film densities for the three investigated targets.

target material	density (g/cm ³)	
	bulk	determined
composite (Cu/37W)		11.4 ± 0.9
copper	8.96	7.4 ± 0.6
tungsten	19.3	11.4 ± 0.8

at a distance of 16 mm to the magnetron target and facing the target (see figure 1). A detailed description of this probe and the evaluation of the measurement is presented here as the understanding of the procedure is important for the discussion of the results in section IV. The probe utilized in the experiments consists of a sensor plate (substrate dummy) made of copper with a diameter of 11 mm and a thickness of 70 μm . Spot-welded to the back of it is a Type K thermocouple and an additional copper wire for biasing and current readings²⁴. The sensor plate is surrounded by a metallic shielding to make sure, that only contributions from the upper half-space are considered. A schematic drawing of the PTP design is shown in figure 3.

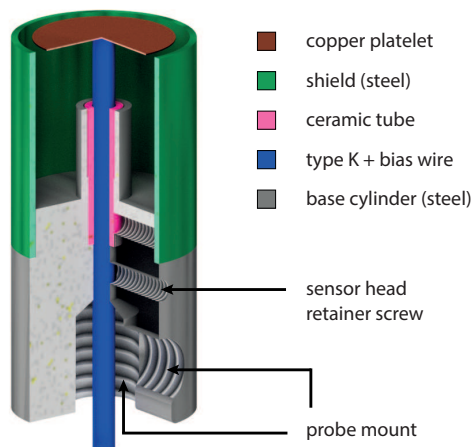


Figure 3: Schematic drawing of the PTP sensor head. The Type K thermocouple and the bias wire are spot-welded to the back of the copper platelet that represents the substrate. The whole sensor is housed in a stainless steel cylinder to shield it from any surrounding influences other than the ones coming from the upper half-space.

It should be noted that the PTP always measures a time-averaged and integrated energy flux that is generated by various energy sources and processes such as charged and neutral particles, surface processes like film formation or radiation from a hot target or chamber walls, respectively. The basic idea of the PTP is to calculate the energy flux from the relation between the time derivative of the enthalpy (\dot{H}) and the time derivative of the temperature (\dot{T}_s) of a well defined substrate dummy. During the heating (T_h - energy source on) and the cooling (T_c - energy source off) of the substrate dummy this relation yields:

$$\text{Heating: } \dot{H}_h = C_s \dot{T}_h = P_{in} - P_{out,h} \quad (1)$$

$$\text{Cooling: } \dot{H}_c = C_s \dot{T}_c = -P_{out,c} \quad (2)$$

Here C_s is the heat capacity of the probe, P_{in} gives the power from the source and $P_{out,h}$ and $P_{out,c}$ denote the power leaving the probe during heating and cooling, respectively. Assuming that the negative cooling terms of equation 1 and 2 are equal for the same substrate temperatures ($P_{out,h}(T_s) = P_{out,c}(T_s)$), the equations for heating and cooling can be combined to calculate the energy flux J_{in} :

$$J_{in} = \frac{P_{in}}{A_s} = \frac{C_s}{A_s} (\dot{T}_h - \dot{T}_c), \quad (3)$$

There are several different methods of evaluating calorimetric temperature curves, however, if the power source is capable of fast switching between off- and on-states, the most desirable method is the so-called *kink method*. The main reason for this is that for the assumption of equal cooling terms during the heating and the cooling phase, any energy flux originating from secondary heat sources has to be constant for the investigated time period. When evaluating with the *kink method*, as described in²⁵, only a short time period of about 2 s around the kinks between the cooling and heating phases are evaluated. This means, that the above-mentioned assumption only needs to apply in this short time frame. Accordingly, any contribution to the energy flux which is relatively constant during this time period does not significantly influence the measured energy flux. Through different measurement procedures, this allows to eliminate certain effects from the measurement results. For example in the case investigated in this study, the contribution from target radiation does not appear in the measurement since the target temperature can be assumed

to be approximately constant during the short measurement time of a few seconds. If instead, the probe would be turned away on plasma shut-off or if a cooled shutter is used to shut off the energy flux, the target radiation would be included in the measurement.

The kink that evolves when switching the power source on from an off-state is referred to as heating kink and the kink that is created when the power source is switched off again, and the next cooling phase starts, is referred to as cooling kink. From both kinks an accurate measurement of the energy flux at these times is obtained and any potential discrepancy between those two results can already be a valuable hint for the stability of the investigated process and the reliability of the measurement method. In figure 4 an exemplary temperature curve with clearly labeled cooling and heating phases as well as evaluated points and corresponding linear fits around the kinks are presented.

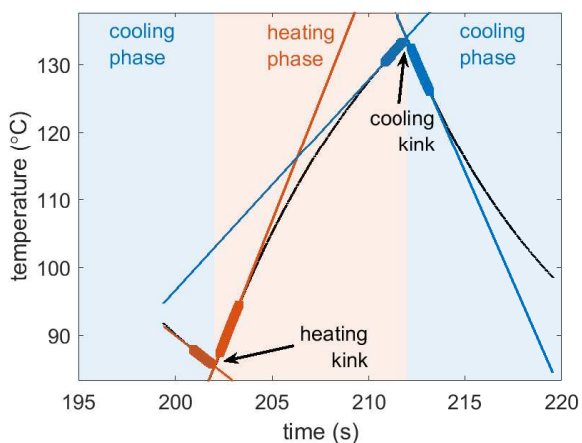


Figure 4: Exemplary evaluation of a PTP curve with heating and cooling kink. The highlighted areas in red and blue denote the data points that were used for the linear fits.

By subtracting the slopes of the two linear fits around the kinks, $\dot{T}_h - \dot{T}_c$ can be easily obtained and the energy flux can be calculated from equation 3, using the heat capacity C_s and surface area A_s of the probe. The heat capacity was determined before and after the measurement campaign using a calibration experiment introduced in²⁴. The obtained values $C_{s,before} = 0.027$ J/K and $C_{s,after} = 0.036$ J/K show a significant deviation which is a result of the film deposited on the probe surface through the course of the measurement campaign. Figure 5 shows a microscopic photograph of the cross section of this film onto the PTP, where the temporal sequence of the measurements are mirrored by the color of the coating; first the copper target was investigated, second the composite target and last the pure tungsten.

To compensate for the gradual increase of the heat capacity, for each variation the value used for the evaluation of the PTP data was approximated by an interpolation taking into account the time the probe was exposed

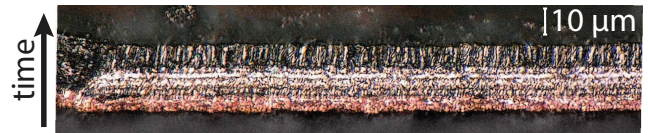


Figure 5: Photograph of the deposited film on the PTP after the measurement campaign. The film was broken off from the probe and investigated under a microscope. Note the copper layer at the bottom exhibiting a somewhat grainy growth structure, followed by the film deposited with the composite target (middle layer) and the top tungsten layer, which exhibits a more columnar growth structure.

to the plasma e.g. for the data from the first variation (distance-Cu) the initial value of 0.027 J/K was used, for the variation in the middle (e.g. pressure-Cu/37W) an adjusted value of 0.030 J/K was used and for the last variation (pressure-W) the final value of 0.036 J/K was used.

IV. RESULTS AND DISCUSSION

A summary of the results obtained with the QCM and the PTP together with the corresponding values of the magnetron power are presented in figure 6. In the following section these complex correlations will be described along the discussion focused on the calorimetric results using QCM and Langmuir data to gain insights into the composition of the energy flux. The SEM images are used to provide a concrete connection between the measured values and the nanoparticle growth and are shortly discussed at the end of this section.

A. Deposition rate

The trends for the deposition rate, which were obtained for the parameter variations introduced in table I, are shown in the second row of figure 6. Here we observe an almost linear trend for the distance- and the magnetron current variation, while the pressure variation exhibits a somewhat more complex dependence.

In a simple model, the deposition rate is mostly defined by two basic processes: (i) the production of sputtered atoms and (ii) the transport of sputtered atoms. The production of sputtered atoms depends on the sputter yield γ_s and the amount of species (energetic ions and neutrals) impinging on the target surface. A characteristic value which can be associated to the latter quantity, is the magnetron current since it is approximately proportional to the amount of kinetic species arriving at the target surface. The sputter yield can be expected to be a function of the mass ratio between target and impinging species as well as of the energy of the impinging particles. This dependence has been investigated and semi-empirically described by many groups, however, especially for the lower energy range, still no universally accepted model is

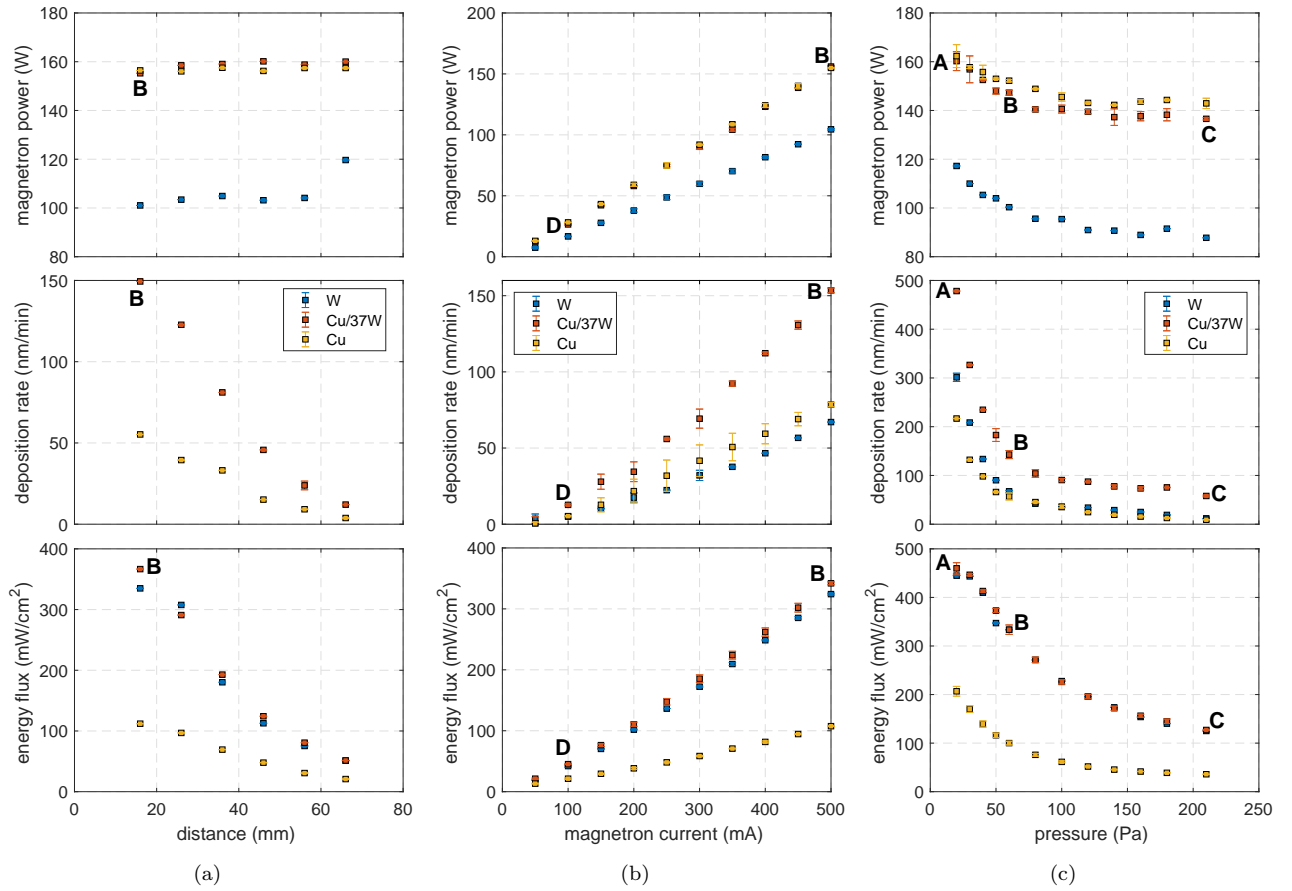


Figure 6: Summary of the deposition rates obtained for the investigated targets and parameter variations. (a) variation of distance between probe and target with 500 mA current and 60 Pa. Unfortunately, no distance variation while measuring the deposition rate for tungsten has been performed. (b) variation of magnetron discharge current at 60 Pa and 16 mm distance, (c) variation of gas pressure with 500 mA current at 16 mm. Error bars obtained from repeated measurements are shown for the variation of magnetron current (b) and argon pressure (c), although in the latter case no repeated measurements were performed with tungsten. For most conditions the energy flux measurements showed a very good reproducibility, making the error bars smaller than the data points. The bold letters mark the data points for the corresponding SEM images (see fig. 9 and 10) in the different conditions.

available^{26,27}. However, qualitatively all studies describe an approximately linear increase with increasing energy of the bombarding species and impinging- to target-mass ratio for the parameter region relevant in this study²⁸. Taking into account the changes of magnetron power presented in the first row of figure 6b, the observed evolution of deposition rate as a function of the magnetron current can be understood directly due to the changes in particle production. For Cu and W we observe an increase of the deposition rate with an approximately linear dependence, while for Cu/37W we observe an above linear increase as a function of the magnetron current. This evolution is mostly driven by the increase of the amount of kinetic atoms arriving at the target cathode which was increased by one order of magnitude. While this would result in a strictly linear dependence, the effect of increased magnetron voltage ($\Delta U_{mdx} \sim 40$ V from 50 mA to 500 mA) provides an additional factor due to the aforementioned

increase in sputter yield.

To explain the results obtained for the variation of distance and pressure (second row figure 6a and 6c), the transport of the species from the target to the probe surface needs to be taken into account as well. In the investigated pressure regime the transport is strongly dominated by collisions with the background gas and with a mean free path in the sub-millimeter range, a diffusion-dominated transport can be expected. Using the common approach based on a Maxwellian gas with collisions described by the Poisson distribution, the mean free path λ_{mfp} for copper and tungsten in argon can be plotted as a function of the background pressure as shown in figure 7²⁹. When comparing this figure to the deposition rate obtained for the pressure variation, the resemblance between the two curves suggests, that the observed dependence is dominantly defined by the collision frequency of the sputtered particles with the background gas. This

trend is additionally amplified by the increase in magnetron power and voltage shown in the first row of figure 6c which leads to an increased sputter yield for lower pressures.

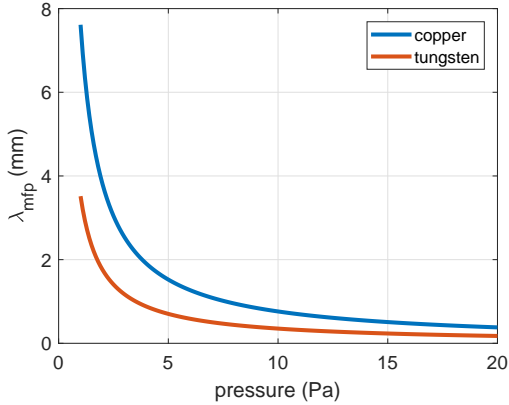


Figure 7: Calculation of the mean free path for copper and tungsten in argon at 300 K according to kinetic gas theory.

The linear decrease for greater distances between target and probe can be directly understood as a result of the linearly increasing number of collisions the sputtered particles undergo as they drift towards the probe. While the axial drift does not result in a decreasing flux, the diffusion perpendicular to the chamber axis and associated losses on the wall result in a decrease of the sputtered flux. For comparable systems with diffusion transport this has been theoretically and experimentally observed by Westwood³⁰ and Ecker et al.³¹.

The conspicuous deviation between the values obtained by the QCM for the compound target compared to the other two targets are not explicable from the data obtained in this study. Since separate determination of the deposition rate by sample deposition and subsequent measurement of the film thickness have not shown a strongly increased deposition rate for Cu/37W, the deviation is likely attributed to some systematic error. Similarly, the absolute QCM values for Cu and W did not match with the values obtained from sample depositions and ex-situ investigations that were performed for selected discharge parameters. The similarity, in spite of different sputtering yields, between copper and tungsten is thus likely attributed to systematic errors as well.

B. Energy flux measurements

As described in section III B, the energy flux obtained with the PTP is a time- and energy integrated quantity which reflects the energy flux originating from a complex set of processes^{29,32}. In the case of magnetron sputtering in the conventional pressure regime of up to a few Pa, important contributions typically arise from the kinetic impact of particles (ions, electrons, energetic neu-

trals), from recombination processes at the surface or from the sublimation enthalpy which is released during film formation on the substrate. In typical DC magnetron sputtering experiments, the contributions originating from the ion-electron recombination and the kinetic flux of ions and electrons to the probe surface only contribute a few percent unless the substrate is biased to voltages significantly different from the floating potential^{33,34}. The Langmuir measurements performed in this study resulted in ion current densities in the range of $10^{-3} - 10^{-1}$ mA/cm², maximum differences between plasma and floating potential of ~ 12 V, approximate electron temperatures of around 2 eV and electron densities of $\sim 10^{15}$ m⁻³. According to the common theory described, e.g. by Kersten et al.³⁵ and Depla et al.³⁶, the contribution due to ions and electrons can be easily calculated to be in the range of only a few mW/cm². Considering the measured energy flux values of up to several 100 mW/cm², the observed trends must, thus, be determined by other contributions like film condensation, kinetic neutral particles or radiation from the plasma or the cathode, respectively.

As the pressure increases and accordingly the mean free paths of ions and neutral particles decreases to values several times smaller than the distance between substrate and cathode, an increasing amount of energy is transferred to the Ar background gas. This transfer of kinetic energy into the gas volume was investigated by Hoffman for a cylindrical magnetron sputtering source and resulted in the concept of 'sputtering wind' which illustrates the directional non-uniform aspect of these energetic fluxes³⁷. Inspired by this work, a detailed study investigating the reduction of the gas density in front of a planar magnetron cathode has been performed by Rosnagel³⁸. Herein, the so called 'rarefaction' of the gas was measured as an apparent pressure reduction and was thoroughly investigated for different combinations of gases and target materials. These investigations revealed a density reduction of up to 85% for high pressure (4 Pa) and high magnetron power and pointed out the sputtered particles as the main driver of the gas rarefaction. Using the Monte Carlo technique, Turner³⁹ calculated similar results which coincided with the observations made by Rosnagel. From these calculations, additional parameters affecting the efficiency of the energy coupling between the sputtered and the background gas atoms have been identified. Besides the sputtering yield, the binding energy of the target material and the collision cross-section and average fraction of energy transferred between sputtered particles and background gas have all been found to produce greater rarefaction for higher values. The corresponding values for the two materials used in this study are summarized in table III.

Although the above-mentioned measurements and simulations were performed in a lower pressure regime (< 20 Pa), the same principles apply in the GAS discharge investigated in this study. As mentioned above, due to the short mean free paths, we expect the sputtered flux to

Table III: Relevant parameters for energy transfer from sputtered atoms to the background gas: sputtering yield Y for sputtering ion energy of 300 eV⁴⁰, binding energy E_{bin} , collision cross-section σ ²⁹ and average fraction of energy transferred from the sputtered atom per collision R_{te} ³⁰. The last column gives the energy reflection coefficient R_E of the target material for bombardment by 400 eV argon ions^{41,42}.

	Y	E_{bin} (eV)	σ (nm ²)	R_{te}	R_E
Cu	1.59	3.5	0.54	0.57	0.01
W	0.40	8.8	1.18	0.31	0.12

be thermalized within a short distance from the cathode surface. However, as demonstrated by Urbassek et al. this distance is significantly underestimated if the coupling between the energetic copper particle flow and the argon background gas is neglected⁴³. It is difficult to estimate the exact distance where the gas reaches the highest temperature or to estimate the actual mean free path, however, taking into account the obtained measurement data, we can make the following assumptions for our system:

- I. strong rarefaction with severe reduction of gas density close to the target surface
- II. the rarefaction is dominantly driven by the sputtered metal atoms
- III. due to the rarefaction, the mean free path for reflected Ar neutrals is sufficiently long for them to reach the probe with high energies

Assumptions I. and II. can be directly derived from the recorded magnetron power. A typical signature of rarefaction is the increase of magnetron voltage due to the increased impedance of the plasma³⁸. From the parameters given in table III it can be expected, that the rarefaction is more pronounced and strongest at a position much closer to the target for the cases where copper is present in the system as compared to the case where only tungsten is driving the rarefaction. This can be understood as a result of the shorter mean free path and more efficient energy exchange between the sputtered atoms and the background gas. The resulting reduction of gas density can be observed as an increase in magnetron voltage and power in the first row of figure 6. Here we see almost identical values for the pure copper and the composite target while for tungsten persistently lower values are obtained. Although this could be an effect of different secondary electron yields of copper (1.3) as compared to tungsten (1.0)⁴⁴, this should actually result in a lower required voltage for copper as for tungsten to sustain the same current setpoint. However, figure 6 exhibits higher voltage values for copper which contradicts with this hypothesis and emphasizes the importance of rarefaction for the discharge parameters in this pressure regime. The similarity observed between the composite target and the pure copper target also underlines the dominance of copper as a driver of the rarefaction close to the target and

it indicates that the rarefaction close to the target is already saturated with the amount of copper available from the composite target.

Assumption III. can be derived from the similarity between the energy flux of the composite and the tungsten target which is observed in all measurements in the third row of figure 6 and from an analysis of the possible contributions to the integral energy flux.

From the Langmuir probe measurements it was derived that the energy flux is not strongly affected by the contribution due to electrons and ions and must, therefore, originate from other processes. The plasma radiation can also be eliminated from the list of possible origins, since the typically observed values^{41,45} are too low and the expected changes do not reflect the observed trends. Thus, the energy flux can only be attributed to the sputtered particles, to the reflected particles or to the conduction from the heated gas.

In terms of energy flux, rarefaction can primarily be understood as a loss mechanism. Since the directed energy flux of the sputtered particles is transformed into thermal energy of the gas, the energy is transferred less directly and with losses due to the isotropic nature of the energy flux from the heated gas. In general the maximum of gas temperature can be expected to be close the region where the majority of the sputtered particles are thermalized. For the investigated high pressures we expect this region to be quite close to the target i.e. less than 16 mm away from the target. While the sputtered atoms are expected to be mostly thermalized, the longer mean free path of the fast reflected argon atoms allows them to reach the probe with a significant fraction of their initial energy. The energy flux should, thus, be a composition of the energy released during the film formation, the kinetic energy transferred upon impact of reflected argon and the heat conducted from the hottest point of the gas towards the substrate surface. As mentioned above, this last contribution increases as a result of stronger energy losses of the sputtered atoms and is expected to be strongest for copper, since the most efficient rarefaction is expected for this material. If this effect would be critical for the energy flux we should expect, analogous to the results of the magnetron power, a similar energy flux for the copper- and the composite target. Instead, we observe a strong resemblance between the energy flux of the composite- and the tungsten target. This observation suggests that the energy flux is directly related to the presence of tungsten in the target. From table III it can be seen that tungsten exhibits more than twice the binding energy of copper, which accordingly results in about twice the energy flux from film condensation per deposited atom. However, to achieve energy flux values as high as obtained here solely from the released heat of condensation, deposition rates five times the values observed in the QCM measurements would be required. Therefore, the energy deposited by the reflected argon is assumed to be the dominant contribution to the integral energy flux, especially in the cases of the composite

and the tungsten target. The energy reflection coefficient R_E describes the ratio of energy reflected from the target upon impact of an ion and is given in table III for the case of 400 eV argon ions. Due to the small mass ratio between argon and tungsten, more than 10% of the energy is reflected in the form of fast neutrals, while for copper only about 1% is reflected. From figure 2 it is visible that for the composite target, a high percentage of the racetrack area is made up of tungsten and we can, thus, expect a comparable amount of fast reflected particles as compared to the pure tungsten target. Taking into account the different magnetron powers, a similarly high energy flux between the two target systems can be expected. We conclude that the kinetic energy from the sputtered particles is likely dissipated by the heating of the gas and that conduction of heat through the gas only contributes a relatively small portion to the integral energy flux. The energy released during film formation is expected to contribute a considerable amount. However, it is found to be significantly smaller than the energy flux attributed to the kinetic impact of reflected neutral particles.

Since the energy flux can be understood as power transfer from the target towards the substrate, it is expected that it changes proportionally with the input power of the magnetron. If a strong change in power is present, this usually dominates the change in the energy flux as it is evident in the strong resemblance between magnetron power and energy flux for the variation of the magnetron current (see figure 6b). Eliminating this direct proportional effect, the measurement data allows for better comparison between different systems and emphasizes other, less dominant effects. One way to achieve this is by combining the results obtained for the magnetron power P_{mag} and the energy flux J_s to calculate a value for ratio η of the power transfer with the following equation:

$$\eta = \frac{J_s}{P_{mag}/A_{mag}}, \quad (4)$$

with A_{mag} being the target surface area. Such normalized results are summarized in figure 8.

After taking into account the increased magnetron power for Cu and Cu/37W, tungsten exhibits the highest energy flux values compared to the other two targets in all variation runs (see figure 8). A similar difference in energy flux between Cu and W has been observed by Harbauer et al.⁴⁶ in the conventional lower pressure regime. Although they observed three times higher deposition rates for copper as compared to tungsten, they obtained three times higher values for the energy flux for tungsten, which was argued to likely be a result of the higher heat of condensation (8.8 eV for W, 3.5 eV for Cu⁴⁷). Thornton et al.^{45,48} obtained similar results from their investigations of the energy flux per deposited atom. They found that the energy transfer per deposited particle of tungsten yields about eight times the one obtained for copper. Additional to the aforementioned higher heat of condensation, Thornton points out the importance of

reflected argon atoms with energies up to the cathode potential as an important contribution.

Although these investigations were done at a pressure of roughly 1 Pa, the findings coincide with our results shown in figure 8 and, thus, they further support the assumption that the relevant contributions to the integral energy flux in the higher pressure regime of 20 - 210 Pa are similar to the ones found in the conventional pressure regime.

Albeit, as argued in section III A, the absolute values obtained for the deposition rate likely exhibit a significant systematic error, for sake of comparison we shall use them here to obtain an estimate for the obtained energy per deposited atom. E.g. for the variation of the magnetron current we calculate relatively constant energies per atom of ~ 500 eV for tungsten and ~ 100 eV and ~ 150 eV for pure copper and the composite target, respectively. As argued above, these values are too high to be only a result of film deposition, but are most likely attributed to the impact of reflected neutrals and heat conduction through the gas. Compared to the values obtained by Thornton et al., our values are approximately 5 times higher and compared to Drüsedau et al.⁴¹, they are 2.5 times higher. In agreement with the observations by Drüsedau who observed a linear increase of the energy per atom in the pressure regime from 0.1 - 10 Pa, we observed a comparable increase for pressures below 60 Pa. Taking this trend into account the higher values obtained in this study fit reasonably well with the results obtained by the studies in the conventional pressure regime. Drüsedau also supports the assumption that reflected neutrals play a significant role as a part to the energy flux since they calculated the fast neutrals to account for roughly 75 % of the energy per atom in the case of tungsten (figure 9b in⁴¹).

The observation that the composite target exhibits slightly lower normalized energy flux values than the pure tungsten can be understood as a combination of the smaller contribution from film formation due to the smaller binding energy of copper and a reduction of the contribution from reflected neutrals as a result of the reduced race track area covered by tungsten.

C. SEM investigations

To investigate the effect of the different energy flux values on film formation and to compare them to the well-established structure zone model, additional investigations have been performed by an ex-situ study of four deposited films using the composite target at a substrate distance of 16 mm. Three films were deposited with 500 mA and pressures of $p = 20$ Pa, $p = 60$ Pa and $p = 210$ Pa and one film was deposited with a lower current of 100 mA at 60 Pa. The deposited films have been investigated using a scanning electron microscope (SEM) and are presented in figures 9 and 10.

In figure 9 it can be seen that the sample for the low-

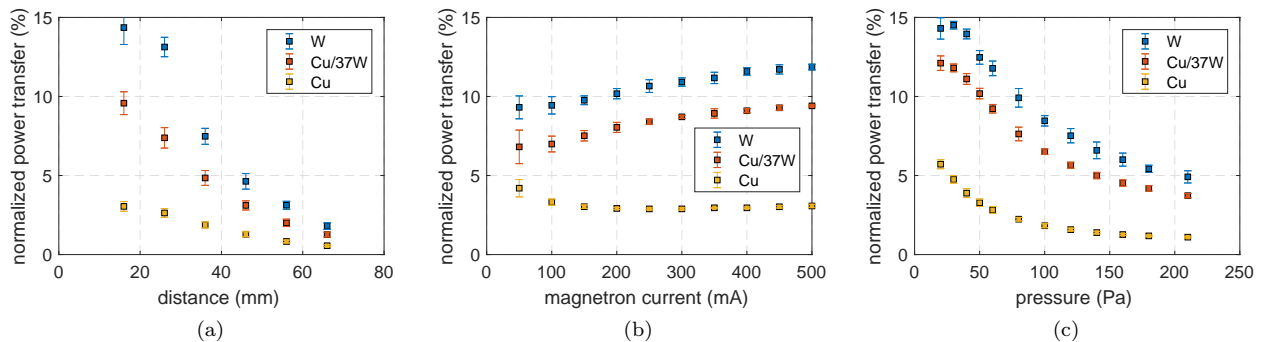


Figure 8: Summary of PTP results normalized with the magnetron power according to equation 4. (a) variation of distance between probe and target with 500 mA current and 60 Pa, (b) variation of magnetron discharge current at 60 Pa and 16 mm distance, (c) variation of gas pressure with 500 mA current at 16 mm.

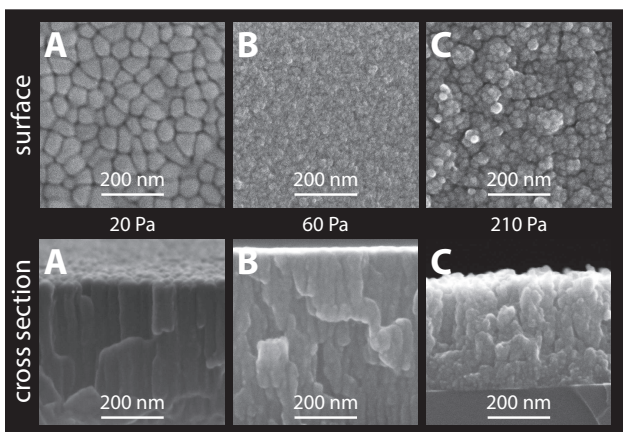


Figure 9: SEM images of deposited film structures using the Cu/37W composite target. The first row shows top view images of the film surface and the second row shows cross sections revealing the growth structure. All depositions were performed at a distance of $d = 16$ mm and a magnetron current of $I_{mag} = 500$ mA. The bold letters correlate to the letters in figure 6, indicating the corresponding magnetron power, deposition rate and energy flux.

est pressure (20 Pa) exhibits a structure as it is known from common film growth. The columnar growth appears to be significantly disrupted by particles and less organized for 60 Pa and at 210 Pa the film appears to be completely composed of bigger particles. Comparing the structure observed for the 20 Pa sample to the structure zone diagram (SZD) by Thornton⁴⁹ or Movchan and Demchishin⁵⁰, we find a zone 1 structure which was observed by Thornton for the highest investigated pressures (~ 4 Pa) or at low substrate temperatures independent of the pressure. The surface exhibits tapered crystallites separated by voids and the structural growth direction is characterized by the incoming particle flux.

Similar to the case for 210 Pa (C), for condition of 100 mA magnetron current and 60 Pa pressure (D) we find a film which is completely composed of particles as

shown in figure 10. However, now the particles exhibit a distinctively different form and size. While in C the film appears to be formed from relatively evenly sized ~ 20 nm particles or clusters of those particles, in D we find a variety of different particles with smooth surfaces and sizes ranging from ~ 20 nm to 100 nm. This difference indicates, that the particles in D were formed at a lower rate by surface growth (attachment of single atoms), whereas the particles in C are likely formed by cluster-cluster collisions. Taking into account the more structured film obtained in B at the same pressure of D but at a significantly higher magnetron current, the role of rarefaction and initial energy of the sputtered atoms for the NP formation becomes apparent.

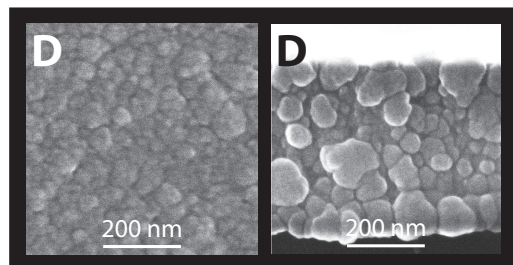


Figure 10: SEM images of deposited film structures using the Cu/37W composite target in 60 Pa at a magnetron current of 100 mA. The left image shows the surface and the right one a cross section of the film. The bold letters correlate to the letters in figure 6, indicating the corresponding magnetron power, deposition rate and energy flux.

V. CONCLUSIONS

Although gas aggregation cluster sources are usually operated in higher pressure regimes than conventional DC magnetron sputtering systems, the basic mechanisms contributing to the integral energy flux are comparable. The current study confirms that contributions from

charged particles (i.e. electrons and ions) and radiation have comparably small influences on the integral energy flux. Similar to the conventional low pressure sputtering regime the integral energy flux is mainly driven by the contribution due to film condensation and reflected neutrals, with the latter being strongly dependent on the mass ratio between gas and target atoms. This was especially evident in the strong resemblance observed in the energy flux between the pure tungsten and the composite target. Gas rarefaction and its accompanying effects were argued to be a significant mechanism in the investigated system as the reduction of the gas density and the associated increase in λ_{mfp} allowed the reflected neutrals to reach the substrate surface with high energies creating a significant contribution to the energy flux.

ACKNOWLEDGEMENTS

This work was partially funded by GACR 17-22016S from the Grant Agency of the Czech Republic.

REFERENCES

- ¹C. Binns, "Nanoclusters deposited on surfaces," *Surface Science Reports*, vol. 44, pp. 1–49, oct 2001.
- ²K. Wegner, P. Piseri, H. V. Tafreshi, and P. Milani, "Cluster beam deposition: a tool for nanoscale science and technology," *Journal of Physics D: Applied Physics*, vol. 39, pp. R439–R459, nov 2006.
- ³C. Cassidy, V. Singh, P. Grammatikopoulos, F. Djurabekova, K. Nordlund, and M. Sowwan, "Inoculation of silicon nanoparticles with silver atoms," *Scientific Reports*, vol. 3, p. 3083, dec 2013.
- ⁴P. Solař, I. Melnichuk, A. Artemenko, O. Polonskyi, O. Kylián, A. Choukourov, D. Slavínská, and H. Biederman, "Nylon-sputtered plasma polymer particles produced by a semi-hollow cathode gas aggregation source," *Vacuum*, vol. 111, pp. 124–130, jan 2015.
- ⁵U. R. Kortshagen, R. M. Sankaran, R. N. Pereira, S. L. Girshick, J. J. Wu, and E. S. Aydil, "Nonthermal Plasma Synthesis of Nanocrystals: Fundamental Principles, Materials, and Applications," *Chemical Reviews*, vol. 116, pp. 11061–11127, sep 2016.
- ⁶K. Sattler, J. Mühlbach, and E. Recknagel, "Generation of Metal Clusters Containing from 2 to 500 Atoms," *Physical Review Letters*, vol. 45, pp. 821–824, sep 1980.
- ⁷H. Haberland, M. Karrais, M. Mall, and Y. Thurner, "Thin films from energetic cluster impact: A feasibility study," *Journal of Vacuum Science & Technology A: Vacuum, Surfaces, and Films*, vol. 10, pp. 3266–3271, sep 1992.
- ⁸T. Takagi, "Ionized cluster beam (ICB) deposition and processes," *Pure and Applied Chemistry*, vol. 60, pp. 781–794, jan 1988.
- ⁹O. Polonskyi, T. Peter, A. Mohammad Ahadi, A. Hinz, T. Strunskus, V. Zaporozhtchenko, H. Biederman, and F. Faupel, "Huge increase in gas phase nanoparticle generation by pulsed direct current sputtering in a reactive gas admixture," *Applied Physics Letters*, vol. 103, p. 033118, jul 2013.
- ¹⁰B. M. Smirnov, I. Shyjumon, and R. Hippler, "Flow of nanosize cluster-containing plasma in a magnetron discharge," *Physical Review E*, vol. 75, p. 066402, jun 2007.
- ¹¹J. Kousal, O. Polonskyi, O. Kylián, A. Choukourov, A. Artemenko, J. Pešička, D. Slavínská, and H. Biederman, "Characterization of nanoparticle flow produced by gas aggregation source," *Vacuum*, vol. 96, pp. 32–38, oct 2013.
- ¹²P. A. Skovorodko, S. A. Brown, and D. Belić, "Gas Dynamic Considerations for Performance of Nanocluster Deposition System," in *AIP Conference Proceedings*, pp. 203–208, 2011.
- ¹³J. Hanuš, M. Vaidulych, O. Kylián, A. Choukourov, J. Kousal, I. Khalakhan, M. Cieslar, P. Solař, and H. Biederman, "Fabrication of Ni@Ti core-shell nanoparticles by modified gas aggregation source," *Journal of Physics D: Applied Physics*, vol. 50, p. 475307, nov 2017.
- ¹⁴A. Caillard, S. Cuynet, T. Lecas, P. Andrezza, M. Mikikian, A.-L. Thomann, and P. Brault, "PdPt catalyst synthesized using a gas aggregation source and magnetron sputtering for fuel cell electrodes," *Journal of Physics D: Applied Physics*, vol. 48, p. 475302, dec 2015.
- ¹⁵M. Benelmekki, J. Vernieres, J.-H. Kim, R.-E. Diaz, P. Grammatikopoulos, and M. Sowwan, "On the formation of ternary metallic-dielectric multicore-shell nanoparticles by inert-gas condensation method," *Materials Chemistry and Physics*, vol. 151, pp. 275–281, feb 2015.
- ¹⁶M. Tchapyguine, T. Andersson, C. Zhang, and O. Björneholm, "Core-shell structure disclosed in self-assembled Cu-Ag nanoalloy particles," *The Journal of Chemical Physics*, vol. 138, p. 104303, mar 2013.
- ¹⁷G. Krishnan, M. A. Verheijen, G. H. ten Brink, G. Palasantzas, and B. J. Kooi, "Tuning structural motifs and alloying of bulk immiscible Mo–Cu bimetallic nanoparticles by gas-phase synthesis," *Nanoscale*, vol. 5, no. 12, p. 5375, 2013.
- ¹⁸A. Vahl, J. Strobel, W. Reichstein, O. Polonskyi, T. Strunskus, L. Kienle, and F. Faupel, "Single target sputter deposition of alloy nanoparticles with adjustable composition via a gas aggregation cluster source," *Nanotechnology*, vol. 28, p. 175703, apr 2017.
- ¹⁹E. Pérez-Tijerina, M. Gracia Pinilla, S. Mejía-Rosales, U. Ortiz-Méndez, A. Torres, and M. José-Yacamán, "Highly size-controlled synthesis of Au/Pd nanoparticles by inert-gas condensation," *Faraday Discuss.*, vol. 138, pp. 353–362, 2008.
- ²⁰V. M. Serdio, M. A. Gracia-Pinilla, S. Velumani, E. G. Pérez-Tijerina, and W. van der Weil, "Synthesis and Characterization of NiCr Self-Assembled Nanorings," *Journal of Nano Research*, vol. 9, pp. 101–108, feb 2010.
- ²¹R. Wang, O. Dmitrieva, M. Farle, G. Dumpich, M. Acet, S. Mejía-Rosales, E. Perez-Tijerina, M. J. Yacaman, and C. Kisielowski, "FePt Icosahedra with Magnetic Cores and Catalytic Shells," *The Journal of Physical Chemistry C*, vol. 113, pp. 4395–4400, mar 2009.
- ²²P. Solař, D. Nikitin, J. Hanuš, O. Kylián, M. Vaidulych, M. Cieslar, H. Valentova, and H. Biederman, "Production of heterogeneous copper-tungsten particles," in *Proceedings of the Nanocon*, (Brno), 2017.
- ²³Intelmetrics Global Ltd, "Model IL150 Thickness Monitor - Instruction Manual."
- ²⁴M. Stahl, T. Trottenberg, and H. Kersten, "A calorimetric probe for plasma diagnostics," *Review of Scientific Instruments*, vol. 81, no. 2, pp. 1–5, 2010.
- ²⁵S. Gauter, M. Fröhlich, W. Garkas, M. Polak, and H. Kersten, "Calorimetric probe measurements for a high voltage pulsed substrate (PBII) in a HiPIMS process," *Plasma Sources Science and Technology*, vol. 26, p. 065013, may 2017.
- ²⁶P. C. Zalm, "Energy dependence of the sputtering yield of silicon bombarded with neon, argon, krypton, and xenon ions," *Journal of Applied Physics*, vol. 54, pp. 2660–2666, may 1983.
- ²⁷P. Sigmund, "Elements of Sputtering Theory," in *Nanofabrication by Ion-Beam Sputtering*, no. September 2016, pp. 1–40, Pan Stanford Publishing, nov 2012.
- ²⁸P. Sigmund, "Theory of Sputtering. I. Sputtering Yield of Amorphous and Polycrystalline Targets," *Physical Review*, vol. 184, pp. 383–416, aug 1969.
- ²⁹D. Depla and S. Mahieu, eds., *Reactive Sputter Deposition*, vol. 109 of *Springer Series in Materials Science*. Berlin, Hei-

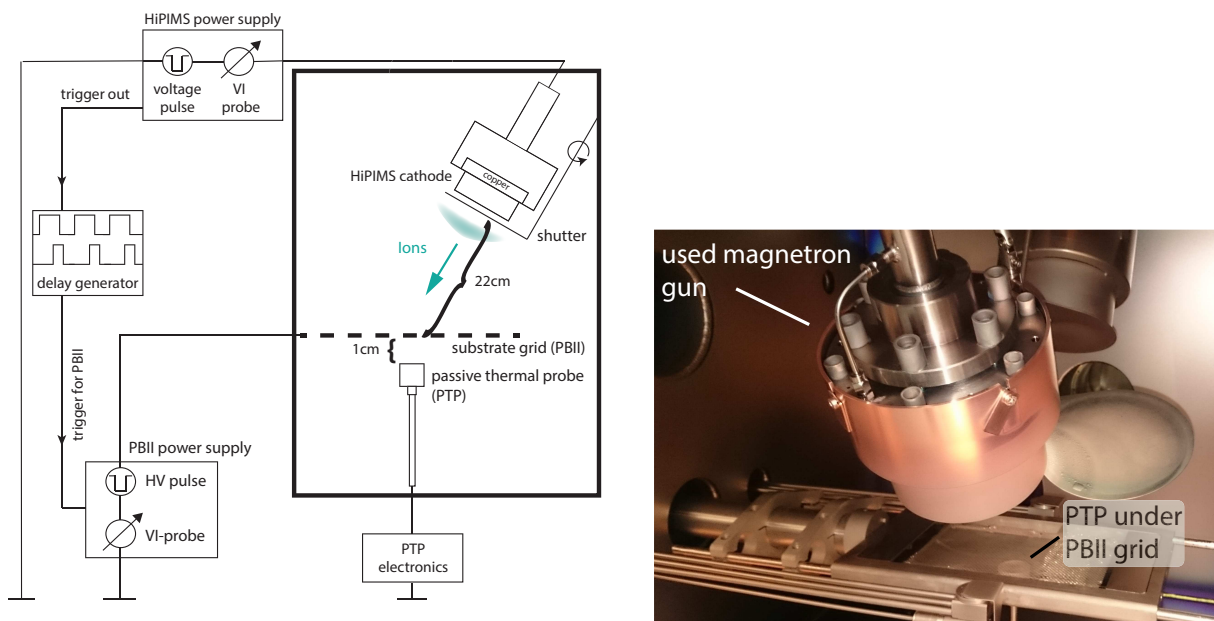
- delberg: Springer Berlin Heidelberg, 2008.
- ³⁰W. D. Westwood, "Calculation of deposition rates in diode sputtering systems," *Journal of Vacuum Science and Technology*, vol. 15, pp. 1–9, jan 1978.
- ³¹G. Ecker and K. G. Emel us, "Cathode Sputtering in Glow Discharges," *Proceedings of the Physical Society. Section B*, vol. 67, pp. 546–552, jul 1954.
- ³²H. Kersten, H. Deutsch, H. Steffen, G. Kroesen, and R. Hippler, "The energy balance at substrate surfaces during plasma processing," *Vacuum*, vol. 63, pp. 385–431, aug 2001.
- ³³R. Wendt, K. Ellmer, and K. Wiesemann, "Thermal power at a substrate during ZnO:Al thin film deposition in a planar magnetron sputtering system," *Journal of Applied Physics*, vol. 82, pp. 2115–2122, sep 1997.
- ³⁴D. Rohde, P. Pecher, H. Kersten, W. Jacob, and R. Hippler, "The energy influx during plasma deposition of amorphous hydrogenated carbon films," *Surface and Coatings Technology*, vol. 149, no. 2-3, pp. 206–216, 2002.
- ³⁵H. Kersten, D. Rohde, H. Steffen, H. Deutsch, R. Hippler, G. H. P. M. Swinkels, and G. M. W. Kroesen, "On the determination of energy fluxes at plasma–surface processes," *Applied Physics A*, vol. 72, no. 5, pp. 531–540, 2001.
- ³⁶D. Depla, S. Heirwegh, S. Mahieu, J. Haemers, and R. De Gryse, "Understanding the discharge voltage behavior during reactive sputtering of oxides," *Journal of Applied Physics*, vol. 101, p. 013301, jan 2007.
- ³⁷D. W. Hoffman, "A sputtering wind," *Journal of Vacuum Science & Technology A: Vacuum, Surfaces, and Films*, vol. 3, pp. 561–566, may 1985.
- ³⁸S. M. Rosnagel, "Gas density reduction effects in magnetrons," *Journal of Vacuum Science & Technology A: Vacuum, Surfaces, and Films*, vol. 6, no. 1, p. 19, 1988.
- ³⁹G. M. Turner, "Monte Carlo calculations of gas rarefaction in a magnetron sputtering discharge," *Journal of Vacuum Science & Technology A: Vacuum, Surfaces, and Films*, vol. 13, pp. 2161–2169, jul 1995.
- ⁴⁰N. Laegreid and G. K. Wehner, "Sputtering Yields of Metals for Ar + and Ne + Ions with Energies from 50 to 600 ev," *Journal of Applied Physics*, vol. 32, pp. 365–369, mar 1961.
- ⁴¹T. P. Dr usedau, T. Bock, T.-M. John, F. Klabunde, and W. Eckstein, "Energy transfer into the growing film during sputter deposition: An investigation by calorimetric measurements and Monte Carlo simulations," *Journal of Vacuum Science & Technology A: Vacuum, Surfaces, and Films*, vol. 17, pp. 2896–2905, sep 1999.
- ⁴²W. Eckstein and J. P. Biersack, "Reflection of heavy ions," *Zeitschrift f ur Physik B Condensed Matter*, vol. 63, pp. 471–478, dec 1986.
- ⁴³H. M. Urbassek and D. Sibold, "Sputtered atom transport in high-current gas discharges: A self-consistent computer simulation study," *Journal of Vacuum Science & Technology A: Vacuum, Surfaces, and Films*, vol. 11, pp. 676–681, may 1993.
- ⁴⁴R. L. Petry, "Secondary Electron Emission from Tungsten, Copper and Gold," *Physical Review*, vol. 28, pp. 362–366, aug 1926.
- ⁴⁵J. A. Thornton, "Substrate heating in cylindrical magnetron sputtering sources," *Thin Solid Films*, vol. 54, no. 1, pp. 23–31, 1978.
- ⁴⁶K. Harbauer, T. Welzel, and K. Ellmer, "A combined sensor for the diagnostics of plasma and film properties in magnetron sputtering processes," *Thin Solid Films*, vol. 520, no. 20, pp. 6429–6433, 2012.
- ⁴⁷W. M. Haynes, *CRC Handbook of Chemistry and Physics*. Boca Raton, FL: CRC Press, 2014.
- ⁴⁸J. A. Thornton and J. L. Lamb, "Substrate heating rates for planar and cylindrical-post magnetron sputtering sources," *Thin Solid Films*, vol. 119, pp. 87–95, sep 1984.
- ⁴⁹J. A. Thornton, "Influence of apparatus geometry and deposition conditions on the structure and topography of thick sputtered coatings," *Journal of Vacuum Science and Technology*, vol. 11, no. 4, p. 666, 1974.
- ⁵⁰B. A. Movchan and A. V. Demshishin, "Study of the structure and properties of thick vacuum condensates of nickel, titanium, tungsten, aluminium oxide and zirconium dioxide," *Phys. Met. Metallogr. (Engl. Trans.)*, vol. 28, pp. 83–90, jan 1969.

Publication V

Calorimetric probe measurements for a high voltage pulsed substrate (PBII) in a HiPIMS process

Authors	S. Gauter, M. Fröhlich, W. Garkas, M. Polak and H. Kersten
Journal	Plasma Sources Science and Technology
Technique	Plasma based ion implantation and deposition (PBII&D)
Utilized Probes	Passive thermal probe (PTP), Substrate voltage and current (VI-probe)
Own contribution	approx. 80%

Experimental Setup:



Motivation:

As a relatively new technique, the combination of HiPIMS and PBII has only been investigated by relatively few researchers. However, from the extensive experience in both separate fields, many findings can be applied here as well. The interaction between the processes is particularly interesting since PBII and HiPIMS are both pulsed processes, which makes the synchronization a critical parameter. Measurement of the energy flux along with the current and voltage characteristics of the PBII substrate, promises to provide insights into processes regarding particle transport and interaction between the HiPIMS plasma and the PBII pulse and can thus help to increase the overall understanding of this new method.

Main results:

Since a direct application of the PBII pulse on the PTP substrate would destroy the probe electronics, a different approach was chosen. By positioning the PTP underneath a grid which acts as the PBII substrate ions passing through the grid and secondary electrons emitted from the grid can be measured. The results confirmed that this setup allowed to indirectly measure the effects present on the PBII substrate. The variation of the delay between HiPIMS and PBII pulse showed a peak-like shape which reflects the evolution of the ion density during the HiPIMS pulse. The peak-like shape indicated, that ions travel as a relatively well-defined bunch from the cathode to the substrate.

Calorimetric probe measurements for a high voltage pulsed substrate (PBII) in a HiPIMS process

Sven Gauter^{1,3}, Maik Fröhlich², Wagdi Garkas², Martin Polak² and Holger Kersten¹

¹Institute of Experimental and Applied Physics, Christian-Albrechts-University Kiel, Germany

²Leibniz Institute for Plasma Science and Technology, Greifswald, Germany

E-mail: gauter@physik.uni-kiel.de, maik.froehlich@inp-greifswald.de, wagdi.garkas@inp-greifswald.de, polak@inp-greifswald.de and kersten@physik.uni-kiel.de

Received 21 December 2016, revised 14 March 2017

Accepted for publication 26 April 2017

Published 22 May 2017



CrossMark

Abstract

The combination of high-power impulse magnetron sputtering (HiPIMS) and plasma based ion implantation (PBII) gives a versatile system which allows successive and simultaneous coating, doping or cleaning of a substrate surface in a single process. The delay between HiPIMS and PBII pulse is a critical parameter for the synchronization of the pulses as it defines at what time during the HiPIMS period the high voltage is applied to the substrate. To investigate the effect of this parameter on the energy flux towards the PBII substrate, VI-probe and calorimetric probe measurements were performed illustrating the effect of the delay for different PBII pulse durations and PBII voltages. The calorimetric measurements were performed utilizing a grid setup which allowed us to derive conclusions even when using a detector that is not at the PBII voltage. A maximum of electrical power and energy flux was observed for delay times significantly longer than the duration of the HiPIMS pulse. The investigation of different PBII pulse durations and PBII voltages confirmed that these parameters affect the absolute values of the energy flux and electrical power but do not significantly affect the transport of the ions as the PBII potential is shielded by a sheath.

Keywords: HiPIMS, PBII, thermal probe, calorimetry, magnetron, ion transport, PBII and D

1. Introduction

Deposition of thin films by magnetron sputtering is commonly used in a variety of technological applications for thin films e.g. photocatalytic coatings or coatings with enhanced wear resistance [1–3]. From this classic technique the more versatile high-power impulse magnetron sputtering (HiPIMS) emerged in the mid 1990s [4]. Here the magnetron discharge is operated in a pulsed mode with duty cycles of only a few percent or less but with a very high peak power ranging up to several kW cm^{-2} [5]. During the pulse which is typical in the range of a few μs up to a few 100 μs very high plasma densities ($\approx 10^{19} \text{ cm}^{-3}$) and a high degree of ionization (10%–80%) of the sputtered particles are achieved, resulting in an

energetic ion flux towards the substrate [6]. Extensive investigations by different groups focusing on the transport of species from target to substrate revealed complex temporal evolutions of the different species during the HiPIMS process [7–10].

By application of a synchronized electrostatic potential on the substrate the temporal evolution as well as the high ionization degree of the sputtered particles can be utilized to achieve an even better control of the film properties. This has been successfully demonstrated in a model system for deposition of $\text{Ti}_{1-x}\text{Al}_x\text{N}$ by Greczynski *et al.*, where the application of synchronized voltage pulses onto the substrate led to lower stress in the coating [11]. Other studies achieved enhanced adhesion properties using a combination of HiPIMS and $\approx -1 \text{ kV DC}$ bias on the substrate as a pretreatment to a regular DCMS deposition [12, 13].

³ Author to whom any correspondence should be addressed.

In this study HiPIMS is combined with plasma based ion implantation (PBII) which is an established method for doping surfaces by application of a short negative high-voltage pulse to the substrate [14]. In the PBII process the substrate is placed in close vicinity of the plasma and due to the negative high voltage pulse, positive ions are extracted from the plasma and accelerated towards the surface where they are implanted [15–17]. In [18] Anders first suggested HiPIMS as an alternative plasma source in plasma-based ion implantation and deposition (PBII and D), pointing out its advantages like very good reproducibility of the ion flux or the possibility of easy scaling to industrial size systems. In 2010 the first studies on such a combined system were presented by Wu *et al* who demonstrated its efficacy by deposition of CrN with excellent adhesion properties [19]. In the following years the method has been further refined and applied in the deposition of varying material systems [20–24].

A combined system of PBII and HiPIMS allows successive or simultaneous coating, doping or etching of substrate surfaces while being able to independently tune deposition parameters e.g. energy of depositing ions or energy flux to the substrate. The energy influx towards the substrate during plasma operation is a crucial process parameter affecting the surface temperature of the substrate and the film properties [25, 26]. For example in [27] Anders presents a structural zone model which is adapted from previous models of Thornton and Movchan, respectively [25, 28]. The substrate temperature due to the energy of the impinging species are pointed out as important parameters for tuning the film's microstructure. Consequently, in the present study the energy flux towards the substrate in the combined HiPIMS/PBII experiment has been investigated. The energy flux is measured by means of a calorimetric probe as described in [29–31] in combination with a grid setup. The combination of grid and calorimetric probe provided a time- and energy-integrated quantitative measure for the power deposited on the substrate and, thus, also for the substrate temperature. In order to monitor the HiPIMS discharge and to obtain information about the transport of ions towards the substrate, time resolved VI-measurements of the magnetron as well as of the substrate are performed.

A crucial parameter of the HiPIMS/PBII system is the triggering of the PBII pulse and in particular the delay between HiPIMS and PBII pulse. The delay time determines at which time during the HiPIMS period the negative high voltage PBII pulse is applied to the substrate. Since the amount and composition of the ions in the vicinity of the substrate are changing strongly during the HiPIMS period, proportional changes in ion flux and energy flux densities can be expected [11, 32–34]. In the present study variations of energy flux density and electrical power on the substrate as a function of the delay time have been investigated for different PBII pulse durations and amplitudes. As expected, the measurements exhibit a direct correlation between the process parameter delay and the ion flux as well as the energy flux towards the substrate for different PBII voltages and pulse durations.

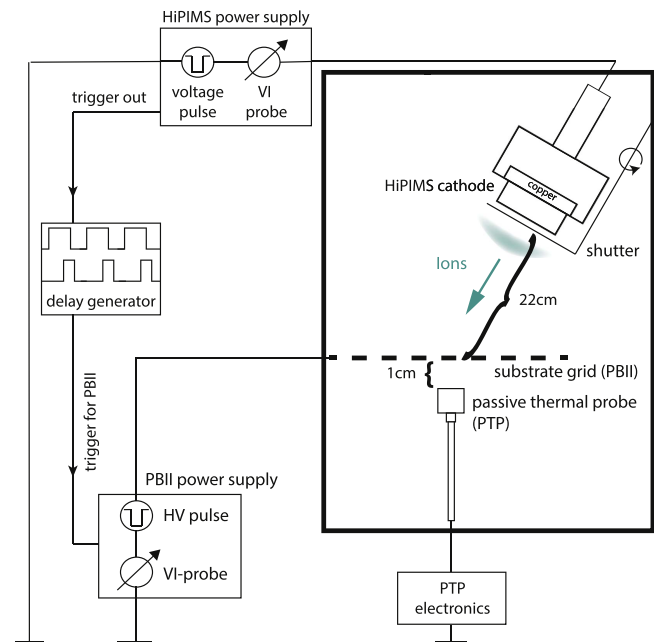


Figure 1. Schematic drawing of the experimental setup. The bold black box resembles the vacuum chamber.

2. Experiment

2.1. Experimental setup and plasma diagnostics

The goal of our study is to investigate the energy flux towards a high voltage pulsed substrate. The direct measurement of the energy influx, however, is very difficult because the high bias voltages would damage the probe electronics if it would be used directly as a substrate. Therefore, a different approach was chosen to achieve an indirect measure of the energy arriving at the PBII substrate during the HiPIMS process. In the utilized setup the calorimetric probe was placed 1 cm below a high voltage pulsed grid (wire diameter 0.25 mm, mesh width 1.66 mm, transparency 73%) and connected to ground, see figure 1. In this setup the grid is the PBII substrate and due to its partial transparency, highly energetic ions can pass through the grid and create a significant energy flux on the calorimetric probe placed below. If no potential is applied to the grid the plasma can move through it quite freely as the Debye length is in the range of a few μm , and thus much smaller than the mesh width of the grid [35].

The probe and the grid were positioned in a rectangular vacuum vessel with a volume of approximately 300 l which was equipped with a 4 inch copper magnetron. The magnetron had balanced magnetic field configuration and was powered by a Melec HiPIMS power supply with rectangular voltage pulses. To realize the calorimetric measurements the magnetron was equipped with a pneumatic shutter which was mounted directly in front of the magnetron. The PBII substrate was a 10 cm \times 20 cm copper grid fixed on a frame, which was mounted on a custom build substrate holder and powered by a GBS power supply designed for PBII processes. The start of the PBII pulse was triggered on the HiPIMS pulse and could be adjusted by an SRS DG645 delay

Table 1. HiPIMS and PBII parameters for the presented measurements with the variation parameter printed **bold**. The HiPIMS and PBII frequency was 100 Hz for all measurements and the on-time of the HiPIMS pulse was kept constant at 200 μ s. The delay is defined as the delay from the start of the HiPIMS pulse to the middle of the PBII pulse.

	HiPIMS parameters		PBII parameters	
Variation of PBII pulse duration	Voltage (V)	600	Voltage (kV)	−3
	Peak power density (kW cm^{-2})	0.88	Delay (μ s)	10–1030
	Pressure (Pa)	1.5	On-time (μ s)	20–60
Variation of PBII voltage	Voltage (V)	580	Voltage (kV)	−3–15
	Peak power density (kW cm^{-2})	1.15	Delay (μ s)	2–1002
	Pressure (Pa)	1	On-time (μ s)	5

generator. The delay is defined as the time from the start of the HiPIMS pulse to the middle of the PBII pulse.

In table 1 a summary is given of the parameters used for the experiments, which were performed in argon and with a distance of about 22 cm between the surface of the magnetron target and the substrate grid.

In addition to the aforementioned calorimetric probe measurement, the PBII substrate as well as the magnetron were monitored with VI-probes. The measurements were performed simultaneously to allow a comparison of the results. While the thermal probe provides an energy and time integrated value over a period of a few seconds, the VI measurements are highly time-resolved. The signals were monitored and recorded by an oscilloscope (40 ns time resolution) which is directly connected to the designated outputs at the power supplies. The recorded signals are averaged over 10 periods.

2.2. Concept of calorimetric probe (PTP)

The measurements of the energy flux density were performed by a passive thermal probe (PTP) as shown in figure 2. This type of probe was introduced by Thornton in 1978 [36] and since that time it has been successfully utilized in a variety of plasma environments [26, 30, 31, 37, 38]. The probe consists of a Type K thermocouple which is attached to a dummy substrate made of copper with a diameter of 20 mm and a thickness of 100 μ m. For probe biasing an additional copper wire is welded to the back of the dummy substrate and a ceramic shield guarantees that only energy influx to the substrate surface facing the plasma is measured. A detailed description of the probe and information about the method for determining its heat capacity C_S can be found in [30, 39].

The concept for the determination of the energy flux is based on the relation between the time derivative of the enthalpy \dot{H} and the time derivative of the temperature \dot{T} during the heating (energy source switched on) and the cooling (energy source switched off) of the PTP's dummy substrate as given in the following equations:

$$\text{Heating: } \dot{H}_h = C_S \dot{T}_h = P_{\text{in}} - P_{\text{out},h}, \quad (1)$$

$$\text{Cooling: } \dot{H}_c = C_S \dot{T}_c = -P_{\text{out},c}. \quad (2)$$

Here C_S stands for the heat capacity of the probe, P_{in} gives the energy influx from the heat source, and $P_{\text{out},h}$ and $P_{\text{out},c}$

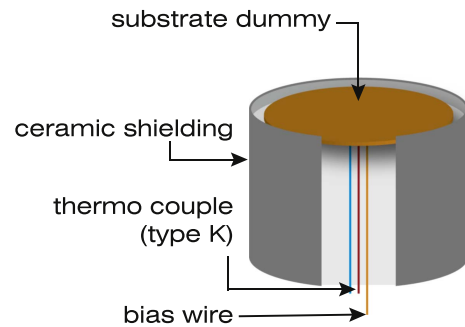


Figure 2. Schematic drawing of the utilized passive thermal probe.

describe the energy leaving the probe during the heating and the cooling phase accordingly. Under the assumption that the energy flux leaving the substrate during the heating phase equals the energy flux during the cooling phase at the same temperatures, equations (1) and (2) can be combined to calculate the energy flux density J_{in} :

$$J_{\text{in}} = \frac{P_{\text{in}}}{A_S} = \frac{C_S}{A_S} (\dot{T}_h - \dot{T}_c). \quad (3)$$

To ensure that the aforementioned assumption $P_{\text{out},h}(T_h) = P_{\text{out},c}(T_c)$ is fulfilled, one has to ensure that any heat flux due to secondary heat sources are constant for the monitored time period. This can be best achieved by minimizing the time where this assumption must apply. To realize this requirement, only the temperature changes in a short time around the start and the shut off of the power source are evaluated. In figure 3 this method of evaluation is demonstrated for a typical measurement curve of the performed experiments. The plot shows the determination of the temperature derivative by linear fits which give a good approximation of the exponential slope of the probe temperature for short times.

2.3. Evaluation of the PBII VI-data

From the combination of HiPIMS and PBII we expect strong changes in the amount of implanted ions as a function of the delay between HiPIMS and PBII pulse due to changes in the ion density at the sheath edge [34]. These changes were monitored using an oscilloscope which measured the substrate current and voltage *in situ*. As the energy flux can be expected to be mainly attributed to the ions impinging on the

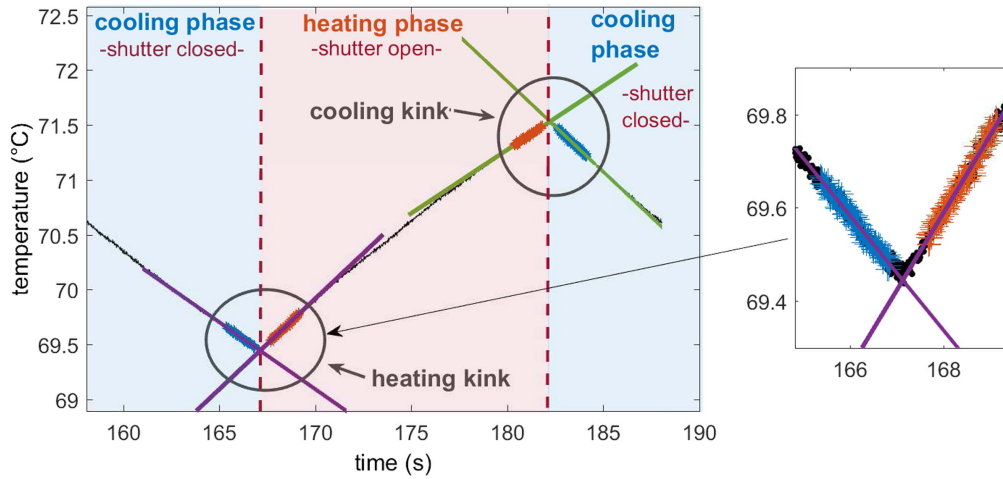


Figure 3. Exemplary evaluation of the temperature curve for a delay of 100 μs , 5 μs PBII pulse duration and 3 kV PBII voltage. The pressure is 1 Pa and the HiPIMS setpoint is 580 V with 200 μs pulse duration at 100 Hz frequency. From a single heating curve which always consists of three phases (two phases with the energy source being switched off and one phase, in-between, with the energy source switched on) two measurement values of the energy flux are obtained. The values correspond to the energy immediately after switching on the plasma (heating kink) and right before switching it off (cooling kink). On the right side of the figure a detailed view of the heating kink with the selected data points for fitting (blue and red) and corresponding fits (violet) is shown.

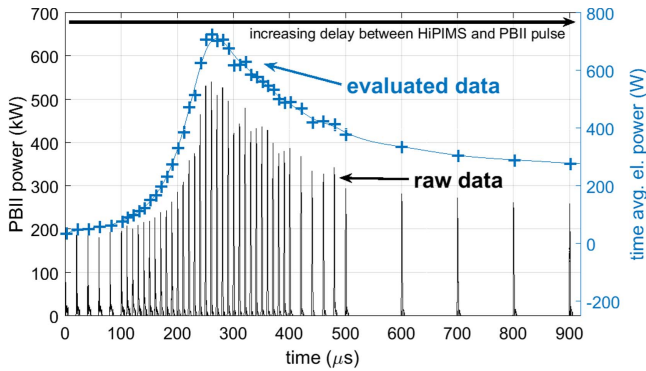


Figure 4. Accumulated data of the grid's VI probe from the delay variation at 15 kV PBII voltage and 5 μs PBII pulse duration. The pressure is 1 Pa and the HiPIMS setpoint is at 580 V with 200 μs pulse duration and 100 Hz frequency. The plot shows a summary of the raw PBII power as measured by the oscilloscope for a complete delay variation with each peak corresponding to one delay value. Additionally to the raw data the evaluated data according to equation (4) is given as blue data points with its axis on the right.

substrate, it is particularly interesting to measure the time averaged amount and power of these ions to obtain a value which is directly comparable to the energy flux measured by the PTP. In order to achieve this, the time resolved VI measurements of the oscilloscope were used to obtain the time averaged PBII power, which allows a direct comparison of both diagnostics. This value can be determined by calculating the time resolved PBII power from the measured current and voltage. Then, the time averaged PBII power during one HiPIMS period is calculated according to the following equation:

$$P_{\text{PBII,avg}} = \bar{P}_{\text{PBII,rec}} \cdot \frac{t_{\text{rec}}}{T_{\text{HiPIMS}}}. \quad (4)$$

Here $\bar{P}_{\text{PBII,rec}}$ is the average of the time resolved power over the recorded time period t_{rec} and T_{HiPIMS} is the HiPIMS

period. To illustrate this evaluation, in figure 4 a compilation of the raw PBII power measurements as recorded with the oscilloscope for a typical delay variation is given as colored curves, with each peak corresponding to one delay value. Each measurement curve is then used to calculate one data point of the *time averaged electrical power* according to equation (4). The resulting values are displayed as blue data points in figure 4. As expected, the raw PBII power is dominated by the strong power pulse during the on-time of the PBII pulse and the value of the calculated time averaged power is defined by the amplitude and width of the raw PBII power pulse. The resulting graph of the evaluated data in figure 4 displays strong changes of the electrical power on the grid as a function of the delay and indicates a maximum of implanted ions around 260 μs .

3. Results and discussion

3.1. HiPIMS VI-probe measurements

As the HiPIMS plasma source is the primary energy source of the combined experiment it was essential to continuously monitor the pulse characteristics. Doing this not only enabled us to ensure the reproducibility of the measurement conditions but also allowed a basic characterization of the HiPIMS conditions, giving a basis for comparison with other systems.

In figure 5 typical current–voltage–time characteristics as obtained by the HiPIMS VI-probe for the two different HiPIMS operation points at 1.5 and 1 Pa are presented. For both operation points the measurements show high peak currents of about 100 and 150 A, respectively, which are typical characteristics of the HiPIMS discharge. Although this results in peak power densities of 0.88 and 1.15 kW cm^{-2} , (calculated for the whole target area), the time averaged HiPIMS power is only in the range of about 20 W cm^{-2} . This

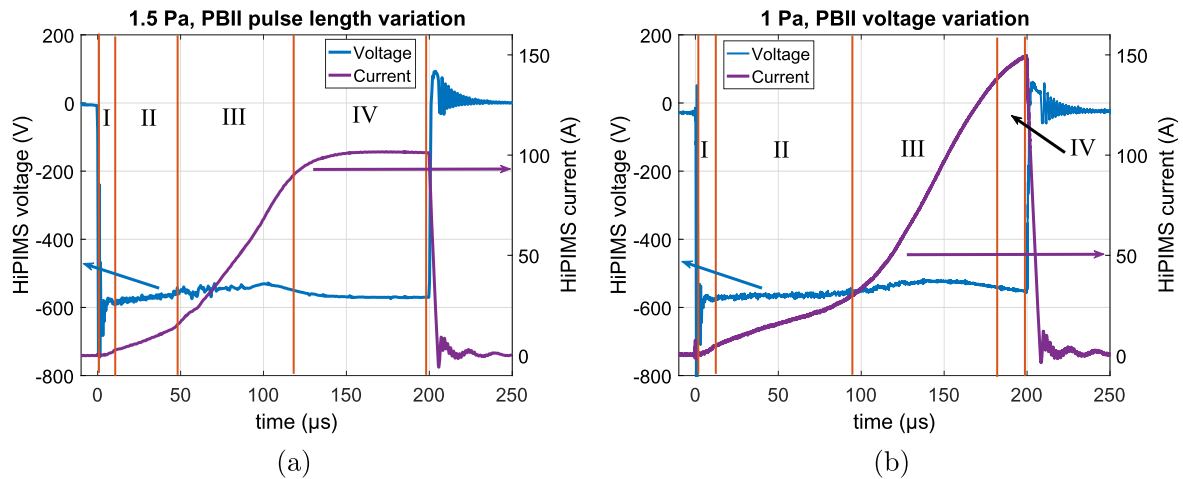


Figure 5. Typical results of the HiPIMS VI-probe for the two HiPIMS operation points. In both cases the pulse duration was $200\ \mu\text{s}$ and the frequency $100\ \text{Hz}$. (a) The setup used for the variation of the PBII pulse duration with $1.5\ \text{Pa}$ and $600\ \text{V}$ setpoint and (b) gives the VI-curves for the setup used for the PBII voltage variation with $1\ \text{Pa}$ and $580\ \text{V}$ setpoint. In both figures the pulse is divided into four characteristic regions: I—voltage applied, no plasma ignition, II—gas ion current and rarefaction, III—self-sputtering, IV—beginning of new steady state. These regions are defined according to works of Anders *et al* [5].

fact emphasizes the advantage of HiPIMS, e.g. a high degree of ionization with low heat load onto the target and substrate, resulting in increased film and deposition properties compared to conventional magnetron sputtering [40]. As the HiPIMS parameters were kept constant within the two parameter sets (table 1), the resulting VI-characteristics were quite similar and have proven not to be affected by any changes in the PBII pulse.

3.2. PBII VI-probe and PTP measurements

Due to the pulsed nature of the HiPIMS discharge, the delay between HiPIMS pulse and PBII pulse is a specifically critical parameter for our combined system. In the following this parameter is investigated by simultaneous measurement of the electrical power at the substrate grid and the energy flux onto the PTP, allowing a direct comparison of the two quantities. To demonstrate the effects of the PBII setup the delay was investigated for different settings of the critical PBII parameters pulse duration and pulse amplitude.

The pulse duration is an important parameter since the sheath—for sufficiently high voltages—is continuously expanding during the PBII pulse. In our case we examined pulse durations of $20\ \mu\text{s}$ and longer for a voltage of $-3\ \text{kV}$. As this is a relatively low voltage compared to typical PBII voltages, the sheath only expands until a certain limit and stays stationary afterwards [41]. Thus, for sufficiently long pulse durations we expect that detected changes are mainly attributed to alterations in the plasma at the sheath edge during the on-time of the PBII pulse. The amplitude is a critical parameter as it directly corresponds to the energy of the arriving ions at the substrate and, thus, primarily defines ion implantation depth or e.g. film stress [17]. For our measurements it is expected to be just as important, since the increased energy directly affects the electrical power and energy flux to the substrate.

In figure 6 the results for the evaluation of the PBII VI-probe and the PTP for the performed delay variations with different PBII pulse durations are compiled. To illustrate any resemblance between the target power and the measured values at the substrate, the corresponding HiPIMS power measurement is added as a gray shade to the graphs. Both electrical power and the energy flux show peak-like shapes with the maximum being delayed by approximately $60\text{--}70\ \mu\text{s}$ from the end of the HiPIMS pulse for all examined PBII pulse durations. While the position of the maximum is not affected by the duration of the PBII pulse, the absolute values increase for all delays.

3.2.1. Shape of the obtained energy-delay characteristic. The relatively long arrival times of the ions indicate that the substrate grid is well shielded for all examined delay times. This is consistent with the results of Mishra *et al* [42] who found a positive plasma potential for the complete off-time of the HiPIMS period. This means for our setup that the PBII substrate only interacts with the ions entering the sheath while all other ions stay unaffected by the strong negative potential. Thus, by triggering the PBII pulse on the HiPIMS pulse the measured values yield a snapshot of the ion population which is present during this particular phase of the HiPIMS period in the substrate region.

The observed shape of the electrical power and energy flux density reflect the changes of the ion density at the sheath edge of the substrate. The strong changes during the HiPIMS period and the appearance of a maximum amount of ions arriving delayed from the end of the HiPIMS pulse agree nicely with observations by other groups [32, 34, 43]. The peak-like shape of the graphs in figure 6 indicate that during the on-time of the HiPIMS pulse, a high number of ions are able to escape the plasma torus and start moving towards the PBII substrate as a relatively confined ion bunch. This ion bunch/wave starts with its initial energy as obtained from the sputter process according to the Thompson distribution

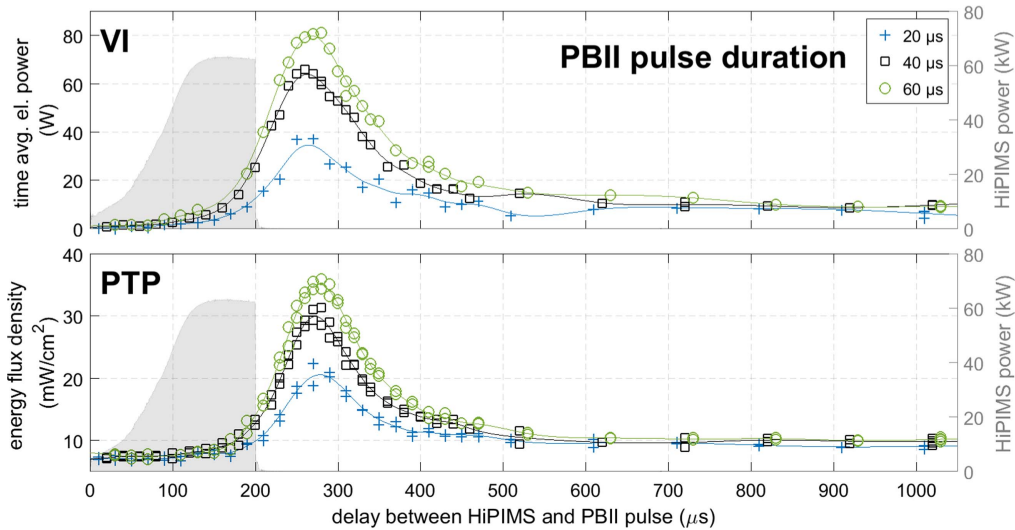


Figure 6. Delay variation the examined PBII pulse duration. The upper graph shows the results obtained from the PBII VI-probe and the lower graph gives the energy flux density as detected by the PTP. The shaded area represents the time resolved course of the HiPIMS power to the magnetron with its axis on the right.

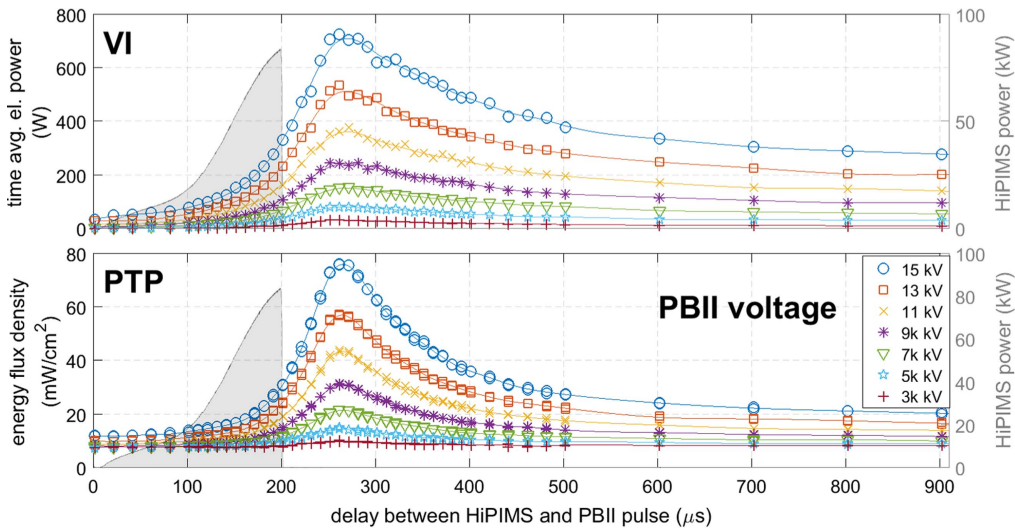


Figure 7. Delay dependence of the obtained results for the examined PBII voltages. The upper graph shows the results obtained from the PBII VI-probe and the lower graph gives the energy flux detected by the PTP. The shaded area represents the time resolved course of the HiPIMS power to the magnetron with its axis on the right.

[44, 45] and gets gradually slowed down and smeared out due to collisions with the background gas. Thus, a strong increase in energy flux and electrical power can be detected as the delay is long enough for the front of the ion wave to arrive at the substrate ($\approx 150 \mu\text{s}$). The measured values keep rising with higher delays as the ion density further increases until the crest of the ion wave has passed ($\approx 270 \mu\text{s}$) where it starts decreasing again.

The investigation of the delay dependence for different PBII voltages shows very similar phenomena as obtained for the variation of the PBII pulse duration, see figure 7. With increasing delay, first a rise in electrical power and energy flux is observed which peaks at a delay of about $270 \mu\text{s}$ and then decreases until it reaches saturation at about $700 \mu\text{s}$. Similar as observed for the variation of the PBII pulse duration, the PBII voltage does not affect the position of the

maximum but only changes its absolute value. This additionally supports the assumption that the PBII substrate grid is continuously shielded during the whole HiPIMS period.

3.2.2. Composition of the energy flux. Former energy flux measurements on magnetron sputtering experiments have shown that the energy flux decreases rapidly with larger distances between magnetron and substrate [31, 46]. Therefore, for our experimental setup with a rather big substrate distance of about 22 cm we only expect a small contribution to the energy flux which is directly attributed to typical plasma surface interactions. Instead, we expect the energy flux to be strongly dominated by the energetic ions which are accelerated in the potential drop close to the grid. This assumption is supported by the strong resemblance

between the measured delay dependencies by both diagnostics which is one of the striking features in figures 6 and 7.

Taking a closer look at the motion of the ions in the sheath of the grid, it becomes clear that the ions must oscillate through the grid and the sheath on both sides of the grid. Theoretical and experimental investigations suggest that for our experiment the sheath dimension for the PBII substrate should be in the range of a few centimeters and that the expansion mostly happens in the first 5–10 μs after switching on the PBII voltage [41, 47–49]. Since for the examined conditions the mean free path is in the same range as the sheath width [50] the motion of the ions in the sheath can be treated as collisionless. A rough calculation of the acceleration in the sheath can be obtained using the space charge restricted potential of the Child–Langmuir sheath, which results in the following equation for the transit time of a single charged copper atom through the sheath [47, 51]:

$$t_{\text{sheath}} = 3 \cdot \sqrt{\frac{m_{\text{Cu}}}{2e \cdot U_{\text{PBII}}}} \cdot d_{\text{sheath}}. \quad (5)$$

Assuming a maximum sheath thickness of $d_{\text{sheath}} = 10$ cm and a minimal potential difference $U_{\text{PBII}} = 3$ kV we get a transit time of about 3 μs . Therefore, with PBII pulse durations of 5 μs and longer, we can expect the majority of the ions entering the sheath during the PBII pulse to surpass it and either hit the surface of the grid or pass through the mesh. While the ions hitting the surface get absorbed and create secondary electrons, an ion passing through the grid will be decelerated until the point where it turns around and starts accelerating towards the grid again. After switching off the potential on the grid, the ions continue with their acquired kinetic energy. In such a way, the ions entering the sheath can swing through the grid several times depending on the duration of the PBII pulse. As the secondary electron yield of copper is approximately 1.5 for 3 keV Argon ions and increasing for higher energies [52] the measured electrical power on the grid should be predominantly created by secondary electrons. And as the released electrons are accelerated by the full PBII potential before arriving at the PTP, they can also be expected to add a major contribution to the measured energy flux, as also observed by Haase *et al* [53]. The measured energy flux, therefore, should be a superposition of the contributions from the energetic ions escaping the potential at the end of the PBII pulse and the secondary electrons created by the collisions on the grid. As the secondary electrons create an increase in the measured electrical power as well, both measured values are equally affected, resulting in the observed resemblance between the measurements by VI probe and PTP.

3.2.3. Effect of PBII duration and PBII voltage. Assuming the qualitative model described above, we can take a closer look at the obtained results for the variation of the PBII pulse duration and amplitude. In case of the PBII pulse duration one would expect no changes in the sheath. The sheath should already be fully expanded and neither the amount of ions entering the sheath nor the sheath voltage were changed.

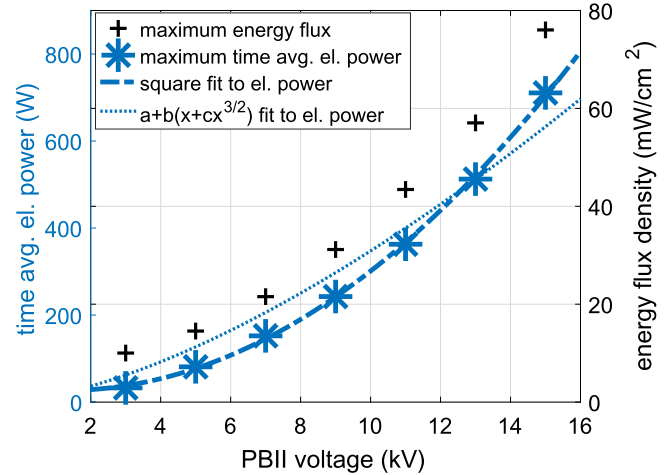


Figure 8. Maximum values of energy flux density and electrical power of the grid from the delay dependencies for the variation of the PBII voltage (see figure 7). The solid lines show different fits to the measured values of the electrical power.

Thus, the biggest change can be expected to be found in the amount of ions trapped in the PBII potential due to the increasing number of ions arriving from the plasma. By this manner the exposure time of the aforementioned snapshot is increased and a wider part of the ion wave is detected. Additionally, with increasing on-time the ions oscillate more frequent through the grid plane and, thus, the chance for absorption by the grid and creation of secondary electrons increases. However, since this is only a secondary effect, the observed increase of the measured electrical power and energy flux (figure 6) can be mainly attributed to the longer sampling rate and the corresponding increased number of ions entering the sheath during the pulse.

For the variation of the PBII voltage U_{PBII} the situation becomes a little bit more complex. The most obvious change for increasing PBII voltages is the increase of the kinetic energy of the impinging ions and electrons. As the ions secondary electron yield λ_{SE} is proportional to $\sqrt{U_{\text{PBII}}}$ [52] the increase in PBII voltage not only affects the kinetic energy but, due to increased secondary electron generation, also increases the current and, thus, the measured electrical power and energy flux. Taking into account these two effects, we would expect the electrical power to be affected according to the following equation:

$$P_{\text{electrical}} = U_{\text{PBII}} \cdot I_{\text{ion}} \cdot (1 + \lambda_{\text{SE}}) \propto I_{\text{ion}} \cdot (U_{\text{PBII}} + A_{\text{SE}} U_{\text{PBII}}^{3/2}), \quad (6)$$

with I_{ion} being the ion current and A_{SE} being a fit parameter for the secondary electron yield. As can be seen from figure 8, however, the maximum electrical power increases quadratically for our measurements and, thus, stronger than predicted by equation (6). Therefore, other effects like larger sheath expansion or increased oscillation frequency through the grid appear to play a non-negligible role for the increase of the electrical power with increasing PBII voltage. Figure 8 also displays the corresponding maximum values of the energy flux density for the different investigated PBII voltages. The

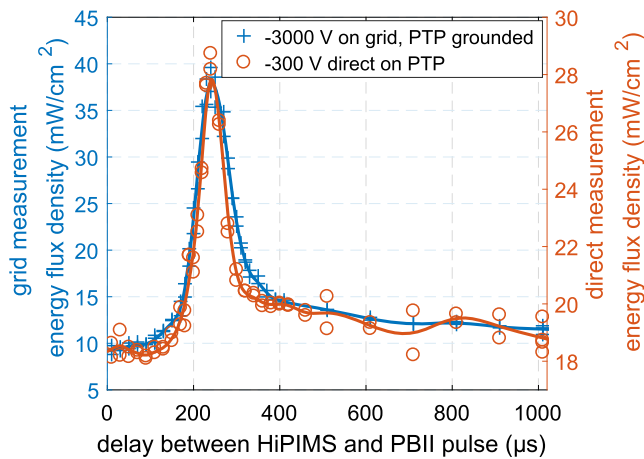


Figure 9. Comparison of the energy flux as a function of the delay for voltage directly applied on the probe and grid setup for indirect measurement.

similar slope of the curves obtained from the two diagnostics confirms the aforementioned proportionality between the detected current on the PBII substrate and the energy flux density onto the PTP.

3.3. Proof of concept of indirect energy flux measurement with PBII grid

To verify, that the experimental setup with the PTP underneath the grid can be used as an indicator for the power deposited on the PBII substrate and that the observed phenomena are not only created due to the presence of the grid, measurements were performed where the PBII pulse was directly applied to the PTP and the grid was removed from the chamber. For these measurements the bias wire of the PTP was directly connected to the PBII power supply. To prevent any damaging of the probe electronics, the power supply was operated at a voltage of -300 V for the direct measurement. The distance between substrate and magnetron was 18 cm, the pressure was 1.5 Pa and the PBII pulse duration was 20 μ s.

In figure 9 the result of the performed delay variation from the direct setup is plotted together with a comparable measurement of the grid setup performed with the same parameters but for a higher PBII voltage of -3 kV. The obtained results reveal an excellent agreement of the delay dependence between both setups. Both measurements show the same characteristic peak-shape reflecting the time evolution of the ion density with its maximum at a delay time of about 240 μ s. The agreement of the delay value for maximum energy flux supports the observations obtained by the variation of the PBII voltage and clearly proves the functionality of the grid setup for indirect measurement of the energy flux onto a PBII substrate.

4. Conclusion

The energy flux density and electrical power on the substrate as a function of the delay time between HiPIMS pulse and PBII pulse

have been investigated, varying the delay from 2 μ s to 1030 μ s. The measurements were performed for different settings of the PBII pulse duration and the PBII voltage. Simultaneous with these measurements time resolved VI-probe measurements of the magnetron were performed.

The VI-measurements of the HiPIMS magnetron showed typical HiPIMS characteristics with rectangular voltage pulses which were not affected by any changes of the substrate's PBII settings. The energy flux was measured with a grid setup, which was designed to obtain qualitative results for the power deposited on the PBII substrate. A direct comparison between energy flux measurements performed with voltages applied directly to the PTP showed excellent agreement, confirming the functionality of the grid setup for indirect energy flux measurements. The analysis of the results for the variation of the delay showed a peak-like shape of the energy flux and the electrical power for all examined conditions, reflecting the evolution of the ion density at the sheath edge. As the PBII substrate is continuously shielded by the HiPIMS plasma, the substrate interacts only with charge carriers in its close vicinity and, thus, the measurements were found to provide time resolved information about the conditions depending on the chosen delay. With this information, the peak-like structure could be explained by a localized ion population which escapes the plasma region during the HiPIMS pulse and travels through the chamber as an ion density wave causing a peak in the measurements as the crest passes by the grid. Due to the efficient shielding of the substrate, the arrival time of the wave crest is not affected by the PBII pulse duration or voltage but is mainly defined by the initial energy of the sputtered target atoms and collisions with the background gas. As expected, both, the increase of the PBII pulse duration and the PBII voltage resulted in amplified values, generated by different mechanisms. While the increase for longer PBII pulse durations seems to be dominantly caused by an increased number of ions arriving during the on-time of the PBII pulse, the observed increase for higher PBII voltages can be understood as a combination of increased ion energy, higher secondary electron yield and larger sheath expansion.

Overall the results underline that the combination of HiPIMS and PBII make a versatile coating system with complex characteristics, which can be controlled by external parameters e.g. the delay between the HiPIMS and PBII pulse. This delay allows direct control of the energy flux towards the substrate and optimization for maximum ion current, even under otherwise fixed HiPIMS and PBII parameters. To exploit the potential of such a combined system it is essential to fully understand the transport of species in the chamber and their dynamics during the HiPIMS period. The presented study revealed some basic information about these questions, however, to obtain a more complete insight extensive analysis, especially of the HiPIMS parameters, are necessary in the future.

References

- [1] Mattox D M 2010 *Handbook of Physical Vapor Deposition (PVD) Processing* 2nd edn (Albuquerque, NM: William Andrew)
- [2] Takeda S, Suzuki S, Odaka H and Hosono H 2001 Photocatalytic TiO₂ thin film deposited onto glass by DC magnetron sputtering *Thin Solid Films* **392** 338–44
- [3] PalDey S and Deevi S C 2003 Single layer and multilayer wear resistant coatings of (Ti,Al)N: a review *Mater. Sci. Eng. A* **342** 58–79
- [4] Mozgrin D, Fetisov I and Khodachenko G 1995 High-current low-pressure quasi-stationary discharge in a magnetic field: experimental research *Plasma Phys. Rep.* **21** 400–9
- [5] Anders A, Andersson J and Ehiasarian A P 2007 High power impulse magnetron sputtering: current–voltage–time characteristics indicate the onset of sustained self-sputtering *J. Appl. Phys.* **102** 113303
- [6] Helmersson U, Lattemann M, Bohlmark J, Ehiasarian A P and Gudmundsson J T 2006 Ionized physical vapor deposition (IPVD): a review of technology and applications *Thin Solid Films* **513** 1–24
- [7] Britun N, Minea T, Konstantinidis S and Snyders R 2014 Plasma diagnostics for understanding the plasma-surface interaction in HiPIMS discharges: a review *J. Phys. D: Appl. Phys.* **47** 224001
- [8] Hecimovic A and Ehiasarian A P 2010 Spatial and temporal evolution of ion energies in high power impulse magnetron sputtering plasma discharge *J. Appl. Phys.* **108** 063301
- [9] Bohlmark J, Lattemann M, Gudmundsson J T, Ehiasarian A P, Gonzalvo Y A, Brenning N and Helmersson U 2006 The ion energy distributions and ion flux composition from a high power impulse magnetron sputtering discharge *Thin Solid Films* **515** 1522–6
- [10] Maszl C, Breilmann W, Benedikt J and von Keudell A 2014 Origin of the energetic ions at the substrate generated during high power pulsed magnetron sputtering of titanium *J. Phys. D: Appl. Phys.* **47** 224002
- [11] Greczynski G et al 2012 Metal versus rare-gas ion irradiation during Ti_{1-x}Al_xN film growth by hybrid high power pulsed magnetron/dc magnetron co-sputtering using synchronized pulsed substrate bias *J. Vac. Sci. Technol. A* **30** 061504
- [12] Lattemann M, Ehiasarian A P, Bohlmark J, Persson P Å O and Helmersson U 2006 Investigation of high power impulse magnetron sputtering pretreated interfaces for adhesion enhancement of hard coatings on steel *Surf. Coat. Technol.* **200** 6495–9
- [13] Ehiasarian A P, Wen J G and Petrov I 2007 Interface microstructure engineering by high power impulse magnetron sputtering for the enhancement of adhesion *J. Appl. Phys.* **101** 054301
- [14] Pelletier J and Anders A 2005 Plasma-blased ion implantation and deposition: a review of physics, technology, and applications *IEEE Trans. Plasma Sci.* **33** 1944–59
- [15] Conrad J R, Radtke J L, Dodd R A, Worzala F J and Tran N C 1987 Plasma source ion-implantation technique for surface modification of materials *J. Appl. Phys.* **62** 4591–6
- [16] Samandi M, Shedden B A, Bell T, Collins G A, Hutchings R and Tendys J 1994 Significance of nitrogen mass transfer mechanism on the nitriding behavior of austenitic stainless steel *J. Vac. Sci. Technol. B* **12** 935
- [17] Manova D, Gerlach J W and Mändl S 2010 Thin film deposition using energetic ions *Materials* **3** 4109–41
- [18] Anders A 2010 High power impulse magnetron sputtering and related discharges: scalable plasma sources for plasma-based ion implantation and deposition *Surf. Coat. Technol.* **204** 2864–8
- [19] Wu Z, Tian X, Shi J, Wang Z, Gong C, Yang S and Chu P K 2011 Novel plasma immersion ion implantation and deposition hardware and technique based on high power pulsed magnetron discharge *Rev. Sci. Instrum.* **82** 033511
- [20] Jeon J-H, Choi J-Y, Park W-W, Moon S-W, Park K-W, Lim S-H and Han S-H 2011 Crystalline Ge quantum dots embedded in SiO₂ matrix synthesized by plasma immersion ion implantation *Nanotechnology* **22** 285605
- [21] Wu Z, Tian X, Wang Z, Gong C, Yang S, Ming Tan C and Chu P K 2011 Microstructure and mechanical properties of CrN films fabricated by high power pulsed magnetron discharge plasma immersion ion implantation and deposition *Rev. Sci. Instrum.* **258** 242–6
- [22] Wu Z, Tian X, Wei Y, Gong C, Yang S, Pan F and Chu P K 2013 Graded nanostructured interfacial layers fabricated by high power pulsed magnetron sputtering—plasma immersion ion implantation and deposition (HPPMS-PIII&D) *Surf. Coat. Technol.* **236** 320–5
- [23] Wu Z, Tian X, Xiao S, Gong C, Pan F and Chu P K 2014 High temperature oxidation of Cr–N coatings prepared by high power pulsed magnetron sputtering—plasma immersion ion implantation & deposition *Vacuum* **108** 66–70
- [24] Kimura T, Kamata H, Nakao S and Azuma K 2016 Preparation of titanium-doped diamond-like high power pulsed magnetron sputtering system *IEEE Trans. Plasma Sci.* **44** 3083–90
- [25] Thornton J A 1974 Influence of apparatus geometry and deposition conditions on the structure and topography of thick sputtered coatings *J. Vac. Sci. Technol.* **11** 666
- [26] Kersten H, Deutsch H, Steffen H, Kroesen G M W and Hippler R 2001 The energy balance at substrate surfaces during plasma processing *Vacuum* **63** 385–431
- [27] Anders A 2010 A structure zone diagram including plasma-based deposition and ion etching *Thin Solid Films* **518** 4087–90
- [28] Movchan B A and Demshishin A V 1969 Study of the structure and properties of thick vacuum condensates of nickel, titanium, tungsten, aluminum oxide and zirconium oxide *Phys. Met. Metallogr.* **28** 653–60
- [29] Bornholdt S, Peter T, Strunskus T, Zaporojtchenko V, Faupel F and Kersten H 2011 The method of conventional calorimetric probes—a short review and application for the characterization of nanocluster sources *Surf. Coat. Technol.* **205** 5388–92
- [30] Bornholdt S and Kersten H 2013 Transient calorimetric diagnostics for plasma processing *Eur. Phys. J. D* **67** 176
- [31] Lundin D, Stahl M, Kersten H and Helmersson U 2009 Energy flux measurements in high power impulse magnetron sputtering *J. Phys. D: Appl. Phys.* **42** 185202
- [32] Vašina P, Meško M, Ganciu M, Bretagne J, Boisse-Laporte C, De Poucques L and Touzeau M 2005 Reduction of transient regime in fast preionized high-power pulsed-magnetron discharge *Europhys. Lett.* **72** 390–5
- [33] Vašina P, Meško M, de Poucques L, Bretagne J, Boisse-Laporte C and Touzeau M 2008 Study of a fast high power pulsed magnetron discharge: role of plasma deconfinement on the charged particle transport *Plasma Sources Sci. Technol.* **17** 035007
- [34] Horwat D and Anders A 2010 Compression and strong rarefaction in high power impulse magnetron sputtering discharges *J. Appl. Phys.* **108** 123306
- [35] Meng L, Yu H, Szott M M, McLain J T and Ruzic D N 2014 Downstream plasma transport and metal ionization in a high-powered pulsed-plasma magnetron *J. Appl. Phys.* **115** 223301
- [36] Thornton J A 1978 Substrate heating in cylindrical magnetron sputtering sources *Thin Solid Films* **54** 23–31
- [37] Bornholdt S, Itagaki N, Kuwahara K, Wulff H, Shiratani M and Kersten H 2013 Characterization of the energy flux toward the

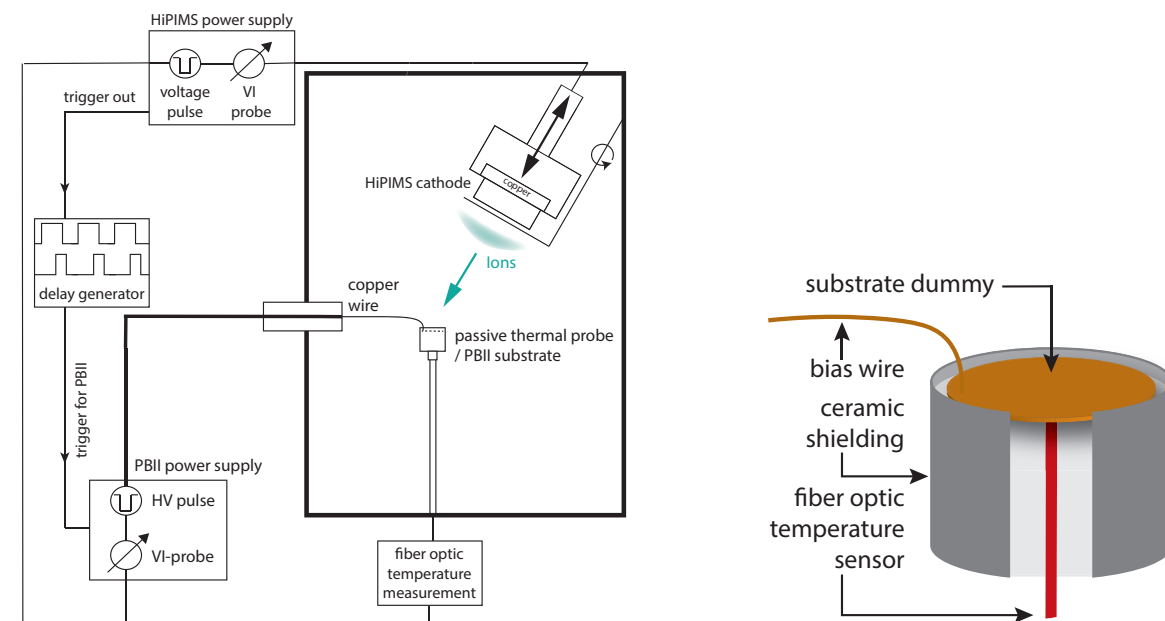
- substrate during magnetron sputter deposition of ZnO thin films *Plasma Sources Sci. Technol.* **22** 025019
- [38] Kersten H, Rohde D, Berndt J, Deutsch H and Hippler R 2000 Investigations on the energy influx at plasma processes by means of a simple thermal probe *Thin Solid Films* **377-378** 585–91
- [39] Stahl M, Trottenberg T and Kersten H 2010 A calorimetric probe for plasma diagnostics *Rev. Sci. Instrum.* **81** 023504
- [40] Schneider J M, Helmersson U, Kouznetsov V, Maca K and Petrov I 1999 A novel pulsed magnetron sputter technique utilizing very high target power densities *Surf. Coat. Technol.* **122** 290–3
- [41] Mändl S, Günzel R and Möller W 1998 Sheath and presheath dynamics in plasma immersion ion implantation *J. Phys. D: Appl. Phys.* **31** 1109–17
- [42] Mishra A, Kelly P J and Bradley J W 2010 The evolution of the plasma potential in a HiPIMS discharge and its relationship to deposition rate *Plasma Sources Sci. Technol.* **19** 045014
- [43] Macak K, Kouznetsov V, Schneider J, Helmersson U and Petrov I 2000 Ionized sputter deposition using an extremely high plasma density pulsed magnetron discharge *J. Vac. Sci. Technol. A* **18** 1533–7
- [44] Thompson M W 1968 II. The energy spectrum of ejected atoms during the high energy sputtering of gold *Phil. Mag.* **18** 377–414
- [45] Breilmann W, Maszl C, Benedikt J and von Keudell A 2013 Dynamic of the growth flux at the substrate during high-power pulsed magnetron sputtering (HiPIMS) of titanium *J. Phys. D: Appl. Phys.* **46** 485204
- [46] Kersten H, Kroesen G M W and Hippler R 1998 On the energy influx to the substrate during sputter deposition of thin aluminium films *Thin Solid Films* **332** 282–9
- [47] Barroso J J, Rossi J O and Ueda M 2003 Modeling plasma immersion ion implantation under trapezoidal voltage pulses *IEEE Trans. Plasma Sci.* **31** 104–11
- [48] Kim G H, Kim Y W, Han S, Uhm H-S, Cho J, Jung M J and Hong M 2003 Measurement of expanding plasma sheath from a target biased by a negative pulse with a fast rise time *J. Appl. Phys.* **93** 1384–8
- [49] Shamim M, Scheuer J T and Conrad J R 1991 Measurements of spatial and temporal sheath evolution for spherical and cylindrical geometries in plasma source ion implantation *J. Appl. Phys.* **69** 2904–8
- [50] Raadu M A, Axnäs I, Gudmundsson J T, Huo C and Brenning N 2011 An ionization region model for high-power impulse magnetron sputtering discharges *Plasma Sources Sci. Technol.* **20** 065007
- [51] Piel A 2010 *Plasma Physics* (Berlin: Springer)
- [52] Szapiro B and Rocca J J 1989 Electron emission from glow-discharge cathode materials due to neon and argon ion bombardment *J. Appl. Phys.* **65** 3713–6
- [53] Haase F, Manova D, Stephan M, Kersten H, Mändl S and Kersten H 2016 Evidence of secondary electron emission during PIII pulses as measured by calorimetric probe *Eur. Phys. J. D* **70** 186

Publication VI

Direct calorimetric measurements in a PBII and deposition (PBII&D) experiment with a HiPIMS plasma source

Authors	S. Gauter, M. Fröhlich and H. Kersten
Journal	Surface & Coatings Technology
Technique	Plasma based ion implantation and deposition (PBII&D)
Utilized Probes	Passive thermal probe (PTP), Substrate voltage and current (VI-probe)
Own contribution	approx. 80%

Experimental Setup:



Motivation:

The results obtained in prior measurements on the combined system of HiPIMS and PBII (see publication [V]) produced interesting results regarding the transport of the sputtered atoms and the synchronization of the two processes. However, due to the indirect measurement method only qualitative results were obtained and the necessary introduction of a grid into the process created additional uncertainties. By modifying the thermal probe to allow for direct high voltage pulsing of the probe substrate, direct quantitative measurements of the energy flux to a PBII substrate can be achieved.

Main results:

Using a modified passive thermal probe, time resolved information about the energy flux to the substrate in a PBII&D system were obtained for different PBII and HiPIMS parameters. The VI-probe and PTP measurements were in good agreement and provided insights into the secondary electron yield of the substrate. The motion of an ion wave moving from the target to the substrate was investigated using a time of flight method, with the results suggesting a collision dominated transport. The arrival of this wave creates a characteristic peak which is likely attributed to metal ions.



Contents lists available at ScienceDirect

Surface & Coatings Technology

journal homepage: www.elsevier.com/locate/surfcoat

Direct calorimetric measurements in a PBII and deposition (PBII&D) experiment with a HiPIMS plasma source

Sven Gauter^{a,*}, Maik Fröhlich^b, Holger Kersten^a

^a Institute of Experimental and Applied Physics, Christian-Albrechts-University Kiel, Germany

^b Leibniz Institute for Plasma Science and Technology, Greifswald, Germany

ARTICLE INFO

Keywords:

Calorimetric probe
HiPIMS
PBII&D
PBII
Magnetron sputtering
Energy flux

ABSTRACT

We report on direct calorimetric probe measurements in a plasma based ion implantation and deposition (PBII&D) system, using HiPIMS as plasma and deposition source. The combination of ion implantation and physical vapor deposition is a versatile system which allows successive and simultaneous coating, doping or cleaning of a substrate surface in a complex, finely adjustable system. Due to the pulsed nature of both processes, the delay between HiPIMS and PBII pulse is a crucial parameter which can be used to effectively tune the process according to the required needs. Since the delay defines at what time during the HiPIMS period the PBII pulse is applied to the substrate, it can also be utilized to obtain time resolved information about the ion density in the substrate's environment.

To allow direct calorimetric measurement of a high voltage pulsed substrate, a common passive thermal probe (PTP) was modified utilizing a fiber optic temperature sensor. With this probe, the effect of PBII voltage, substrate distance and pressure, on the energy flux and ion current towards the PBII substrate was investigated as a function of the delay between HiPIMS and PBII pulse. The results were successfully compared to a basic model and revealed important information regarding substrate position, process pressure and the effect of secondary electrons in this combined system.

1. Introduction

The utilization of HiPIMS as a source in plasma based ion implantation and deposition (PBII&D) effectively combines the advantages of magnetron sputtering and ion implantation [1]. By utilizing very low duty cycles, HiPIMS, as an enhancement of the common DC magnetron sputtering, allows to use very high peak powers ranging up to several kW/cm² [2] while keeping the thermal load on the sputtering target and the substrate low. In this way, during the pulse, very high plasma densities ($\sim 10^{19}/\text{m}^3$) and a high degree of ionization (10%–80%) of the sputtered particles are achieved [3]. The resulting flux of energetic ions towards the substrate can be effectively exploited by application of high voltage pulses to the substrate such as used in plasma based ion implantation (PBII).

Due to the complex temporal evolution of the particle density during the HiPIMS period [4], critical deposition parameters such as the energy of the depositing particles (PBII voltage), the ratio between highly energetic and less energetic particles (delay), or even the ratio between the different contributions in reactive sputtering (delay and PBII voltage) can be adjusted in a straight forward manner [5]. In 2010,

first studies on such a combined system were presented by Wu et al. who demonstrated its efficacy by deposition of CrN with excellent adhesion properties [6]. In the following years the method has been further refined and applied in the deposition of various material systems [7–11].

As in most deposition systems, the energy influx towards the substrate during plasma operation plays a critical role as it is directly affecting the surface temperature of the substrate and the film properties [12,13]. In [14], Anders presents a refined structural zone model based on previous models by Thornton [12] and Movchan [15], which points out the substrate temperature and the energy flux from impinging particles as an important parameter for tuning the film's microstructure. Recently, we emphasized the difficulties of energy flux measurements on high voltage pulsed substrates and introduced an indirect method which allows to obtain qualitative results without major modifications to the setup of the classical passive thermal probe [16]. However, this method also showed some drawbacks like the complexity associated with the use of a grid in the plasma and the lack of absolute values. To eliminate these disadvantages we modified the thermal probe to allow direct application of high voltages onto the dummy substrate of the

* Corresponding author.

E-mail addresses: gauter@physik.uni-kiel.de (S. Gauter), maik.froehlich@inp-greifswald.de (M. Fröhlich), kersten@physik.uni-kiel.de (H. Kersten).

<https://doi.org/10.1016/j.surfcoat.2018.03.094>

Received 12 June 2017; Received in revised form 1 March 2018; Accepted 13 March 2018
0257-8972/ © 2018 Elsevier B.V. All rights reserved.

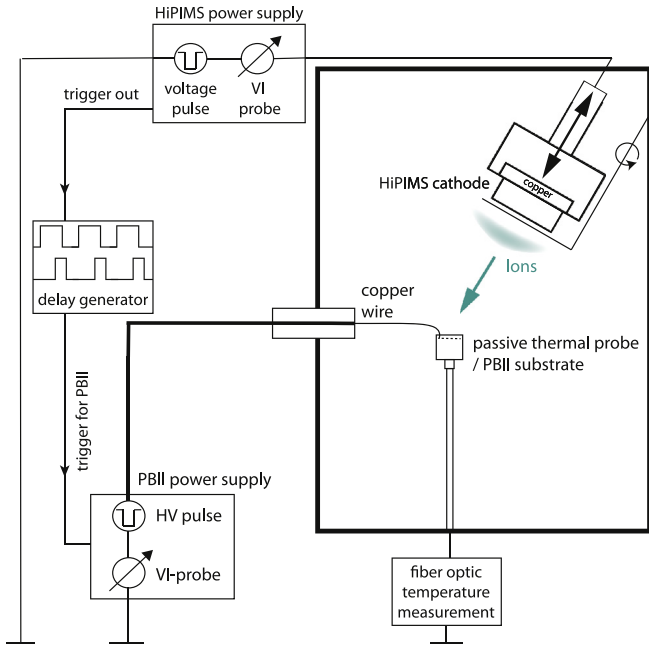


Fig. 1. Schematic drawing of the experimental setup. The bold black box resembles the vacuum chamber.

probe. With this setup, the grid can be removed and absolute values for the energy flux in a PBII&D process can be obtained, allowing for direct comparison with the measured electrical PBII power.

2. Experiment

2.1. Experimental setup and plasma diagnostics

The probe was placed in a rectangular vacuum vessel with a volume of approximately 300 l which was equipped with a 4 in. copper magnetron. The magnetron had a balanced magnetic field configuration and was powered by a Melec HiPIMS power supply with rectangular voltage pulses. To realize the calorimetric measurements with passive thermal probe (PTP), the magnetron was equipped with a pneumatic shutter mounted directly in front of the magnetron. The substrate dummy of the PTP was pulsed with a RUP6 high voltage power supply from GBS Elektronik GmbH designed for PBII processes. The PTP dummy substrate (100 μm thick copper disc with 2 cm diameter) was thus both, PBII substrate, and sensor for the calorimetric measurements. The PBII pulse was triggered on the HiPIMS pulse and the delay between the pulses was adjusted by a Stanford Research Systems DG645 delay generator (Fig. 1). The delay is defined as the time from the start of the HiPIMS pulse to the middle of the PBII pulse. All experiments were performed in argon at a HiPIMS voltage setpoint of −700 V, the values used for the performed parameter variation are summarized in Table 1.

In addition to the calorimetric measurement, the current and voltage of the PBII pulsed dummy substrate and the magnetron were monitored. To allow accurate comparison of the results, the measurements were performed simultaneously. Due to the measurement principle, the thermal probe provides an energy and time integrated value over a period of a few seconds. The VI measurements on the opposite have a high time resolution (40 ns) and are performed with an oscilloscope connected to the designated outputs of the power supplies. For better signal quality, the recorded values were averaged over 10 periods. To allow a direct comparison of the VI measurements and the energy flux, the time resolved current and voltage signals are used to calculate the time averaged electrical power density. This is achieved by calculating the time averaged PBII power, which is described in

Table 1

HiPIMS and PBII parameters for the presented measurements with the varied values printed **bold**. The HiPIMS and PBII frequency was 100 Hz for all measurements and the on-time was kept constant at 200 μs and 5 μs for HiPIMS and PBII, respectively. The HiPIMS discharge was operated in voltage regulated mode at −700 V for all measurements. The delay is defined as the delay from the start of the HiPIMS pulse to the middle of the PBII pulse and was varied between 2 and 1002 μs.

	Variation of PBII voltage	Variation of distance	Variation of pressure
PBII voltage (kV)	−3 to −7	−3	−3
Distance (cm)	24	16–33	24
Pressure (Pa)	1	1	0.5–3

greater detail in [16], and normalizing it to the probe area to obtain the power density.

2.2. Concept of the calorimetric probe (PTP)

The measurements of the energy flux were performed by a passive thermal probe (PTP). This type of probe was introduced by Thornton in 1978 [17] and since that time it has been successfully utilized in a variety of plasma environments [13, 18–22].

To allow measurement with a high voltage biased substrate, the measurement electronics for the temperature detection had to be electrically isolated from the dummy substrate. This was achieved by replacing the commonly used thermocouple with a GaAs-based fiber optic temperature sensor from Optocon AG. In Fig. 2 a schematic drawing of the probe is given which shows the bias wire made of copper welded to the top of the dummy substrate. The tip of the fiber optic sensor is attached to the back of the substrate with conductive silver glue to enhance the thermal connection. The ceramic shield guarantees that only energy influx to the substrate surface facing the plasma is measured. The heat capacity of the readily assembled probe was determined to be $C_s = 0.103 \text{ J/K}$ by calibration in an electron beam experiment as described in [23].

The concept for determination of the energy flux is based on the relation between the probe's time derivative of the enthalpy \dot{H} and the time derivative of the temperature. Specifically distinguishing between heating (\dot{T}_h - energy source switched on) and cooling (\dot{T}_c - energy source switched off) of the PTP's dummy substrate:

$$\text{Heating: } \dot{H}_h = C_s \dot{T}_h = P_{in} - P_{out,h} \quad (1)$$

$$\text{Cooling: } \dot{H}_c = C_s \dot{T}_c = -P_{out,c} \quad (2)$$

Here C_s stands for the heat capacity of the probe, P_{in} marks the energy influx from the heat source, and $P_{out,h}$ and $P_{out,c}$ describe the energy loss of the probe during the heating and the cooling phase accordingly. For

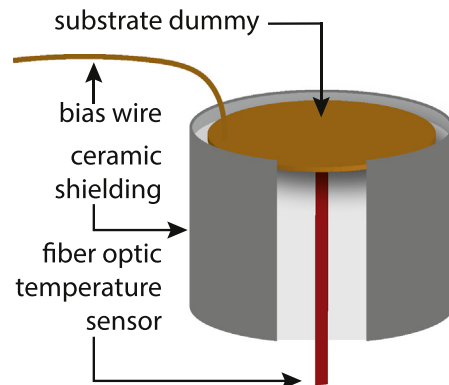


Fig. 2. Schematic drawing of the utilized passive thermal probe.

the assumption, that the energy loss during the heating phase equals the energy loss during the cooling phase at the same temperatures, Eqs. (1) and (2) can be combined to calculate the energy flux

$$J_{in} = \frac{P_{in}}{A_s} = \frac{C_s}{A_s} (\dot{T}_h - \dot{T}_c), \quad (3)$$

where A_s is the surface area of the PTP. The energy flux is thus obtained as a relative measurement where all contributions which are equal for the same temperature during the heating and the cooling, such as conductive cooling or radiative cooling, do not appear in the measurement.

To calculate the energy flux from Eq. (3), one only has to determine the slope of the temperature curve during the heating phase and the cooling phase at the same temperature. Due to the relatively low measurement frequency (2 Hz) of the utilized fiber optic sensor, the temperature curve has to be fitted over a longer time frame to obtain a reliable result. In this case, $\dot{T}_h - \dot{T}_c$ can best be obtained from the dT-curve which gives the time derivative of the temperature plotted as a function of the temperature. Since the majority of the heat loss is due to conduction, the course of the temperature can be approximated by an exponential function which results in two parallel linear functions in the dT-curve. The sought after value for $\dot{T}_h - \dot{T}_c$ can be directly extracted, as it is given by the mean of the vertical distance between the two linear fits in the evaluated temperature range [24]. In Fig. 3 this evaluation method is illustrated for an exemplary measurement.

2.3. Sources of errors and uncertainties

Due to arcing problems, the isolation of the bias wire connecting the HV feed-through to the PTP had to be removed. The drawback of this is, that during the PBII pulse the ions are not only accelerated towards the substrate dummy, but also towards the bare bias wire. As the ions collected by the wire cause a significant electric current but only a small heat flux towards the thermal probe, this can result in a discrepancy between the electrical measurement and the determined energy flux. This discrepancy scales with the sheath area of the bias wire as it determines the amount of ions being extracted from the plasma. With a length of ~20 cm and a diameter of 0.3 mm, the bias wire has a comparable surface area (~1.9 cm²) to the measurement surface of the PTP

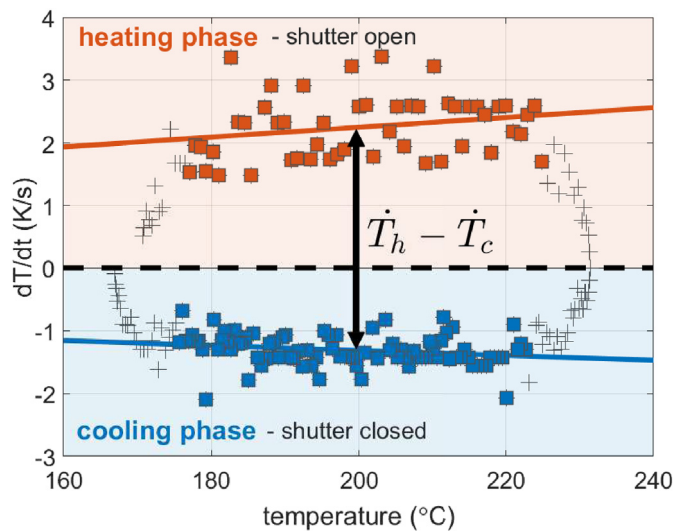


Fig. 3. Exemplary evaluation of the temperature curve for a delay of 300 μ s between HiPIMS and PBII at -7 kV PBII voltage. The pressure is 1 Pa and the HiPIMS setpoint is -700 V with 200 μ s pulse duration at 100 Hz frequency. The shown dT-curve is obtained by plotting the time derivative of the temperature as a function of the temperature. The vertical distance between the two resulting linear regions directly yield $\dot{T}_h - \dot{T}_c$.

(3.14 cm²). However, the effective area for ion collection can be expected to be much smaller, since only a limited fraction of the wire is exposed to a region with significant plasma density. Additionally, since the directed flow of ions from the target to the substrate create a much higher current as compared to the current from the background plasma, the effective area for collection is better approximated by the smaller, projected area instead of the complete surface area.

Nonetheless, this erroneous influence should be taken into account when comparing the results of energy flux to the measured electrical power, specifically when significant differences in sheath expansion can be expected such as for the variation of the PBII voltage.

Another point arises from the evaluation of the temperature curve over long times (~100 s) and wide temperature regions (up to $\Delta T \sim 100$ K) – this can cause errors in the determination of the energy flux as the heating of the shielding, shutter or other objects in the vicinity of the probe are additional energy sources which are not necessarily at the same temperature during heating and cooling phase [24].

Finally, due to the relatively time consuming method, the measurements have been performed over a considerable target run time. And although the voltage setpoint was kept constant through all the experiments, significant changes in the HiPIMS current were observed with longer erosion times resulting in higher currents. Thus, absolute comparison should only be done between values obtained with similar target run times.

3. Results and discussion

3.1. Variation of PBII voltage

The PBII voltage is a crucial parameter in the combined PBII&D system. By altering the voltage it is possible to switch the process between a deposition dominated system to a system with equal deposition and implantation to a system dominated by etching and implantation processes [14]. As the differences between these modes are characterized by substantially different energy fluxes, an investigation of this parameter is of particular interest. The combined diagnostics of energy flux and electrical power allow to obtain valuable information about the relation of these values and allow to gain information about critical processes such as the emission of secondary electrons [25].

For most plasma processes, the energy flux measured with the passive thermal probe consists of a complex set of contributions [13,26]. In the case of magnetron sputtering, important contributions typically come from the kinetic impact of particles (ions, electrons, energetic neutrals), from recombination processes on the surface or from the sublimation enthalpy which is released during film formation on the substrate [21,27]. In our case these contributions create a ‘background’ energy flux, on which the energy flux from the short on-time of the PBII pulse is superimposed. This background energy flux can be easily obtained by measurement without PBII pulse, but with the probe left at floating potential.

In Fig. 4 the results for electrical power and energy flux investigated for three different PBII voltages as a function of the delay are given, with the obtained background energy flux shown as a black dashed line at ~20 mW/cm². The curves show a close resemblance between the two diagnostics and a peak which is shifted approximately 30 μ s from the end of the HiPIMS pulse. Furthermore, it can be noted that the peak increases for both diagnostics as a function of the PBII voltage but does not change its position. From the measurement of the energy flux, it can be seen that, in spite of the small PBII duty cycle (0.05%), the energy flux originating from the highly energetic ions accelerated by the PBII voltage, can become the dominant contribution to the integrated, time averaged energy flux measured by the PTP. Expectedly, the magnitude of this contribution strongly depends on the ion density in the vicinity of the probe during the PBII pulse, e.g. in the beginning of the HiPIMS period, where a small ion density is expected, the background energy flux yields up to 70% of the overall energy flux, while at the peak of the

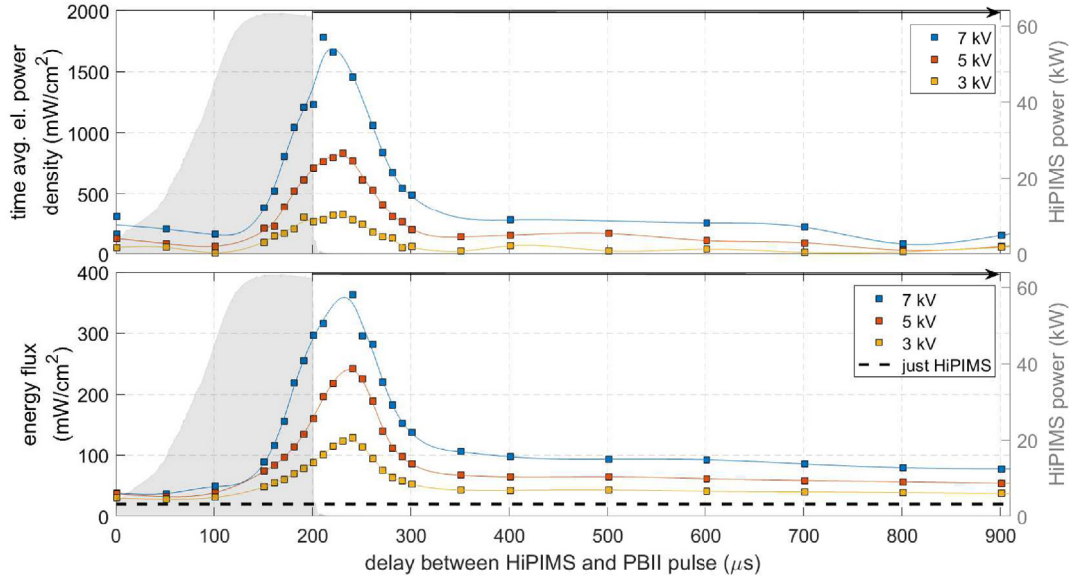


Fig. 4. Delay variation for the examined PBII voltages. The upper graph shows the results obtained from the PBII VI-probe and the lower graph gives the energy flux as detected by the PTP. The dashed black line shows the energy flux originating solely from the HiPIMS plasma, with no PBII pulse and the probe at floating potential. The shaded area represents the waveform of the HiPIMS power to the magnetron with its axis on the right.

ion density, this contribution drops to 5% for 7 kV PBII voltage. To compensate for this effect, in the following analysis, the energy flux J_{ptp} was corrected by subtracting the background energy flux. The corrected energy flux J_{ptp}^* can then be approximated by the following equation:

$$J_{ptp}^* A_s = I_{ion} U_{pbii}. \quad (4)$$

Here I_{ion} is the ion current arriving at the substrate, U_{pbii} the PBII voltage and A_s the area of the substrate. The electrical power density J_{vi} measured with the substrate's VI probe can be described by

$$J_{vi} A_s = U_{pbii} (I_{ion} + I_{se}) = U_{pbii} I_{ion} (1 + \gamma_{se}), \quad (5)$$

with I_{se} being the current generated by secondary electrons emitted from the substrate and γ_{se} the secondary electron emission coefficient. The sum $I_{ion} + I_{se}$ is the net current which is detected by the VI probe. By combining Eqs. (4) and (5) we can therefore calculate the secondary electron yield of our dummy substrate:

$$\gamma_{se} = \frac{J_{vi}}{J_{ptp}^*} - 1. \quad (6)$$

In Fig. 5 the secondary electron yield, as calculated with Eq. (6) from the maximum measured values shown in Fig. 4, is plotted as a function of the energy of the impinging ions. Additionally, we plotted reference values reported by Szapiro and Rocca [28] and Phelps and

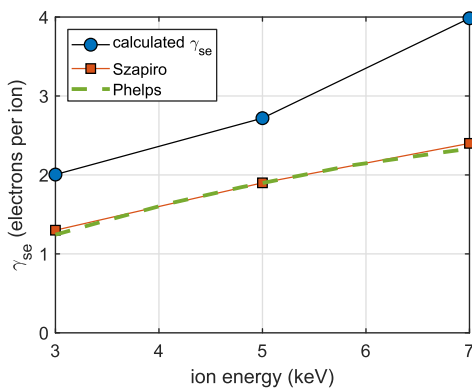


Fig. 5. Results for calculation of γ_{se} according to Eq. (6) and comparison to reference data from Szapiro [28] and Phelps and Petrovic [29].

Petrovic [29]. Szapiro et al. used argon ions which were accelerated by an ion gun onto a copper sample. The secondary electron yield was then calculated from the sample current and current of argon ions. The plotted values from Phelps and Petrovic [29] are the result of a fit to a collection of reviewed data.

The calculated values of γ_{se} from our measurements are in the same order of magnitude and exhibit a similar trend for increasing ion energy as compared to the reference data. The secondary electron yield is known to be effected by numerous parameters such as the surface condition of the bombarded material, the mass-ratio between impinging and bombarded species or the charge state of the impinging particle [28, 30-32]. The observed differences could thus be explained by a number of different factors. Comparing to Szapiro's experiments where only single charged argon ions are used, the ions arriving at our substrate are a mixture of argon and copper ions in single and double charged state [33,34]. While it is difficult to estimate the effect of the higher mass of the copper particles, it is well known, that a higher state of charge increases the yield due to potential emission [32].

Independently of these experimental parameters, the erroneous influence of the exposed bias wire described in Section 2.3, will generally result in a higher electrical current as compared to the expected energy flux. This deviation can generally be expected to increase with bigger sheath expansion since the collection area of the wire increases linearly, while the collection area of the probe substrate increases by a lesser amount due to its flat geometry. In spite of the short PBII pulse length, a significant increase of sheath expansion for increasing PBII voltage can be expected [35-37]. Accordingly, the observed deviation from the reference values and also its increase for higher ion energies could be explained by a disproportionately high increase of measured electrical power due to the erroneous influence of the exposed bias wire. From Eqs. (5) and (6) it can be seen that this would result in an increase of the calculated γ_{se} , such as observed in Fig. 5.

3.2. Variation of substrate distance

To achieve a better understanding of the ion wave which travels from the HiPIMS source to the PBII substrate, the ion wave can be probed at different distances from the target. In Fig. 6 the obtained measurement results for the variation of the distance are compiled.

Generally, the ions arriving at the substrate are expected to be a mix

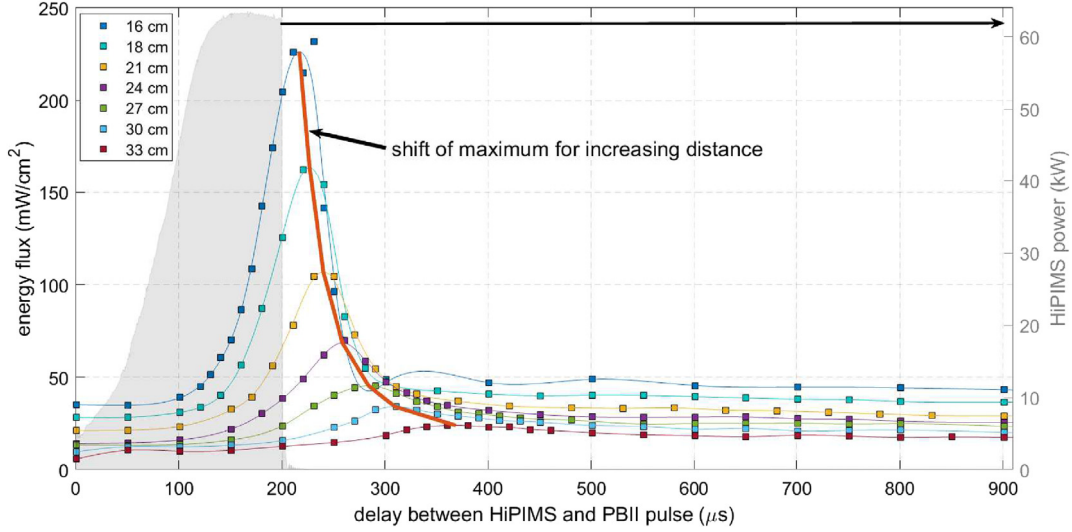


Fig. 6. Results for the determination of the energy flux for delay variation at different substrate distances.

of copper and argon, with the composition depending on various parameters, such as distance, delay-time or pressure. In a comparable system, Horwat et al. observed that for higher distances and pressures, the initial flux of ions, which is attributed to argon ions from the beginning of the pulse, is mostly dissipated. Under these conditions, the remaining ion current in their measurements showed a peak, which they associated to the self-sputtering phase of the pulse [38]. Since we observe comparable peaks in our system, in the following we assume that the maximum and especially the delay-time of the maximum in our curves are majorly influenced by the motion of the copper ions.

The motion of the ions traveling from the cathode plasma to the substrate is strongly affected by the collisions with the background gas. To give a simple approximation of the deceleration due to these collisions, a 1D model for momentum exchange collisions with head-on collisions and neglecting wall losses of the copper can be used [39].

For 1D elastic collisions between two objects we can calculate the deceleration of the copper hitting an argon atom of the background gas from the momentum and energy conservation [40]:

$$v_{Cu,after} = \frac{m_{Cu} - m_{Ar}}{m_{Cu} + m_{Ar}} v_{Cu,before} + \frac{2m_{Ar}}{m_{Cu} + m_{Ar}} v_{Ar,before}, \quad (7)$$

with m_{Cu} and m_{Ar} being the atomic mass of copper and argon, $v_{Cu,before}$ and $v_{Cu,after}$ the velocity of the copper ion before and after the collision and $v_{Ar,before}$ being the velocity of the background gas. If we assume, that the argon atom is initially at rest we can calculate the ratio of change for each collision to be:

$$R_{v,change} = \frac{\Delta v}{v_{Cu,before}} = \frac{v_{Cu,after} - v_{Cu,before}}{v_{Cu,before}} = \frac{-2m_{Ar}}{m_{Cu} + m_{Ar}} \quad (8)$$

The change of velocity per distance dx is then given by

$$\frac{dv}{dx} = \frac{\Delta v}{\lambda_{mfp}} = \frac{R_{v,change} \cdot v_{Cu,before}}{\lambda_{mfp}}, \quad (9)$$

where λ_{mfp} denotes the mean free path. The resulting first-order linear ordinary differential equation can be solved to obtain the velocity of the copper ions passing through the background gas as a function of the distance to be

$$v_{Cu}(x) = v_0 \cdot \exp\left(-\frac{x}{\lambda_{mfp}} \cdot R_{v,change}\right), \quad (10)$$

with v_0 being the initial velocity of the copper ions. The equation of motion can then be derived through

$$\exp\left(-\frac{x}{\lambda_{mfp}} \cdot R_{v,change}\right) dx = v_0 dt. \quad (11)$$

After integrating and applying the boundary condition $x(t_0) = 0$ we get

$$x_{Cu}(t) = -\frac{\lambda_{mfp}}{R_{v,change}} \ln\left(1 + \frac{v_0 R_{v,change}}{\lambda_{mfp}} (t_0 - t)\right). \quad (12)$$

The mean free path of the copper ions is assumed to be identical to the neutral mean free path, which is given by the following equation [41]:

$$\lambda_{mfp} = (n_{Ar} \cdot \sigma_{Cu,Ar})^{-1}. \quad (13)$$

Here n_{Ar} is the density of the background gas and $\sigma_{Cu,Ar}$ is the cross section for a collision between copper and argon. To take into account the reduction of the cross section for higher projectile energies, the variable soft sphere model (VSS) introduced by Koura and Matsumoto was used [42,43]. In this model, the total cross section is given by

$$\sigma_i = C \left(\frac{\epsilon}{k_B}\right)^{-\omega}, \quad (14)$$

with the projectile energy ϵ , Boltzmann constant k_B and constants C , ω which are characteristic for the present combination of projectile and background gas. I.e. for the collision between argon and argon ($C = 124.8$, $\omega = 0.19$) with a projectile energy of $\epsilon = 2$ eV, the mean free path yields ~ 2.2 cm as compared to a mean free path of ~ 1.2 cm for a plain hard sphere model [43].

The particle density of the background gas n_{Ar} can be calculated from the ideal gas law if the pressure ($p = 1$ Pa) and the temperature ($T = 300$ K) are known:

$$n_{Ar} = \frac{p}{k_B T}. \quad (15)$$

With these assumptions for the mean free path, cross section and ratio of change for collisions, we can compare our measurements with the model. To obtain values comparable to Eq. (12), a time of flight approach was used by extracting the delay values of the maxima in our curves for the different investigated distances from Fig. 6. This gives us the time of arrival for the crest of the ion wave at the respective distance and, thus, allows us to observe the motion of the ion wave from target to substrate. Fig. 7 shows the result of this analysis together with the fit according to Eq. (12). The parameters used for the fit are summarized in Table 2 along with the theoretical values calculated from Eqs. (8) and 13 and the starting velocity calculated from the energy of 12.5 eV acquired from the sputter process (SRIM [44]). For the presented fit, only the ratio of change was fixed at the theoretical value

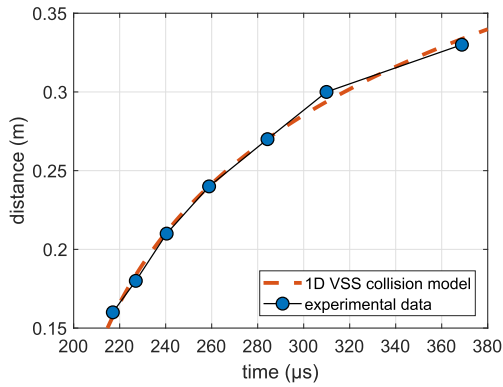


Fig. 7. Measured data for the progression of the ion wave. The blue dots represent the experimental data which were obtained from the position of the maximum values from Fig. 6. The dashed line gives the result of the fit based on Eq. (12) with the parameters described in Table 2. (For interpretation of the references to color in this figure legend, the reader is referred to the web version of this article.)

Table 2

Parameters for the fit of Eq. (12) to the experimental data and comparison to theoretical values, calculated as described in the text. Since no suitable data regarding the cross section between copper and argon were available, the theoretical value for the mean free path was calculated for argon-argon collision at 2 eV (~velocity at 20 cm taken from Fig. 7) as described in the text. The theoretical value for the starting velocity v_0 acquired from the sputter process was calculated from an energy of 12.5 eV (SRIM [44]). The fixed values are printed in bold, the values in normal letters are determined by the fit algorithm and the errors represent the 95% confidence bounds.

	λ_{mfp} (cm)	$R_{v,change}$	v_0 (km/s)	t_0 (μ s)
Theoretical values	2.24 (Ar-Ar)	- 0.228	6.160	-
1D VSS collision model	2.40 ± 0.8	- 0.228	13 ± 11	182 ± 15

while the values for the mean free path, v_0 and t_0 were determined by the fit algorithm.

As it can be recognized from Fig. 7, the theoretical values fit the measured data quite well albeit the uncertainties associated with the assumptions of the model. From Table 2 it can further be seen, that the calculated fit parameters are in the expected range and exhibit reasonably low uncertainties. The starting time of the wave was calculated to be shortly before the end of the HiPIMS pulse and the starting velocity is also roughly in the range of the value calculated from the

sputter process. The mean free path is in the same range as the exemplary value calculated for argon, which is reasonable due to the similar atomic radii of the two species.

Gylfason et al. observed a comparable ion motion in their experiment, using a Langmuir probe and interpreted it as an ion-acoustic solitary wave moving away from the target [45]. In the constant relation between peak amplitude and width, a typical feature of such a wave can be found in our experiment as well [46]. However, comparing to Gylfason we do not observe a constant velocity of the ions but a deceleration of the ion wave (Fig. 7) which might be attributed to the larger distance to the target and emphasizes the role of collisions in this pressure regime.

3.3. Variation of pressure

To investigate the effect of the gas pressure onto the transport of the sputtered particles and its effect on the energy flux arriving at the substrate, the argon pressure was varied between 0.5 and 3 Pa. Since the discharge was operated in voltage regulated mode, the plasma was changing strongly for the different gas pressures as indicated by the strong changes in the HiPIMS current, see Fig. 8 (a).

Analog to the observations made by Anders et al. [2], we find a change of the slope in the beginning of all current curves which is associated with the onset of the runaway regime. Due to the increasing mean free path with decreasing pressure, this point is reached later for lower pressures and, correspondingly, the onset of the saturation regime is delayed as well. Another feature from the curves which has also been observed by Horwat and Anders et al. [2,38], can be found in the end of the HiPIMS pulse. For all conditions where the saturation regime is reached, the current shows increasingly similar values towards the end of the pulse where it tends towards a steady state. This trend is a convincing argument for the significance of rarefaction in our system as the sputtered copper and the associated feedback mechanism increasingly displace the argon in front of the target and, thus, decrease the effect of chamber pressure [47,48].

In Fig. 8 (b), the PTP results for the variation of the gas pressure are summarized. As expected, the curves show an increase of the energy flux as a function of the pressure which can predominantly be attributed to the increasing HiPIMS power caused by the earlier onset of the current as seen in Fig. 8 (a). Furthermore it can be observed, that, in spite of the increasing average HiPIMS power, the maximum detected energy flux saturates for pressures above 1 Pa. This saturation seems to be correlated to the assimilation of the HiPIMS currents towards the end of the pulse caused by rarefaction and, thus, supports the assumption that the peak observed in all delay dependencies of the PTP is likely

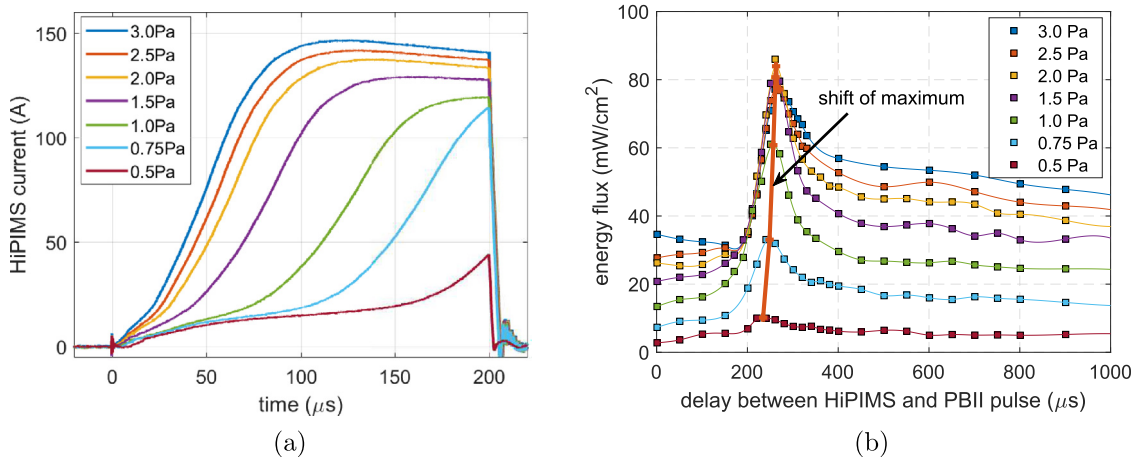


Fig. 8. (a) Current measurements of the HiPIMS waveform for different pressures at a fixed voltage of -700 V. (b) Results from the PTP for the variation of the delay for different gas pressures.

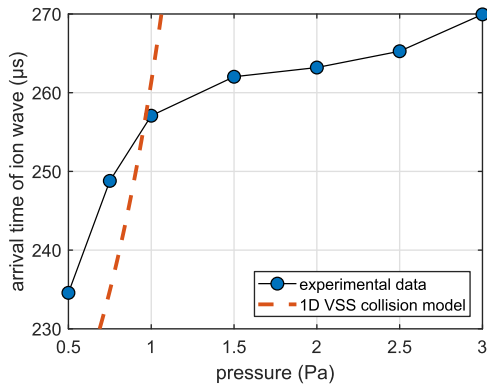


Fig. 9. Analysis of the results obtained from variation of the delay for different gas pressures. The blue dots show the experimental data obtained from Fig. 8 (b) and the thick solid line gives a prediction according to Eq. (16) with the parameters from Table 2. (For interpretation of the references to color in this figure legend, the reader is referred to the web version of this article.)

caused by metal ions. Another striking feature, which is likely also attributed to the self-sputtering phase and the associated rarefaction, can be found in the similar values and slopes in the region around 200–220 μs for the curves measured at pressures above 0.75 Pa.

Comparing the obtained data for the variation of the gas pressure with theoretical values comes with a number of difficulties. A major uncertainty is associated with the effect of the aforementioned rarefaction since the pressure between target and substrate most likely differs significantly from the value detected at the wall of the chamber. It can further be expected, that, represented by the strong changes in HiPIMS current, distinctively different plasma conditions appear which might additionally affect the transport of the ions. Taking these uncertainties into account we can now take a closer look at the results obtained from the variation of the pressure in our system.

Fig. 9 shows the position of the maximum values of the PTP results from Fig. 8 (b) as a function of the pressure. Along the experimental data, a theoretical curve is plotted obtained from solving Eq. (12) for the time and rewriting it as a function of the gas pressure:

$$t_{\text{arrival}}(p) = t_0 - \frac{k_B T}{v_0 R_{v,\text{change}} \sigma_{Ar,Cu} P} \left(\exp \left(-\frac{x R_{v,\text{change}} \sigma_{Ar,Cu} P}{k_B T} \right) - 1 \right). \quad (16)$$

The model curve in Fig. 9 is plotted using the determined values from Table 2. As it can be clearly seen, this model roughly describes the results up to 1 Pa but it does not explain the observed dependence for pressures above 1 Pa. As mentioned before, the variation of pressure must be associated with a diverse change of the plasma parameters. Thus, to predict the effect of the pressure on the motion of the observed ion wave, a much more sophisticated model must be utilized which is not covered by the scope of this study.

4. Conclusion

Using a modified passive thermal probe, time resolved information about the energy flux to the substrate in a PBII&D system were obtained for different PBII and HiPIMS parameters. The combination of VI- and energy flux measurements allowed us to obtain information about the secondary electron yield of our substrate which could be reasonably matched with comparable values from literature. All results showed a peak-like shape for the delay dependence which reflects the evolution of the ion density in the substrate environment and underlines the importance of the contribution from kinetic ions to the integral energy flux in this system. The transport of the sputtered and ionized copper was dominated by an ion wave/bunch moving from the target towards the substrate. The measurements at different distances allowed us to investigate the motion of this wave by a time of flight method which

suggested a strongly collision dominated transport. The investigation at different gas pressures suggested that the observed peak is likely caused by metal ions and emphasized the complexity associated with changes in the process pressure.

References

- [1] A. Anders, High power impulse magnetron sputtering and related discharges: scalable plasma sources for plasma-based ion implantation and deposition, *Surf. Coat. Technol.* 204 (18–19) (2010) 2864–2868.
- [2] A. Anders, J. Andersson, A.P. Ehasarian, High power impulse magnetron sputtering: current-voltage-time characteristics indicate the onset of sustained self-sputtering, *J. Appl. Phys.* 102 (11) (2007) 1–11.
- [3] U. Helmersson, M. Lattemann, J. Bohlmark, A.P. Ehasarian, J.T. Gudmundsson, Ionized physical vapor deposition (IPVD): a review of technology and applications, *Thin Solid Films* 513 (2006) 1–24.
- [4] N. Britun, T. Minea, S. Konstantinidis, R. Snyders, Plasma diagnostics for understanding the plasma-surface interaction in HiPIMS discharges: a review, *J. Phys. D: Appl. Phys.* 47 (22) (2014) 224001.
- [5] G. Greczynski, J. Lu, J. Jensen, I. Petrov, J.E. Greene, S. Bolz, W. Kölker, C. Schiffer, O. Lemmer, L. Hultman, Metal versus rare-gas ion irradiation during Ti1-xAlxN film growth by hybrid high power pulsed magnetron/dc magnetron co-sputtering using synchronized pulsed substrate bias, *J. Vac. Sci. Technol. A* 30 (6) (2012) 061504.
- [6] Z. Wu, X. Tian, J. Shi, Z. Wang, C. Gong, S. Yang, P.K. Chu, Z. Wu, X. Tian, J. Shi, Z. Wang, C. Gong, Novel plasma immersion ion implantation and deposition hardware and technique based on high power pulsed magnetron discharge, *Rev. Sci. Instrum.* 82 (2011) 033511.
- [7] J.-H. Jeon, J.-Y. Choi, W.-W. Park, S.-W. Moon, K.-W. Park, S.-H. Lim, S.-H. Han, Crystalline Ge quantum dots embedded in SiO2 matrix synthesized by plasma immersion ion implantation, *Nanotechnology* 22 (2011) 285605.
- [8] Z. Wu, X. Tian, Z. Wang, C. Gong, S. Yang, C. Ming, P.K. Chu, C. Ming Tan, P.K. Chu, Microstructure and mechanical properties of CrN films fabricated by high power pulsed magnetron discharge plasma immersion ion implantation and deposition, *Rev. Sci. Instrum.* 258 (1) (2011) 242–246.
- [9] Z. Wu, X. Tian, Y. Wei, C. Gong, S. Yang, F. Pan, P.K. Chu, Graded nanostructured interfacial layers fabricated by high power pulsed magnetron sputtering - plasma immersion ion implantation and deposition (HPPMS-PIII&D), *Surf. Coat. Technol.* 236 (2013) 320–325.
- [10] Z. Wu, X. Tian, S. Xiao, C. Gong, F. Pan, P.K. Chu, High temperature oxidation of Cr-N coatings prepared by high power pulsed magnetron sputtering - plasma immersion ion implantation & deposition, *Vacuum* 108 (2014) 66–70.
- [11] T. Kimura, H. Kamata, S. Nakao, K. Azuma, Preparation of titanium-doped diamond-like high power pulsed magnetron sputtering system, *IEEE Trans. Plasma Sci.* 44 (12) (2016) 3083–3090.
- [12] J.A. Thornton, Influence of apparatus geometry and deposition conditions on the structure and topography of thick sputtered coatings, *J. Vac. Sci. Technol.* 11 (4) (1974) 666.
- [13] H. Kersten, H. Deutsch, H. Steffen, G. Kroesen, R. Hippler, The energy balance at substrate surfaces during plasma processing, *Vacuum* 63 (3) (aug 2001) 385–431.
- [14] A. Anders, A structure zone diagram including plasma-based deposition and ion etching, *Thin Solid Films* 518 (15) (2010) 4087–4090.
- [15] B.A. Movchan, A.V. Demshishin, Study of the structure and properties of thick vacuum condensates of nickel, titanium, tungsten, aluminum oxide and zirconium oxide, *Phys. Met. Metallogr. (Engl. Trans.)* 28 (1969) 83–90.
- [16] S. Gauter, M. Fröhlich, W. Garkas, M. Polak, H. Kersten, Calorimetric probe measurements for a high voltage pulsed substrate (PBII) in a HiPIMS process, *Plasma Sources Sci. Technol.* 26 (6) (2017) 1–17.
- [17] J.A. Thornton, Substrate heating in cylindrical magnetron sputtering sources, *Thin Solid Films* 54 (1) (1978) 23–31.
- [18] S. Bornholdt, N. Itagaki, K. Kuwahara, H. Wulff, M. Shiratani, H. Kersten, Characterization of the energy flux toward the substrate during magnetron sputter deposition of ZnO thin films, *Plasma Sources Sci. Technol.* 22 (2) (2013) 025019.
- [19] S. Bornholdt, H. Kersten, Transient calorimetric diagnostics for plasma processing, *Eur. Phys. J. D* 67 (8) (2013) 176.
- [20] H. Kersten, D. Rohde, J. Berndt, H. Deutsch, R. Hippler, Investigations on the energy influx at plasma processes by means of a simple thermal probe, *Thin Solid Films* 377–378 (0) (2000) 585–591.
- [21] D. Lundin, M. Stahl, H. Kersten, U. Helmersson, Energy flux measurements in high power impulse magnetron sputtering, *J. Phys. D: Appl. Phys.* 42 (18) (2009) 185202.
- [22] R. Wendt, K. Ellmer, K. Wiesemann, Thermal power at a substrate during ZnO:Al thin film deposition in a planar magnetron sputtering system, *J. Appl. Phys.* 82 (5) (1997) 2115–2122.
- [23] M. Stahl, T. Trottenberg, H. Kersten, A calorimetric probe for plasma diagnostics, *Rev. Sci. Instrum.* 81 (2) (feb 2010) 023504.
- [24] T. Kewitz, M. Fröhlich, H. Kersten, Analysis of passive calorimetric probe measurements at high energy influxes, *EPJ Tech. Instrum.* 4 (1) (2017) 1.
- [25] F. Haase, D. Manova, M. Stephan, H. Kersten, S. Mändl, H. Kersten, Evidence of secondary electron emission during PIII pulses as measured by calorimetric probe, *Eur. Phys. J. D* 70 (9) (2016) 186.
- [26] D. Depla, S. Mahieu, T. Ono, T. Kenmotsu, T. Muramoto, *Reactive Sputter Deposition*, Springer Series in Materials Science vol. 109, Springer Berlin Heidelberg, Berlin, Heidelberg, 2008.

- [27] S. Bornholdt, J. Ye, S. Ulrich, H. Kersten, Energy fluxes in a radio-frequency magnetron discharge for the deposition of superhard cubic boron nitride coatings, *J. Appl. Phys.* 112 (12) (2012).
- [28] B. Szapiro, J.J. Rocca, Electron emission from glow-discharge cathode materials due to neon and argon ion bombardment, *J. Appl. Phys.* 65 (9) (1989) 3713–3716.
- [29] A.V. Phelps, Z.L. Petrovic, Cold-cathode discharges and breakdown in argon: surface and gas phase production of secondary electrons, *Plasma Sources Sci. Technol.* 8 (3) (1999) R21–R44.
- [30] B. Szapiro, J.J. Rocca, T. Prabhuram, Electron yield of glow discharge cathode materials under helium ion bombardment, *Appl. Phys. Lett.* 53 (5) (1988) 358–360.
- [31] E. Cawthron, Secondary electron emission from solid surfaces bombarded by medium energy ions, *Aust. J. Phys.* 24 (4) (1971) 859.
- [32] H. Eder, W. Messerschmidt, H. Winter, F. Aumayr, Electron emission from clean gold bombarded by slow Auq⁺ (q = 1 – 3) ions, *J. Appl. Phys.* 87 (11) (jun 2000) 8198–8200.
- [33] S. Kadlec, C. Quaeys, G. Knuyt, L. Stals, Energy-resolved mass spectrometry and Monte Carlo simulation of atomic transport in magnetron sputtering, *Surf. Coat. Technol.* 97 (1-3) (1997) 633–641.
- [34] T.D.L. Arcos, R. Schröder, Y.A. Gonzalvo, V.S.-v.D. Gathen, J. Winter, Description of HiPIMS plasma regimes in terms of composition, spoke formation and deposition rate, *Plasma Sources Sci. Technol.* 23 (5) (2014) 54008.
- [35] S. Mändl, R. Günzel, W. Möller, Sheath and presheath dynamics in plasma immersion ion implantation, *J. Phys. D. Appl. Phys.* 31 (9) (may 1998) 1109–1117.
- [36] P.K. Chu, S. Qin, C. Chan, N.W. Cheung, L.A. Larson, Plasma immersion ion implantation - a fledgling technique for semiconductor processing, *Mater. Sci. Eng. R. Rep.* 17 (6–7) (1996) 207–280.
- [37] G.-H. Kim, Y.-W. Kim, S. Han, H.-S. Uhm, J. Cho, M.J. Jung, M. Hong, Measurement of expanding plasma sheath from a target biased by a negative pulse with a fast rise time, *J. Appl. Phys.* 93 (3) (2003) 1384–1388.
- [38] D. Horwat, A. Anders, Compression and strong rarefaction in high power impulse magnetron sputtering discharges, *J. Appl. Phys.* 108 (12) (2010) 123306.
- [39] M.A. Raadu, I. Axnäs, J.T. Gudmundsson, C. Huo, N. Brenning, An ionization region model for high-power impulse magnetron sputtering discharges, *Plasma Sources Sci. Technol.* 20 (6) (2011) 065007.
- [40] W. Demtröder, *Experimentalphysik 1*, vol. 5, (2008).
- [41] A. Piel, *Plasma Physics*, vol. 1, Springer, Berlin, Heidelberg, 2013.
- [42] K. Koura, H. Matsumoto, Variable soft sphere molecular model for inverse-power-law or Lennard–Jones potential, *Phys. Fluids A* 3 (10) (oct 1991) 2459–2465.
- [43] K. Koura, H. Matsumoto, Variable soft sphere molecular model for air species, *Phys. Fluids A* 4 (5) (may 1992) 1083–1085.
- [44] J.F. Ziegler, J. Biersack, Monte Carlo Code SRIM2006.02, (2006).
- [45] K.B. Gylfason, J. Alami, U. Helmersson, J.T. Gudmundsson, Ion-acoustic solitary waves in a high power pulsed magnetron sputtering discharge, *J. Phys. D. Appl. Phys.* 38 (18) (2005) 3417–3421.
- [46] H. Washimi, T. Taniuti, Propagation of ion-acoustic solitary waves of small amplitude, *Phys. Rev. Lett.* 17 (19) (1966) 996–998.
- [47] J. Vlček, A.D. Pajdarová, J. Musil, Pulsed DC magnetron discharges and their utilization in plasma surface engineering, *Contrib. Plasma Physics* 44 (56) (sep 2004) 426–436.
- [48] S.M. Rossnagel, Gas density reduction effects in magnetrons, *J. Vac. Sci. Technol. A* 6 (1) (jan 1988) 19–24.

7 Conclusion and Outlook

This chapter will summarize the different results obtained in each publication to provide a complete overview. Based on this comprehensive summary, the main findings across the different projects and a resulting outlook of interesting possibilities for improvements and experimental paths are given.

- As part of an ESA/ESTEC project, the active thermal probe (ATP) was integrated into a diagnostic platform designed to characterize ion beams and ion thrusters (publication [I]). Test campaigns have been performed in two different vacuum facilities, where the same two thrusters were investigated for sake of comparison. The thrusters were chosen to represent two extreme points of the typical thrust range for ion beams: the RIT- μ X in the μ N range and the SPT-100D EM1 in the 100 mN range. Using the measurements from the RIT- μ X thruster as exemplary results, it is shown that the different diagnostics show good reproducibility and a first analysis resulted in good agreement between them. The comprehensive characterization of a thruster is an essential part in the development and optimization process of ion thrusters and a standardized platform would allow for reliable comparison between different models. The results obtained in this project mean an important step towards standardization and have also pointed out difficulties which are associated with different test environments. In general, the combination of a five-axis positioning system combined with several complementary diagnostics, provides a versatile platform not only for comparison but especially for the scientific investigation of ion beams. Furthermore, being able to switch between different diagnostics without breaking the vacuum, also allows to learn more about the different diagnostic tools and on how they could complement each other. For example, the addition of a force probe to the platform would provide another interesting measurement value which can be directly correlated to the energy flux or the ion energy.
- The ratio between neutral, depositing particles and bombarding ions, which transmit energy mainly by kinetic impact to the film, is known to strongly affect the film growth on the substrate. To control this parameter, a confocal magnetron sputtering system was equipped with an external electromagnetic coil which allowed to change the magnetic 'balance' of the system (publication [II]). The effect of the magnetic field was investigated using the active thermal probe, a Langmuir probe and sample depositions. The results showed that the energy flux as well as the ion current onto the substrate changes strongly for the case that the magnetic coil is set up to create a strongly 'unbalanced' configuration. In this configuration, the ion-to-neutral ratio was found to be increased by a factor of 30 compared to the case with no external field. Test depositions of AlN showed a transition from tensile to compressive stress for increasing ion flux density, which is in good agreement with the theory.

- Understanding the energy flux to a growing film has always been of key interest and particularly in magnetron sputtering systems much work has been performed in this field. Comparing former studies it becomes apparent, that the contributions to the energy flux change strongly depending on various parameters. Due to the differences in the studies (experimental setup, magnetrons, probes, etc.), it is difficult to develop a complete picture which is applicable in a more universal way. To provide a ground for such a more complete picture, we investigated 15 combinations of three gases with five target materials for variations of the most relevant process parameters (publication [III]). To unravel the integral energy flux measured with the PTP, additional LP and QCM measurements were performed and backed up by SRIM simulations. The results confirmed, that neither the composition nor the absolute value of the energy flux is at any means universal; even in this intentionally simple system, strong changes are observed. Three mechanisms were identified which can dominate the energy flux: (i) sputtered atoms create a significant energy flux in most systems, however, they only dominate the energy flux for cases with high sputtering yields, (ii) the contribution from reflected neutrals is of particular importance for heavy target materials or light sputter gas, (iii) in cases with poor thermal conductivity of the target material, even for moderate powers, the target heats up strongly and produces a high radiative energy flux. Since these results were all obtained at floating potential, the contribution from electrons and ions was found to be low for all conditions and materials.
- The two cases above are examples which represent the typical dc magnetron sputtering, using the same technique which is also found in many industrial applications. To provide a high purity and high deposition rate, in these systems the pressure usually does not exceed ~ 2 Pa. In gas aggregation sources (GAS) on the opposite, collisions with the background gas are an essential mechanism to cool the sputtered atoms and, thus, allow for formation of nanoparticles and clusters. Accordingly, the typical pressure in these systems is in the range of 20 - 200 Pa, which means a transition from the molecular to the collisional regime as compared to conventional lower pressure magnetron sputtering. Measurements inside the aggregation chamber of such a GAS can provide information relevant to the particle formation mechanism inside the aggregation chamber. Therefore, energy flux measurements along with deposition rate and Langmuir measurements were performed for different process parameters as part of a collaboration with colleagues from the Charles University in Prague (publication [IV]). The results obtained with different targets made from copper, tungsten and a compound of both materials, showed that the composition of the energy flux is comparable to that found in the lower pressure regime. For copper with its high sputter yield, the main fraction of the energy flux is likely attributed to the depositing atoms, while for the cases where tungsten is part of the cathode, reflected neutrals are argued to dominate the energy flux. The effect of the higher pressure and accordingly increased thermal conductivity of the gas was not found to directly transfer more energy from the target to the substrate, but instead had to be viewed from the point of gas-rarefaction. The measurements indicate that the main effect of the energy transfer to the gas is the rarefaction and accordingly longer mean free path for sputtered atoms and reflected neutrals.

- In an extensive collaboration with the INP in Greifswald a newly developed system for parallel implantation and coating has been investigated (publication [V] and publication [VI]). As in all surface treatment systems, the energy flux to the substrate is of central interest. For the combination of HiPIMS and PBII an additional aspect arises from the synchronization between these two pulsed processes. As a first approach, this parameter was investigated using a system which provides quantitative information about the energy flux onto the high voltage pulsed substrate. This was achieved, by combining a grid, which acted as the PBII substrate, and a passive thermal probe positioned underneath the grid. The setup was found to correctly represent the processes on the substrate and provide an indirect measurement method for the energy flux. By varying the delay between HiPIMS pulse and PBII pulse, time-resolved information about the ion density in the substrate region were obtained. These indicated, that the ions travel as a relatively well-defined bunch or wave from the target to the substrate.

The development of an electrically insulated version of the passive thermal probe allowed to directly use the probe substrate as the PBII-substrate and, thus, provide absolute values. This new probe was used to verify and extend the measurements obtained with the grid setup in a subsequent set of measurements. The absolute values allowed for direct comparison to the recorded electrical current of the substrate which provided insights about the emission of secondary electrons from the high-voltage pulsed substrate. By investigation of the influence of selected parameters on the form and arrival time of the ion-wave, the transport of this wave was found to be strongly dominated by collisions with the background gas. The main peak in the energy flux and current density was argued to be attributed to metal ions.

The results demonstrate the universal importance of the energy flux in any plasma based application and that through carefully designed measurement procedure and combination with other diagnostics, far more than the thermal load on a substrate can be obtained. A common theme which emerged in the measurements on magnetron sputtering systems was the importance of reflected neutral particles. These are created as an ion, which is accelerated in the cathode potential and gets neutralized and reflected back towards the substrate where it deposits its high kinetic energy. This contribution is often underestimated as it is comparatively difficult to measure those fast neutral particles.

Inspired by the extensive work with thermal probes and the optimization performed on those probes, a few points have emerged which would further improve the diagnostic methods or would generally be a starting point for future investigations:

- Investigations performed with high bias potential applied to the PTP substrate have shown that valuable information regarding the secondary electron emission from the probe surface can be gained from comparison to the electric current to the probe. The experimental setup in these investigations where at no means optimized to measure the secondary electron yield, but nonetheless resulted in realistic values. A specifically designed experiment based on calorimetric measurements could provide a relatively simple and flexible method for the determination of the secondary electron emission yield γ_{se} . A possible setup for such an experiment could be based on an ion beam which works at a sufficiently low pressure to ensure that the PTP is mainly exposed to ions.

From the precisely defined energy of the ions and the electric current measured on the PTP substrate, a theoretical value of the energy flux to the probe can be calculated. By comparison of this theoretical value to the energy flux determined by the PTP, γ_{se} can be determined from the offset created by the increased current due to secondary electron emission.

- The work on pulsed systems like the HiPIMS discharge have pointed out the advantages that time resolved determination of the energy flux would provide. Since both the PTP and ATP are limited to a time resolution in the range of seconds by their heat capacity, they cannot simply be optimized by a change in probe design. One possibility would be to add a sophisticated shutter system as it has been demonstrated by Breilmann et al. for deposition rate measurements [94]. The idea here is, to add a rotating shutter which is synchronized with the HiPIMS pulse. Proper design of the shutter would result in the substrate only being exposed to the energy flux at a specific time during the HiPIMS period, while no energy flux is present when the substrate is covered. This would result in a constant energy flux on the slower time scale of the thermal probe which is only attributed to a specific time frame. When designing such a system, specific attention has to be paid to the radiative energy flux coming from the shutter i.e. one has to make sure that the shutter remains at a low temperature to minimize the influence of radiative energy flux.
- The measurements with the ATP have pointed out the advantages this probe has especially in environments with little heat radiation from surrounding holders or chamber walls. However, to make this diagnostic more adjustable to different environments and further improve its performance, the design must be optimized and the speed of the electronics must be increased.
- One of the disadvantages of the PTP is the fact that it can only measure the energy flux with a relative measurement procedure i.e. it is mandatory to shut off the energy flux to obtain a measurement. In section 4.3.2, a possible solution is indicated in the paragraph describing the equilibrium temperature method. In principle, the maximum temperature that the probe will reach for a certain energy flux, can be extrapolated from the dT-curve of the temperature for a measurement time of only a few seconds. If the temperature of the heat reservoir for conductive cooling T_{cond} and the conduction coefficient α is known, the energy flux can be obtained without the need for shutting off the plasma. Since T_{cond} can be obtained by temperature measurement and α can be calibrated using the standard calibration experiment, the PTP could be modified to provide continuous energy flux data, which is also independent of the probe's heat capacity. However, one has to make sure to minimize the influence from gas cooling by proper probe design, as this contribution is not compensated by this method.
- Measurements in challenging environments like atmospheric plasma jets or surface DBD discharges have pointed out the amount of information that can be gained from careful evaluation of the dT-curve of the PTP. To fully understand the influence of different effects on the dT-curve, it would be desirable to create a theoretical model which is capable of simulating different contributions, with a special attention on the

cooling effect by surrounding surfaces. In principle this could be achieved by combining the theory presented in sections 2.2 and 4.3.2 to produce a theoretical dT-curve as a function of multiple external parameters.

- Collaborations with colleagues from the thin-film community have shown that often a precise knowledge of the substrate temperature during the deposition is just as desirable as the knowledge of the energy flux. However, due to different mounting systems and substrate holders, the cooling of the substrate is often not well-defined, which makes a calculation of the substrate temperature from the energy flux impossible. Therefore, it would be desirable to create a standardized substrate holder and mounting procedure which is carefully designed to provide a well-defined cooling of the substrate.
- Finally, the extensive investigations presented in publication [III] have indicated that the energy flux from any process gas-target-combination can be described by an empirical law as a function of the gas-target mass ratio. Additional investigations in this direction could provide universally applicable rules regarding the energy flux and could be used to define areas of not accessible energy flux values.

Bibliography

- [1] F. F. Chen and J. P. Chang. *Lecture Notes on Principles of Plasma Processing*. Springer US, 2003.
- [2] Stock Photo - FreeImages.com.
- [3] M. A. Lieberman and A. J. Lichtenberg. *Principles of plasma discharges and materials processing*. John Wiley & Sons, Inc., Hoboken, NJ, USA, apr 2005.
- [4] R. Hippler, H. Kersten, M. Schmidt, and K. H. Schoenbach. *Low Temperature Plasmas*. Wiley-Vch, 2007.
- [5] A. Piel. *Plasma Physics*, volume 1. Springer, Berlin, Heidelberg, 2013.
- [6] B. N. Chapman. *Glow Discharge Processes*. Wiley-Vch, 1980.
- [7] F. F. Chen. *Introduction to Plasma Physics and Controlled Fusion*. Springer International Publishing, Cham, 2016.
- [8] I. Langmuir. Oscillations in Ionized Gases. *Proceedings of the National Academy of Sciences of the United States of America*, 14(8):627–37, aug 1928.
- [9] U. Stroth. *Plasmaphysik Phänomene, Grundlagen, Anwendungen*. Vieweg+Teubner Verlag / Springer Fachmedien Wiesbaden GmbH, Wiesbaden, 2011.
- [10] D. Bohm. *The Characteristics of Electrical Discharges in Magnetic Fields*. McGraw-Hill, New York, 1949.
- [11] J. R. Roth. *Industrial Plasma Engineering*, volume 1. Institute of Physics Publishing, London, 1995.
- [12] J. Friedrich. *The Plasma Chemistry of Polymer Surfaces*. Wiley-VCH Verlag GmbH & Co. KGaA, Weinheim, Germany, apr 2012.
- [13] A. Anders. A structure zone diagram including plasma-based deposition and ion etching. *Thin Solid Films*, 518(15):4087–4090, 2010.
- [14] B. Movchan and A. Demshishin. Study of the structure and properties of thick vacuum condensates of nickel, titanium, tungsten, aluminum oxide and zirconium oxide. *Phys. Met. Metallogr. (Engl. Trans.)*, 28(653):60, 1969.
- [15] J. A. Thornton. Influence of apparatus geometry and deposition conditions on the structure and topography of thick sputtered coatings. *Journal of Vacuum Science and Technology*, 11(4):666, 1974.

-
- [16] H. Kersten, H. Steffen, D. Vender, and H. E. E. Wagner. On the ion energy transfer to the substrate during titanium deposition in a hollow cathode arc discharge. *Vacuum*, 46(3):305–308, 1995.
- [17] K. Ellmer, R. Mientus, and K. Et al. Calorimetric measurements with a heat flux transducer of the total power influx onto a substrate during magnetron sputtering. *Surface & Coatings Technology*, 116-119(1102-1106):1102–1106, sep 1999.
- [18] H. Kersten, H. Deutsch, H. Steffen, G. Kroesen, and R. Hippler. The energy balance at substrate surfaces during plasma processing. *Vacuum*, 63(3):385–431, aug 2001.
- [19] A. Pahl. Electron Energy Distribution Function — COMSOL Blog, 2014.
- [20] M. J. Druyvesteyn and F. M. Penning. The mechanism of electrical discharges in gases of low pressure. *Reviews of Modern Physics*, 12(2):87–174, 1940.
- [21] D. M. Mattox and G. J. Kominiak. Structure Modification by Ion Bombardment during Deposition. *Journal of Vacuum Science and Technology*, 9(1):528–532, 1972.
- [22] J.-W. Lim, Y. Ishikawa, K. Miyake, M. Yamashita, and M. Isshiki. Influence of Substrate Bias Voltage on the Properties of Cu Thin Films by Sputter Type Ion Beam Deposition. *Materials Transactions*, 43(6):1403–1408, 2002.
- [23] S. Kadlec, C. Quaeyhaegens, G. Knuyt, and L. Stals. Energy distribution of ions in an unbalanced magnetron plasma measured with energy-resolved mass spectrometry. *Surface & Coatings Technology*, 89(1-2):177–184, 1997.
- [24] N. Laegreid and G. K. Wehner. Sputtering Yields of Metals for Ar + and Ne + Ions with Energies from 50 to 600 ev. *Journal of Applied Physics*, 32(3):365–369, mar 1961.
- [25] A. Goehlich, D. Gillmann, and H. F. Döbele. Angular resolved energy distributions of sputtered atoms at low bombarding energy. *Nuclear Instruments and Methods in Physics Research, Section B: Beam Interactions with Materials and Atoms*, 164:834–839, 2000.
- [26] G. Betz and K. Wien. Energy and angular distributions of sputtered particles. *International Journal of Mass Spectrometry and Ion Processes*, 140(1):1–110, dec 1994.
- [27] D. Depla, S. Mahieu, T. Ono, T. Kenmotsu, and T. Muramoto. *Reactive Sputter Deposition*, volume 109 of *Springer Series in Materials Science*. Springer Berlin Heidelberg, Berlin, Heidelberg, 2008.
- [28] M. W. Thompson. II. The energy spectrum of ejected atoms during the high energy sputtering of gold. *Philosophical Magazine*, 18(152):377–414, 1968.
- [29] J. F. Ziegler, M. D. Ziegler, and J. P. Biersack. SRIM, the stopping and range of ions in matter. In *Web Science Conference*, 2010.

- [30] H. F. Winters, H. J. Coufal, and W. Eckstein. Influence of energy reflected from the target on thin film characteristics. *Journal of Vacuum Science & Technology A: Vacuum, Surfaces, and Films*, 11(3):657–663, may 1993.
- [31] W. D. Westwood. Calculation of deposition rates in diode sputtering systems. *Journal of Vacuum Science and Technology*, 15(1):1–9, 1978.
- [32] M. Stahl, T. Trottenberg, and H. Kersten. A calorimetric probe for plasma diagnostics. *The Review of scientific instruments*, 81(2):023504, feb 2010.
- [33] T. Trottenberg, V. Schneider, and H. Kersten. Measurement of the force on microparticles in a beam of energetic ions and neutral atoms. *Physics of Plasmas*, 17(10):774–780, 2010.
- [34] J. B. Hudson. *Surface science : an introduction*. Butterworth-Heinemann, 1992.
- [35] J. A. Thornton. Substrate heating in cylindrical magnetron sputtering sources. *Thin Solid Films*, 54(1):23–31, 1978.
- [36] S. D. Ekpe and S. K. Dew. Theoretical and experimental determination of the energy flux during magnetron sputter deposition onto an unbiased substrate. *Journal of Vacuum Science & Technology A: Vacuum, Surfaces, and Films*, 21(2):476, 2003.
- [37] A. Roth. *Vacuum technology*. North-Holland, 1990.
- [38] S. Dushman. *Scientific foundations of vacuum technique*. John Wiley & Sons, Inc., New York, 2 edition, 1962.
- [39] R. Piejak, V. Godyak, B. Alexandrovich, and N. Tishchenko. Surface temperature and thermal balance of probes immersed in high density plasma. *Plasma Sources Science and Technology*, 7(4):590–598, 1999.
- [40] M. Knudsen. Die molekulare Wärmeleitung der Gase und der Akkommodationskoeffizient. *Annalen der Physik*, 339(4):593–656, jan 1911.
- [41] R. G. Jahn. *Physics of electric propulsion*. Dover Publications, 2006.
- [42] A. Bouchoule, J.-P. Boeuf, A. Heron, and O. Duchemin. Physical investigations and developments of Hall plasma thrusters. *Plasma Physics and Controlled Fusion*, 46:B407–B421, dec 2004.
- [43] F. Cichocki, M. Merino, E. Ahedo, M. Smirnova, A. Mingo, and M. Dobkevicius. Electric Propulsion Subsystem Optimization for “Ion Beam Shepherd” Missions. In *Joint Conference of 30th ISTS, 34th IEPC and 6th NSAT*, 2015.
- [44] Ariane-group. Electric Ion Space Propulsion Systems and Thrusters.
- [45] T. Trottenberg, A. Spethmann, V. Schneider, M. Stahl, M. Giesenhagen, and H. Kersten. Non-Electrostatic Diagnostics for Ion Beams. *Contributions to Plasma Physics*, 52(7):584–592, aug 2012.

- [46] H. Leiter, R. Killinger, M. Boss, R. Braeg, M. Gollor, S. Weis, D. Feili, M. Tartz, H. Neumann, J. Haderspeck, D. Bock, and D. M. Di Cara. RIT-muX - The New Modular High Precision Micro Ion Propulsion System. In *43rd AIAA/ASME/SAE/ASEE Joint Propulsion Conference & Exhibit*, volume 5250, pages 1–12, 2007.
- [47] P. J. Kelly and R. D. Arnell. Magnetron sputtering: a review of recent developments and applications. *Vacuum*, 56(3):159–172, mar 2000.
- [48] J. A. Thornton. Magnetron sputtering: basic physics and application to cylindrical magnetrons. *Journal of Vacuum Science and Technology*, 15(2):171–177, mar 1978.
- [49] W. D. Westwood. *Sputter Deposition*. AVS, New York, 2003.
- [50] B. Window and N. Savvides. Charged particle fluxes from planar magnetron sputtering sources. *Journal of Vacuum Science & Technology A: Vacuum, Surfaces, and Films*, 4(2):196, 1986.
- [51] F. Adibi, I. Petrov, J. E. Greene, L. Hultman, and J. Sundgren. Effects of high-flux low-energy (20–100 eV) ion irradiation during deposition on the microstructure and preferred orientation of Ti_{0.5}Al_{0.5}N alloys grown by ultra-high-vacuum reactive magnetron sputtering. *Journal of Applied Physics*, 73(12):8580–8589, jun 1993.
- [52] I. Petrov. Use of an externally applied axial magnetic field to control ion/neutral flux ratios incident at the substrate during magnetron sputter deposition. *Journal of Vacuum Science & Technology A: Vacuum, Surfaces, and Films*, 10(5):3283, 1992.
- [53] M. Trant, M. Fischer, K. Thorwarth, S. Gauter, J. Patscheider, and H. J. Hug. Tunable ion flux density and its impact on AlN thin films deposited in a confocal DC magnetron sputtering system. *Surface & Coatings Technology*, 2018.
- [54] J. T. Gudmundsson, N. Brenning, D. Lundin, and U. Helmersson. High power impulse magnetron sputtering discharge. *Journal of Vacuum Science & Technology A*, 30(3):30801–30834, 2012.
- [55] V. Kouznetsov, K. Macák, J. M. Schneider, U. Helmersson, and I. Petrov. A novel pulsed magnetron sputter technique utilizing very high target power densities. *Surface and Coatings Technology*, 122(2-3):290–293, 1999.
- [56] A. Anders, J. Andersson, and A. P. Ehiasarian. High power impulse magnetron sputtering: Current-voltage-time characteristics indicate the onset of sustained self-sputtering. *Journal of Applied Physics*, 102(11):1–11, 2007.
- [57] S. Gauter, M. Fröhlich, W. Garkas, M. Polak, and H. Kersten. Calorimetric probe measurements for a high voltage pulsed substrate (PBII) in a HiPIMS process. *Plasma Sources Science and Technology*, 26(6):1–17, 2017.
- [58] J. Andersson and A. Anders. Gasless sputtering: Opportunities for ultraclean metal-lization, coatings in space, and propulsion. *Applied Physics Letters*, 92(22):221503, jun 2008.

- [59] M. Samuelsson, D. Lundin, J. Jensen, M. A. Raadu, J. T. Gudmundsson, and U. Helmersson. On the film density using high power impulse magnetron sputtering. *Surface & Coatings Technology*, 205(2):591–596, 2010.
- [60] H. Haberland, M. Karrais, and M. Mall. A new type of cluster and cluster ion source. *Zeitschrift für Physik D Atoms, Molecules and Clusters*, 20(1-4):413–415, mar 1991.
- [61] K. Wegner, P. Piseri, H. V. Tafreshi, and P. Milani. Cluster beam deposition: a tool for nanoscale science and technology. *Journal of Physics D: Applied Physics*, 39(22):R439–R459, nov 2006.
- [62] A. Choukourov, P. Pleskunov, D. Nikitin, V. Titov, A. Shelemin, M. Vaidulych, A. Kuzminova, P. Solař, J. Hanuš, J. Kousal, O. Kylián, D. Slavínská, and H. Biederman. Advances and challenges in the field of plasma polymer nanoparticles. *Beilstein Journal of Nanotechnology*, 8:2002–2014, sep 2017.
- [63] J. Pelletier and A. Anders. Plasma-blased ion implantation and deposition: A review of physics, technology, and applications. *Ieee Transactions on Plasma Science*, 33(6):1944–1959, 2005.
- [64] A. Anders. High power impulse magnetron sputtering and related discharges: Scalable plasma sources for plasma-based ion implantation and deposition. *Surface & Coatings Technology*, 204(18-19):2864–2868, 2010.
- [65] M. A. Lieberman. Model of plasma immersion ion implantation. *Journal of Applied Physics*, 66(7):2926–2929, oct 1989.
- [66] Z. Wu, X. Tian, Z. Wang, C. Gong, S. Yang, C. Ming, P. K. Chu, C. Ming Tan, and P. K. Chu. Microstructure and mechanical properties of CrN films fabricated by high power pulsed magnetron discharge plasma immersion ion implantation and deposition. *Review of Scientific Instruments*, 258(1):242–246, 2011.
- [67] H. M. Mott-Smith and I. Langmuir. The theory of collectors in gaseous discharges. *Physical Review*, 28(4):727–763, 1926.
- [68] I. H. Hutchinson. *Principles of plasma diagnostics*. Cambridge University Press, 2002.
- [69] G. Sauerbrey. Verwendung von Schwingquarzen zur Wägung dünner Schichten und zur Mikrowägung. *Zeitschrift für Physik*, 155(2):206–222, 1959.
- [70] I. G. Ltd. Model IL150 Thickness Monitor - Instruction Manual. pages 1–38.
- [71] C. G. Abbot. The silver disk pyrheliometer (with one plate). *Smithsonian Miscellaneous Collections*, 56(19):1–10, 1911.
- [72] S. Bornholdt, T. Peter, T. Strunskus, V. Zaporojtchenko, F. Faupel, and H. Kersten. The method of conventional calorimetric probes - A short review and application for the characterization of nanocluster sources. *Surface & Coatings Technology*, 205:5388–5392, 2011.

- [73] S. Bornholdt and H. Kersten. Transient calorimetric diagnostics for plasma processing. *The European Physical Journal D*, 67(8):176, 2013.
- [74] H. Kersten, D. Rohde, J. Berndt, H. Deutsch, and R. Hippler. Investigations on the energy influx at plasma processes by means of a simple thermal probe. *Thin Solid Films*, 377-378(0):585–591, 2000.
- [75] D. Lundin, M. Stahl, H. Kersten, and U. Helmersson. Energy flux measurements in high power impulse magnetron sputtering. *Journal of Physics D: Applied Physics*, 42(18):185202, 2009.
- [76] M. Čada, J. W. Bradley, G. C. B. Clarke, and P. J. Kelly. Measurement of energy transfer at an isolated substrate in a pulsed dc magnetron discharge. *Journal of Applied Physics*, 102:063301, 2007.
- [77] P.-A. Cormier, M. Stahl, A.-L. Thomann, R. Dussart, M. Wolter, N. Semmar, J. Mathias, and H. Kersten. On the measurement of energy fluxes in plasmas using a calorimetric probe and a thermopile sensor. *Journal of Physics D: Applied Physics*, 43(46):465201, 2010.
- [78] R. Gardon. An Instrument for the direct measurement of intense thermal radiation. *Review of Scientific Instruments*, 24:366, 1953.
- [79] H. Kersten, D. Rohde, H. Steffen, H. Deutsch, and R. Hippler. Die Bestimmung von Energieflüssen bei Plasmaoberflächenprozessen. *Galvanotechnik*, 96(12):2996–3007, 2005.
- [80] H. Steffen, H. Kersten, and H. Wulff. Investigation of the energy transfer to the substrate during titanium deposition in a hollow cathode arc. *Journal of Vacuum Science & Technology A*, 12:2780, 1994.
- [81] R. Wiese. *Neue Methoden der Diagnostik von Plasmaquellen*. PhD thesis, Ernst- Moritz- Arndt- Universität Greifswald, 2007.
- [82] M. Stahl. *Energiestrommessungen in Prozessplasmen*. Diplomarbeit, Christian-Albrechts-Universität zu Kiel, 2009.
- [83] Analog Devices. Monolithic Thermocouple Amplifiers with Cold Junction Compensation (AD594/AD595), 1999.
- [84] T. Kewitz, M. Fröhlich, and H. Kersten. Analysis of passive calorimetric probe measurements at high energy influxes. *EPJ Techniques and Instrumentation*, 4(1):1, 2017.
- [85] A. L. Thomann, N. Semmar, R. Dussart, J. Mathias, and V. Lang. Diagnostic system for plasma/surface energy transfer characterization. *Review of Scientific Instruments*, 77(3), 2006.
- [86] R. Wiese and H. Kersten. Einsatz einer Aktiven Thermosonde zur Diagnostik von Prozessplasmen. *Galvanotechnik*, 99(6), 2008.

- [87] B. Koch, W. Bohmeyer, G. Fussmann, P. Kornejew, and H.-D. Reiner. Energy flux measurements in a steady-state discharge at PSI-2. *Journal of Nuclear Materials*, 290-293:653–657, mar 2001.
- [88] R. Wendt, K. Ellmer, and K. Wiesemann. Thermal power at a substrate during ZnO:Al thin film deposition in a planar magnetron sputtering system. *Journal of Applied Physics*, 82(5):2115–2122, 1997.
- [89] R. F. Stebbings and B. G. Lindsay. Comments on the accuracy of absolute electron-impact ionization cross sections for molecules. *Journal of Chemical Physics*, 114(10):4741–4743, 2001.
- [90] U.-T. G. Limited. Model UT61A/61B/61C/61D/61E: Operating manual, 2008.
- [91] S. Gauter. *Energiestrommessungen in Plasmen mittels aktiver Thermosonde*. Master thesis, Kiel University, 2014.
- [92] National Instruments. USB-6009 Datasheet.
- [93] C. Bundesmann, C. Eichhorn, F. Scholze, D. Spemann, H. Neumann, F. Scortecci, H. Leiter, K. Holste, P. Klar, A. Bulit, K. Dannenmayer, and J. G. del Amo. Advanced Electric Propulsion Diagnostic Tools at IOM. *Procedia Engineering*, 185:1–8, jan 2017.
- [94] W. Breilmann, C. Maszl, J. Benedikt, and A. von Keudell. Dynamic of the growth flux at the substrate during high-power pulsed magnetron sputtering (HiPIMS) of titanium. *Journal of Physics D: Applied Physics*, 46(48):485204, 2013.

Curriculum Vitae

Name	Sven Gauter
Date of birth	15.10.1988
Place of birth	Eutin
Citizenship	German

Education

1995 - 1999	Grundschule Pönitz
1999 - 2008	Ostsee Gymnasium Timmendorfer Strand
2008	Abitur
2008 - 2012	Bachelor of Science in Physics at Kiel University
2012	Bachelor thesis: <i>Plasmadiagnostik an ATI-haltigen Plasmen unter Zugabe von Stickstoff</i>
2012 - 2014	Master of Science in Physics at Kiel University
2014	Master thesis: <i>Energiestrommessungen in Plasmen mittels aktiver Thermosonde</i>
2014 - 2018	Phd Student at Kiel University in the Plasma Technology group

Acknowledgments

First and foremost, I would like to thank Prof. Dr. Holger Kersten for giving me the opportunity to work as a PhD student in the Plasma Technology Group. I particularly enjoyed and valued the trustful atmosphere which created a flexible and creative working environment. I appreciate the constructive discussions -scientific and non-scientific- and the support he provided through good advice or simply through his relaxed, down-to-earth attitude.

A major part of the great working environment is attributed to the members of the Plasma Technology group, who I would like to thank for the constructive scientific exchange and the good company during coffee and lunch breaks etc.. A special thanks goes to Michael Poser and Volker Rohwer who were always available to fix, troubleshoot or help with mechanical or electrical challenges and provided a good amount of extra knowledge along the way. Without the company of my dear colleague and friend Fabian Haase, the work would have surely been less fun and motivating. His critical thinking and IT-expertise were of great value in our shared projects and in general as a second opinion on difficult questions.

Efficient adaption and modification of experiments and probes were only possible with the help of the competent and well equipped CAU workshop, which is why I would like to thank Michael Brix, Frank Brach and their whole team.

A special thanks goes to Tim Riedel from the Surface Physics working group at Kiel University for enduring countless spontaneous visits to his office and helping us out with the spot-welding machine and glass burners.

During the last three years I had the opportunity to visit other institutes and collaborate with many great scientists from all over the world. I particularly would like to thank

- Dr. Maik Fröhlich and colleagues from the INP in Greifswald for the opportunity to work on such an innovative system at the INP and for the nice month I spent in the picturesque town of Greifswald as part of the plasma surface technology group.
- Prof. Dr. Jörg Patscheider, Mathis Trant and Dr. Kerstin Thorwarth from the EMPA in Switzerland for their hospitality and interesting collaboration.
- Prof. Dr. Jeon Geon Han and his entire working group from the CAPST institute in South Korea for the fantastic months I spent in their beautiful country. Their kindness and hospitality made the work there a pleasure.
- Prof. Dr. Hyněk Biederman, Pavel Solar and their whole working group from the Charles University of Prague for their hospitality and the successful cooperation.

Finally, I would like to extend my special gratitude towards my whole family and my friends for their company and support during the last years.

Eidesstattliche Erklärung

Hiermit versichere ich an Eides statt, dass ich die vorliegende Arbeit selbstständig und ohne fremde Hilfe angefertigt habe. Ausschnitte, welche wörtlich oder sinngemäß aus Arbeiten anderer Autoren beruhen, sind als solche klar gekennzeichnet. Ich versichere außerdem, dass ich keine andere als die angegebene Literatur verwendet habe. Diese Versicherung schließt alle in dieser Arbeit enthaltenen Grafiken, Skizzen, bildlichen Darstellungen und dergleichen ein.

Die Arbeit als Ganzes wurde bisher keiner anderen Prüfungsbehörde vorgelegt. Teile dieser Arbeit wurden bereits in begutachteten wissenschaftlichen Fachzeitschriften veröffentlicht und sind als solche gekennzeichnet. Die in den Veröffentlichungen angeführten Quellenverweise sind in den Veröffentlichungen selbst und nicht zusätzlich im Literaturverzeichnis dieser Arbeit aufgeführt.

Abschließend erkläre ich, dass diese Arbeit unter Einhaltung der Regeln guter wissenschaftlicher Praxis der Deutschen Forschungsgemeinschaft entstanden ist.

Kiel, Juli 2018